

---

Electronic Theses and Dissertations, 2004-2019

---

2012

## Structure, Stability, Vibrational, Thermodynamic, And Catalytic Properties Of Metal Nanostructures: Size, Shape, Support, And Adsorbate Effects

Farzad Behafarid  
*University of Central Florida*



Part of the [Physics Commons](#)

Find similar works at: <https://stars.library.ucf.edu/etd>

University of Central Florida Libraries <http://library.ucf.edu>

This Doctoral Dissertation (Open Access) is brought to you for free and open access by STARS. It has been accepted for inclusion in Electronic Theses and Dissertations, 2004-2019 by an authorized administrator of STARS. For more information, please contact [STARS@ucf.edu](mailto:STARS@ucf.edu).

---

### STARS Citation

Behafarid, Farzad, "Structure, Stability, Vibrational, Thermodynamic, And Catalytic Properties Of Metal Nanostructures: Size, Shape, Support, And Adsorbate Effects" (2012). *Electronic Theses and Dissertations, 2004-2019*. 2299.

<https://stars.library.ucf.edu/etd/2299>

STRUCTURE, STABILITY, THERMODYNAMIC, AND CATALYTIC  
PROPERTIES OF METAL NANOSTRUCTURES: SIZE, SHAPE,  
SUPPORT AND ADSORBATE EFFECTS

by

FARZAD BEHAFARID

B.S. Sharif University of Technology, 2004

M.Sc. University of Tehran, 2007

M.Sc. University of Central Florida, 2010

A dissertation submitted in partial fulfillment of the requirements  
for the degree of Doctor of Philosophy  
in the Department of Physics  
in the College of Science  
at the University of Central Florida  
Orlando, Florida

Fall Term  
2012

Major Professor: Beatriz Roldan Cuenya

© 2012 Farzad Behafarid

## **ABSTRACT**

Recent advances in nanoscience and nanotechnology have provided the scientific community with exciting new opportunities to rationally design and fabricate materials at the nanometer scale with drastically different properties as compared to their bulk counterparts. In this dissertation, several challenges have been tackled in aspects related to nanoparticle (NP) synthesis and characterization, allowing us to make homogenous, size- and shape-selected NPs via the use of colloidal chemistry, and to gain in depth understanding of their distinct physical and chemical properties via the synergistic use of a variety of ex situ, in situ, and operando experimental tools. A variety of phenomena relevant to nanosized materials were investigated, including the role of the NP size and shape in the thermodynamic and electronic properties of NPs, their thermal stability, NP-support interactions, coarsening phenomena, and the evolution of the NP structure and chemical state under different environments and reaction conditions.

## OUTLINE

Recent advances in nanoscience and technology have provided the scientific community with new exciting opportunities to rationally design and fabricate materials at the nanometer scale with drastically different properties as compared to their bulk counterparts. A variety of challenges related to nanoparticle (NP) synthesis and materials characterization have been tackled, allowing us to make more homogenous, well defined, size- and shape-selected NPs, and to probe deeper and more comprehensively into their distinct properties. In this dissertation, a variety of phenomena relevant to nanosized materials are investigated, including the thermal stability of NPs and coarsening phenomena in different environments, the experimental determination of NP shapes, gaining insight into NP-support interactions, epitaxial relationships, and unusual thermodynamic and electronic properties of NPs, including the effect of adsorbates on the electron density of states of small clusters, and the chemical, and structural evolution of NPs under reaction conditions.

In chapter 2, a general description of different characterization tools that are used in this dissertation is provided. In chapter 3, the details of two different methods used for NP synthesis, namely inverse micelle encapsulation and physical vapor deposition (PVD) are described.

Chapter 4 describes the thermal stability and coarsening behavior of Pt NPs supported on  $\text{TiO}_2(110)$  and  $\gamma\text{-Al}_2\text{O}_3$  as a function of the synthesis method, support pre-treatment, and annealing environment. For the Pt/ $\text{TiO}_2(110)$  system, micelle-synthesized NPs showed remarkable stability against coarsening for annealing temperatures up to  $1060^\circ\text{C}$  in vacuum, in contrast to PVD-grown NPs. When comparing

different annealing environments ( $\text{H}_2$ ,  $\text{O}_2$ ,  $\text{H}_2\text{O}$ ), Pt NPs on  $\gamma\text{-Al}_2\text{O}_3$  annealed in  $\text{O}_2$  were found to be the least affected by coarsening, followed by those heated in  $\text{H}_2\text{O}$  vapor. The largest NP growth was observed for the sample annealed in  $\text{H}_2$ . The role of the  $\text{PtO}_x$  species formed under oxidizing conditions will be discussed.

In chapter 5, the shape of Pt and Au NPs and their epitaxial relationship with the  $\text{TiO}_2(110)$  support was extracted from scanning tunneling microscopy (STM) measurements. Three main categories of NP shapes were identified, and through shape modeling, the contribution of facets with different orientations was obtained as a function of the number of atoms in each NP. It was also shown that the micelle-synthesized Pt and Au NPs have an epitaxial relationship with the support, which is evident from the fact that they always have one symmetry axis parallel to  $\text{TiO}_2(110)$  atomic rows in  $[001]$  directions.

Chapter 6 describes how the presence of NPs on  $\text{TiO}_2(110)$  surface affects its reconstruction upon high temperature annealing in vacuum. In contrast to NP-free  $\text{TiO}_2(110)$  substrates, long and narrow  $\text{TiO}_2$  stripes are observed for Pt NP-decorated surfaces. This phenomenon is explained based on the stabilization of  $\text{TiO}_2$ , induced by Pt NPs, which hinders the desorption of oxygen atoms in  $\text{TiO}_2$  to vacuum.

In chapter 7, a systematic investigation of the thermodynamic properties of  $\gamma\text{-Al}_2\text{O}_3$ -supported Pt NPs and their evolution with decreasing NP size is presented. A combination of *in situ* extended x-ray absorption fine structure spectroscopy (EXAFS), *ex situ* transmission electron microscopy (TEM) measurements, and NP shape modeling is used to obtain the NPs shape, thermal expansion coefficient, and Debye

temperature. The unusual thermodynamic behavior of these NPs such as their negative thermal expansion and enhanced Debye temperature are discussed in detail.

Chapter 8 presents an investigation of the electronic properties of size-controlled  $\gamma$ -Al<sub>2</sub>O<sub>3</sub>-supported Pt NPs and their evolution with decreasing NP size and adsorbate (H<sub>2</sub>) coverage. The hydrogen coverage of Pt NPs at different temperatures was estimated based on XANES data and was found to be influenced by the NP size, and shape. In addition, correlations between the shift in the center of the unoccupied d-band density of states (theory) and energy shifts of the XANES spectra (experiment) upon hydrogen chemisorption as well as upon modification of the NP structure were established.

Chapter 9 is dedicated to an *operando* study, describing the evolution of the structure and oxidation state of ZrO<sub>2</sub>-supported Pd nanocatalysts during the *in-situ* selective reduction of NO in H<sub>2</sub> via EXAFS and XANES measurements.

To my wife, Roxana.



## ACKNOWLEDGEMENT

I would like to thank my supervisor and mentor, Prof. Beatriz Roldan Cuenya for her unwavering support and insightful guidance throughout my endeavor as a PhD candidate, and for giving me numerous research opportunities that have allowed me to achieve my goals as a researcher. Her enthusiasm and hard work, and her honest pursuit of scientific knowledge, have set a great example for me as a successful scientist. I feel lucky to be among her students and I am hopeful that our scientific collaborations will be continued in my entire professional carrier, in the same way that I am confident our friendship will be lasting through my personal life.

I want to also thank my lab members, Dr. Luis Ono, Dr, Jason Croy, Dr. Ahmed Naitabdi, Dr, Lindsay Merte, Dr. Estephania Lira, , Simon Mostafa, Jeronimo Matos, Mahdi Ahmadi, Hemma Mistry, and Sudeep Pandey for continuous scientific discussions and collaborations and above all for their life lasting friendship. Thanks also to our collaborators, Prof. Talat Rahman, Prof. Werner Keune, Prof. Anatoly Frenkel, and Prof. Judith Yang for providing me with their support and scientific insight.

Thanks also to my committee members Prof. Abdelkader Kara, Prof. Helge Heinrich, Prof. Lee Chow, and Prof. Winston Schoenfeld, for taking time to evaluate my work and for their constructive comments and discussions.

Special thanks to my wife and my best friend Roxana, who has been a great source of hope, joy and support, without whom this work would not have been accomplished.

# TABLE OF CONTENTS

ACKNOWLEDGEMENT .....	viii
LIST OF FIGURES .....	xii
LIST OF TABLES .....	xxiv
LIST OF ACRONYMS .....	xxvii
CHAPTER 1: INTRODUCTION .....	1
CHAPTER 2: MEASUREMENT TECHNIQUES .....	6
2.1 Scanning tunneling microscope (STM) .....	6
2.1.1 Fundamentals .....	6
2.1.2 Instrumentation .....	8
2.1.3 Tip preparation .....	12
2.1.4 STM images .....	13
2.2 Atomic force microscope (AFM) .....	14
2.2.1 Fundamentals .....	14
2.2.2 Instrumentation .....	18
2.2.3 AFM images .....	20
2.3 X ray photoelectron spectroscopy (XPS) .....	21
2.3.1 Fundamentals .....	21
2.3.2 Instrumentation .....	24
2.3.3 XPS spectra .....	26
2.4 X-ray absorption spectroscopy (XAS): extended X-ray absorption fine- structure (EXAFS) and X-ray absorption near-edge structure (XANES) spectroscopy .....	28
2.4.1 Fundamentals .....	28
2.4.2 Instrumentation .....	32
2.4.3 XAS data .....	33
CHAPTER 3: NANOPARTICLE SYNTHESIS METHODS .....	37
3.1 Inverse micelle encapsulation .....	37
3.2 Physical vapor deposition via electron beam evaporation .....	40
CHAPTER 4: THERMAL STABILITY AND COARSENING PHENOMENA OF METAL NANOPARTICLES AND THE INFLUENCE OF THE ENVIRONMENT AND SUPPORT PRE-TREATMENT: Pt/TiO <sub>2</sub> (110) AND Pt/ $\gamma$ -Al <sub>2</sub> O <sub>3</sub> .....	43

4.1	Introduction .....	43
4.2	Sample preparation methods and experimental.....	48
4.3	Theoretical and simulation methods.....	53
4.3.1	Ostwald ripening .....	54
4.3.2	Diffusion-coalescence .....	57
4.4	Results .....	60
4.4.1	Pt NPs evaporated on pristine TiO <sub>2</sub> (110) (STM) .....	60
4.4.2	Pt NPs evaporated on polymer-modified TiO <sub>2</sub> (110) (STM) .....	64
4.4.3	Micellar Pt NPs/TiO <sub>2</sub> (110) (STM) .....	68
4.4.4	Micellar Pt NPs/ $\gamma$ -Al <sub>2</sub> O <sub>3</sub> (EXAFS).....	73
4.5	Discussion.....	81
4.5.1	STM observations .....	81
4.5.2	Simulation of coarsening mechanisms.....	88
4.5.3	<i>In situ</i> investigation of coarsening phenomena: environmental effects .....	98
4.6	Conclusions.....	102
CHAPTER 5: SHAPE DETERMINATION OF NANOPARTICLES AND EPITAXIAL RELATION WITH THE UNDERLYING SUPPORT .....		104
5.1	Introduction .....	104
5.2	Experimental .....	106
5.3	Results and discussion .....	108
5.4	Conclusions.....	128
CHAPTER 6: NANOPARTICLE-SUPPORT INTERACTIONS .....		130
6.1	Introduction .....	130
6.2	Experimental .....	131
6.3	Results and discussion .....	132
6.4	Conclusions.....	144
CHAPTER 7: THERMODYNAMIC PROPERTIES OF $\gamma$ -Al <sub>2</sub> O <sub>3</sub> SUPPORTED Pt NANOPARTICLES: SIZE, SHAPE, SUPPORT, AND ADSORBATE EFFECTS ..		146
7.1	Introduction .....	146
7.2	Experimental and theoretical methods .....	150
7.2.1	Sample preparation.....	150
7.2.2	Morphological characterization (TEM).....	151
7.2.3	Structural and vibrational characterization (EXAFS) .....	153
7.2.4	Nanoparticle shape modeling.....	159
7.3	Results .....	163
7.4	Discussion.....	175
7.4.1	Anomalous lattice dynamics and thermal properties of supported, size-and shape-selected Pt nanoparticles.....	175
7.4.2	Debye temperature .....	180
7.5	Conclusions.....	187

CHAPTER 8: ELECTRONIC PROPERTIES AND CHARGE TRANSFER PHENOMENA IN Pt NANOPARTICLES SUPPORTED ON $\gamma$ -Al <sub>2</sub> O <sub>3</sub> : SIZE, SHAPE, SUPPORT, AND ADSORBATE EFFECTS.....	189
8.1 Introduction .....	189
8.2 Experimental and theoretical methods .....	192
8.2.1 Sample preparation.....	192
8.2.2 Structural, and electronic characterization (XAFS).....	192
8.3 Results .....	197
8.4 Discussion.....	212
8.4.1 Adsorbate effects .....	214
8.4.2 Support effects.....	220
8.5 Conclusions.....	223
CHAPTER 9: EVOLUTION OF THE STRUCTURE AND CHEMICAL STATE OF Pd NANOPARTICLES DURING THE <i>IN SITU</i> CATALYTIC REDUCTION OF NO WITH H <sub>2</sub> .....	224
9.1 Introduction .....	224
9.2 Experimental .....	226
9.2.1 Sample preparation and characterization.....	226
9.2.2 Reactivity data .....	227
9.2.3 Structural and chemical analysis (EXAFS, XANES).....	228
9.3 Results .....	228
9.3.1 Structure, and morphological (TEM) .....	228
9.3.2 Catalytic reactivity .....	229
9.3.3 Evolution of the structure and chemical composition of Pd NP catalysts under <i>operando</i> condition (XANES, EXAFS) .....	231
9.4 Discussion.....	239
9.5 Conclusions.....	246
REFERENCES.....	248
LIST OF PUBLICATIONS .....	282

## LIST OF FIGURES

- Fig. 1: (a) Free electron waves near the metal surface decay exponentially outside the metal (into the vacuum). (b) If the insulating gap (e.g. vacuum) is small enough, an overlap between the two electron wave functions will be observed. However, no net current would be detected, since the Fermi energies are in the same level. (c) A net current is obtained when a bias voltage is applied between the two metals. .... 7
- Fig. 2: Schematic of the STM setup. (a) The apex of the tip is in tunneling distance from the sample. The tip atom closest to the sample surface is responsible for most of the tunneling current. (b) Schematic of the STM setup and electronic controllers. The scanner tube can move the tip in x, y and z directions. The pre-amplifier is installed as close as possible to the STM setup to minimize noise on the tunneling current (~ 0.1 nA). In one of the most common STM operation modes, the feedback loop maintains a constant tunneling current by adjusting the tip height..... 9
- Fig. 3: Two different STM measurement modes: (a) constant height mode, in which the changes in the tunneling current are used to extract information on the morphology of the sample, and (b) constant current mode, in which the changes in the tip height determine the morphology. .... 10
- Fig. 4: Different stages during the movement of a piezoelectric inchworm motor one step upward. Three sections of the motor, namely up, center, and down could be activated separately. By applying the voltage to sections U and D they expand laterally and lock inside the outer cylinder. The middle section C expands vertically upon applying the voltage. The parts activated by the voltage are shown with red color, while the inactive sections are shown with blue color. In the first stage, only section D is locked and the upper part is free (a). Then the middle part expands (b), and section U locks as well (c). Subsequently, the lower part releases (d), and section C contracts to its initial length (e). Now section D locks (f) and section U unlocks (g). The latter motion returns the setup to a similar position as that depicted in (a), but vertically displaced upward. By tuning the expansion of the middle section, the length of each step of the inchworm motor could be adjusted..... 11
- Fig. 5: (a) Partially etched tungsten wire inside a NaOH solution. (b) Example of a tungsten tip prepared by wet etching acquired with an optical microscope. ... 13
- Fig. 6: STM images of (a) a Au(111) single crystal showing atomic resolution and (b) a TiO<sub>2</sub>(110) surface with a (1x2) surface reconstruction. The color coding shows the higher points with a yellow color and the lower points with a dark red color. TiO<sub>2</sub> atomic rows in the [001] direction could be seen

	on the three terraces of the TiO <sub>2</sub> surface displayed. The height of each TiO <sub>2</sub> step is 3.2 Å and the distance between atomic rows is 13 Å (twice that in between the rows in the 1x1 reconstruction). The images were obtained using a SPECS Aarhus-150 STM. ....	14
Fig. 7:	(a) Schematic of a mass-spring harmonic oscillator driven by a periodic force. The amplitude (b) and phase of the oscillation for different damping constant is shown as a function of the frequency of the driving force.....	15
Fig. 8:	Change in the resonance frequency induced by the tip-sample interaction. The shift in resonance frequency is positive for repulsive forces and negative for attractive forces. ....	17
Fig. 9:	(a) Schematic of an AFM setup including the laser source, the cantilever reflecting the laser, and the mirror guiding the reflected beam towards a four-panel photodetector. (b) Schematic of an actual multimode AFM head from digital instruments (VEECO metrology group) used for the measurements shown in this thesis.....	19
Fig. 10:	AFM image of Pt NPs supported on SiO <sub>2</sub> /Si(111). ....	20
Fig. 11:	Schematic of the XPS process. Absorption of the x-ray photon ejects one of the core electrons (in this case from a 1s level) to the vacuum level. Such electron is subsequently collected by the electron analyzer. The Fermi levels of the sample and the analyzer are equal since both are grounded. The photoelectron's kinetic energy is measured by the electron energy analyzer. ....	21
Fig. 12:	Spin-orbit energy splitting for different energy levels. The degeneracy is (2J+1) for each state. For instance, for 2p states, the degeneracy is four for 2p <sub>3/2</sub> (3/2, 1/2, -1/2, -3/2) and two for 2p <sub>1/2</sub> (1/2 and -1/2). Therefore, the intensity ratio obtained when comparing both XPS peaks should be proportional to the number of electrons in each state. The XPS area obtained for 2p <sub>3/2</sub> states should be twice as large as that of 2p <sub>1/2</sub> . Similarly, it could be shown that the count rate ratio (i.e. ratio of XPS peak areas) for 3d <sub>5/2</sub> and 3d <sub>3/2</sub> states is 6/4. ....	23
Fig. 13:	Schematic illustration of a monochromatic XPS setup including a double anode x-ray source, monochromator, sample, lens system, hemispherical analyzer, and multichannel electron detector. ....	25
Fig. 14:	XPS spectrum of a Si(111) wafer terminated by a thin SiO <sub>2</sub> layer. (a) The survey spectrum measured over a large energy range is used for the initial identification of the elemental composition of the sample including Si and O peaks. (b) High resolution spectrum of the Si-2p core level region showing silicon in three different chemical states: Si, Si <sup>4+</sup> in SiO <sub>2</sub> , and an intermediate state of Si <sup>δ+</sup> in SiO <sub>x</sub> with x having a value between 0 and 2.	

The red curve shows the overall fit to the black experimental data (noisy black curve). .....	27
Fig. 15: Schematic of the origin of EXAFS oscillations. Constructive (destructive) interference of outgoing and back scattered photoelectron waves results in higher (lower) density of electronic states at the position of the absorbing atom. In the region close to the absorption edge (XANES region), the photoelectrons have low kinetic energy (large wavelength), and therefore, the interference phenomena are not contributing to the absorption coefficient. Only in the EXAFS region (>150 eV above the edge) the absorption coefficient is affected by interferences of photoelectrons.....	30
Fig. 16: Schematic of the EXAFS and XANES measurement setup including (i) a large synchrotron loop accelerating electrons with high speed, (ii) undulators that produce a high brilliance white x-ray, (iii) the monochromator that selects the x-ray energy to the desired value for the excitation of a given absorption edge, (iv) ionization chambers that measure the x-ray intensity before and after transmission through the sample and also the reference sample. The inset shows a plot of the measured absorption coefficient with two absorption edges. ....	33
Fig. 17: (a) Pt-L <sub>3</sub> absorption edge and the pre- and post-edge background fitted to the data for normalization. (b) Normalized absorption coefficient, using the equation $\mu_{normalized}(E) = \frac{\mu(E) - \text{Pre\_edge}(E)}{\text{Post\_edge}(E) - \text{Pre\_edge}(E)}$ .....	34
Fig. 18: K <sup>2</sup> weighted EXAFS data of a platinum foil in k- and r-space representations.....	36
Fig. 19: Schematic of the nanoparticle preparation via inverse micelle encapsulation. (a) Poly-(styrene)-block-poly(2-vinylpyridine) (PS-b-P2VP) diblock copolymer (b) Formation of micelles after dissolving the polymer in toluene. (c) Addition of metal atoms to the micelle core upon dissolution of the metal-salt precursor. (d) Deposition of one monolayer of micellar NPs on a flat substrate by dip-coating. (e) Array of micellar NPs deposited on a flat substrate. (f) Polymer removal using an O <sub>2</sub> -plasma treatment, resulting in the formation of a clean array of size-selected NPs.....	38
Fig. 20: XPS spectra from the C-1s core level region of micellar Pt NPs supported on TiO <sub>2</sub> (110) (S3) acquired before and after O <sub>2</sub> -plasma exposure at room temperature (RT) for 120 min. No residual C was observed on this sample after the atomic oxygen treatment. ....	39
Fig. 21: Schematic of an electron beam evaporator. The hot filament around the metal anode emits electrons toward the metal target which are accelerated since the metal target is connected to a positive voltage (~1000V). In this	

manner, material from the heated metal target is sublimated and deposited on the sample surface. ....	41
Fig. 22: STM images of Pt NPs supported on TiO <sub>2</sub> (110) synthesized via (a) inverse micelle encapsulation and (b) physical vapor deposition. Both images were obtained at RT after annealing at 1060°C in vacuum. ....	42
Fig. 23: STS measurements (I-V curve) of a sputtered-annealed reduced TiO <sub>2</sub> (110) surface showing a characteristic ~3.2 eV bandgap.....	49
Fig. 24: Heat of sublimation of Pt atoms (H <sub>SUB</sub> ) calculated using the MBA model and adatom formation energy (E <sub>AF</sub> ) calculated by Yang et al. <sup>87</sup> , using molecular dynamics and nudged elastic band calculations for Pt clusters with Wulff polyhedral shape. The horizontal dashed line indicates the heat of sublimation of bulk Pt. ....	55
Fig. 25: STM images of 0.09 ML of Pt evaporated on pristine TiO <sub>2</sub> (110) acquired at RT after annealing in UHV at 930°C (a,b), 1030°C (c,d), and 1060°C (e,f) for 10 min. ....	61
Fig. 26: Height (a) and interparticle distance (b) histograms obtained from the STM data of Pt NPs evaporated on pristine TiO <sub>2</sub> (110) shown in Fig. 25 after annealing at 930°C (squares), 1030°C (triangles), and 1060°C (circles).....	62
Fig. 27: STM images of 0.09 ML of Pt evaporated on polymer-coated TiO <sub>2</sub> (110) taken at RT after an O <sub>2</sub> -plasma treatment and subsequent annealing in UHV at 930°C (a,b), 1030°C (c,d), and 1060°C (e,f) for 10 min. ....	66
Fig. 28: (a) Height and (b) interparticle distance histograms obtained from the STM data of Pt NPs evaporated on polymer-coated TiO <sub>2</sub> (110) shown in Fig. 3 after an O <sub>2</sub> -plasma treatment and subsequent annealing at 930°C (squares), 1030°C (triangles), and 1060°C (circles). The population has been normalized for different measurements to have the same area under the curve of 100.....	68
Fig. 29: <i>In situ</i> STM images (200 nm x200 nm) of Pt NPs deposited on TiO <sub>2</sub> (110) after an <i>in situ</i> O <sub>2</sub> -plasma treatment and subsequent annealing in UHV at (a) 300°C for 20 min and (b) 1000°C for 10 min.....	69
Fig. 30: <i>In situ</i> STM images of Pt NPs deposited on TiO <sub>2</sub> (110) acquired after O <sub>2</sub> -plasma and subsequent annealing in UHV at (a,b) 1010°C, (c,d) 1040°C, (e,f) 1060°C, and (g,h) 2 <sup>nd</sup> 1060°C, for 10 min at each temperature. The size of the images in the left column is (200 x 200 nm) and in the right is (100 x 100 nm). ....	70
Fig. 31: Normalized histograms of (a) NP height and (b) interparticle distance obtained from STM images acquired after isochronical annealing in 10°C	



intervals (10 min) from 1010°C to 1060°C. The lines in (a) are guides for the eye, while the data in (b) were fitted using Gaussian curves. For each temperature, the above statistics include 300-670 NPs..... 71

Fig. 32: Fourier transform magnitudes of  $k^2$ -weighted Pt-L<sub>3</sub> edge EXAFS spectra acquired for samples S4-S6 at RT in H<sub>2</sub> after an initial common pre-treatment in O<sub>2</sub> at 375°C followed by reduction at 375°C in H<sub>2</sub> and subsequent annealing in O<sub>2</sub> (S4), H<sub>2</sub>O (S5) and H<sub>2</sub> (S6) at 450°C for 3 hours. All samples were reduced *in situ* at 375°C in H<sub>2</sub> before the acquisition of the EXAFS data. A representative first-shell fit of the EXAFS data of S6 is included as inset..... 74

Fig. 33:  $k^2$ -weighted EXAFS in k-space of similarly prepared samples acquired at RT in H<sub>2</sub> after annealing at 450°C for 3 hours in different environments: O<sub>2</sub> (S4), H<sub>2</sub>O (S5), and H<sub>2</sub> (S6)..... 75

Fig. 34: Pt-L<sub>3</sub> XANES absorption peak of sample S5 acquired *in situ* during a thermal treatment at 450°C in H<sub>2</sub>O vapor+He. The progressive increase in the intensity of the absorption peak (or white line) with increasing annealing time (together with changes in the EXAFS region) reveal the gradual oxidation of the NPs under this environment. For reference, the data of the as-prepared sample after reduction in H<sub>2</sub> at 375°C are shown..... 77

Fig. 35: (a) Normalized absorption coefficient corresponding to the Pt-L<sub>3</sub> edge and (b)  $k^2$ -weighted Fourier transform magnitudes of Pt L<sub>3</sub>-edge EXAFS spectra of samples S4-S6 acquired at 450°C in O<sub>2</sub>, H<sub>2</sub>O and H<sub>2</sub>. ..... 79

Fig. 36:  $k^2$ -weighted Fourier transform magnitudes of Pt L<sub>3</sub>-edge EXAFS spectra acquired for samples S4, S5 and S6 at 450°C under different environments. The data were fitted with two components: a Pt-Pt scattering path (hatched area) and a Pt-O path (filled area). The fit results are shown in Table 4. .... 80

Fig. 37: Thermal evolution of the number of Pt NPs present on terraces and at step edges for (a) PVD-grown and (b) micellar NP samples..... 84

Fig. 38: Best fits obtained from Ostwald-ripening simulations of the pristine (a,c) and polymer-coated (b,d) Pt/TiO<sub>2</sub>(110) samples. The hatched and solid filled areas are the initial and the final experimental size distributions, respectively. The solid line displays the simulated final size distribution obtained after annealing treatments in UHV at 1030 °C (a,b) and 1060 °C (c,d). .... 89

Fig. 39: Best fits obtained from a diffusion-coalescence simulation for pristine (a,c) and polymer-coated (b,d) Pt/TiO<sub>2</sub>(110) samples. The hatched and solid filled areas are the initial and the final experimental size distributions, respectively. The solid line displays the simulated final size distribution

obtained after annealing treatments in UHV at 1030 °C (a,b) and 1060 °C (c,d). Since the independent parameter in the diffusion-coalescence model is the NP volume [eq. (19)], the calculations were done using NP volume histogram (graph above) and were subsequently rescaled to display the NP height in Fig. 40. .... 92

Fig. 40: Best fits obtained from a diffusion-coalescence simulation for pristine (a,c) and polymer-coated (b,d) Pt/TiO<sub>2</sub>(110) samples. The hatched and solid filled areas are the initial and the final experimental size distributions, respectively. The solid line displays the simulated final size distribution obtained after annealing treatments in UHV at 1030 °C (a,b) and 1060 °C (c,d). .... 93

Fig. 41: Spline fits to the experimental STM data (a) and to the Ostwald ripening simulation results (b) for a polymer pre-coated sample (S2) annealed at 1060°C. The graph in (c) compares the smoothed (spline-fit) Ostwald-ripening simulation histogram to the smoothed experimental histogram. From the latter comparison, the fit quality parameter Q is obtained. .... 95

Fig. 42: Schematic representation of the evolution of the structure and chemical state of our inverse micelle prepared Pt/γ-Al<sub>2</sub>O<sub>3</sub> samples (S4-S6) under various thermal and chemical treatments inferred from the analysis of *in situ* EXAFS and *ex situ* STEM data. .... 100

Fig. 43: Schematic representation of the evolution of the structure of micellar NPs supported on TiO<sub>2</sub> after different chemical and thermal treatments. STM images of polymer-free micellar Pt NPs on TiO<sub>2</sub>(110) acquired at RT after annealing at (e) 150°C and (f) 1000°C are also shown. The hexagonal NP arrangement is observed in (e), but also significant roughness of the TiO<sub>2</sub> support. A flatter and atomically-resolved TiO<sub>2</sub> surface with shape-resolved Pt NPs is evident in (f). Typical large scale AFM images of micellar NPs prepared using two different PS(x)-P2VP(y) polymers with (x: 53000, y: 43800) in (g) and (x: 27700, y: 4300) in (h). .... 107

Fig. 44: STM images of micellar Pt NPs supported on TiO<sub>2</sub>(110) acquired at RT after annealing at 1000°C. Four main categories of NP shapes are displayed (a-d) with the corresponding models (e-h). The facets at the perimeter of TD NPs are perpendicular to the NP/support interface. The apparent slopes observed around them in (d) are due to tip convolution effects. .... 109

Fig. 45: STM images of micellar Au NPs on TiO<sub>2</sub>(110) acquired at RT after sample annealing at 1000°C. The following NP shapes are shown: (a) TA, (b) TB, and (c) tilted TA. The STM cross section of the NP in (c) (along the dotted line) and a schematic of the corresponding facets are shown in (d). A Au(211) facet was found at the NP/support interface. The inset in (d) shows a model of the reconstructed NP shape. .... 111

- Fig. 46: STM images of micellar Pt NPs on TiO<sub>2</sub>(110) acquired at RT after annealing at 1000°C. Examples of variations in the shapes of NPs within a given category (TA-TD) based on distinct  $A_{100}/A_{111}$  ratios are shown (a,c,e,f). NPs of TA and TD in (a, c, f) have a lower  $A_{100}/A_{111}$  ratio than those in Fig. 44(a, b, d), respectively. In rare cases, some NPs were found to be rotated by (b) 30° (TA) and (d) 45° (TB) with respect to the TiO<sub>2</sub>(110)-[001] direction. .... 113
- Fig. 47: Morphological features within different types of NP shapes which are not affected by tip-convolution effects are shown in (a-d) and highlighted in pink. The height of the NPs and the dimensions of the top facet (L1 and L2) in (a-d) are used to reconstruct the 3D shape of the NPs (e-h) using a MATLAB code. .... 114
- Fig. 48: (a) Ratios of {100}/{111} surface areas ( $A_{100}/A_{111}$ ) as a function of the corresponding surface energy ratios ( $\gamma_{100}/\gamma_{111}$ ) following the Wulff theorem. Representative model NP shapes are shown as inset. For  $\gamma_{100}/\gamma_{111} > 1.7$ , no {100} facets are present, and the NPs adopt octahedron shapes. For  $0.87 < \gamma_{100}/\gamma_{111} < 1.15$ , the NPs adopt cuboctahedron and truncated cuboctahedron shapes. For  $\gamma_{100}/\gamma_{111} > 0.58$ , cubic shapes are found. (b) STM-resolved  $A_{100}/A_{111}$  ratios (left axis) and corresponding  $\gamma_{100}/\gamma_{111}$  ratios (right axis) obtained from (a) plotted versus the number of atoms within each NP. Schematics of the NP shapes observed are included as insets in (b). .... 117
- Fig. 49: Total overlap between different strained interfacial Pt facets and the TiO<sub>2</sub>(110) surface. In the schematics of (b, d), the TiO<sub>2</sub> lattice is shown as grey rods separated by 2.94 Å in the [001]-direction and 6.48 Å in [1 $\bar{1}$ 0]. The maximum overlap was found by changing the values of the strain parameters  $\epsilon_x$ ,  $\epsilon_y$  and in-plane rotation angle ( $\theta$ ) for a Pt(100) facet. For the purpose of display,  $\epsilon_y$  was fixed in (a) to its calculated optimum value (6.4%). For the Pt(100) facet, the rotational angles giving rise to the optimum interfacial match were 0°, 90°, and 180° for  $\epsilon_x = -6.4\%$ . These orientations are in agreement with our STM observations. To investigate the epitaxial relation of the rotated NPs, the rotation angle ( $\theta$ ) was fixed to the value observed via STM, i.e. 45° for the TB NP in (c), Fig. 46(d). The strain coefficients  $\epsilon_x$  and  $\epsilon_y$  were then varied until the maximum overlap between the Pt and TiO<sub>2</sub> lattices was obtained. The maximum overlap for the 45° rotated TB NP was achieved for  $\epsilon_x = -0.3\%$  and  $\epsilon_y = -10.0\%$ . .... 123
- Fig. 50: (a,c) Calculations of the epitaxial relationship between Pt(111) interfacial facets in TA NPs and the TiO<sub>2</sub>(110) support. Pt atoms overlapping with the TiO<sub>2</sub>(110) surface unit cell are drawn in blue and highlighted by open black

circles. The remaining Pt atoms are drawn in red. The data in (a) and (b) correspond to Pt NPs analogous to those in Fig. 44(a) and Fig. 46(a) (TA, not rotated). Due to the 6-fold symmetry of the Pt(111) facet, the best overlap between both lattices was found at 0°, 60°, 120° and 180°. For better visibility, only a cross sectional view of the complete plot is shown in (a). The overlap corresponds to a Pt(111) interfacial layer expanded by 6.4% in the [001] direction of TiO<sub>2</sub>(110) and contracted by 10.0% along 110, as shown in (b). For the rotated TA NP in (c), the rotation angle was kept fixed to the STM-observed value ( $\theta=30^\circ$ ), and the strain parameters ( $\epsilon_x$ , and  $\epsilon_y$ ) were varied until a maximum overlap of the Pt(111) interfacial facet and the substrate lattice was obtained for  $\epsilon_x=1.7\%$  and  $\epsilon_y=6.5\%$  (c). .. 124

- Fig. 51: RT STM images of micellar NPs in S1 (a,c-f) and S2 (b), deposited on TiO<sub>2</sub> (110) and acquired after polymer removal by an *in situ* O<sub>2</sub>-plasma treatment and subsequent isochronal annealing in UHV at 1010 °C (a,b), 1020 °C (c,d), 1060 °C (e,f). ..... 133
- Fig. 52: (100 x 100 nm) *In-situ* STM images obtained on (a) micellar Pt NPs deposited on TiO<sub>2</sub>(110) and (b) the pristine TiO<sub>2</sub>(110) substrate after annealing at 1060°C and 1030°C for 10 min, respectively. The TiO<sub>2</sub> substrate appears atomically resolved. The circles in (a) highlight the presence of NPs at different substrate sites: (1) NPs on the center of TiO<sub>2</sub> terraces [blue circles]; (2) NPs on steps parallel to the [001] direction [green circles]; (3) NPs at the end of TiO<sub>2</sub> nanostripes, at [1 $\bar{1}$ 0] steps [white circles]. ..... 135
- Fig. 53: RT STM images of Pt NPs in S2 (a,b), and Au NPs in S3 (c,d) on TiO<sub>2</sub>(110) acquired after annealing in UHV at 1000°C for 10 min. .... 137
- Fig. 54: Schematics showing the formation of nanostripes attached to micellar NPs. Upon sample annealing above 1000°C in UHV, oxygen desorbs from the TiO<sub>2</sub>(110) surface to vacuum and Ti<sup>3+</sup> goes into the bulk of the crystal. TiO<sub>2</sub> rows along the [001] direction shrink in length and in some cases disappear. However, the stabilization of [1 $\bar{1}$ 0] TiO<sub>2</sub> step edges by micellar NPs prevents the disruption of the rows attached to the NPs, resulting in the formation of nanostripes. The insets in (b) correspond to STM images representative of this process. The white scale bars in the STM images correspond to 10 nm..... 142
- Fig. 55: (a) HAADF STEM image of micellar Pt NPs on  $\gamma$ -Al<sub>2</sub>O<sub>3</sub> (S1) obtained by L. Li, and Z. Zhang (Prof. Judith Yang's group) at the University of Pittsburgh. (b) Histogram of the NP diameter distribution..... 152
- Fig. 56: k<sup>2</sup>-weighted EXAFS data in k-space for reduced Pt NPs on  $\gamma$ -Al<sub>2</sub>O<sub>3</sub> measured in H<sub>e</sub>: (a) S2 and in H<sub>2</sub>: (b) S3, (c) S4, (d) S5 at different temperatures (from 173 to 648 K)..... 164

- Fig. 57: (a)  $k^2$ -weighted EXAFS data in r-space of Pt NPs supported on  $\gamma$ - $\text{Al}_2\text{O}_3$  in samples S1, S2, S8 and a bulk Pt foil. All samples were measured in a  $\text{H}_2$  atmosphere at RT after NP reduction. The range of the Fourier transform is  $2\text{-}11 \text{ \AA}^{-1}$ . (b) Temperature-dependent EXAFS data in r-space of S2 measured in  $\text{H}_2$ . The inset displays the experimental data acquired at 173 K together with the corresponding multiple-scattering fit. .... 165
- Fig. 58: Fourier transform magnitudes of  $k^2$ -weighted EXAFS data and 1<sup>st</sup>-shell multiple-data-set fit for sample S5 measured in  $\text{H}_2$  at 183 K (a), 293 K (b), 408 K (c), 528 K (d), and 648 K (e)..... 167
- Fig. 59: (a) Temperature-dependent Pt-Pt bond lengths (R) obtained from EXAFS measurements on samples S1, S2, S7, S8 and a bulk Pt foil. All samples were measured in  $\text{H}_2$ . (b) Pt-Pt distances from S2 measured in He and  $\text{H}_2$ . In (a) and (b) solid lines represent linear fits to the experimental data. (c) Calculated median of the Pt-Pt bond-lengths of an unsupported clean  $\text{Pt}_{22}$  NP (open symbols, *ab initio* MD calculations) and a H-covered  $\text{Pt}_{22}\text{H}_M$  NP (solid symbols, model for S1) plotted as a function of temperature. Calculations were performed by M. Alcántara Ortigoza and G. Shafai in Prof. Talat Rahman's group at the University of Central Florida. Additional details on the calculations can be found in Ref. 38. .... 168
- Fig. 60: Average thermal expansion coefficient ( $\alpha$ ) extracted from the linear fit of the EXAFS data shown in Fig. 59a and those from additional samples described in Table 13, plotted as a function of (a) the 1<sup>st</sup> NN coordination number, and (b) the average TEM NP diameter. The inset in (a) displays calculated thermal expansion coefficients for an unsupported clean (adsorbate-free)  $\text{Pt}_{22}$  NP (model of S1) and a H-covered  $\text{Pt}_{22}$  NP. .... 171
- Fig. 61: Dynamic contribution ( $\sigma_d^2$ ) to the total EXAFS Debye-Waller factor obtained for micellar Pt NPs on  $\gamma$ - $\text{Al}_2\text{O}_3$  (S1-S5, S7) under  $\text{H}_2$  flow and analyzed with the CDM (solid lines). Symbols correspond to the temperatures at which the EXAFS data were measured. For reference, analogous data of a bulk-like Pt foil are also shown. In addition, the calculated thermal evolution of the mean square bond-projected bond-length fluctuations ( $\sigma_d^2$ )<sub>th</sub> of a H-covered  $\text{Pt}_{22}$  NP (model of S1) for several thermodynamically stable states ( $\text{Pt}_{22}\text{H}_{22}$ ,  $\text{Pt}_{22}\text{H}_{25}$  and  $\text{Pt}_{22}\text{H}_{29}$ ) are also included. .... 172
- Fig. 62: Debye temperature extracted from the CDM fit of EXAFS data displayed in Fig. 61 as a function of (a) the TEM NP diameter, and (b) the total number of atoms in a NP ( $N_t$ ) normalized by the number of surface atoms ( $N_s$ ),  $N_t/N_s$ . The values in (b) were obtained for the model NP shapes that best fitted the coordination numbers extracted from the MS analysis of low-temperature EXAFS data and the measured TEM NP diameters. The insets in (b) display the model NP shapes representative of each sample.

The error margins reported for the  $N_t/N_s$  values reflect the degeneracy of NP shapes obtained as best representation of each experimental sample. The Debye temperature of a bulk-like Pt foil is also shown for reference (dashed line). In (a), the Debye temperatures calculated for  $Pt_{22}H_{22}$  and  $Pt_{22}$  (models for S1) are also shown. .... 174

Fig. 63: Normalized absorption coefficient,  $\mu(E)$ , versus energy (XANES region) for the Pt-L<sub>3</sub> edge of Pt NPs. The samples were measured at (a) RT and (b) low temperature (173 K for S1 and S2, 180 K for S8 and S9) in H<sub>2</sub> after reduction. Similar data from a Pt foil (bulk) are also displayed for reference in (a). .... 198

Fig. 64: Normalized absorption coefficient,  $\mu(E)$ , versus energy (XANES region) for the Pt-L<sub>3</sub> edge of Pt NPs (~0.8 nm for S1 and S2, ~1 nm for S3 and S4) on  $\gamma$ -Al<sub>2</sub>O<sub>3</sub>. Samples were measured at RT in H<sub>2</sub> after reduction. Similar data from a Pt foil (bulk) are also shown for reference. .... 199

Fig. 65: Normalized absorption coefficient,  $\mu(E)$ , versus energy (XANES region) for the Pt-L<sub>3</sub> edge of Pt NPs on  $\gamma$ -Al<sub>2</sub>O<sub>3</sub>. The samples in (a-c) were measured at RT in H<sub>2</sub> after reduction (S1-S4). Similar data from a Pt foil are also displayed for reference. Sample S2 was measured in H<sub>2</sub> and He at 173 K (d). .... 200

Fig. 66: Normalized absorption coefficient,  $\mu(E)$ , versus energy (XANES region) for the Pt-L<sub>3</sub> edge of Pt NPs on  $\gamma$ -Al<sub>2</sub>O<sub>3</sub>: (a) S1, (b) S2, (c) S4, (d) S3, (e) S9, (f) S8. Temperature dependent data acquired in H<sub>2</sub> from 173 K to 648 K are shown for all samples. The insets correspond to model NP shapes representative of the NPs in each of the samples. For the large NPs (S8 and S9), a large degeneracy of shapes was obtained, and the models shown in (e,f) are only a guide of the possible NP structures. .... 201

Fig. 67: Shift in the energy of the Pt-L<sub>3</sub> absorption edge of Pt NPs on  $\gamma$ -Al<sub>2</sub>O<sub>3</sub> with respect to a bulk Pt reference as a function of: (a) the 1<sup>st</sup> nearest neighbor coordination number ( $N_1$ ), (c) the TEM NP diameter from Ref. 41 (b) Evolution of the  $\Delta$ XANES area (peak B) of NPs with different sizes as a function of  $N_1$ . The  $\Delta$ XANES plots were obtained by subtracting XANES spectra measured under H<sub>2</sub> at 648 K (nearly adsorbate-free) from those measured at RT under H<sub>2</sub> (nearly H-saturated). .... 203

Fig. 68: Shift in the energy of the Pt-L<sub>3</sub> absorption edge of Pt NPs on  $\gamma$ -Al<sub>2</sub>O<sub>3</sub> with respect to a bulk Pt reference as a function of: (a) the 1<sup>st</sup> nearest neighbor (NN) coordination number ( $N_1$ ) and (c) the TEM NP diameter from Ref. 41 (b) Evolution of the  $\Delta$ XANES area (peak B) of NPs with different sizes as a function of  $N_1$ . The  $\Delta$ XANES plots were obtained by subtracting XANES spectra measured in H<sub>2</sub> at 648 K (nearly adsorbate-free) from those measured at low temperature under H<sub>2</sub> (H-saturated). The minimum low temperature achieved in our experimental setup was slightly different for

different samples: 173K (S1, S2), 188K (S4), 183K (S5, S6), 166 K (S7), 180 K (S8,S9)..... 204

Fig. 69: Difference XANES spectra ( $\Delta$ XANES) from the Pt-L<sub>3</sub> absorption edge of Pt NPs on  $\gamma$ -Al<sub>2</sub>O<sub>3</sub> displayed as a function of the NP size (a), and the measurement temperature for NPs in S1 (b) and S9 (c). All measurements were conducted in a H<sub>2</sub> environment. In all plots, the 648 K data are subtracted from those acquired at lower temperatures [RT in (a) and variable temperatures in (b) and (c)] in order to deconvolute the adsorbate effect, since no significant H<sub>2</sub> effect is expected at 648 K..... 206

Fig. 70: (a) Temperature dependence of the absorption peak energy (Pt-L<sub>3</sub>) of a selected set of Pt NPs on  $\gamma$ -Al<sub>2</sub>O<sub>3</sub> samples: S1, S2, S4-S9. All samples were measured in H<sub>2</sub> after reduction. (b) Shift in the Pt-L<sub>3</sub> absorption peak energy of NPs with different sizes measured in H<sub>2</sub> at RT with respect to data from the same samples acquired at 648 K plotted versus the relative number of surface atoms in each NP ( $N_s/N_t$ ). A bulk Pt foil has been used as reference. (c) Energy shift of the Pt-L<sub>3</sub> absorption edge of Pt NPs measured at 648 K with respect to bulk Pt (RT) versus the relative number of atoms within the NPs in contact with the NP support ( $N_c/N_t$ ). All samples were measured in H<sub>2</sub> after NP reduction. .... 208

Fig. 71: (a) Energy shift (LT-648 K) versus  $N_s/N_t$ . (b)  $\Delta$ XANES (LT-648 K) peak B area versus  $N_s/N_t$ , and (c) versus the number of broken bonds at the NP surface normalized by the total number of atoms within the NP ( $N_t$ ) for S1-S6..... 209

Fig. 72: (a) Evolution of the  $\Delta$ XANES peak B area (see inset for definition of peak B) of NPs with different sizes as a function of temperature. All samples were measured in H<sub>2</sub> after NP reduction. (b) the area of the  $\Delta$ XANES peak B normalized by  $N_s/N_t$  and by the area of peak B of S6 measured at 183 K (1H for each surface Pt atom for larger NPs). The  $N_s/N_t$  normalization compensates for the fact that larger NPs have a lower number of atoms at their surface affected by H adsorption.  $\Delta$ XANES (RT – 648 K) peak B area versus (c) the relative number of atoms at the NP surface ( $N_s/N_t$ ), and (d) the relative number of broken bonds at the NP surface ( $broken/N_t$ ). The broken bonds reflect the presence of Pt atoms at the NP surface with coordination less than 12. The inset in (a) displays a typical  $\Delta$ XANES spectra and the shaded area corresponds to peak B..... 211

Fig. 73: Conversion and selectivity data as a function of temperature for the steady state H<sub>2</sub>-SCR NO reduction over micellar Pd NPs supported on ZrO<sub>2</sub>. .... 230

Fig. 74: Pd-K edge XANES spectra recorded after polymer removal (in O<sub>2</sub> at 375°C, as-prepared), after reduction (in H<sub>2</sub> at 240°C), and at different temperatures during the H<sub>2</sub>-SCR NO reduction. Reference spectra for PdO and bulk Pd are shown as well. .... 232

- Fig. 75:  $\Delta$ XANES spectra obtained at various stages of the H<sub>2</sub>-SCR NO reduction. The data correspond to XANES spectra acquired at different temperatures from which the spectrum of the bulk-like Pd foil measured at RT has been subtracted..... 233
- Fig. 76: k<sup>2</sup>-weighted Fourier transform Pd K-edge EXAFS spectra (*r*-space) taken after reduction and during various stages of the H<sub>2</sub>-SCR NO reduction. Bulk Pd and PdO spectra are shown as reference. The k-range for the Fourier transform was 2.5 Å<sup>-1</sup> < k < 10 Å<sup>-1</sup> ..... 235
- Fig. 77: (a) Fourier transform Pd K-edge EXAFS spectrum (*r*-space) recorded at 120°C, along with the total fit and the Pd-Pd and Pd-X contribution. (b) Dependence of the 1<sup>st</sup> NN coordination number on the reaction temperature during the H<sub>2</sub>-SCR NO reduction over Pd NPs supported on ZrO<sub>2</sub>: the Pd-Pd and the Pd-X contribution obtained from the fitting of *in situ* EXAFS spectra are shown. The dashed gray line indicates the Pd-Pd coordination number after NP reduction in H<sub>2</sub> and before reactant exposure. (c) Pd-Pd bond distance as a function of temperature. The dashed gray line indicates the Pd-Pd distance after NP reduction in H<sub>2</sub>, while the dashed blue line corresponds to the bulk value..... 238
- Fig. 78: Schematic representation of the structure and chemical state of our Pd nanocatalysts at various stages of the H<sub>2</sub>-SCR NO reduction..... 246



## LIST OF TABLES

Table 1:	Summary of the <i>ex situ</i> and <i>in situ</i> treatments applied to samples S4-S6....	52
Table 2:	Average NP height (h), interparticle distance (IP), density of NPs on the support, and aspect ratio extracted from the analysis of RT STM measurements acquired after annealing at the indicated temperatures. The data displayed correspond to Pt NPs evaporated on (a) pristine TiO <sub>2</sub> (110), (b) polymer-coated TiO <sub>2</sub> (110), and (c) micellar Pt NPs deposited on TiO <sub>2</sub> (110). The standard deviations are included in parenthesis.....	64
Table 3:	First nearest neighbor coordination numbers (NN1), Pt-Pt distances (R), atomic disorders ( $\sigma^2$ ), and NP sizes extracted from EXAFS and STEM data (diameter) after sample exposure to different <i>in situ</i> thermal treatments in O <sub>2</sub> (S4), H <sub>2</sub> O (S5), and H <sub>2</sub> (S6). .....	76
Table 4:	First-nearest neighbor coordination number (NN1), interatomic distance (R) and disorder ( $\sigma^2$ ) parameters of the Pt-Pt and Pt-O contributions extracted from <i>in situ</i> EXAFS measurements acquired during thermal treatments in O <sub>2</sub> (S4), H <sub>2</sub> O (S5), and H <sub>2</sub> (S6) at 450°C. ....	78
Table 5:	Total energy barrier ( $E_{tot}$ ), support effect ( $K_S$ ), and diffusion coefficient ( $D_C$ ) obtained from the best fit of the Ostwald-ripening and diffusion-coalescence models to our experimental NP size distributions. The experimental data correspond to UHV evaporated Pt NPs deposited on pristine and polymer-coated TiO <sub>2</sub> (110). The estimated errors are given within parenthesis.....	90
Table 6:	Simulation quality factors (Q) for pristine (S1) and polymer pre-coated (S2) samples obtained for the Ostwald-ripening and diffusion-coalescence coarsening models. ....	96
Table 7:	Epitaxial relation between different strained interfacial Pt facets and the TiO <sub>2</sub> (110) surface, including the corresponding lattice mismatch. The number of TiO <sub>2</sub> and Pt unit cells giving rise to the obtained overlap is represented by the parameter $n_{TiO_2}:n_{Pt}$ . For example, $n_{TiO_2}:n_{Pt} = 3:2$ reflects that the overlap between the Pt and TiO <sub>2</sub> lattices occurs every 3 surface unit cells of TiO <sub>2</sub> and 2 of Pt. ....	125
Table 8:	Epitaxial relation between different strained interfacial Au facets and the TiO <sub>2</sub> (110) surface, including the corresponding lattice mismatch.....	126

Table 9: Number of relevant independent data points and variables in the fits of temperature-dependent EXAFS data, as well as the values of the reduced $\chi^2$ and r-factor obtained from the fits.....	155
Table 10: The best fit values of the third cumulants (in $\text{\AA}^3$ ) obtained from multiple-data-set fits at different temperatures.....	156
Table 11: Coordination numbers (N), distances of each coordination shell to the absorbing atom (r), and bond length disorder parameters ( $\sigma^2$ ) obtained from the multiple scattering analysis of EXAFS data acquired in $\text{H}_2$ on reduced micellar Pt NPs supported on $\gamma\text{-Al}_2\text{O}_3$ (sample S2) at 173 K. Uncertainties are shown in parentheses. More examples of similar data obtained for some of the other samples and bulk Pt are included in Ref. 36. The best fit value for the energy origin correction $E_0$ was 9.9 (4) eV, the third cumulant was 0.00000 (2) $\text{\AA}^3$ , and the disorder parameter of the double-scattering path to the 1NN was 0.0033(22) $\text{\AA}^2$ . Only the distance correction to the 1NN was varied independently from the others, the rest were constrained with the isotropic lattice expansion/contraction factor, $\varepsilon$ . The best fit value of $\varepsilon$ was 0.0000(7), and its uncertainty was used to evaluate the error bars of the distances to 2NN through 4NN.....	158
Table 12: Model polyhedron shapes for fcc-Pt NPs providing the best fit to the experimental coordination numbers (EXAFS) and volume-weighted NP diameters (TEM). The average and volume-weighted TEM diameters, the total number of atoms in each NP ( $N_t$ ), the ratio of the number of Pt atoms at the NP surface and perimeter to $N_t$ ( $N_s/N_t$ ), and the ratio of the number of Pt atoms in contact with the support to $N_t$ ( $N_c/N_t$ ) are given. A factor (Q) representing the deviations of the coordination numbers and diameter of each of the model shapes with respect to the experimental samples are also included.....	161
Table 13: Parameters used for the synthesis of micellar Pt NPs, including polymer type (PS-PVP) and the ratio (L) between the metal salt loading and the molecular weight of the polymer head (P2VP). Also included are the mean and the volume-weighted TEM diameters. By comparing structural information obtained via EXAFS (1 <sup>st</sup> -4 <sup>th</sup> NN CNs) and TEM (NP diameters) with a database containing fcc-cluster shapes, the ratio of the number of surface atoms to the total number of atoms in a NP ( $N_s/N_t$ ) and the ratio of the number of atoms in contact with the substrate to the total number of atoms ( $N_c/N_t$ ) were obtained. The largest facets within each NP were selected as facets in contact with the support: (111) for S1-S4, S6, and (100) for S5. The static disorders ( $\sigma_s^2$ ) obtained from the analysis of EXAFS data are also shown. The largest values of $\sigma_s^2$ were generally observed for the samples with the largest NP/support interface (S1 and S4). .....	162

Table 14: Experimental (EXAFS) and theoretical (DFT) average 1 <sup>st</sup> -NN bond lengths of Pt NPs with different sizes and shapes given as a fraction of the respective bulk values. All experimental samples but S2 were H <sub>2</sub> -passivated and supported on $\gamma$ -Al <sub>2</sub> O <sub>3</sub> . S2 was also measured in He. The NPs analyzed theoretically were unsupported and free of adsorbates, with the exception of S1, which was also investigated with different H coverages. The experimental bulk Pt-Pt reference distances are 2.762 (2) Å at 154 K, 2.765 (4) Å at 300 K, and 2.78 (1) Å at 700 K. The calculated bulk Pt-Pt distance is 2.805 Å at 0 K. The DFT calculations were only carried out on Pt NPs containing less than 100 atoms.....	170
Table 15: First nearest-neighbor coordination number ( $N_1$ ), thermal expansion coefficient ( $\alpha$ ), and Debye temperature ( $\Theta_D$ ) of samples S1–S9 and of a bulk-like Pt foil. All samples were measured in H <sub>2</sub> . S2 was also measured in He.....	175
Table 16: Parameters used for the synthesis of micellar Pt NPs, including polymer type (PS-PVP) and the ratio (L) between the metal salt loading and the molecular weight of the polymer head (P2VP). Also included are the mean TEM diameters from Ref. 41. By comparing structural information obtained via EXAFS (1 <sup>st</sup> -4 <sup>th</sup> nearest neighbor coordination numbers) and TEM (NP diameters) with a database containing fcc-cluster shapes, the ratio of the number of surface atoms to the total number of atoms in a NP ( $N_s/N_t$ ) and the ratio of the number of atoms in contact with the substrate to the total number of atoms ( $N_c/N_t$ ) were obtained (see details in Ref. 41). The NP shapes obtained for large NPs in S7-S9 are not shown in this table due to the large shape degeneracy for the obtained coordination number and TEM diameter. ....	195
Table 17: Summary of the EXAFS results acquired on micellar Pd NPs supported on ZrO <sub>2</sub> : 1 <sup>st</sup> NN coordination numbers [ $N_{Pd-Pd}$ , $N_{Pd-O}$ ], the corresponding distances [ $d_{Pd-Pd}$ , $d_{Pd-O}$ ], and Debye Waller factors [ $\sigma^2_{Pd-Pd}$ , $\sigma^2_{Pd-O}$ ]. In addition, fit quality parameters such as the R-factor and reduced $\chi^2$ are also given, together with the $k$ - and $r$ -ranges. Fit uncertainties are presented in parentheses.....	237

## LIST OF ACRONYMS

AFM	Atomic Force Microscopy
BNL	Brookhaven National Laboratory
CDM	Correlated Debye Model
CN	Coordination Number
DFT	Density Functional Theory
EFM	Electrostatic Force Microscopy
EXAFS	Extended X-ray Absorption Fine-Structure
HAADF	High Angle Annular Dark Field
LDOS	Local Density of (Electronic) States
MBE	Molecular Beam Epitaxy
NN	Nearest Neighbor
NP	Nanoparticle
NSLS	National Synchrotron Light Source
P2VP	Poly-2-Vinyl Pyridine
PDOS	Phonon Density of States
PVD	Physical Vapor Deposition
PS	Polystyrene
RT	Room Temperature
SCR	Selective Catalytic Reduction
SEM	Scanning Electron Microscopy
SMSI	Strong Metal-Support Interaction

SPM	Scanning Probe Microscope
STM	Scanning Tunneling Microscopy
STEM	Scanning Transmission Electron Microscopy
STS	Scanning Tunneling Spectroscopy
TEM	Transmission Electron Microscopy
XAFS	X-ray Absorption Fine Structure
XANES	X-ray Absorption Near Edge Structure
XAS	X-ray Absorption Spectroscopy
XPS	X-ray Photoelectron Spectroscopy
UHV	Ultra High Vacuum

## CHAPTER 1: INTRODUCTION

Numerous recent exciting technological developments are based on taking advantage of unusual properties of metal nanostructures as compared to bulk materials, such as their different electronic, chemical, structural, magnetic, and optical properties.<sup>1-</sup>

<sup>34</sup> In order to fully exploit these opportunities and to rationally design, fabricate, and utilize nano-sized materials, not only a thorough understanding of their properties is needed, but also a comprehensive picture of how these properties evolve under different environmental conditions, such as at elevated temperatures, and under different chemical atmospheres. In fact, the physical and chemical properties of nanosized materials might be significantly altered depending on their size, shape, crystalline structure, chemical state, support material, gaseous environment, surrounding pressure, and temperature. Therefore, great care should be taken in understanding and controlling these parameters in order to conclude whether the scientific findings of a given study could be generalized to other material systems.

Different surface science and spectroscopy techniques were used in this dissertation, including atomic force microscopy (AFM), scanning tunneling microscopy (STM), x-ray photoelectron spectroscopy (XPS), and x-ray absorption spectroscopy (XAS). In chapter 2, the fundamental physical concepts underlying the experimental tools are described together with instrumentation details and examples of typical data.

Two methods for synthesizing metal NPs are used throughout this dissertation, namely, the inverse micelle encapsulation method and physical vapor deposition (PVD). Micelle prepared NPs can be deposited on planar substrates using dip coating, drop

coating, and spin coating, and on powder substrates *via* impregnation. The PVD method can be used to deposit metal NPs on planar surfaces under vacuum conditions. These synthetic routes are described in chapter 3.

One of the most important challenges in the synthesis of NPs for a variety of industrial applications is to avoid their agglomeration. NP growth phenomena could adversely affect their performance (e.g. catalytic deactivation) or change the NP's chemical properties toward undesired products (e.g. change in selectivity). Synthesizing the NPs via inverse micelle encapsulation, guarantees the lateral separation of the NPs by the polymer tails (PS group), that extend outward from the micelle core. The PS groups repel other micelles and keep the metal NPs away from each other. However, after polymer removal, coarsening may still occur. In chapter 4, two different coarsening pathways, namely, Ostwald ripening and diffusion-coalescence, are investigated using STM upon high temperature annealing of PVD and micelle-prepared Pt NPs supported on TiO<sub>2</sub>(110). The role of different surface pre-treatments in the stability of NPs was studied. A comparison was also made between micelle- and PVD-prepared NPs, with the micellar NPs demonstrating a superior stability against coarsening or NP mobility. In addition, the effect of different environments, namely O<sub>2</sub>, H<sub>2</sub> and H<sub>2</sub>O on the coarsening behavior of micelle-synthesized Pt NPs supported on  $\gamma$ -Al<sub>2</sub>O<sub>3</sub> was investigated using extended x-ray absorption fine structure (EXAFS) and x-ray absorption near-edge structure (XANES) spectroscopies.

Another factor that has recently attracted a lot of attention is the effect of NP shape on its properties, including chemical reactivity. NPs with different shapes feature different ratios of crystalline facets, which might lead to distinct catalytic activity and

selectivity. Also, the NP shape affects the number of low-coordinated surface atoms at corners and edges, which are known to display distinct electronic and chemical properties. Furthermore, for supported NPs, the NP-support interaction is expected to influence the thermodynamic equilibrium shape of the NPs depending on the interfacial binding energy as well as the degree of interfacial order, e.g. the absence or presence of an epitaxial relationship. Such interaction should also be more pronounced for 2D nanoparticles with high interfacial area as compared to 3D NPs. In chapter 5, the shapes of micellar Pt NPs supported on  $\text{TiO}_2(110)$  are directly resolved by STM. With the aid of NP shape modeling, the number of atoms in each NP and also the ratio of different facet areas were extracted for all resolved NP shapes. In addition, certain epitaxial relationships between the NPs and the  $\text{TiO}_2 [110]$  substrate were observed, with the edge of the NPs being in registry with  $\text{TiO}_2(110)$ -[001] rows. A good NP-support epitaxial relationship could facilitate charge transfer phenomena and lead to strain in the system, both of which might lead to novel NP functionalities.

NP-support interactions are also one of the main factors affecting the thermodynamical and electronic properties of NPs. For some systems, the so called strong metal-support interaction (SMSI) is known to dramatically affect the NPs' catalytic reactivity *via* their encapsulation with a thin support overlayer blocking the NPs' surface active sites. Nevertheless, the support itself might also be affected by the presence of NPs. For instance, NPs can catalytically facilitate the oxidation or reduction of certain support materials such as  $\text{TiO}_2$  depending on the heat treatment environment. In chapter 6, it is demonstrated that the presence of Pt and Au NPs also affects the morphology of the  $\text{TiO}_2(110)$  surface upon high temperature treatments in vacuum. In



particular, the formation of long nanostripes (up to 80 nm) attached to the NPs and having similar width as the NP diameter was evidenced.

X-ray absorption spectroscopy (XAS) is a powerful technique for studying nanoscale systems under realistic industrial-conditions, such as at elevated temperatures and under atmospheric or high pressure gas or liquid environments. This technique is able to provide information regarding the composition, chemical state, and crystalline properties of NPs such as crystalline structure, lattice parameter, and bond length disorder, as well as thermodynamic properties such as the coefficient of thermal expansion, and the Debye temperature. Insight on the electronic properties of NPs such as charge transfer phenomena and adsorbate effects can also be inferred. Chapter 7 is dedicated to discussing the unusual thermodynamic properties of  $\gamma\text{-Al}_2\text{O}_3$  supported Pt NPs measured by XAS, including their enhanced Debye temperature and negative thermal expansion. These effects are attributed to adsorbate and support effects, and to some extent also to the specific way that EXAFS probes such thermodynamic properties.

In chapter 8 XANES measurements are used to assess the electronic properties of Pt NPs supported on  $\gamma\text{-Al}_2\text{O}_3$ . In particular, the hydrogen coverage on the surface of Pt NPs is estimated at different temperatures, and it was shown that for small Pt NPs, more than one hydrogen atom could be stabilized per surface Pt atom.

As was mentioned before, one of the most exciting aspects of XAS measurements is the fact that they can be carried out under *operando* conditions, while the samples are effectively contributing to a catalytic reaction. In chapter 9, structure, chemical state,

and reactivity correlations are investigated during the selective reduction of NO over Pd NPs on ZrO<sub>2</sub>.

## CHAPTER 2: MEASUREMENT TECHNIQUES

### 2.1 Scanning tunneling microscope (STM)

#### 2.1.1 Fundamentals

The technique of STM was developed in 1981 by Gerd Binnig and Heinrich Rohrer to image conductive surfaces with atomic resolution. Since then it has revolutionized our understanding of surface science by allowing us to directly image surfaces with exceptional resolution. Unlike normal optical microscopes and scanning electron microscopes (SEM), there is no lens system involved in the STM imaging process.

The working principle of STM is based on a quantum tunneling effect that allows electrons to tunnel through a small vacuum gap (a few Angstroms) between a sharp conductive tip and a conductive or semiconducting sample when a bias voltage is applied (Fig. 1). Although the electrons could tunnel through the tip-sample gap without a bias voltage, no net current would be obtained (Fig. 1b). By applying the bias voltage, a net current is obtained due to the difference between the Fermi levels of the sample and the tip. The STM tip can approach and feel the sample surface through the tunneling current without any physical contact.

For small bias voltages and assuming a constant density of empty electronic states for the tip, the tunneling current ( $I_t$ ) decreases exponentially away from the sample surface within the vacuum gap between the tip and the sample:

$$I_t \sim \rho_s(E_F)V_b \exp\left(-\sqrt{\frac{8m\Phi}{\hbar}}z\right) \quad (1)$$

, where  $V_b$  is the applied bias voltage between the tip and the sample,  $z$  is the distance between the tip and the sample,  $\bar{\Phi}$  is the average work function of the tip and sample, and  $\rho_s(E_F)$  is the electron density of states near the Fermi level.

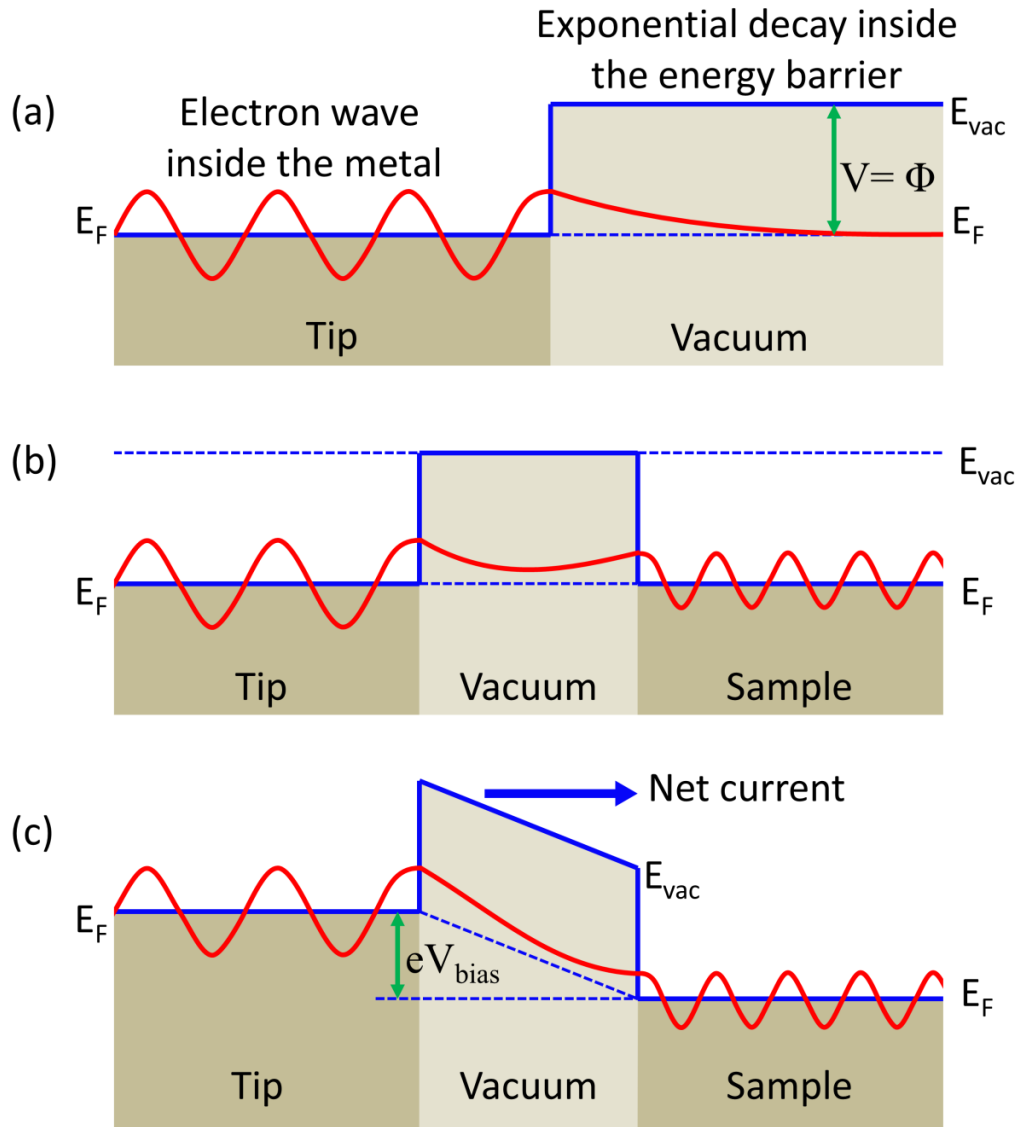


Fig. 1: (a) Free electron waves near the metal surface decay exponentially outside the metal (into the vacuum). (b) If the insulating gap (e.g. vacuum) is small enough, an overlap between the two electron wave functions will be observed. However, no net current would be detected, since the Fermi energies are in the same level. (c) A net current is obtained when a bias voltage is applied between the two metals.

The exponential behavior of the tunneling current as a function of the vacuum gap size results in drastic changes in the measured current with small changes in tip-sample distance and is responsible for the excellent z-resolution of STM ( $\sim 0.1 \text{ \AA}$ ). In fact, the outmost atom of the tip apex (the closest to the surface) is responsible for as much as 90% of the tunneling current, since other atoms only a few Angstroms further away do not contribute significantly due to the exponential dependence of  $I_t$  with distance, Fig. 2a.

### **2.1.2 Instrumentation**

A schematic of the STM scanner and the electronic controllers is shown in Fig. 2b. The STM scanner tube is made of a piezoelectric material. Piezoelectric materials have the property of converting mechanical stress to voltage and vice versa. Therefore, such materials are ideal for applications in which very small deformations ( $<4\%$ ) are desired. In our example, by applying a voltage to four electrical pads on the side of a scanner tube (X+, X-, Y+, Y-), it bends in x and y directions. Applying the voltage to electrical pads on the top and bottom of the scanner tube also allows control of the tip position in the z direction. The STM tip scans the surface line by line and the controller collects the data (height or current) to image the surface.

STM works in two different modes: constant height and constant tunneling current. In both cases the voltage is constant. In constant height mode, the tip moves above the surface without any height adjustment (no feedback) and the system measures the tunneling current. The changes in the tunneling current determine the surface morphology, with higher current when the tip is closer to the surface (Fig. 3a) or when

regions of higher electron density of states are probed. This measurement mode could only be used for flat surfaces since otherwise the tip may crash on the surface.

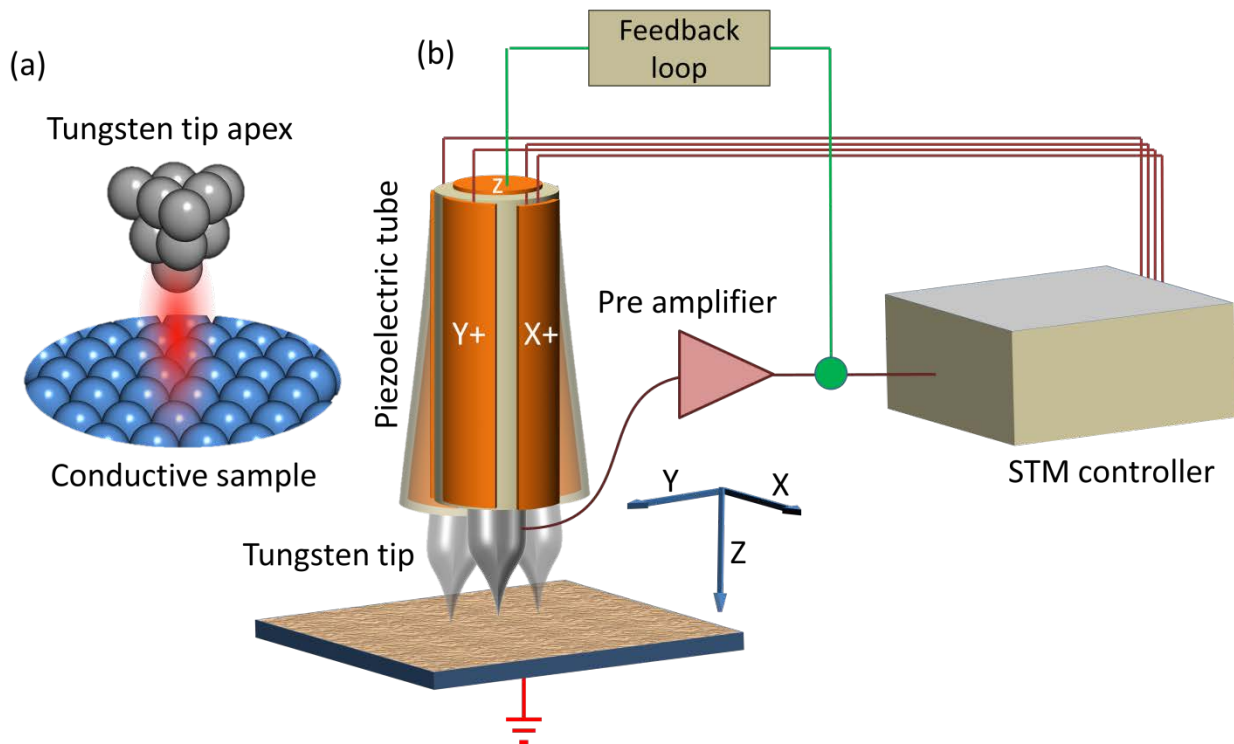


Fig. 2: Schematic of the STM setup. (a) The apex of the tip is in tunneling distance from the sample. The tip atom closest to the sample surface is responsible for most of the tunneling current. (b) Schematic of the STM setup and electronic controllers. The scanner tube can move the tip in x, y and z directions. The pre-amplifier is installed as close as possible to the STM setup to minimize noise on the tunneling current ( $\sim 0.1$  nA). In one of the most common STM operation modes, the feedback loop maintains a constant tunneling current by adjusting the tip height.

In constant current mode, a feedback loop continuously adjusts the distance between the tip and the sample to obtain the desired constant tunneling current. If the current increases (due to either the presence of a protrusion on the surface or a region of higher electron density of states), the tip is moved away from the surface and vice versa. In this way, the changes in the height of the tip (z) are used to image the

morphology and electronic properties of the surface (Fig. 3b). This method was used throughout the next chapters of this dissertation.

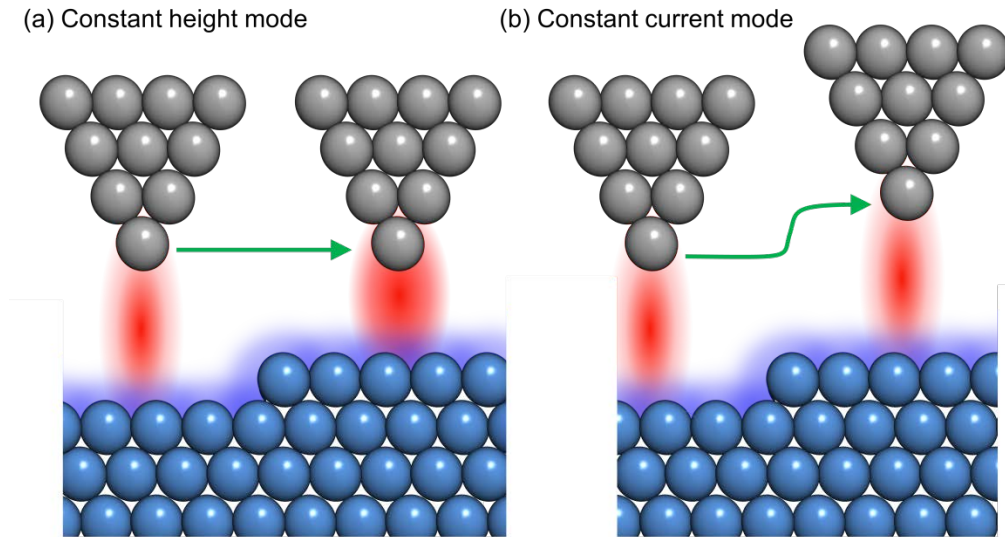


Fig. 3: Two different STM measurement modes: (a) constant height mode, in which the changes in the tunneling current are used to extract information on the morphology of the sample, and (b) constant current mode, in which the changes in the tip height determine the morphology.

It should be mentioned that the images obtained by STM are the result of both, morphology and electronic properties of the surface, as indicated in eq. (1) by the term [  $I_t = f(\rho_s, z)$  ]. For instance, if there is a region on a flat surface that is more conductive than its surroundings, it will result in a higher tunneling current and therefore, when scanning in constant current mode, the feedback loop will move the tip away from the surface to compensate for the change. Hence, such area would be seen as a region protruding from the surrounding surface.

To bring the tip close to the surface, a piezoelectric inch worm motor is used. This motor is capable of moving the tip in one dimension (vertically up and down) with step

sizes as small as a few Angstroms. Different stages involved in the movement of an inchworm motor one step upward are depicted in Fig. 4.

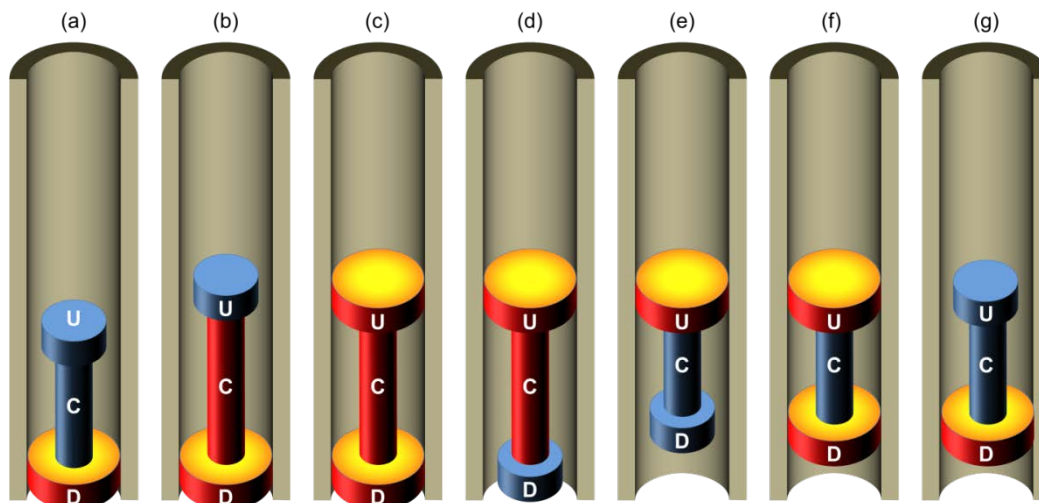


Fig. 4: Different stages during the movement of a piezoelectric inchworm motor one step upward. Three sections of the motor, namely up, center, and down could be activated separately. By applying the voltage to sections U and D they expand laterally and lock inside the outer cylinder. The middle section C expands vertically upon applying the voltage. The parts activated by the voltage are shown with red color, while the inactive sections are shown with blue color. In the first stage, only section D is locked and the upper part is free (a). Then the middle part expands (b), and section U locks as well (c). Subsequently, the lower part releases (d), and section C contracts to its initial length (e). Now section D locks (f) and section U unlocks (g). The latter motion returns the setup to a similar position as that depicted in (a), but vertically displaced upward. By tuning the expansion of the middle section, the length of each step of the inchworm motor could be adjusted.

The inchworm motor moves the tip toward the sample until it detects the tunneling current. At this point, the motor stops and the STM scanner starts to control the tip position ( Fig. 2).



### 2.1.3 Tip preparation

The STM tips are prepared either by cutting Pt-Ir wires at a glazing angle or from tungsten wires etched chemically in a 5 Molar NaOH solution under a bias voltage of ~ 3 V. I designed and tested a tip-etching setup for this project. In such setup, the cathode is a gold wire positioned on the side of a beaker, while the anode (tungsten wire) is in the middle. During the tip etching process, the W wire dissolves into the solution gradually following the reaction below:



However, the rate of dissolution is greater close to the meniscus, Fig. 6(a), since the lower parts are shielded partially by the falling  $WO_4^{2-}$  salt generated by wire sections above. When the neck gets too thin, it breaks off and releases the lower hanging piece. An electronic setup monitors the current and shuts down the voltage if any sudden change in current is detected. The detachment of the lower piece of the etched W wire, results in a sudden change in the current, triggers the electronic setup to shut off the voltage immediately. This is a very important step in order to avoid further etching of the tip, which might lead to a dull tip. A schematic of the setup and an image of an STM tip prepared with this method are shown in Fig. 5.

After the electrochemical etching, the tungsten tips were further cleaned before the STM measurements via an *in situ* (UHV)  $Ar^{+}$  sputtering process ( $4 \times 10^{-6}$  mbar, 4 kV, 15 min) inside the STM chamber.

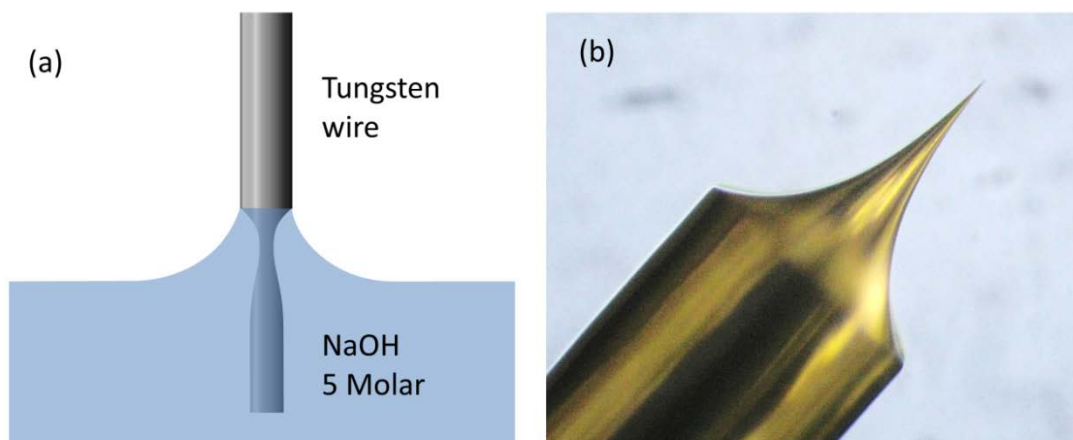


Fig. 5: (a) Partially etched tungsten wire inside a NaOH solution. (b) Example of a tungsten tip prepared by wet etching acquired with an optical microscope.

#### 2.1.4 STM images

Two examples of STM images obtained on Au(111) and  $\text{TiO}_2(110)$ -[1x2] surfaces are shown in Fig. 6. As was mentioned in the previous section, in STM images the electronic and morphological properties of a sample are convoluted.

As an example, STM images of the  $\text{TiO}_2(110)$ -[1x1] surface show bright and dark (up and down) atomic rows corrugating the surface. Interestingly, the bright rows correspond to Ti rows on the surface that are vertically located lower than the oxygen rows. Thus, although with respect to the surface morphology, the O atoms are located above the Ti atoms, in STM images they seem to be below the Ti rows due to different electronic properties of titanium and oxygen, with the Ti atoms having a higher electron density of states.

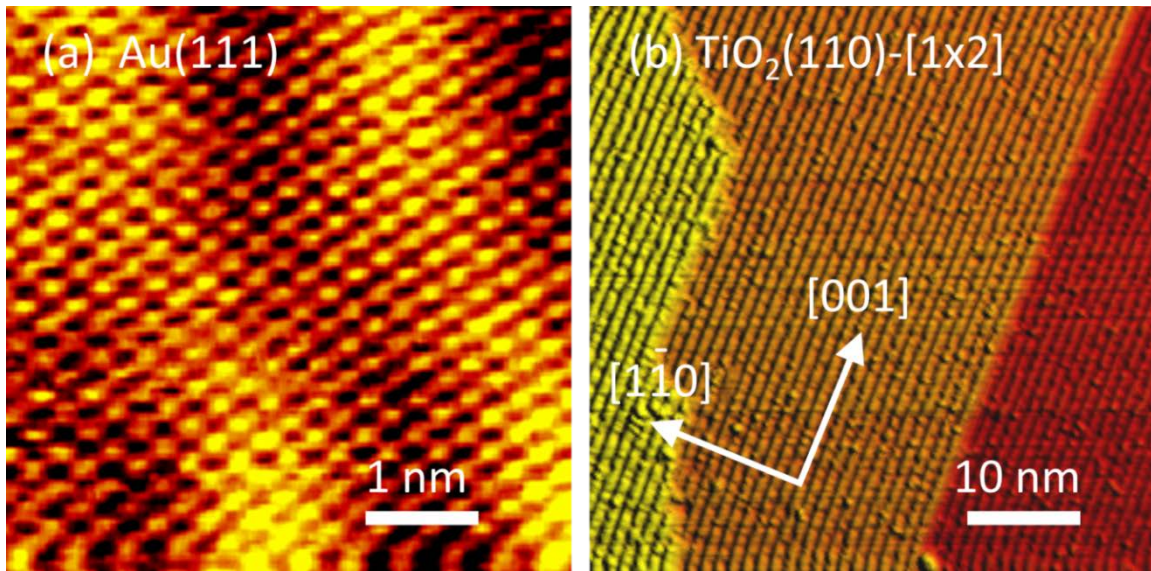


Fig. 6: STM images of (a) a Au(111) single crystal showing atomic resolution and (b) a TiO<sub>2</sub>(110) surface with a (1x2) surface reconstruction. The color coding shows the higher points with a yellow color and the lower points with a dark red color. TiO<sub>2</sub> atomic rows in the [001] direction could be seen on the three terraces of the TiO<sub>2</sub> surface displayed. The height of each TiO<sub>2</sub> step is 3.2 Å and the distance between atomic rows is 13 Å (twice that in between the rows in the 1x1 reconstruction). The images were obtained using a SPECS Aarhus-150 STM.

## 2.2 Atomic force microscope (AFM)

### 2.2.1 Fundamentals

The atomic force microscope is another tool for imaging nanometer scale features on surfaces. It was also developed by Binnig and Rohrer in 1986. In AFM, a cantilever that has a sharp tip at the end is brought close to the sample surface until an interaction between the tip and the surface exerts a force on the cantilever that bends it upward or downward depending on the direction of the force. The interaction between the tip and the surface could involve van der Waals forces (always present), capillary forces,

electrostatic forces, magnetic forces, etc. The dominant interaction probed would depend on the AFM setup, sample properties, and tip-sample distance.

The AFM cantilever could be understood as a system comprising of a mass  $m$ , a spring with a force constant  $k$ , and a damper  $\zeta$ . This system is driven by an external periodic force  $F_0 \sin(\omega t)$  and is interacting with the surface via the force  $F_{in}$  (Fig. 7a).

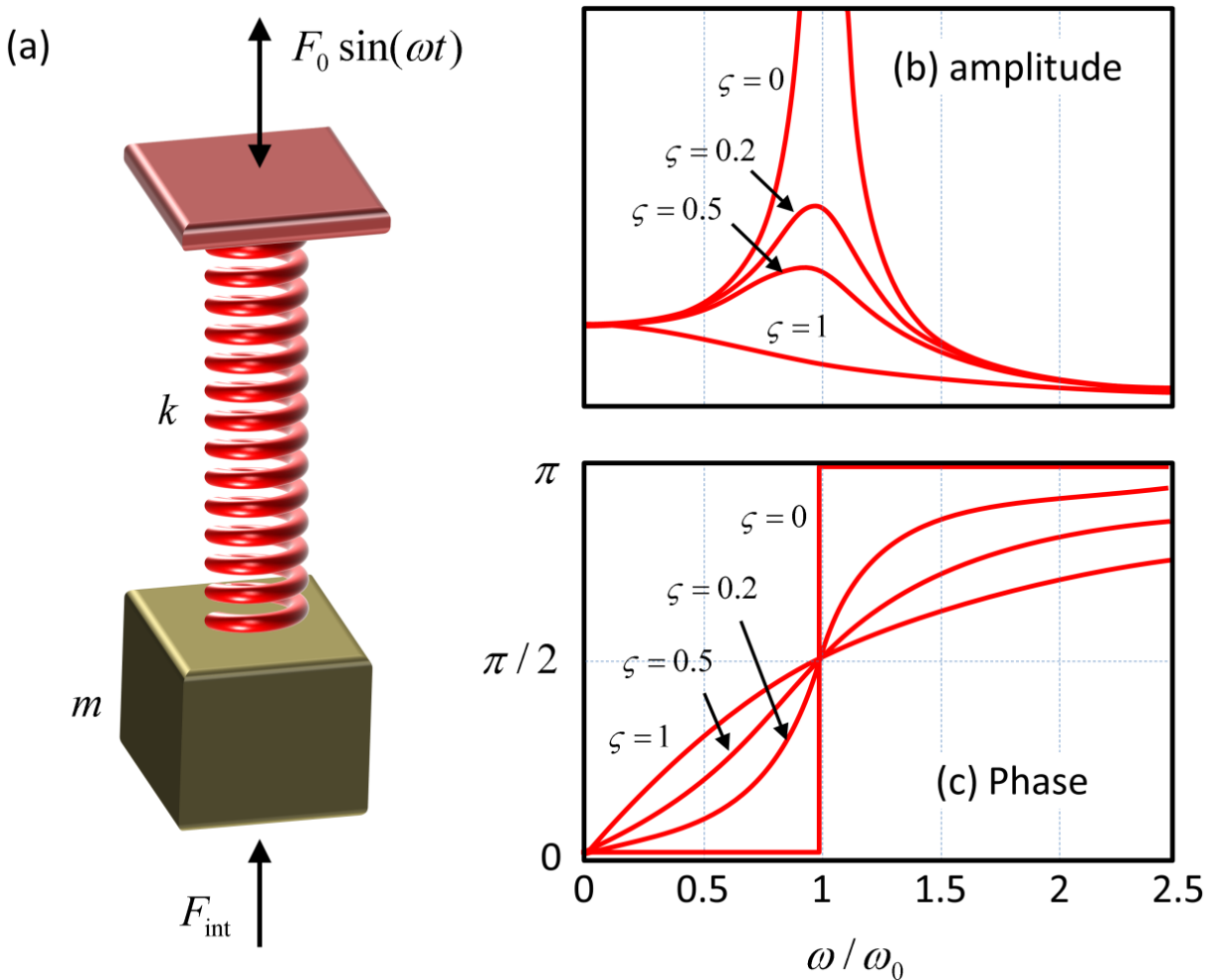


Fig. 7: (a) Schematic of a mass-spring harmonic oscillator driven by a periodic force. The amplitude (b) and phase of the oscillation for different damping constant is shown as a function of the frequency of the driving force.

The equation of motion could be derived as:

$$m\ddot{z} + kz + 2\zeta\omega_0\dot{z} = F_{\text{int}} + F_0 \sin(\omega t) \quad (3)$$

, where  $\omega_0 = \sqrt{k/m}$  is the undamped natural frequency of the system.

The steady state solution for the damped harmonic oscillator (without  $F_{\text{int}}$ ) could be written as:

$$z(t) = A(\omega) \sin(\omega t + \varphi) \quad (4)$$

, where the oscillation amplitude  $A(\omega)$  and the phase  $\varphi$  are:

$$A(\omega) = \frac{F_0}{m\sqrt{(2\zeta\omega\omega_0)^2 + (\omega^2 - \omega_0^2)^2}} \quad (5)$$

$$\varphi = \arctan\left(\frac{2\zeta\omega\omega_0}{\omega^2 - \omega_0^2}\right) \quad (6)$$

The amplitude and phase of the oscillation are shown in Fig. 7 as function of the angular frequency of the driving force for different damping values. For large values of the damping constant, no significant resonance occurs (Fig. 7a).

The maximum oscillation amplitude occurs at a resonance frequency,  $\omega_r$  :

$$\omega_r = \omega_0 \sqrt{1 - 2\zeta^2} \quad (7)$$

After finding the solution for the derived damped harmonic oscillator, the tip-sample interaction,  $F_{\text{int}}$  could be added to the solution following first order perturbation

theory. The effect of such additional force could be simply understood as a modification of the spring constant of the system from  $k$  to  $k_{eff}$  and consequently of the system's natural frequency from  $\omega_0$  to  $\omega_{eff}$  :

$$k_e = -\frac{dF}{dz} = \left( k - \frac{dF_{int}}{z} \right)_{z_0} \quad (8)$$

$$\omega_{eff} = \left[ \frac{k - (dF_{int} / z)}{m} \right]^{1/2} \quad (9)$$

A schematic of the changes induced in the resonance frequency due to tip-sample interactions is shown in Fig. 8 for attractive and repulsive forces.

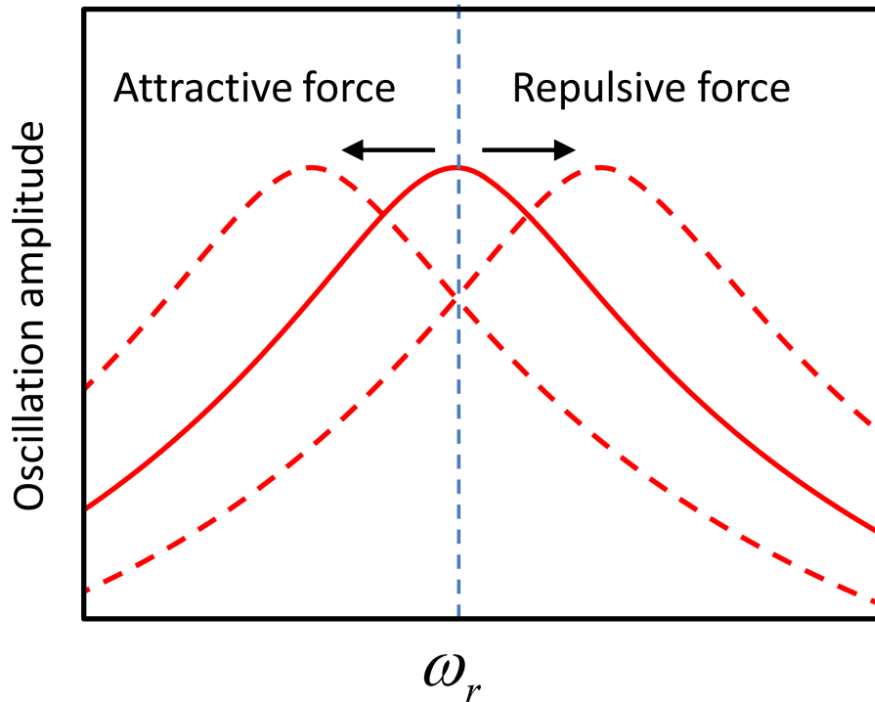


Fig. 8: Change in the resonance frequency induced by the tip-sample interaction. The shift in resonance frequency is positive for repulsive forces and negative for attractive forces.

However, in both cases the tip-sample interaction results in the reduction of the oscillation amplitude. The change brought about by the tip-sample interaction is the shift of the resonance curve without any change in the shape of the curve (Fig. 8)

### **2.2.2 Instrumentation**

In order to approach the sample toward the tip (or the tip toward the sample in a different microscope configuration), AFM uses either a piezoelectric inchworm motor or a stepper motor. Similar to STM, it also has a piezoelectric scanner. However, unlike STM, AFM could work with both conductive and nonconductive samples, since rather than using the tunneling current as measurement parameter, it relies on tip-sample interaction forces.

The small deflection of the cantilever could be detected using an optical setup as shown in Fig. 9. A laser beam is focused on the cantilever and reflects back to reach a photo-diode. The photo-diode has four separate panels. A small deflection of the cantilever results in the displacement of the laser spot on the position-sensitive detector, increasing the photoelectric signal in some of the panels and decreasing it in others. By comparing the photoelectric signal of the four panels, the upward and downward deflection of the cantilever as well as its sidewise deflections could be detected.

AFM works in different modes, namely contact mode, tapping mode, and non-contact mode. In contact mode, the tip is brought into direct contact with the surface (actually within a few Angstroms from the surface) and the cantilever deflects due to the tip-sample interaction. The scanner feedback loop changes the height of the tip to maintain a constant deflection and therefore, the tip can follow the morphology of the

surface. However the tip-sample contact could eventually damage both the tip and the sample, especially under ambient conditions in which the surface is usually covered with a thin liquid film. Nevertheless, this operation mode could be used to intentionally damage the surface to for example measure surface mechanical properties such as friction and nanoparticle-support adhesion energies by detaching the NPs from the surface.

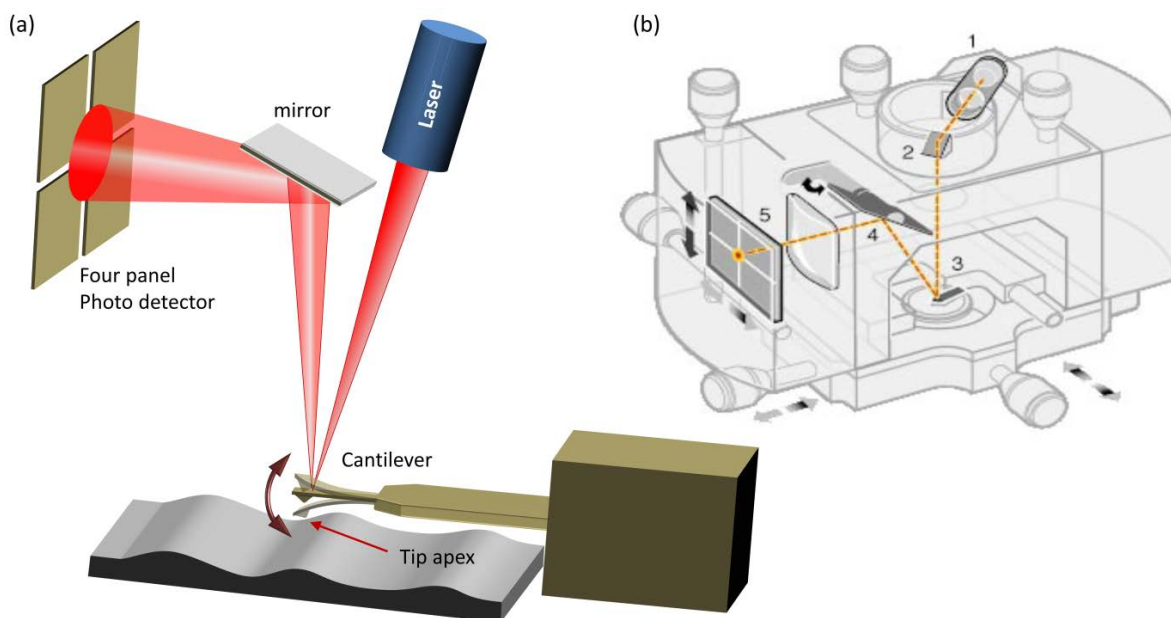


Fig. 9: (a) Schematic of an AFM setup including the laser source, the cantilever reflecting the laser, and the mirror guiding the reflected beam towards a four-panel photodetector. (b) Schematic of an actual multimode AFM head from digital instruments (VEECO metrology group) used for the measurements shown in this thesis.

Another AFM operation mode is known as tapping mode, in which a piezoelectric element drives the cantilever to oscillate at or close to its resonance frequency with a typical frequency of 200-400 KHz and oscillations 20-100 nm in magnitude. The cantilever vibration produces an AC signal in the photodetector output. The tip is brought close to the surface until it feels the interaction with the surface at the lowest



point of its oscillation. Due to the external force applied by the surface to the tip, the magnitude of the oscillation amplitude and also the phase changes. At that instance, the feedback loop activates a piezo-actuator in the scanner to move the cantilever in the z direction to maintain a constant oscillation magnitude, allowing the tip to follow the surface morphology. This technique provides the best results for ambient measurements and was used for the acquisition of all AFM images shown in the coming chapters.

Non-contact mode AFM is similar to tapping mode but with much lower oscillation magnitude (2-30 nm) and therefore, can provide better resolution (up to atomic resolution), although it is mainly appropriate for measurements under UHV conditions.

### 2.2.3 AFM images

An example of an AFM image of an array of Pt NPs supported on SiO<sub>2</sub>/Si(111) obtained in tapping mode is shown in Fig. 8.

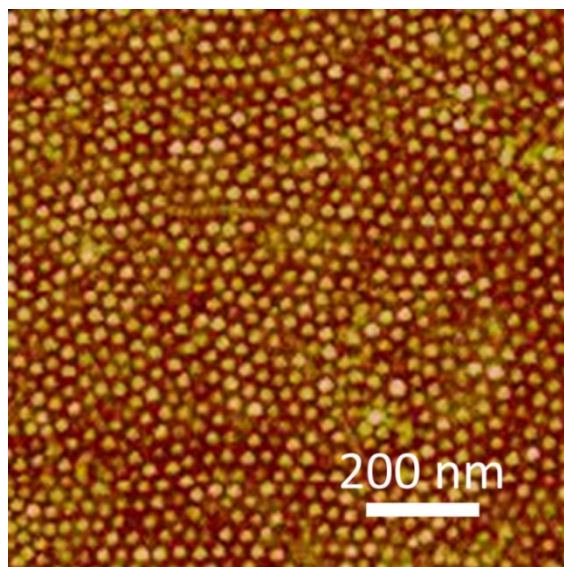


Fig. 10: AFM image of Pt NPs supported on SiO<sub>2</sub>/Si(111).

## 2.3 X ray photoelectron spectroscopy (XPS)

### 2.3.1 Fundamentals

XPS is a quantitative, surface sensitive technique that provides information on the composition, chemical state and charging phenomena of different chemical elements present at/near the sample surface (1-10 nm).

XPS is a spectroscopy technique in which the sample under study is irradiated by x-rays resulting in the ejection of core level electrons (photoelectrons) having binding energies lower than the incident photon energy,  $h\nu$  (Fig. 11).

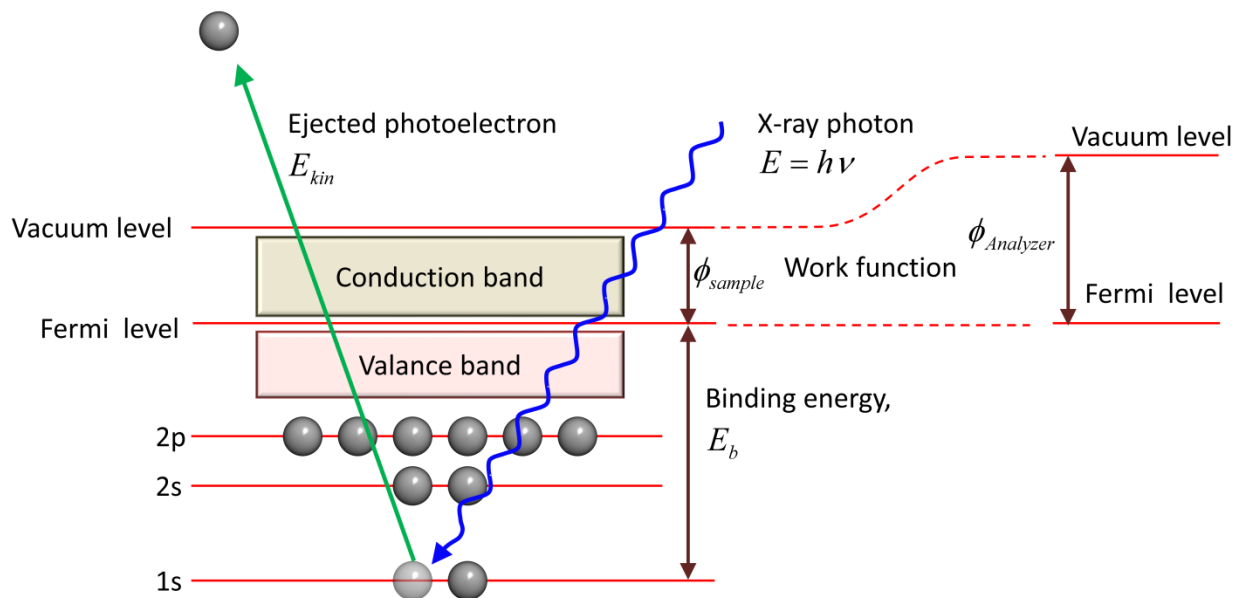


Fig. 11: Schematic of the XPS process. Absorption of the x-ray photon ejects one of the core electrons (in this case from a 1s level) to the vacuum level. Such electron is subsequently collected by the electron analyzer. The Fermi levels of the sample and the analyzer are equal since both are grounded. The photoelectron's kinetic energy is measured by the electron energy analyzer.

Usually in XPS the energy of the x-ray ( $h\nu$ ) is fixed, and by measuring the electron kinetic energy, its binding energy can be obtained:

$$\begin{aligned}
E_{kin} &= h\nu - E_b - \phi_{sample} - (\phi_{analyzer} - \phi_{sample}) \\
&= h\nu - E_b - \phi_{analyzer}
\end{aligned}
\tag{10}$$

, where  $h\nu$  is the incident x-ray energy,  $\phi_{sample}$  and  $\phi_{analyzer}$  are work functions of the sample and the analyzer respectively, and  $E_b$  is the binding energy of the electron excited by the x ray photon.  $\phi_{analyzer}$  is constant for a specific analyzer and therefore can be compensated in the energy calibration process. Fortunately, the sample work function  $\phi_{sample}$  is not needed to obtain the binding energy, eq. (10).

Each element has a unique set of electron energy levels and therefore, XPS can be used to determine the elemental composition. Also the relative concentration of each individual element can be extracted by comparing the different photoelectron count rates of distinct elements, while considering their sensitivity factors.

With the exception of electrons in s-levels, other electron energy levels appear in XPS as two peaks with two different energies, due to spin-orbit coupling. Such energy splitting is shown in Fig. 12.

The interaction between the electron spin,  $S$ , and its orbital angular momentum,  $l$ , results in two different values of the total angular momentum,  $J$ . The antiparallel configuration is more energetically favorable resulting in lower electron binding energy while the opposite is true for the parallel configuration. For instance, for p electrons, the possible total angular momenta are 3/2 and 5/2. There is a maximum of 4 electrons in  $p_{3/2}$  states, and only two in  $p_{1/2}$  states and therefore, the photoelectron count rate for  $p_{3/2}$  states should be twice as large as that of  $p_{1/2}$ .

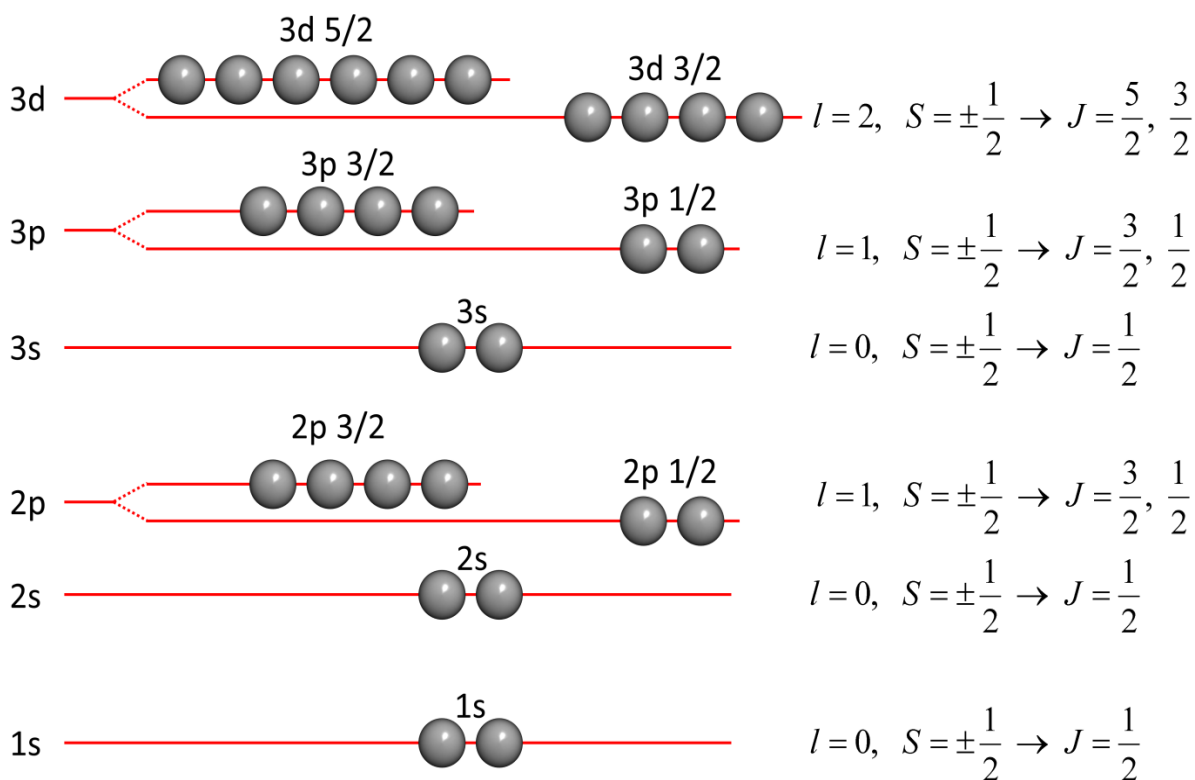


Fig. 12: Spin-orbit energy splitting for different energy levels. The degeneracy is  $(2J+1)$  for each state. For instance, for 2p states, the degeneracy is four for  $2p_{3/2}$  ( $3/2, 1/2, -1/2, -3/2$ ) and two for  $2p_{1/2}$  ( $1/2$  and  $-1/2$ ). Therefore, the intensity ratio obtained when comparing both XPS peaks should be proportional to the number of electrons in each state. The XPS area obtained for  $2p_{3/2}$  states should be twice as large as that of  $2p_{1/2}$ . Similarly, it could be shown that the count rate ratio (i.e. ratio of XPS peak areas) for  $3d_{5/2}$  and  $3d_{3/2}$  states is  $6/4$ .

XPS peaks are also sensitive to the chemical state of the element. For instance, for most elements a higher oxidation state results in the shift of the electron binding energy to higher values. This is due to the fact that oxygen has a high electronegativity and could attract electrons resulting in lower electron density around the target nucleus and therefore, higher binding energies for the remaining electrons, which are pulled closer to the nucleus.

### 2.3.2 Instrumentation

An x-ray beam is generated by electron bombardment of an anode (e.g. Al, Mg, Ag). The x-ray is subsequently filtered through a quartz single crystal monochromator, based on Bragg diffraction to achieve an x-ray beam with a narrower energy distribution (Fig. 13). This leads to a better energy resolution and narrower width of the XPS spectra. In our system, half of the dual-anode target is made of Al and the other half of Ag. The energy of the Al-K $\alpha$  radiation is 1486.6 eV, and that of Ag-L $\alpha$  is 2984.2 eV.

Following Bragg's law for any given crystalline material (e.g. quartz in this case), a constructive interference could occur for certain wavelengths depending on the reflection angle:

$$n\lambda = 2d \sin(\theta) \quad (11)$$

,where  $\lambda$  is the x-ray wavelength,  $d$  is the interplanar atomic distance,  $\theta$  is the reflection angle.  $d$  is a characteristic parameter of the single crystal used for the monochromator, and  $\theta$  can be adjusted to obtain a constructive interference for the main x-ray energy of the incident beam.

Since the energy of the x-ray generated by Ag is almost twice as that generated by Al, the same monochromator used for Al could be used for Ag (second order Bragg diffraction,  $n=2$  in eq.11) with minor angular adjustments.

Photoelectrons ejected from the sample due to x-ray irradiation are collected through a lens system and are filtered based on their kinetic energy in a hemispherical analyzer.

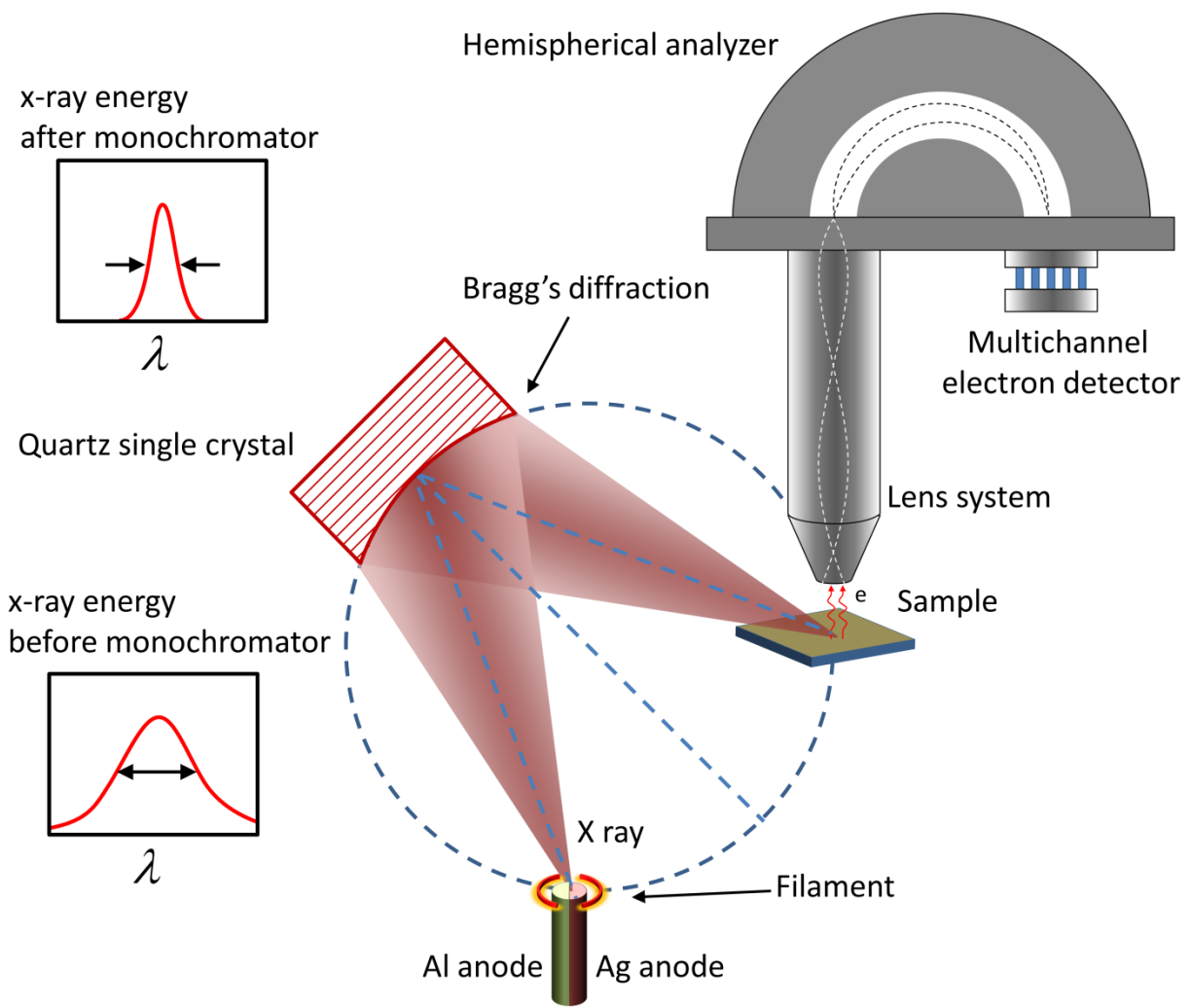


Fig. 13: Schematic illustration of a monochromatic XPS setup including a double anode x-ray source, monochromator, sample, lens system, hemispherical analyzer, and multichannel electron detector.

The analyzer has a hemispherical capacitor that bends the trajectory of the photoelectrons (Fig. 13). Only electrons with certain energy will be able to reach the multichannel detector (made of 5 channeltrons in our case) that is located on the other side of the analyzer, opposite to the photoelectron entrance port. Channeltrons are made of low work function materials that are able to multiply any single electron they

receive by a factor of  $\sim 10^8$  at their output. This allows the acquisition setup to count the number of electrons reaching the channeltrons based on the number of generated electrical pulses. The voltage of the capacitor in the hemispherical analyzer is swept gradually, changing the energy of the electrons reaching the channeltrons. Therefore, a spectrum of photoelectron count rates as a function of their energy could be obtained.

### 2.3.3 XPS spectra

Each chemical element has its own specific finger-print in XPS spectra appearing as a set of peaks at certain energies. Fig. 14a shows an example of an XPS spectrum of a Si(111) single crystal with a thin oxide film on top showing Si-2p, Si-2s, and O-1s as three main peaks. The high resolution spectra of the Si-2p region, is shown in Fig. 14b.

The data were fitted using a commercial XPS analysis software; CASA XPS (copyright © 1999-2008 Neal Fairley).<sup>35</sup> Several constraints used in the fitting process are described below. As can be seen in Fig. 14b, each Si species has two components due to the spin-orbit splitting effect, described in Fig. 12.

The ratio of the area under the  $2p_{3/2}$  and  $2p_{1/2}$  peaks is set to be 2. Also, the split in energy for  $2p_{3/2}$  and  $2p_{1/2}$  is constant, in this example 0.6 eV, and is used as another constraint during the spectral fitting, Fig. 14.

Three different chemical states could be seen for Si-2p. The first peak at  $\sim 99.3$  eV is  $\text{Si}^0$  from the Si substrate underneath the oxide, and the second largest peak at  $\sim 103.3$  eV is  $\text{Si}^{4+}$  from the top  $\text{SiO}_2$  thin film. There is also a smaller component in between the two main peaks at  $\sim 101$  eV that shows an intermediate oxidation state. This component is assigned to  $\text{SiO}_x$  species that usually formed at the  $\text{SiO}_2/\text{Si}$  interface.

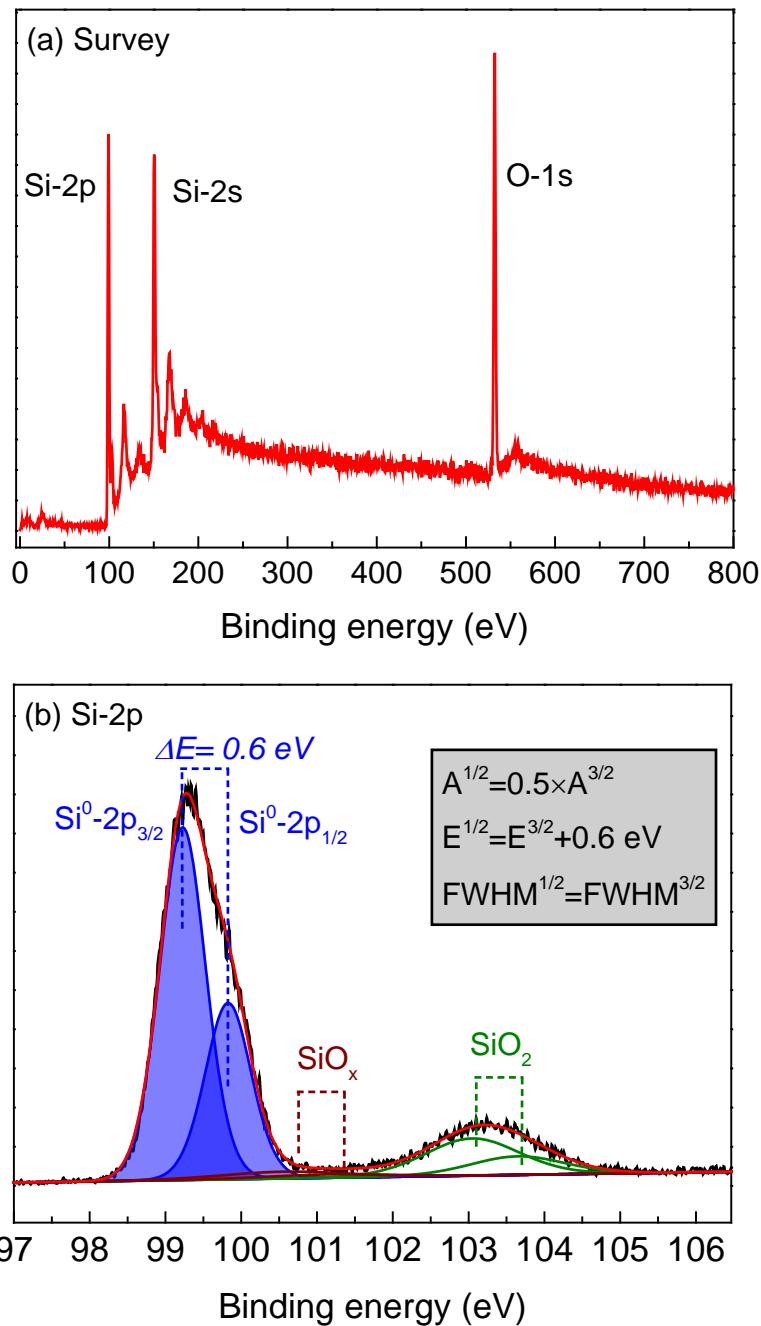


Fig. 14: XPS spectrum of a Si(111) wafer terminated by a thin  $\text{SiO}_2$  layer. (a) The survey spectrum measured over a large energy range is used for the initial identification of the elemental composition of the sample including Si and O peaks. (b) High resolution spectrum of the Si-2p core level region showing silicon in three different chemical states: Si,  $\text{Si}^{4+}$  in  $\text{SiO}_2$ , and an intermediate state of  $\text{Si}^{\delta+}$  in  $\text{SiO}_x$  with  $x$  having a value between 0 and 2. The red curve shows the overall fit to the black experimental data (noisy black curve).



## 2.4 X-ray absorption spectroscopy (XAS): extended X-ray absorption fine-structure (EXAFS) and X-ray absorption near-edge structure (XANES) spectroscopy

### 2.4.1 Fundamentals

EXAFS and XANES are powerful, element sensitive, ensemble-averaging synchrotron-based techniques that provide information about the NPs' size, shape, oxidation state, charge transfer phenomena, adsorbate effects, interatomic distances, crystalline disorder, as well as thermodynamic properties of the material, such as the Debye temperature and the thermal expansion coefficient.

For these techniques, a brilliant synchrotron-generated x-ray beam is shone into the sample and the absorption coefficient is measured by varying the x-ray energy using a monochromator (Fig. 16).

In the transmission XAS geometry, the x-ray intensity decays inside the sample exponentially:

$$I_t = I_0 \exp(-\mu d) \quad (12)$$

, where  $I_0$  and  $I_t$  are the incident and transmitted x ray intensities respectively,  $\mu$  is the absorption coefficient and  $d$  is the sample thickness. Therefore the absorption coefficient could be obtained as:

$$\mu = \frac{-\ln(I_0 / I_t)}{d} \quad (13)$$

By measuring the absorption signal while the x-ray energy is changed, the energy dependence of the absorption coefficient can be extracted. In general, the absorption

coefficient decreases with increasing energy, but for any given material, sudden increases in the absorption coefficient appear at certain energies which are known as absorption edges.

X-ray photons could be absorbed by the material resulting in the excitation of photoelectrons. However, only electrons with binding energies lower than the x-ray photon energy could interact with it. By increasing the x-ray energy, electrons with higher binding energy could also be excited and contribute to the absorption process. Therefore, by increasing the x-ray photon energy and after adding each new electron energy level, the absorption coefficient shows a sudden increase. In contrast to XPS, the photoelectron energy is irrelevant to EXAFS, and only the amount of x-ray photons absorbed by the material is measured.

Interestingly, after each absorption edge, fine oscillations appear in the absorption coefficient. Such oscillations are not expected for individual atoms (e.g. gas phase). The origin of these oscillations could be understood based on the interference of photoelectron waves. The ejected photoelectron waves are scattered back by neighboring atoms (Fig. 15).

If the reflected photoelectrons interfere constructively with the outgoing electron wave, the electron density of states in the excited state at the position of the absorbing atom increases. This results in a higher probability of absorption of the x-ray photon. On the other hand, a destructive interference would result in lower probability of electron excitation with the concomitant decrease in the absorption coefficient (Fig. 15). This explains why for a single atom no oscillation is expected to occur.

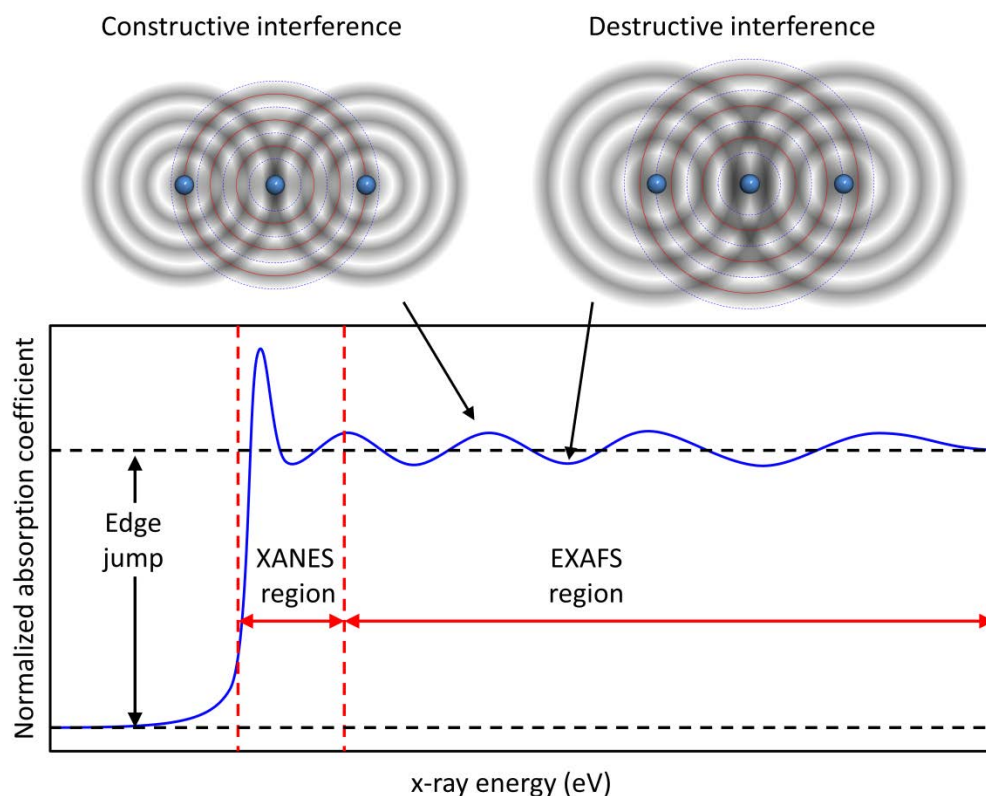


Fig. 15: Schematic of the origin of EXAFS oscillations. Constructive (destructive) interference of outgoing and back scattered photoelectron waves results in higher (lower) density of electronic states at the position of the absorbing atom. In the region close to the absorption edge (XANES region), the photoelectrons have low kinetic energy (large wavelength), and therefore, the interference phenomena are not contributing to the absorption coefficient. Only in the EXAFS region (>150 eV above the edge) the absorption coefficient is affected by interferences of photoelectrons.

Since in EXAFS we are only interested in the oscillations of the absorption coefficient, we can normalize the data using a single atom background:

$$\chi(E) = \frac{\mu(E) - \mu_0(E)}{\Delta\mu_0(E_0)} \quad (14)$$

, where  $\mu(E)$  is the absorption coefficient,  $\mu_0(E)$  is the absorption coefficient for one atom, and  $\Delta\mu_0(E_0)$  is the edge jump. A typical Pt-L<sub>3</sub> XAS spectrum acquired in

transmission mode is shown in Fig. 17. Depending on the energy of the x-ray photon, the kinetic energy of the emitted photoelectrons changes, resulting in photoelectrons with different wavelengths:

$$k = \sqrt{\frac{2m_e(E - E_0)}{\hbar^2}} \quad (15)$$

, where  $k$  is the photoelectron kinetic energy,  $m_e$  is the electron mass,  $E$  is the x-ray energy, and  $E_0$  is the energy at the absorption edge.

Theoretical models were developed to explain the EXAFS data, and the fundamental EXAFS equation is shown below:

$$\chi(E) = \sum_j \frac{S_0^2 N_j f_j(k) \exp[-2R_j / \lambda(k)] \exp(-2k^2 \sigma_j^2)}{kR_j^2} \sin[2kR_j + \delta_j(k)] \quad (16)$$

, where the sum over all the neighboring atoms involved in scattering process is considered.  $f_j(k)$  and  $\delta_j(k)$  are the scattering amplitude and the phase shift, respectively.  $R_j$  is the distance of the scatterer atom from the absorbing atom,  $\lambda(k)$  is the photoelectron mean free path,  $N_j$  is the degeneracy or the coordination number of the scatterer, and  $\sigma_j^2$  is the mean square disorder of a given neighbor distance.  $S_0^2$  is the amplitude reduction term due to the slight relaxation of all other electrons in the presence of the core hole generated by the ejected photoelectron. Since  $S_0^2$  and  $N_j$  have a 100% correlation, the value of  $S_0^2$  should be obtained from a reference sample. Equation 16 could be used to fit the experimental data.

## 2.4.2 Instrumentation

A schematic of the experimental setup used for XAS measurements is shown in Fig. 16. The electrons are accelerated in several steps until they reach a very high energy inside the synchrotron ring (e.g. 2800 MeV at the National Synchrotron Light Source at Brookhaven National Laboratory, NSLS-I ).

Then, the electrons that are stored inside the synchrotron ring are forced to oscillate using an undulator, which is a set of periodic dipole magnets (left and right) that bend the electron beam upward and downward. The accelerated electrons produce a very bright white x-ray beam that could be used for a variety of applications in material characterization, including XAS. Although only one undulator is shown in Fig. 16, each synchrotron has several undulators and several end-stations for different type of measurements.

The white x-ray beam is filtered using a monochromator to obtain the desired energy, with a narrow energy width. By changing the angle of the two single crystals inside the monochromator, the energy of the x-ray obtained after the monochromator could be varied. There are three ionization chambers that could measure the intensity of the x-rays. The first one measures the initial intensity of the x-ray,  $I_0$ , and the second one measures the signal transmitted through the sample,  $I_t$ . These two measurements are enough to study the sample.

However, for energy calibration purposes another ionization chamber is used to measure the transmitted photon intensity through a reference sample,  $I_{ref}$ , (e.g. a thin foil from the same material under study). Comparing the  $I_{ref}$  and  $I_t$  signals, the

absorption edge of the reference sample could be measured. This is used in order to align the energy of the real sample to that of the bulk sample.

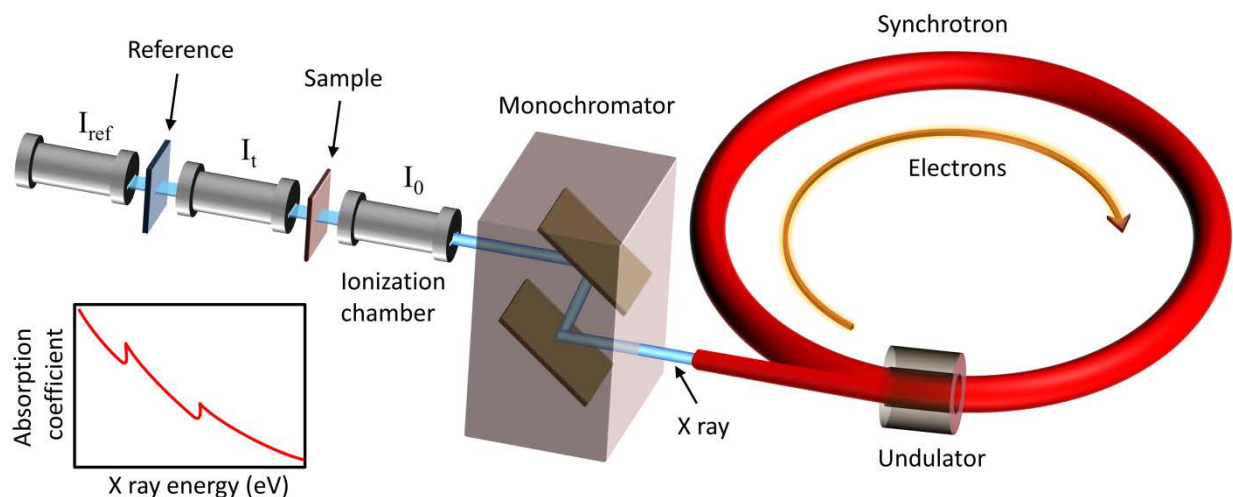


Fig. 16: Schematic of the EXAFS and XANES measurement setup including (i) a large synchrotron loop accelerating electrons with high speed, (ii) undulators that produce a high brilliance white x-ray, (iii) the monochromator that selects the x-ray energy to the desired value for the excitation of a given absorption edge, (iv) ionization chambers that measure the x-ray intensity before and after transmission through the sample and also the reference sample. The inset shows a plot of the measured absorption coefficient with two absorption edges.

### 2.4.3 XAS data

Fig. 17a shows a spectrum of the absorption edge measured for the Pt- $L_3$  edge of a platinum foil. Two polynomial lines were used to fit the pre-edge and post-edge in order to normalize the data. As it could be seen in eq. (13), the absorption coefficient depends on the thickness of the sample. The edge jump also depends on the concentration of the given element in the sample. To compensate for these effects, the absorption edge is normalized to 1 ( Fig. 17b).

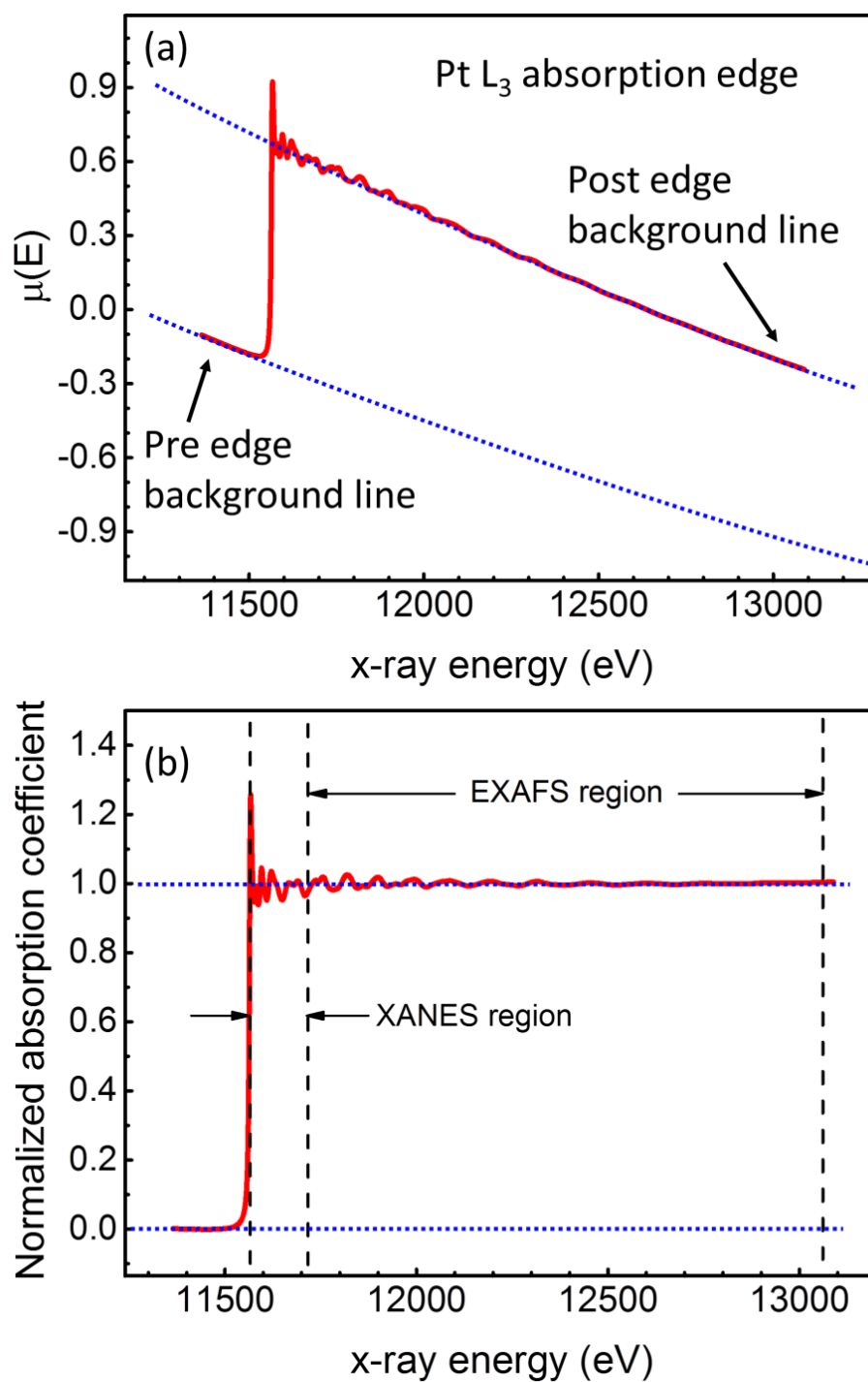


Fig. 17: (a) Pt-L<sub>3</sub> absorption edge and the pre- and post-edge background fitted to the data for normalization. (b) Normalized absorption coefficient, using the

$$\mu_{normalized}(E) = \frac{\mu(E) - \text{Pre\_edge}(E)}{\text{Post\_edge}(E) - \text{Pre\_edge}(E)}.$$

The region between the absorption edge and 150 eV above it, is known as the XANES region ( Fig. 17b). In this energy range, the photoelectrons have very low kinetic energy (long wavelengths) and therefore, the interference phenomena are not important. The XANES region is the most sensitive to changes in the electronic properties of the absorbing atoms such as the density of unoccupied states, charge transfer, and oxidation state.

Beyond ~150 eV above the edge, the effect of photoelectron interference plays a crucial role as it is shown in Fig. 15, and this region is called the EXAFS region. As it is seen in Fig. 15, the absorption coefficient shows some oscillation after the edge. These oscillations could be explained based on the constructive and destructive interference of the outgoing and back-scattered photoelectrons (those that are reflected from neighboring atoms).

It is more common to represent the EXAFS data as a function of the wavenumber,  $k$ , (Fig. 18a) since it appears as the independent parameter in eq. 16. Also, due to the decay of the oscillations at higher energies, it is common to weight the signal by  $k$ ,  $k^2$ , or  $k^3$  to emphasize the oscillations at higher energies. Another common representation of EXAFS data is in  $r$ -space (Fig. 18b) which could be obtained by Fourier transforming the  $k$ -space data.



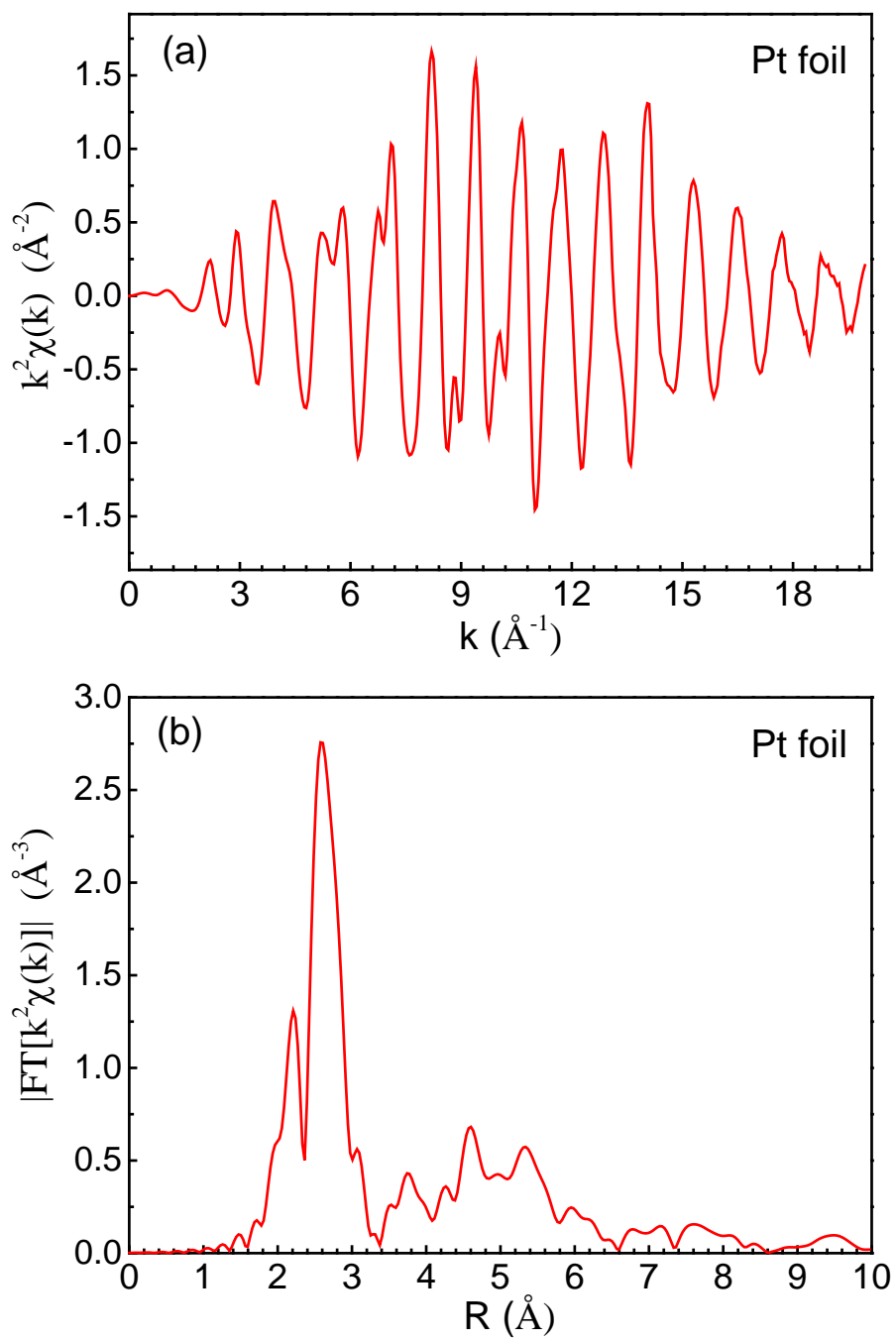


Fig. 18:  $K^2$  weighted EXAFS data of a platinum foil in  $k$ - and  $r$ -space representations.

## CHAPTER 3: NANOPARTICLE SYNTHESIS METHODS

### 3.1 Inverse micelle encapsulation

Commercial poly-(styrene)-block-poly(2-vinylpyridine) (PS-b-P2VP) diblock copolymers of different molecular weight and PS/PVP ratios were used to synthesize size- and shape-selected metal (Pt, Au, Pd, Fe) nanoparticles (NPs)<sup>5, 28, 36-39</sup>.

A schematic of the inverse micelle encapsulation synthesis process is shown in Fig. 19. Following the method introduced by Spatz et al.<sup>40</sup>, PS(x)-b-P2VP(y) diblock copolymers are first dissolved in toluene (5 mg/ml) and stirred for about 4 hours. Since the PS block (tail) of the polymer is hydrophobic (nonpolar) and the PVP part (core) is hydrophilic (polar), inverse micelles are formed in a non-polar solvent such as toluene (Fig. 19b). In the next step, a metal precursor (e.g.  $\text{H}_2\text{PtCl}_6 \cdot 6\text{H}_2\text{O}$  or  $\text{HAuCl}_4 \cdot 3\text{H}_2\text{O}$ ) with the desired ratio of metal precursor to P2VP (0.02 to 0.6) is added to the solution under a nitrogen atmosphere (glovebox) and stirred for more than 48 hours. The time required to dissolve the metal salt into the polymeric solution depends on the type of metal and polymer used and varies from two to seven days. The metal ions bind to the polar core of the micelles (Fig. 19c). The size of the NPs can be adjusted by changing the molecular weight of the P2VP group or the metal loading of the micelles (metal salt to P2VP ratio), resulting in NP sizes ranging from 0.5 to 40 nm.

To deposit the NPs on planar supports such as Si(111) or  $\text{TiO}_2(110)$  single crystals, the substrates were dip coated into the NP solution with a speed of 200  $\mu\text{m}/\text{sec}$  (Fig. 19d). One monolayer of micelles is stabilized on the substrate surface with a hexagonal arrangement (Fig. 19e). The PS part of the polymer keeps the micelles apart

and therefore controls the interparticle distance. This distance can be adjusted by changing the length (molecular weight) of the PS part of the polymer.

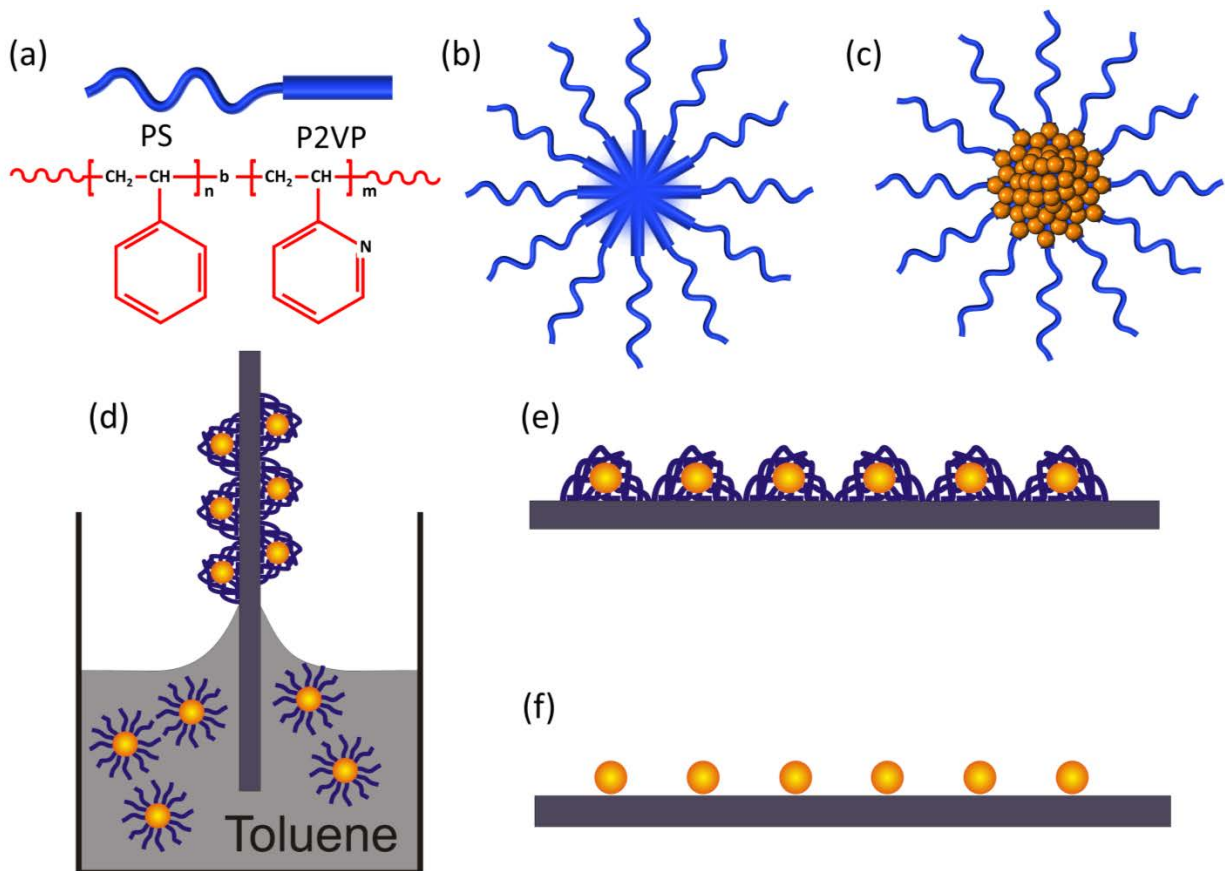


Fig. 19: Schematic of the nanoparticle preparation via inverse micelle encapsulation. (a) Poly-(styrene)-block-poly(2-vinylpyridine) (PS-b-P2VP) diblock copolymer (b) Formation of micelles after dissolving the polymer in toluene. (c) Addition of metal atoms to the micelle core upon dissolution of the metal-salt precursor. (d) Deposition of one monolayer of micellar NPs on a flat substrate by dip-coating. (e) Array of micellar NPs deposited on a flat substrate. (f) Polymer removal using an  $O_2$ -plasma treatment, resulting in the formation of a clean array of size-selected NPs.

The same NP solutions can also be used to prepare powder (high surface area) samples on nanocrystalline supports such as  $\gamma\text{-Al}_2\text{O}_3$ ,  $\text{ZrO}_2$ ,  $\text{TiO}_2$ . The metal loading was adjusted to be 1-2 percent of the support material by weight. The solutions were impregnated on the supports by stir drying at  $60^\circ\text{C}$  for about 24 hours.

All measurements that are reported in this thesis were carried out on ligand-free NPs. Two different treatments for the removal of the polymers were used depending on the type of support. On the planar (single-crystal) supports the polymer was removed in UHV by an O<sub>2</sub>-plasma treatment ( $4 \times 10^{-5}$  mbar, 120 min). The atomic oxygen generated by an O<sub>2</sub>-plasma source removes the polymer (Fig. 19f) leaving a clean array of oxidized NPs on the surface.

The powder samples were annealed in an oxygen environment (atmospheric pressure) at 375-425°C for 24 hours for polymer removal purposes. The complete removal of the organic ligands from our samples was corroborated by monitoring the carbon signal via XPS, Fig. 20.

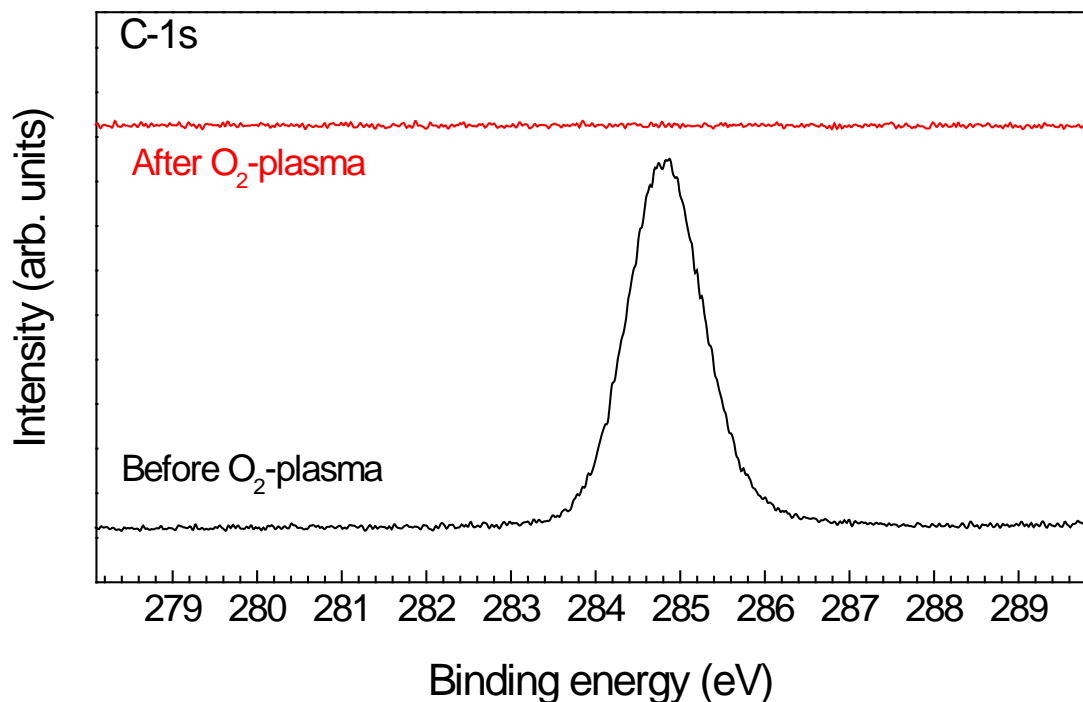


Fig. 20: XPS spectra from the C-1s core level region of micellar Pt NPs supported on TiO<sub>2</sub>(110) (S3) acquired before and after O<sub>2</sub>-plasma exposure at room temperature (RT) for 120 min. No residual C was observed on this sample after the atomic oxygen treatment.

The reduction of our NPs supported on planar substrates was achieved by either annealing in vacuum or by hot H<sub>2</sub>-plasma treatments ( $1 \times 10^{-4}$  mbar at 500°C). Powder samples were reduced by annealing in hydrogen from 240°C to 375 °C. An example of STM images of micellar Pt NPs supported on TiO<sub>2</sub>(110), obtained after polymer removal and vacuum annealing at 1060 °C, is shown in Fig. 22a.

### **3.2 Physical vapor deposition via electron beam evaporation**

Metal NPs (e.g. Pt) were also obtained by depositing sub-monolayer coverages of metal using an electron beam evaporator<sup>41</sup>. Electron beam physical vapor deposition (EBPVD) is a form of physical vapor deposition in which a target anode is bombarded with an electron beam given off by a charged tungsten filament under high vacuum, Fig. 21.

The evaporation can be carried out at different sample temperatures, since our sample holder can be heated via electron bombardment up to 1300 K and cooled by liquid nitrogen to about 100 K.

To measure the evaporation rate, a quartz microbalance was used. The sample was moved away and the microbalance was positioned at the same location. The quartz microbalance measures the thickness of the deposited metal based on the change of the quartz natural resonance frequency induced by the mass of the material being deposited. Certain calibration factors should be used for measuring the thickness of different materials, as for example the density and the acoustic impedance of the deposited material.

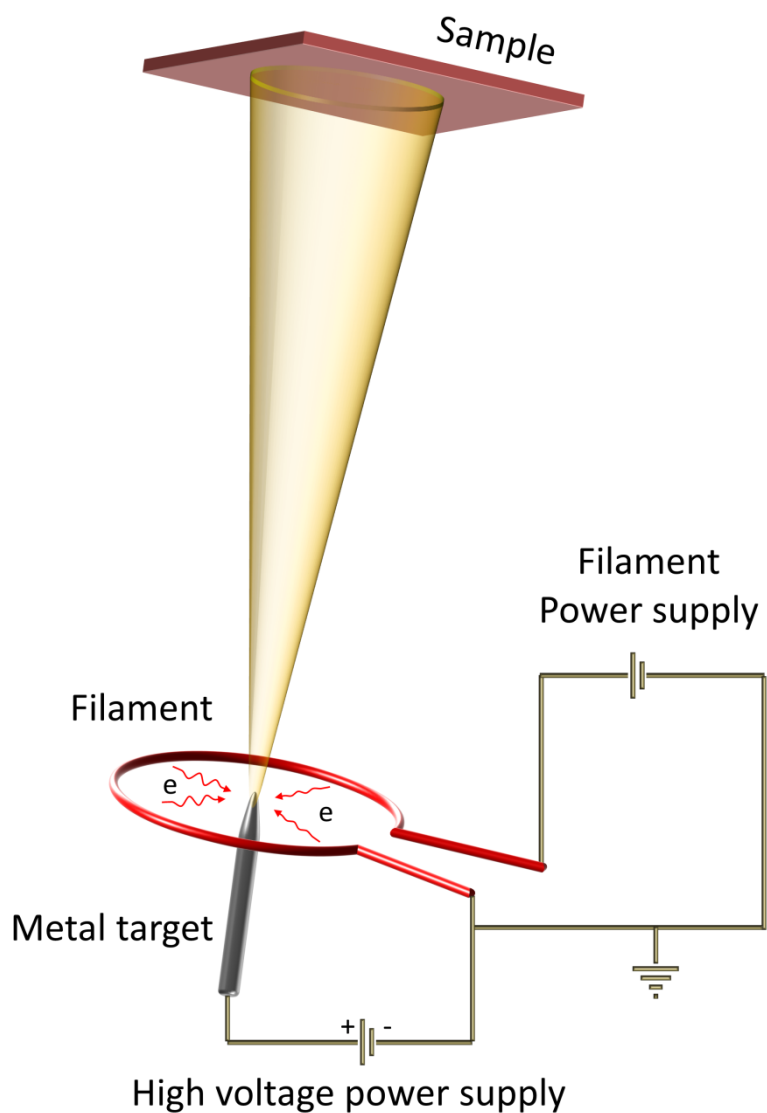


Fig. 21: Schematic of an electron beam evaporator. The hot filament around the metal anode emits electrons toward the metal target which are accelerated since the metal target is connected to a positive voltage ( $\sim 1000\text{V}$ ). In this manner, material from the heated metal target is sublimated and deposited on the sample surface.

After determining the evaporation rate, the quartz microbalance is moved away and the sample is moved back to its original position in front of the evaporator. At this point the evaporation on the sample was carried out with similar conditions as those used during the microbalance measurements. The base pressure of our molecular

beam epitaxy (MBE) chamber was held in the  $10^{-10}$  mbar range during metal evaporation. An example of an STM image obtained from PVD-prepared Pt NPs on  $\text{TiO}_2(110)$  is shown in Fig. 22b.

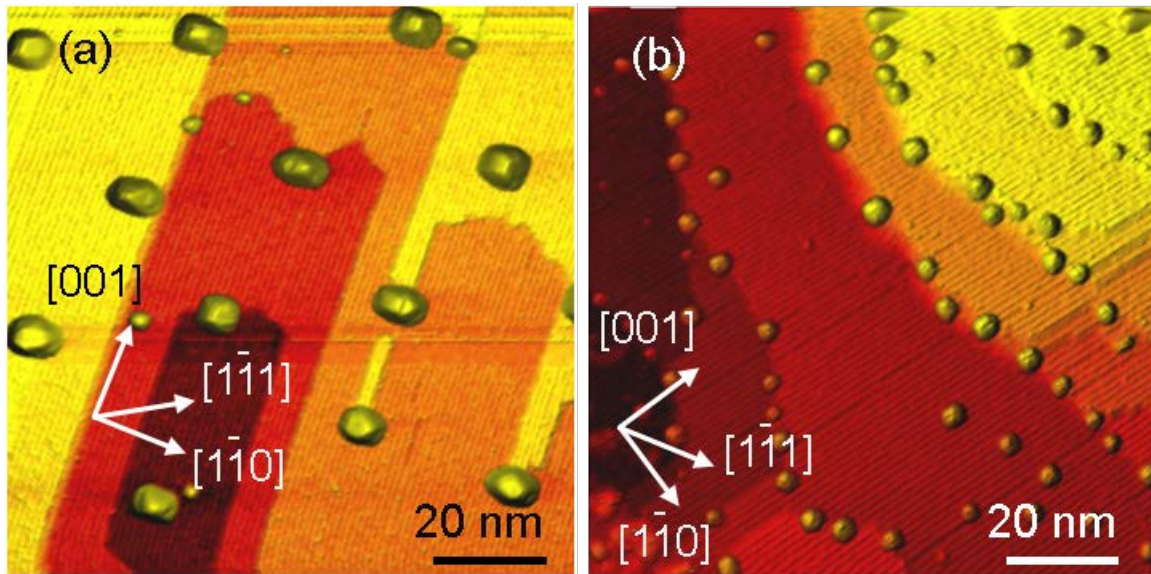


Fig. 22: STM images of Pt NPs supported on  $\text{TiO}_2(110)$  synthesized via (a) inverse micelle encapsulation and (b) physical vapor deposition. Both images were obtained at RT after annealing at  $1060^\circ\text{C}$  in vacuum.

# CHAPTER 4: THERMAL STABILITY AND COARSENING PHENOMENA OF METAL NANOPARTICLES AND THE INFLUENCE OF THE ENVIRONMENT AND SUPPORT PRE-TREATMENT: Pt/TiO<sub>2</sub>(110) AND Pt/ $\gamma$ -Al<sub>2</sub>O<sub>3</sub>

## 4.1 Introduction

The unusual structural, electronic, magnetic, and chemical properties of metal NPs have found numerous applications in technologically important areas such as catalysis, molecular electronics, and plasmonics.<sup>1-4</sup> Nevertheless, in order to take advantage of these new material systems in a real-world industrial setting, a thorough understanding of the evolution of those properties under different environmental conditions, as for example elevated temperatures and exposure to liquid/gas reactants is needed. Although new developments in NP synthesis methods provide the capability of fabricating NPs in the sub-nanometer size regime, unwanted coarsening phenomena commonly lead to the disappearance of the small NP sizes and a broadening of the initially narrow size distributions. This is a major drawback in fields such as catalysis, because a number of chemical processes are structure sensitive, and thermally-induced changes in NP size and shape can result in a dramatic drop of activity due to the loss of surface area<sup>42</sup>, a change in selectivity towards unwanted byproducts, as well as catalyst deactivation.<sup>43</sup>

The present study provides insight into an important aspect influencing the commercial use of oxide-supported metal NPs, namely, their tendency to coarsen at elevated temperatures. Despite the fact that in industrially relevant catalytic combustion processes NP sintering occurs at elevated temperatures ( $\sim 900$  °C)<sup>44-48</sup>, most of the basic *in situ* studies published to date describe a much lower temperature regime ( $\sim 700$



°C). We study here coarsening phenomena in PVD and micellar Pt NPs at more realistic temperatures, namely, in the temperature regime of 930°C to 1060°C. We also pay attention to the effect of the substrate pretreatment (morphology and state of reduction) on the NP coarsening mechanisms. Our model system, Pt/TiO<sub>2</sub>, is presently extensively used in catalysis applications such as water splitting<sup>49</sup>, sulfuric acid decomposition<sup>47</sup>, and photo-oxidation reactions.<sup>50</sup>

Coarsening phenomena in nanoscale systems have been the subject of intensive research efforts since a number of years, with particular emphasis given to the effect of the initial NP size and size distribution,<sup>51-54</sup> as well as the structure, morphology, and stoichiometry of the support.<sup>54-58</sup>

The two main coarsening pathways are: (i) Ostwald ripening, in which individual atoms or molecules detach from small clusters and diffuse over the support surface until they join larger NPs, and (ii) diffusion coalescence, where entire NPs diffuse across the support surface until they coarsen with other NPs. Previous literature reports have described coarsening phenomena in metal NP systems based on either Ostwald-ripening, diffusion coalescence, or both mechanisms, a distinction which was proven to be strongly dependent on the specific material system under investigation. For instance, Thiel et al.<sup>54</sup> reported different coarsening trends for Ag islands on a Ag single crystal depending on the orientation of substrate surface, with Ostwald-ripening phenomena preferentially occurring on Ag(111), and diffusion-coalescence on Ag(100). Additionally, the dominant coarsening pathway was also found to be susceptible to changes in the annealing temperature, time, and chemical environment, with oxidizing environments typically leading to Ostwald ripening, and reducing atmospheres to diffusion-

coalescence<sup>59</sup>. Furthermore, a transition from diffusion-coalescence to Ostwald-ripening was described for Cu islands on Cu(100) with increasing temperature from 300 K to 343 K. On more closely related systems to the one under study here, Ostwald ripening phenomena were held responsible for the sintering of Au NPs on TiO<sub>2</sub><sup>53-60</sup>, while diffusion-coalescence processes were found to occur for Pd/TiO<sub>2</sub>.<sup>56, 57, 61</sup>

Numerous previous studies have used the evolution of the NP size or the shape of the NP size histogram as an indirect diagnostic tool to get insight into the underlying coarsening mechanism, namely, whether it is Ostwald ripening or diffusion/coalescence.<sup>53, 56, 57, 59, 62-68</sup> Following conventional coarsening models<sup>62-67</sup>, NP size distributions with a tail skewed towards lower NP sizes and a sharp cut-off have been commonly assigned to Ostwald ripening processes, while distributions with a long tail (log-normal distribution) towards large NP sizes have been attributed to processes dominated by NP diffusion and coalescence. Surprisingly, the majority of experimental NP size distributions available in the literature are of the log-normal type<sup>67, 69</sup>, even for processes where Ostwald-ripening has been demonstrated to be the main coarsening mechanism.<sup>59, 68</sup> In the past, such discrepancy was attributed to the limitations of most microscopic methods at detecting small NPs, but this is not true for the most recent studies.<sup>59, 69</sup> The work by Datye et al.<sup>59</sup> demonstrated that the shape of the NP size distribution cannot be used to discern different coarsening mechanism, especially in cases where Ostwald ripening and diffusion coalescence processes may occur simultaneously. In such complex cases, the small NPs that should always be present during Ostwald ripening processes could quickly disappear due to their enhanced size-dependent mobility if the diffusion/coalescence pathway occurs concurrently.

Furthermore, in cases where the initial NP size distribution might be of the log-normal type, it might take a very long time for a low-size tail to develop in the size histogram, even when Ostwald ripening is dominant.

A better agreement between experimental data and coarsening simulations following the Ostwald ripening model was obtained by Parker and Campbell<sup>51-53</sup> through the incorporation of a size-dependent surface energy in their model and by using an exponential function in the formulation of the ripening rates instead of a first-order approximation of the associated Taylor series. Both modifications lead to less asymmetric NP size histograms, although broadening and a low-size tail were still observed. Using the mean field approximation, a model for diffusion-coalescence processes was introduced by Smoluchowski.<sup>62, 63</sup> Assuming a simple power law for the NP's diffusion coefficient, the scaling behavior of this model was studied by Kandel,<sup>66</sup> and a size histogram with a tail skewed toward larger sizes was found to gradually develop over long periods of time.<sup>66</sup> However, the former model fails at providing the correct description of coarsening phenomena occurring over short periods of time.

Despite the high level of detail included in the various coarsening models available<sup>53, 57, 66</sup>, relatively little attention has been given to the effect of the morphology and stoichiometry of the NP support, the strength of the NP/support bonding, and the NP synthesis method.

In the present work we use a combination of controlled NP preparation, STM, and theoretical modeling to address these effects. First, we use bench-mark Pt NPs grown by PVD in UHV on pristine TiO<sub>2</sub>(110) surfaces (sample S1) to illustrate NP mobility, step decoration and coarsening phenomena. Secondly, we introduce modifications in the

morphology and reducibility of the TiO<sub>2</sub> support (polymer-coating followed by an oxygen plasma treatment), and study how such modifications relate to the observed changes in the coarsening behavior (sample S2). Finally, we discuss the enhanced thermal stability of self-assembled and geometrically well-defined metal NPs synthesized by inverse micelle encapsulation methods<sup>28, 70</sup> (Sample S3). The narrow NP size distributions that can be achieved by using the micelle encapsulation synthesis allow us to better follow any coarsening phenomena occurring in these samples, since log-normal distributions with tails skewed towards high NP sizes are not present on the as-prepared samples.

Several explanations could be held responsible for the enhanced thermal stability of the micellar NPs, such as the possible existence of residual polymeric carbon trapped underneath the NPs, or the effect of the O<sub>2</sub>-plasma pretreatment. To gain further insight into the different processes, we have mimicked the micellar NPs by depositing PVD-grown NPs on polymer-coated TiO<sub>2</sub> and subsequently exposing those clusters to atomic oxygen (S2). For reference, this sample was then compared with conventional PVD-grown NPs deposited on pristine TiO<sub>2</sub> (S1).

In addition to the pre-treatment effect, designing NP-support systems that ensure the stability of the NPs under reaction conditions, e.g., under a given chemical environment and at high temperature, is essential in order to maintain their catalytic performance and lifetime in an industrial setting.<sup>71</sup> The second part of this study describes the role of the annealing environment on the thermal stability and coarsening behavior of inverse micelle prepared Pt NPs supported on high surface area  $\gamma$ -Al<sub>2</sub>O<sub>3</sub>. Our *in situ* real-time EXAFS measurements were carried out in the presence of O<sub>2</sub>, H<sub>2</sub>O,

or H<sub>2</sub> up to 450°C. Our spectroscopic results are compared to *ex situ* TEM data acquired after the same annealing treatment in the three different environments.

## 4.2 Sample preparation methods and experimental

Two samples were synthesized by evaporating submonolayer coverages (0.09 ML) of Pt on two differently-prepared TiO<sub>2</sub>(110) substrates at a deposition rate of 1.5x10<sup>-3</sup> ML/s (1 ML is defined as 1.5x10<sup>15</sup> atoms/cm<sup>2</sup>) measured by a quartz microbalance. Sample 1 (S1) consisted of Pt NPs evaporated at room temperature (RT) on pristine TiO<sub>2</sub>(110) and subsequently annealed in UHV at 830°C, 930°C, 1030°C and 1060°C for 10 min. Prior to the Pt deposition, the TiO<sub>2</sub>(110) crystal was cleaned by several cycles of Ar<sup>+</sup> sputtering ( $P_{[Ar^+]}$  = 1x10<sup>-6</sup> mbar, 1 keV, 5 μA) for 45 min and annealing at 900-1000 °C for 20 min. This procedure was repeated until large (1x2)-TiO<sub>2</sub> terraces were observed by STM.<sup>72</sup> All experiments were conducted on a TiO<sub>2</sub>(110) crystal of dark blue color, which indicates its bulk reduction. Such crystal has sufficient conductivity for STM imaging, and displays a bandgap of about 3.2 eV according to our scanning tunneling spectroscopy (STS) measurements (Fig. 23).

In order to test whether the roughness of the substrate (e.g. terrace width, presence of defects, etc.) and/or stoichiometry (degree of TiO<sub>2</sub> reduction) affects the coarsening behavior of the deposited NPs, a second sample (S2) with a polymer-modified surface [PS(27700)-P2VP(4300) dissolved in toluene] was prepared. The same Pt coverage as in S1 (0.09 ML) was evaporated at RT on the polymer-modified TiO<sub>2</sub>(110) support (S2).

A third sample was prepared consisting of micellar Pt NPs supported on TiO<sub>2</sub>(110) (S3) synthesized by reverse micelle encapsulation<sup>70</sup> as described in detail elsewhere.<sup>28, 73-76</sup> The diblock copolymer used for this synthesis was the same one employed to modify the TiO<sub>2</sub> surface in S2, with the difference that in the latter case the polymeric micelles were loaded with Pt, with a metal salt-to-P2VP weight ratio of 0.6.

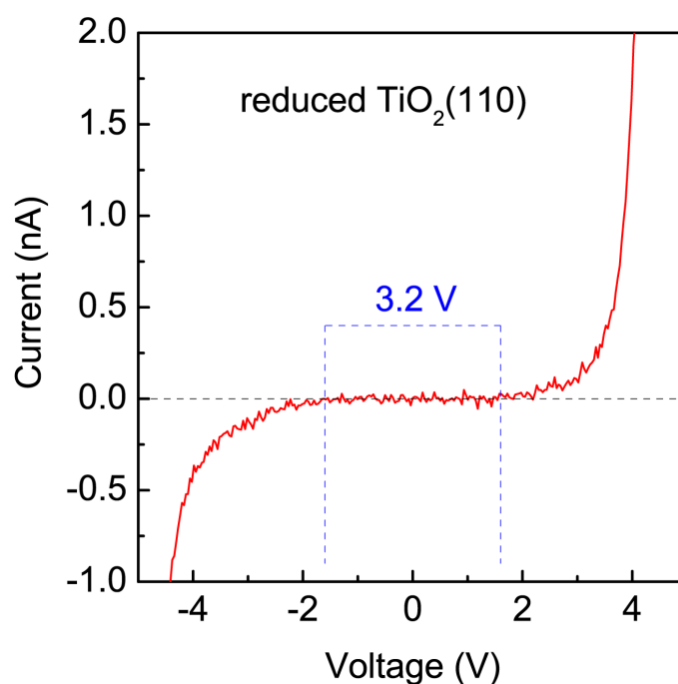


Fig. 23: STS measurements (I-V curve) of a sputtered-annealed reduced TiO<sub>2</sub>(110) surface showing a characteristic ~3.2 eV bandgap.

Sample 1 was prepared in UHV, while S2 and S3 were introduced into our UHV system after substrate functionalization with the PS-P2VP polymer (before Pt NP deposition for S2 and after the dip-coating of the micellar Pt NPs for S3). The removal of the polymeric ligands from S3 was achieved by an *in situ* oxygen-plasma treatment (O<sub>2</sub> pressure =  $4 \times 10^{-5}$  mbar, 120 min) at RT. Sample 2 was subjected to an analogous treatment to remove the polymer from the substrate surface after the deposition of Pt in

UHV. XPS measurements (Al-K $\alpha$ , 1486.6 eV) conducted after the latter treatment corroborated the complete disappearance of the polymeric C-1s signal from the micellar sample (S3). Although the C-1s signal completely disappeared after the O<sub>2</sub>-plasma for S3 (micellar NPs surrounded by a thin polymeric layer), a small C signal was detected for S2 (evaporated NPs deposited on a thicker polymer layer) after the first annealing treatment at 930°C, which was assigned to polymeric carbon leftover from the TiO<sub>2</sub> pre-treatment likely trapped underneath the NPs. Nevertheless, no C was detected by XPS in any of the samples after the subsequent annealing at high temperature (>930°C), which is the starting point of our coarsening study.

After the atomic oxygen exposure, the micellar sample (S3) was isochronally annealed in UHV in 100°C intervals from 300°C to 900°C for 20 min and from 1000°C to 1060°C for 10 min. Sample 2 experienced a thermal treatment identical to that of S1. The NPs in S3 are oxidized (PtO<sub>2</sub>) after the O<sub>2</sub>-plasma treatment but subsequently reduced after annealing above 300°C.<sup>76</sup>

The comparison of the morphology of all three samples directly after NP deposition at RT was not possible via STM due to the strong enhancement of the roughness of the TiO<sub>2</sub> substrate observed after the O<sub>2</sub>-plasma treatment applied to S2 and S3 to remove the organic ligands used in the synthesis. Such treatment gives rise to TiO<sub>x</sub> clusters on the support surface which cannot be easily distinguished from small Pt NPs based exclusively on morphological measurements. Therefore, the comparison of the sintering behavior of all three samples was done after annealing treatments above 900°C, which were found to lead to a flatter TiO<sub>2</sub> morphology that could be atomically resolved.

STM images were acquired at RT after annealing from 930°C to 1060°C. An electrochemically-etched W tip was used. The tip was cleaned in UHV by Ar<sup>+</sup> sputtering before each STM session. The base pressure of the STM chamber was 1×10<sup>-10</sup> mbar. The scanning parameters used were: I<sub>t</sub> = 0.1 nA and V<sub>t</sub> = 1.2 V. Due to tip convolution effects, the NP diameter obtained by STM overestimates the real diameter<sup>56, 57, 77, 78</sup>, and since the tip shape might also change during the measurements, it cannot be reliably used for comparison purposes. Since the measured NP height is independent of the tip shape, it is used here as representative size parameter, Table 2. Throughout this manuscript, when NPs were observed at TiO<sub>2</sub> step-edges, the average height of the top and bottom TiO<sub>2</sub> terraces was used as height background reference.

In the second part of this study, γ-Al<sub>2</sub>O<sub>3</sub> supported micellar NPs were prepared for EXAFS and TEM measurements. Inverse micelles were created by dissolving polystyrene 2-vinylpyridine, [PS(16000)-P2VP(3500)] in toluene. Subsequently, the micellar cages were loaded with Pt (H<sub>2</sub>PtCl<sub>6</sub> precursor) with a 0.05 ratio for S4-S6. The NP solution was then mixed with nanocrystalline γ-Al<sub>2</sub>O<sub>3</sub> (surface area > 150 m<sup>2</sup>/g) at a loading of 1 % wt. Pt, and allowed to dry in air at 60°C. Additional details on the sample preparation can be found in Refs. 5, 28, 39, 79-81.

For this part of the study, we have prepared 3 separate but identically synthesized samples, and exposed them to three different annealing environments in order to explore their influence on the dispersion and thermal stability of the NPs. Samples 4, 5, 6 were pre-treated in O<sub>2</sub> (70% balance by He) at 375°C for 24 h and subsequently reduced *in situ* in H<sub>2</sub> (50% balance by He) at 375°C for 30 min. Next, sample S4 was annealed in O<sub>2</sub> at 450°C for 3 hours and sample S5 was exposed to water vapor at



atmospheric pressure using a bubbler and annealed in the presence of water vapor and He at 450°C for 3 hours. Finally, sample S6 was annealed in H<sub>2</sub> at 450°C for 3 h. At the end of each thermal treatment, all three samples were reduced in hydrogen at 375°C and the final NP size evaluated *in situ* via EXAFS (in H<sub>2</sub>) and *ex situ* via STEM, both at RT. The summary of different treatments for each sample is provided in Table 1.

Table 1: Summary of the *ex situ* and *in situ* treatments applied to samples S4-S6

SAMPLE Pt NPs/ $\gamma$ -Al <sub>2</sub> O <sub>3</sub>	<i>Ex situ</i> pre-treatment	<i>In situ</i> pre-treatment	<i>In situ</i> thermal treatment
S4	375°C (24h in O <sub>2</sub> )	375°C (0.5h in H <sub>2</sub> )	450°C (3h in O <sub>2</sub> )
S5	375°C (24h in O <sub>2</sub> )	375°C (0.5h in H <sub>2</sub> )	450°C (3h in H <sub>2</sub> O vapor)
S6	375°C (24h in O <sub>2</sub> )	375°C (0.5h in H <sub>2</sub> )	450°C (3h in H <sub>2</sub> )

TEM measurements were carried out by A. DeLaRiva in Prof. Datye's group at the University of New Mexico, Albuquerque. HAADF STEM measurements were performed on our samples before and after the coarsening investigation to obtain information on the NP size. The high absorption of the nanocrystalline alumina support makes measurements of very small Pt NPs (<1 nm) difficult, even in the HAADF STEM mode, due the poor contrast. TEM measurements were carried out on as-prepared, and 450°C H<sub>2</sub>O, O<sub>2</sub>, and H<sub>2</sub>-annealed samples<sup>82</sup>, to obtain the NP sizes, Table 3. The average NP diameters were obtained from measuring the full width at half-maximum of at least 600 particles per sample.<sup>82</sup> The error bars provided for the average TEM diameters are the standard deviation of the measured NP diameters.

EXAFS measurements at the Pt-L<sub>3</sub> edge were conducted *in situ* during the different thermal treatments at the NSLS at Brookhaven National Laboratory. The

experiments were carried out in fluorescence mode at beamline X19A with the powder samples pressed into thin pellets and placed inside a reactor cell with heating and cooling capabilities. The furnace was positioned on a motorized stage and the quartz tube axis was aligned along the x-ray beam direction. The samples were reduced *in situ* at 375°C in H<sub>2</sub> and subsequently annealed in different environments (O<sub>2</sub>, H<sub>2</sub>O, and H<sub>2</sub>) up to 450°C for 3 hours.

The Athena and Artemis programs from the Iffeffit software package were used to process and analyze the EXAFS data acquired.<sup>83, 84</sup> A Pt foil measured in reference mode was used to align different scans of the NP samples. The Artemis program<sup>83-85</sup> was used to fit the 1<sup>st</sup> nearest neighbor (NN1) Pt-Pt component of the EXAFS data. Theoretical EXAFS signals were constructed with the FEFF6 program<sup>86</sup> using the model structure of face centered cubic (fcc) Pt. The crystalline structure of all reduced Pt NPs investigated here is consistent with the fcc structure. The influence of the annealing environment on NP coarsening is illustrated by comparing reduced samples measured in H<sub>2</sub> at RT before and after a given annealing treatment in O<sub>2</sub>, H<sub>2</sub>O, or H<sub>2</sub> (S4-S6).

### **4.3 Theoretical and simulation methods**

The following models have been applied to simulate the coarsening mechanisms of Pt NPs prepared using two distinct synthesis methods (PVD and inverse micelle encapsulation) and supported on differently treated TiO<sub>2</sub>(110) surfaces. Each simulation requires two sets of measurements: (i) one initial experimental NP size distribution as the starting point of the simulation which is being subjected to a thermal treatment, and (ii) a measurement of the final state of the sample after the thermal treatment, which is

used to compare with the results of the simulation. Therefore, based on three sets of STM images acquired after annealing at 930°C, 1030°C and 1060°C, two sets of simulations can be carried out: (i) from 930°C to 1030°C, and (ii) from 1030° to 1060°C. The former will be compared with the experimental 1030°C and 1060°C STM size histograms, respectively.

### 4.3.1 Ostwald ripening

Following the Ostwald-ripening model, atoms detach from small NPs and move randomly over the substrate surface until they find another NP to join. It should be considered that small NPs lose atoms at a higher rate as compared to larger clusters due to size-dependent energetics. As a result of this phenomenon, the larger NPs grow in size at the expense of the smaller ones, until the latter completely disappear. The overall result is a shift of the NP size distribution to higher values and a decrease in the density of NPs on the substrate surface. For an interface-limited Ostwald-ripening process, in which the rate limiting step is the detachment of metal atoms from the NP perimeter (in contact with the support), the rate of change of the size of a NP with radius  $R$  is<sup>51, 53, 64, 65</sup>:

$$\frac{dR}{dt} = \frac{K}{R} \exp\left[\frac{-E_{tot}}{k_B T}\right] \left( \exp\left[\frac{E(R^*)}{k_B T}\right] - \exp\left[\frac{E(R)}{k_B T}\right] \right) \quad (17)$$

, where  $k_B$  is the Boltzmann constant and  $R^*$  is a critical NP radius that represents the unstable equilibrium size for which the NP radius remains constant due to a compensation effect based on the number of incoming atoms arriving to a NP being the

same as that of the atoms leaving the NP.  $E(R)$  is the difference between the heat of adsorption of a metal atom in a NP of radius  $R$  and the corresponding bulk sublimation enthalpy ( $H_{\text{SUB}}$  in Fig. 24),  $E_{\text{tot}}$  is the total energy barrier of the system, and  $K$  is a parameter that depends on the specific NP material, the vibrational frequency of a monomer on the NP, and the contact angle of the metal NP with the support (assumed to be  $90^\circ$  here).<sup>52, 53, 64, 65</sup>

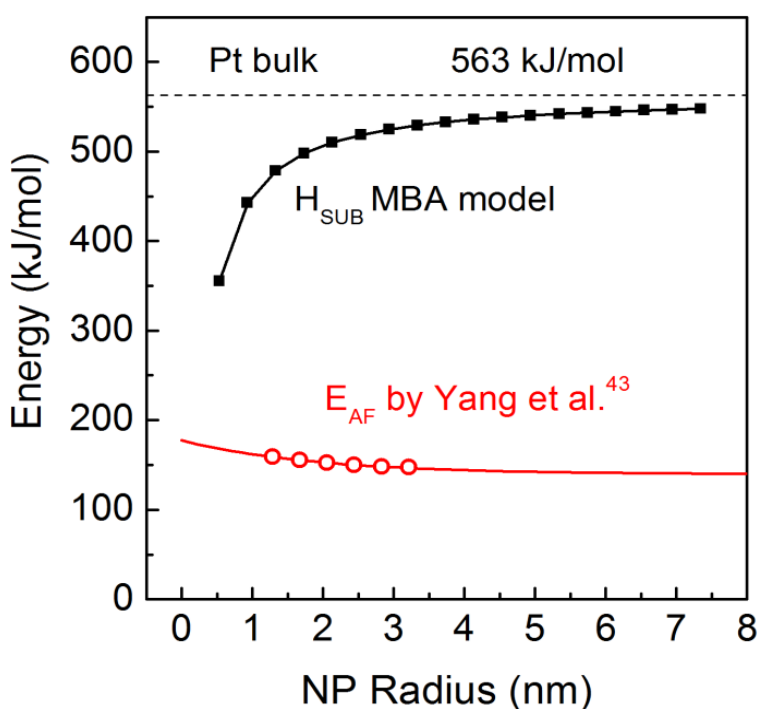


Fig. 24: Heat of sublimation of Pt atoms ( $H_{\text{SUB}}$ ) calculated using the MBA model and adatom formation energy ( $E_{\text{AF}}$ ) calculated by Yang et al.<sup>87</sup>, using molecular dynamics and nudged elastic band calculations for Pt clusters with Wulff polyhedral shape. The horizontal dashed line indicates the heat of sublimation of bulk Pt.

Since the surface energy is expected to be size-dependent for NPs smaller than  $\sim 5$  nm, the formulation of the heat of sublimation previously used by other groups<sup>55-57, 64, 67</sup> assuming a constant surface energy and giving rise to a  $1/R$  size dependency is not valid for the calculations of  $E(R)$  in eq. (1). Instead, the modified bond-additivity model

(MBA) must be used.<sup>51-53</sup> Fig. 24 displays the heats of sublimation that we have extracted following the MBA model using Wulff-like NP shapes<sup>1, 5, 88-90</sup> instead of previously considered pyramidal shapes.<sup>51-53</sup> The former shapes are expected to be a better representation of the most commonly observed experimental NP geometries.<sup>1, 5, 88, 89</sup>

$E(R)$  was obtained by subtracting the heat of sublimation of bulk Pt (563 kJ/mol) from that obtained from the MBA model for the Pt NPs, Fig. 24.

In addition, the critical radius ( $R^*$ ) in eq. (1) should be defined in a way that satisfies the mass conservation pre-requisite, e.g., no atoms are expected to be lost during the coarsening process at the particular temperatures considered.<sup>90</sup> We have ensured mass conservation by setting  $\sum dV_{tot}/dt=0$ , where  $V_{tot}$  is the total volume of the NPs. This allows us to determine the critical energy  $E(R^*)$  in eq. (1) following:

$$E(R^*) = k_B T \ln \left[ \frac{\sum R_i \exp \left[ \frac{E(R_i)}{k_B T} \right]}{\sum R_i} \right] \quad (18)$$

One important practical challenge in the use of eq. (1) to obtain the time dependent  $R(t)$  for many NPs is the fact that widely different time scales are involved in the coarsening phenomena. The size reduction of NPs with a radius well below the critical radius and the continued reappearance of small clusters occur extremely rapidly at elevated temperatures ( $10^{-4} - 10^{-7}$  s). In order to follow such effects while maintaining mass conservation using eq. (18), very fine time steps are needed during the entire thermal treatment.<sup>90</sup> Such small time steps result in computationally intensive calculations, especially for the industrially relevant time scales of coarsening, which are

in the order of months to years. To overcome this issue we have introduced a new method to reduce the computation time by several orders of magnitude while ensuring mass conservation. Our approach is to use numerical methods to find the effective critical energy  $E(R^*)$  that conserves the total mass during the desired time step (as large as several seconds). The change in the total volume ( $\Delta V$ ) obtained from an initial guess of  $R^*$  is calculated, and a bisection method implemented to find the root of  $\Delta V[E(R^*)]$ . Since the change in  $R^*$  is gradual, the bisection method was found to converge very fast, and  $E(R^*)$  can be calculated within a few iterations. Therefore, instead of running the simulation with a very fine time step (e.g. a time step of  $10^{-5}$  s needs  $10^5$  calculations for each second of simulation), similar results satisfying mass conservation can be achieved by using larger time steps (e.g. 1 s) and doing just a few numerical calculations.

#### 4.3.2 Diffusion-coalescence

In addition to the model discussed above, the possibility of NP diffusion and sintering must also be taken in to account. Following the mean field approximation, the rate of change of the density of NPs on a substrate is given by:<sup>55-57, 62, 63</sup>

$$\frac{\partial f(v,t)}{\partial t} = \int_0^v D_C(v') f(v',t) f(v-v',t) dv' - \int_0^\infty [D_C(v) + D_C(v')] f(v,t) f(v',t) dv' \quad (19)$$

, where  $D_C$  is the diffusion constant of the NPs<sup>55-57</sup>,  $v$  is the NP volume, and  $f(v)$  is the density of NPs with volume  $v$ . It is assumed that the NPs are distributed randomly on the support and that the probability of interparticle collision is proportional to their surface density as well as to their mobility.

The diffusion constant of the NPs ( $D_C$ ) is proportional to the density of adatoms on the NP surface ( $\rho$ ) and has a  $1/r^4$  size dependence.<sup>55-57</sup> However, the previous formulations were only valid for the comparison of isothermal experiments.<sup>55, 56</sup> In order to overcome this shortcoming, we have introduced the following expression for  $\rho$ :

$$\rho = \rho_0 \exp\left[\frac{-E_{AF}(R)}{k_B T}\right] \quad (20)$$

, where  $\rho_0$  is the density of adatoms at infinite T, which is the same as the surface density of metal atoms [ $\approx 1.5 \times 10^{19}$  atoms/m<sup>2</sup> for the platinum (111) surface]. The adatom formation energy barrier ( $E_{AF}$ ) is the energy needed for an atom to migrate from the core of the NP to the surface, and is equal to the heat of sublimation minus the binding energy of the adatom to the surface. Here, the size effect is implicitly included in  $E_{AF}(R)$ , and therefore, using the proper  $E_{AF}(R)$  is the key to obtain the correct diffusion equation. We have used in our simulations the results of molecular dynamics (MD) and nudged elastic band (NEB) calculations by Yang et al.<sup>91</sup> for the adatom formation energy of clusters with Wulff polyhedral shape, Fig. 24.

Following the above considerations, a modified description of the diffusion coefficient of a NP with radius R is proposed:

$$D_c(R, T) = K_S \rho_0 D_0^{Pt} \frac{3\Omega^2}{\pi R^4} \exp\left[\frac{-(E_d + E_{AF})}{k_B T}\right] \quad (21)$$

, where  $K_S$  is a constant which takes into account the support effect,  $D_0^{Pt}$  is a pre-exponential factor,  $\Omega$  is the atomic volume of Pt, and  $E_d$  is the Pt self-diffusion barrier.  $\Omega$  is the Pt atomic volume, and R is the NP radius.

Equations (19) and (21) can be used to calculate the time evolution of the NP size distribution. We have introduced an efficient matrix-based calculation to simulate eq. (19) which is equivalent to its direct integration, but that overcomes the statistical errors associated with the random collision method.<sup>66</sup> First, a volume vector  $\mathbf{V}$  is constructed containing monotonically increasing values of NP volumes,  $v_i$ . Then, for a given instant of time, the volume histogram vector is constructed,  $\mathbf{F}_i = f(v_i)$ , in which each element contains the population of NPs with volume  $v_i$ . In the next step, the diffusion coefficient vector  $\mathbf{D}_i = \mathbf{D}(v_i)$  is calculated, with each element being the diffusion coefficient of a cluster with size  $v_i$ . The time evolution matrix is given by:

$$\mathbf{T} = \mathbf{F}^T (\mathbf{D} \circ \mathbf{F}) \text{ or } \mathbf{T}_{ij} = \mathbf{F}_i (\mathbf{D}_j \cdot \mathbf{F}_j) \quad (22)$$

, where “o” denotes the Hadamard product of the two matrixes.  $\mathbf{T}_{ij}$  is the collision rate of clusters with volume  $v_j$  moving towards clusters with volume  $v_i$ . This simple matrix multiplication provides all the information needed to determine the time evolution of a NP size distribution within a given time step. The change in the population of clusters with volume  $v_i$  after a time step  $dt$  is obtained from:

$$df(v_i) = \sum_{k=j-i} \mathbf{T}_{jk} dt + \sum_j (\mathbf{T}_{ij} + \mathbf{T}_{ji}) dt \quad (23)$$

, where the first and second terms on the right hand side, represent the first and second integrals in eq. (19)



## 4.4 Results

### 4.4.1 Pt NPs evaporated on pristine TiO<sub>2</sub>(110) (STM)

RT STM images of NPs grown by evaporating 0.09 ML of Pt on pristine (sputtered/annealed) TiO<sub>2</sub>(110) are shown in Fig. 25. The images correspond to a sample that was subsequently isochronally annealed in UHV at 930°C (a,b), 1030°C (c,d), and 1060°C (e,f) for 10 min. The atomically-resolved (1×2) reconstruction of the partially reduced TiO<sub>2</sub>(110) support can be seen in these images. This surface reconstruction is typical of strongly reduced TiO<sub>2</sub> crystals.<sup>55, 72</sup> Fig. 25 shows the presence of Pt NPs over the entire TiO<sub>2</sub> surface at 930°C. However, with increasing annealing temperature (>1000°C), preferential decoration of TiO<sub>2</sub> step sites is observed, although some NPs still remain on terraces of the support even at 1060°C. The steps on this TiO<sub>2</sub> surface are not primarily oriented along [001], which is known to be one of the most stable step orientations after high temperature annealing.<sup>55</sup> The latter is attributed to insufficient annealing time during our experiments to achieve the most stable step orientation.

Histograms of the NP height and interparticle distance obtained from these STM images are included in Fig. 26. An increase in the average NP height from  $0.5 \pm 0.2$  nm to  $1.0 \pm 0.3$  nm is observed with increasing annealing temperature from 930°C to 1060°C, Fig. 26(a). As expected in coarsening processes, the increase in the NP height is accompanied by a parallel decrease in the NP density on the support, Fig. 26(a), and an increase in the interparticle distance, Fig. 26(b).

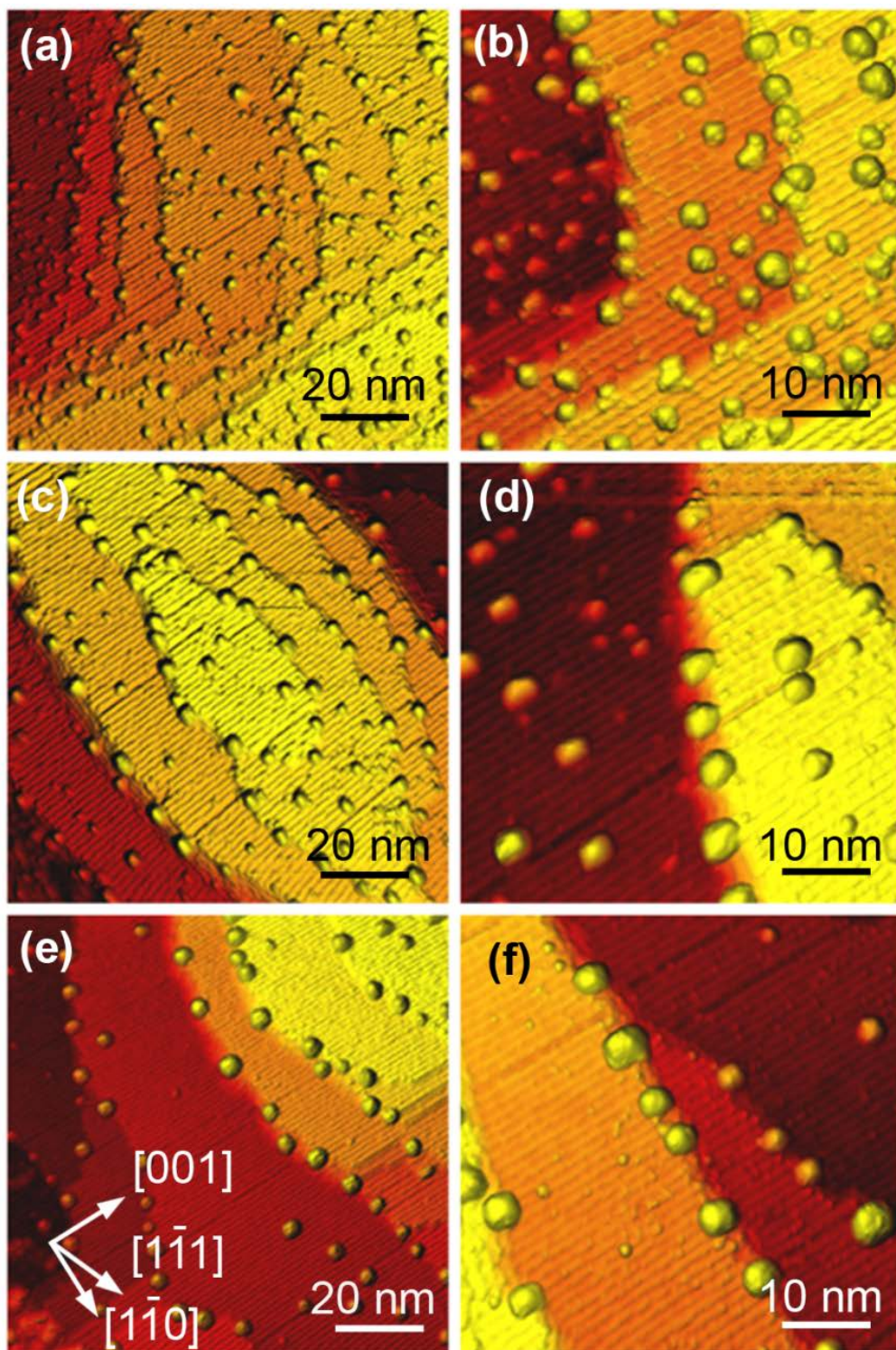


Fig. 25: STM images of 0.09 ML of Pt evaporated on pristine TiO<sub>2</sub>(110) acquired at RT after annealing in UHV at 930°C (a,b), 1030°C (c,d), and 1060°C (e,f) for 10 min.

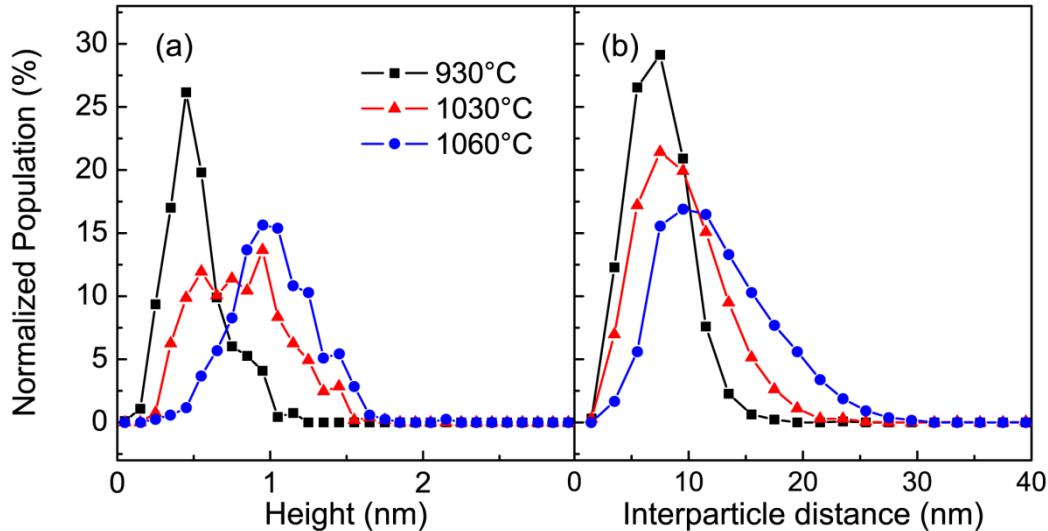


Fig. 26: Height (a) and interparticle distance (b) histograms obtained from the STM data of Pt NPs evaporated on pristine TiO<sub>2</sub>(110) shown in Fig. 25 after annealing at 930°C (squares), 1030°C (triangles), and 1060°C (circles).

As mentioned before, the NP diameter obtained via STM for 3D NPs cannot be trusted due to tip-convolution effects.<sup>55-57, 77, 78</sup> However, STM measurements provide reliable information on the NP height ( $h$ ) and surface density, parameters that in combination with the total evaporated thickness estimated from the quartz microbalance can be used to gain insight into the NP shape. By assuming that no material has been lost during the different annealing treatments, the total volume of all Pt NPs in our sample should be the same at each temperature. This volume can be extracted from the quartz microbalance measurements. In order to gain insight into the NP shape (aspect ratio  $\phi = \text{height}/\text{radius}$ ), an initial guess of the shape can be made, for example, hemispherical, and the total volume of Pt can be calculated based on the STM-measured NP height and cluster density. If the latter total STM volume is different from the one obtained from the quartz microbalance, it could be concluded that a wrong

assumption for the NP shape was made, and that a different aspect ratio must be considered. Following this idea, the NP aspect ratio can be adjusted ( $0 < \phi < 2$ ) for all STM measurements at a given temperature in order to satisfy the mass conservation criterion. For truncated spherical NPs (of radius R and height  $< 2R$ ), the NP volume is

$$\text{obtained from: } V_i = \pi h_i^3 \left( \frac{1}{\phi} - \frac{1}{3} \right)$$

These calculations were done using individual NP heights ( $h_i$ ) measured by STM. Table 1 shows the calculated aspect ratios following the above approach after each annealing treatment. The aspect ratios represent an average of those from small and large NPs present on the support surface at a given temperature. An increase in the average aspect ratio is observed with increasing average NP size (height), suggesting that NP-support interactions are weaker for the larger NPs. Although this result is obtained for truncated spherical NP shapes, it is also expected to be valid for other shapes.

Since the pristine substrate was already annealed at high temperature before Pt evaporation, the support is not expected to change significantly upon annealing [the original (1×2) reconstruction remains], and the change in the shape of the NPs cannot be attributed to morphological changes of the support surface.

For our 3D NPs, the larger the NPs, the lower will be the influence of interfacial effects. A similar effect was reported by Yang et al.<sup>91</sup>, since Au NPs larger than 4.6 Å deposited on TiO<sub>2</sub>(110) were found to be less sensitive to the oxygen content on the TiO<sub>2</sub> surface than smaller NPs. Jak et al.<sup>55-57</sup> also described an increase in the aspect ratio of Pd NPs supported on TiO<sub>2</sub>(110) upon annealing treatments in UHV at 672 K.

Table 2: Average NP height (h), interparticle distance (IP), density of NPs on the support, and aspect ratio extracted from the analysis of RT STM measurements acquired after annealing at the indicated temperatures. The data displayed correspond to Pt NPs evaporated on (a) pristine TiO<sub>2</sub>(110), (b) polymer-coated TiO<sub>2</sub>(110), and (c) micellar Pt NPs deposited on TiO<sub>2</sub>(110). The standard deviations are included in parenthesis.

	Height (nm)	IP distance (nm)	Surface density (NP/m <sup>2</sup> × 10 <sup>15</sup> )	Aspect ratio $\phi$
(a) Pt NPs evaporated on pristine TiO <sub>2</sub> (110) – S1				
930°C	0.5 (2)	7 (3)	25.6	0.6
1030°C	0.8 (3)	9 (4)	11.3	0.9
1060°C	1.0 (3)	12 (5)	7.3	1.0
(b) Pt NPs evaporated on polymer-coated TiO <sub>2</sub> (110) – S2				
930°C	0.8 (3)	9 (4)	13.5	0.9
1030°C	1.0 (4)	11 (5)	7.5	1.0
1060°C	1.3 (6)	13 (7)	3.8	1.1
(c) Micellar Pt NPs deposited on pristine TiO <sub>2</sub> (110) – S3				
1000°C	3.1 (6)	28 (5)	1.3	-
1060°C	3.0 (7)	31 (7)	1.3	-
1060°C 2 <sup>nd</sup>	3.0 (9)	30 (7)	1.4	-

#### 4.4.2 Pt NPs evaporated on polymer-modified TiO<sub>2</sub>(110) (STM)

In order to test whether the roughness of the substrate (e.g. terrace width, presence of defects, etc.) and/or stoichiometry (degree of TiO<sub>2</sub> reduction) can affect the mobility of the deposited NPs, we have prepared a second sample in which the clean pristine TiO<sub>2</sub>(110) substrate was initially *ex situ* coated by a thin layer of the PS-P2VP diblock copolymer. Pt NPs (0.09 ML) were evaporated in UHV on the polymer-coated

TiO<sub>2</sub> surface at RT and subsequently exposed to an O<sub>2</sub>-plasma treatment and isochronal annealing from 930°C to 1060°C for 10 min, Fig. 27.

Although the strong reduction of our bulk TiO<sub>2</sub>(110) crystal used in these experiments was evident from its dark blue color, the former treatment results in a lower degree of reduction of the TiO<sub>2</sub> surface as compared to the pristine sample. Nevertheless, after our high temperature annealing, the same (1×2) reconstruction is observed for both samples. The STM images in Fig. 27 reveal a rougher morphology (narrow terraces) of the TiO<sub>2</sub> surface after the above treatment as compared to pristine TiO<sub>2</sub>, which is characterized by much wider terraces at the same temperatures. Moreover, straight TiO<sub>2</sub> steps with a preferential [001] orientation are observed in the polymer-coated TiO<sub>2</sub> sample after O<sub>2</sub>-plasma and annealing, while rounder steps appear on pristine TiO<sub>2</sub>.

This result indicates that the initial presence of the polymer and atomic oxygen pre-treatment affect the subsequent morphology (terrace width and preferential step direction) of the TiO<sub>2</sub> surface upon high temperature annealing. Even in the absence of NPs, the TiO<sub>2</sub> surface is known to form elongated steps along [001] at high temperature (>900°C) in order to accommodate a non-stoichiometric composition without destroying the crystalline structure.<sup>55</sup>

It is interesting that we do not see these steps on the pristine TiO<sub>2</sub> sample after an analogous annealing treatment. We attribute the difference to the distinct roughness and stoichiometry of both supports. An enhanced roughness is expected for the polymer-coated and O<sub>2</sub>-plasma-treated surface.

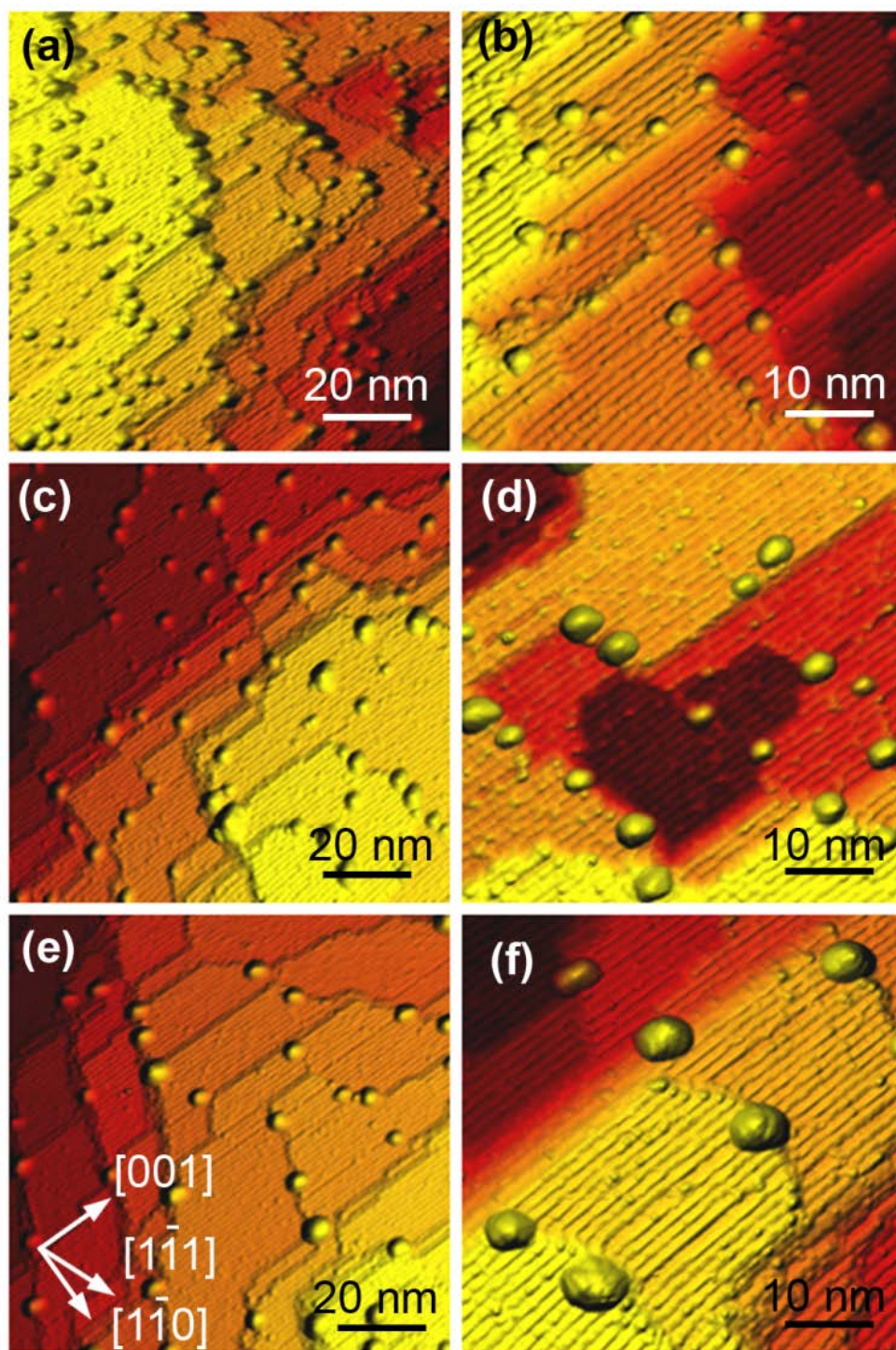


Fig. 27: STM images of 0.09 ML of Pt evaporated on polymer-coated TiO<sub>2</sub>(110) taken at RT after an O<sub>2</sub>-plasma treatment and subsequent annealing in UHV at 930°C (a,b), 1030°C (c,d), and 1060°C (e,f) for 10 min.

*Ex situ* AFM investigations of the TiO<sub>2</sub>(110) surface by Jak<sup>55</sup> also revealed relatively narrow [001] steps on rough TiO<sub>2</sub> surfaces upon air exposure.

After annealing at 1060°C [Fig. 27(e,f)], the majority of the NPs on this sample can be found at TiO<sub>2</sub> steps. Since during Pt evaporation all the steps and defect sites on the TiO<sub>2</sub> surface were masked by the polymer in this sample, our NPs did not initially form by nucleation at steps (strong binding sites). Instead, significant mass transport (Pt atoms and/or clusters) must have occurred during the O<sub>2</sub>-plasma and subsequent thermal treatment. In analogy to the case of the Pt NPs evaporated on the pristine TiO<sub>2</sub>(110) surface, the size histogram from this sample reveals an increase in the average NP height (from ~0.8 nm at 930°C to 1.3 nm at 1060°C) [Fig. 28(a)] and an increase in the interparticle distance [Fig. 28(b)] with increasing annealing temperature.

These effects are accompanied by a decrease in the NP density on the support surface, Table 1(b). An increase in the NP aspect ratio is also observed for this sample with increasing annealing temperature, indicating the decrease in the binding energy of the NPs to the support. As mentioned before, the TiO<sub>2</sub> substrate in this sample was exposed to air (*ex situ* polymer coating) before NP deposition, and subsequently O<sub>2</sub>-plasma treated in UHV (after Pt NP deposition), leading to an oxidized TiO<sub>2</sub> surface. However, each subsequent annealing cycle in UHV at high temperature is expected to further reduce the TiO<sub>2</sub> surface, strengthening thus the binding of the Pt NPs to TiO<sub>2</sub>, since oxygen vacancies have been reported to be preferential binding sites for metal NPs.<sup>18, 56, 78, 91-95</sup>

However, the increase in the aspect ratio observed (more 3D-like NPs) in spite of the increase in the degree of reduction of the support surface (that should have lead to



2D NPs) can be understood as a size effect, since the interface effect is not as important for the larger NPs formed due to coarsening.

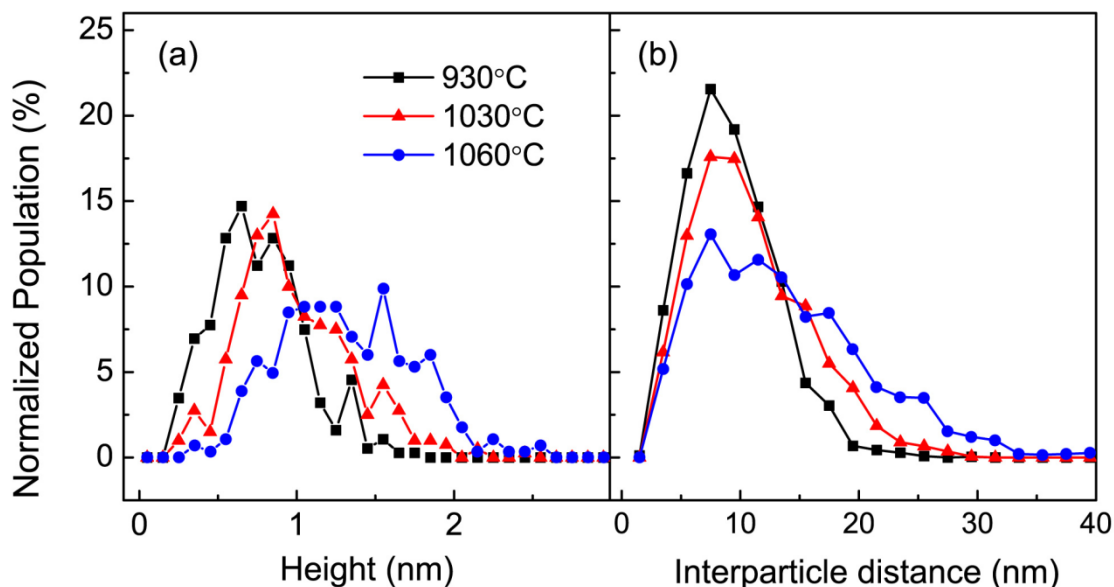


Fig. 28: (a) Height and (b) interparticle distance histograms obtained from the STM data of Pt NPs evaporated on polymer-coated  $\text{TiO}_2(110)$  shown in Fig. 3 after an  $\text{O}_2$ -plasma treatment and subsequent annealing at 930°C (squares), 1030°C (triangles), and 1060°C (circles). The population has been normalized for different measurements to have the same area under the curve of 100.

#### 4.4.3 Micellar Pt NPs/ $\text{TiO}_2(110)$ (STM)

Fig. 29 displays STM images from micellar Pt NPs dip-coated on  $\text{TiO}_2(110)$  (S3) after polymer removal by atomic oxygen exposure and subsequent annealing at (a) 300°C and (b) 1000°C.

Surprisingly, neither the NP size nor their surface distribution was found to change significantly upon annealing at 1000°C, Fig. 29(b). However, a decrease in the

roughness of the TiO<sub>2</sub> support (induced by the initial O<sub>2</sub>-plasma treatment) from  $0.3 \pm 0.05$  nm after annealing at 300°C to  $0.07 \pm 0.03$  nm at 1000°C can be seen.

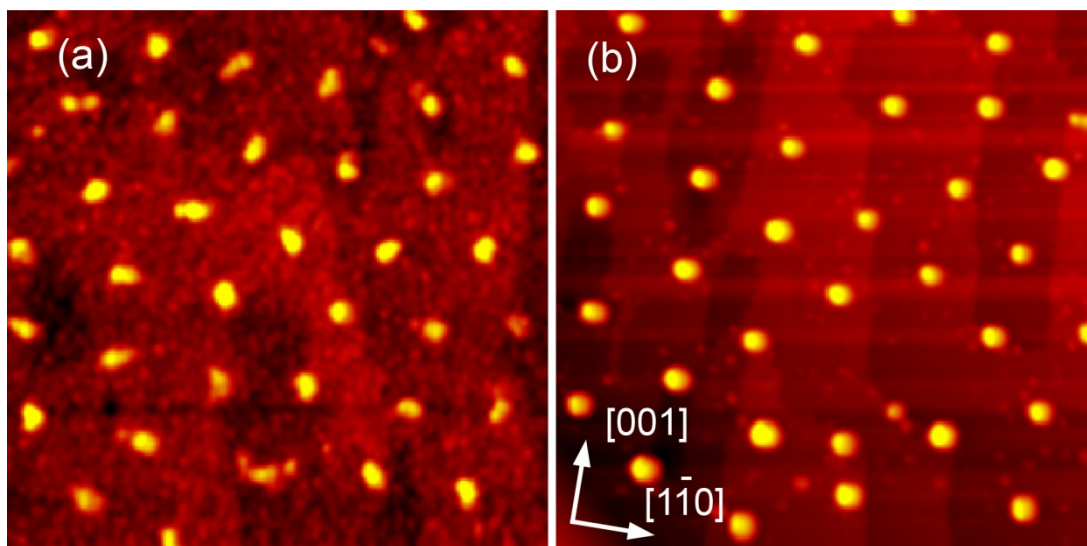


Fig. 29: *In situ* STM images (200 nm x200 nm) of Pt NPs deposited on TiO<sub>2</sub>(110) after an *in situ* O<sub>2</sub>-plasma treatment and subsequent annealing in UHV at (a) 300°C for 20 min and (b) 1000°C for 10 min.

The TiO<sub>2</sub>(110) substrate demonstrates a (1x2) surface reconstruction after high temperature annealing (>900°C). Further stepwise annealing from 1010°C to 1060°C, Fig. 30(a-f), demonstrated the enhanced thermal stability and low mobility of the micellar Pt NPs. Only upon annealing at 1060°C for additional 10 min, were small changes in the NP size and in the local NP arrangement noticed, Fig. 30(g,h).

Fig. 31 shows histograms of the NP height (a) and interparticle distance (b) obtained from the analysis of numerous STM images acquired after different *in situ* thermal treatments from 1000°C to 1060°C.

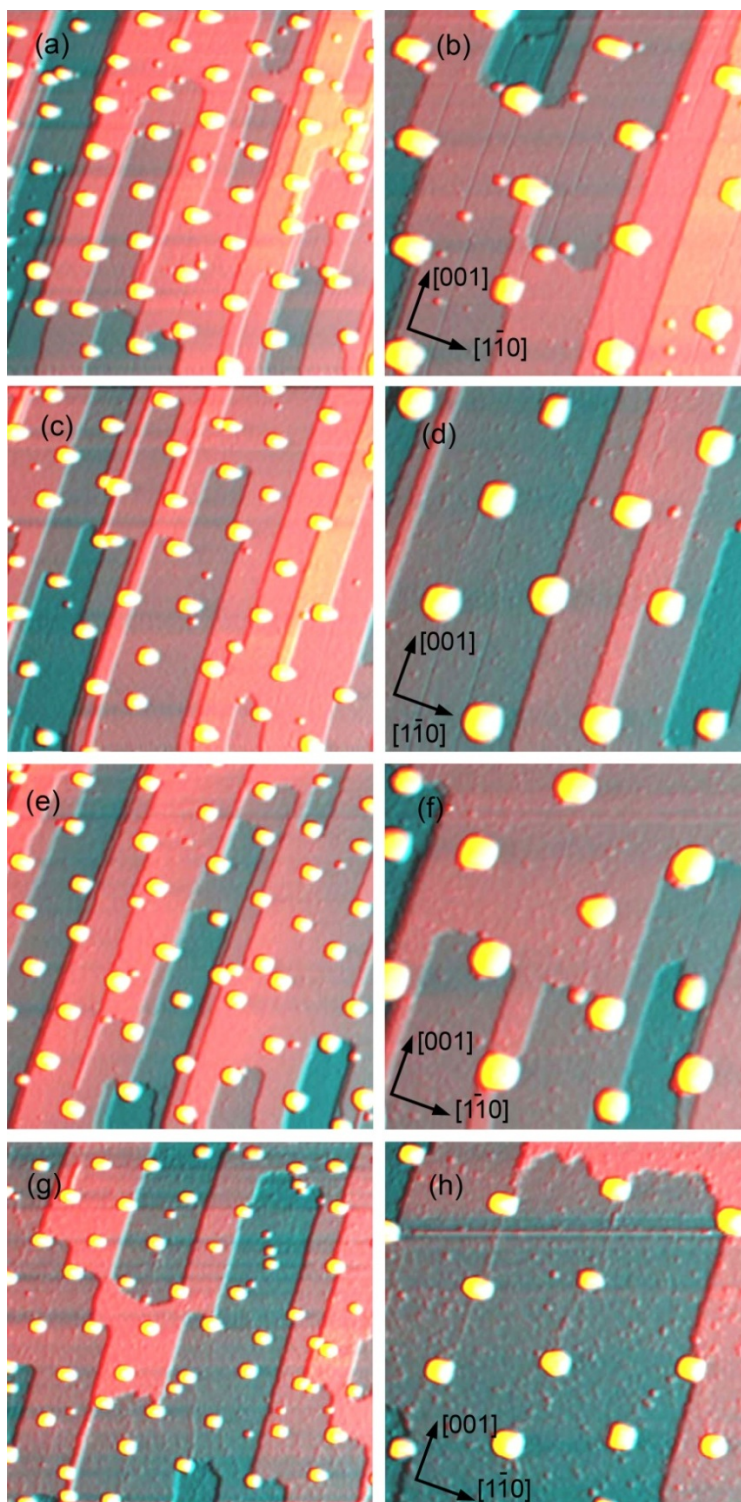


Fig. 30: *In situ* STM images of Pt NPs deposited on  $\text{TiO}_2(110)$  acquired after  $\text{O}_2$ -plasma and subsequent annealing in UHV at (a,b)  $1010^\circ\text{C}$ , (c,d)  $1040^\circ\text{C}$ , (e,f)  $1060^\circ\text{C}$ , and (g,h) 2<sup>nd</sup>  $1060^\circ\text{C}$ , for 10 min at each temperature. The size of the images in the left column is (200 x 200 nm) and in the right is (100 x 100 nm).

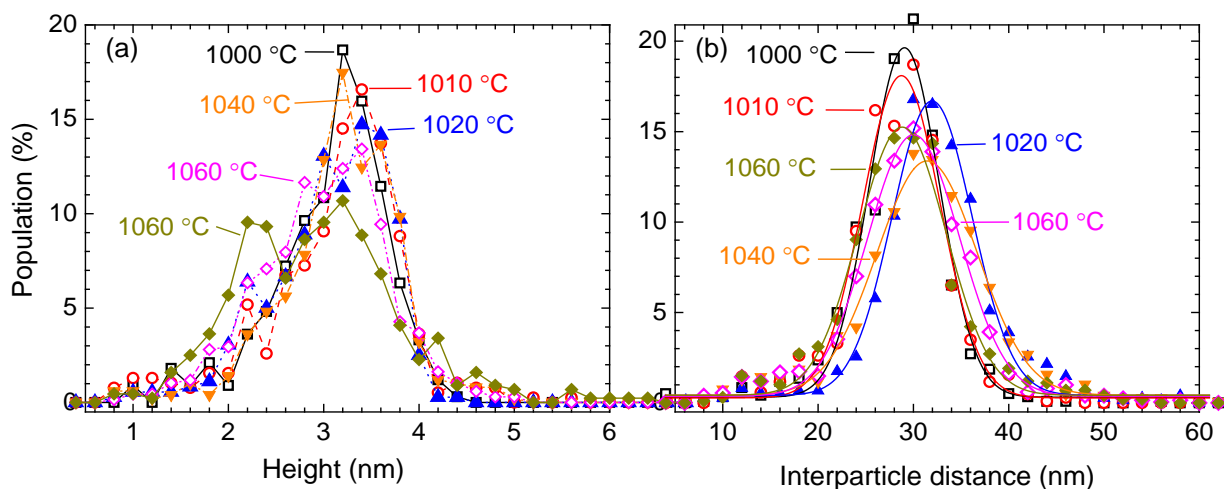


Fig. 31: Normalized histograms of (a) NP height and (b) interparticle distance obtained from STM images acquired after isochronal annealing in 10°C intervals (10 min) from 1010°C to 1060°C. The lines in (a) are guides for the eye, while the data in (b) were fitted using Gaussian curves. For each temperature, the above statistics include 300-670 NPs.

The data in Fig. 31(a) indicate that the average NP height is nearly constant up to the first annealing treatment at 1060°C for 10 min ( $3.4 \pm 0.2$  nm).

However, a clear increase in the width of the NP height distribution and bimodal shape is observed upon further annealing at the same temperature (1060°C, 20 min), with maxima at 3.2 nm and 2.3 nm. In addition, the width of the height distribution increased from 0.9 nm at 1000°C to 1.6 nm at 1060°C-2<sup>nd</sup>. Since NPs larger than the original average size were not found on this sample upon annealing (Fig. 31a), the bimodal size distribution observed here cannot be attributed to coarsening. Possible reasons for such NP size distribution are either Pt desorption after prolonged annealing at 1060°C, or intrinsic errors in the determination of the NP height for this sample by using as reference either the top or the bottom terraces of the TiO<sub>2</sub> substrate for NPs located at step edges.

Due to the initial hexagonal arrangement of our NPs, this type of sample constitutes an ideal model system to investigate NP mobility at high temperature. The nearest-neighbor interparticle distance histograms shown in Fig. 31(b) demonstrate that our initial NP arrangement is basically preserved after high temperature annealing, with an average interparticle distance (peak of the distribution) of  $30 \pm 2$  nm from 1000°C to 1060°C. If entire NPs were to desorb at high temperature, a shift of the histograms' peak maximum towards higher interparticle distances should have been observed. On the other hand, significant NP mobility would have led to a broadening of the interparticle distance distribution and a corresponding reduction in the peak height. Only small changes in the peak position of  $\pm 0.5$  nm were detected in the temperature range of 1000°C-1060°C. In addition, a small increase in the width (standard deviation) of the interparticle distance distribution (from  $\sim 7.3$  nm at 1000°C to 9.1 nm at 1060°C, 20-min anneal) and a decrease in its height (peak population) can be observed above 1040°C. This result might indicate a weakening of the NP-support adhesion and the consequent onset of NP mobility. Since after our second annealing at 1060°C some smaller NPs ( $\sim 2.3$  nm) are present on the sample, the possibility of NPs break-up and local cluster mobility is more likely. Despite the observation of some local disorder, the majority of our scans still showed clear signs of a hexagonal NP arrangement up to the first thermal treatment at 1060°C.

A striking observation is the formation of TiO<sub>2</sub> nanostripes running preferentially along the [001] direction in the Pt-decorated samples upon annealing above 1000°C, Fig. 30. This phenomenon will be explained in more details in chapter 6.

#### 4.4.4 Micellar Pt NPs/ $\gamma$ -Al<sub>2</sub>O<sub>3</sub> (EXAFS)

Table 3 shows the size of the Pt NPs, obtained using HAADF-STEM measurement for samples S4-S6 after different thermal treatments: (a) as-prepared (all three identical samples annealed in O<sub>2</sub> at 375°C for 24 h), (b) S4 after annealing in O<sub>2</sub>+He at 450°C (3 h), (c) S5 after annealing in H<sub>2</sub>O+He at 450°C (3 h), and (d) S6 after annealing in H<sub>2</sub>+He at 450°C (3 h). All three samples were reduced in H<sub>2</sub> at 375°C (30 min) after the former treatments before the subsequent RT EXAFS and STEM analyses.

The ligand-free as-prepared samples were characterized by an average NP size distribution of:  $0.5 \pm 0.1$  nm. Water dosing and subsequent annealing at 450°C in H<sub>2</sub>O+He did not lead to drastic changes in the overall sample morphology, although some sintering was observed:  $0.8 \pm 0.3$  nm (S5). On the other hand, a drastic increase in the average NP size was observed when the same sample (a different portion of the same identical starting sample) was annealed in hydrogen,  $1.2 \pm 0.3$  nm (S6), suggesting enhanced atomic/NP mobility in the reducing environment. Surprisingly, when the same sample type was annealed in O<sub>2</sub>, lack of sintering was observed:  $0.6 \pm 0.2$  nm (S4).

Fig. 32 displays *r*-space Fourier-transform EXAFS data of samples S4-S6 measured at RT in H<sub>2</sub> after reduction at 375°C in H<sub>2</sub> (30 min) before (labeled as-prepared) and after *in situ* thermal treatments at 450°C in O<sub>2</sub>, H<sub>2</sub>O vapor, and H<sub>2</sub>, in each case for 3 hours.

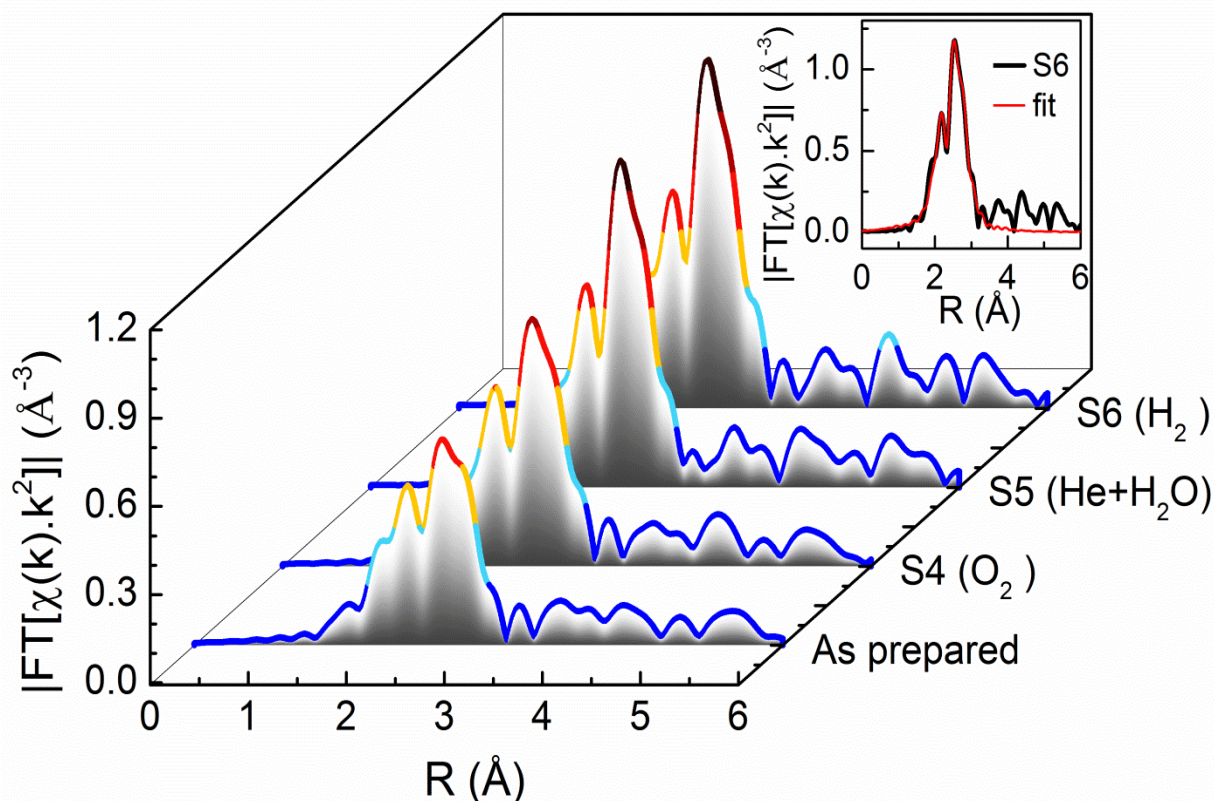


Fig. 32: Fourier transform magnitudes of  $k^2$ -weighted Pt- $L_3$  edge EXAFS spectra acquired for samples S4-S6 at RT in  $H_2$  after an initial common pre-treatment in  $O_2$  at  $375^\circ C$  followed by reduction at  $375^\circ C$  in  $H_2$  and subsequent annealing in  $O_2$  (S4),  $H_2O$  (S5) and  $H_2$  (S6) at  $450^\circ C$  for 3 hours. All samples were reduced *in situ* at  $375^\circ C$  in  $H_2$  before the acquisition of the EXAFS data. A representative first-shell fit of the EXAFS data of S6 is included as inset.

Representative EXAFS data in  $k$ -space of S4-S6 measured at RT in  $H_2$  after annealing ( $450^\circ C$ ) under different environments, together with similar data from the as-prepared sample (after reduction in  $H_2$  at  $375^\circ C$ ) are shown in Fig. 33.

After the former treatments, all samples were reduced in  $H_2$  at  $375^\circ C$  before the acquisition of the final RT-EXAFS data in  $H_2$  shown in Fig. 32 and Fig. 33. A representative 1<sup>st</sup>-shell fit is shown as inset in Fig. 32, and the results from those fits,

including 1<sup>st</sup> nearest neighbor CNs, Pt-Pt distances and atomic disorder ( $\sigma^2$ ) are included in Table 3.

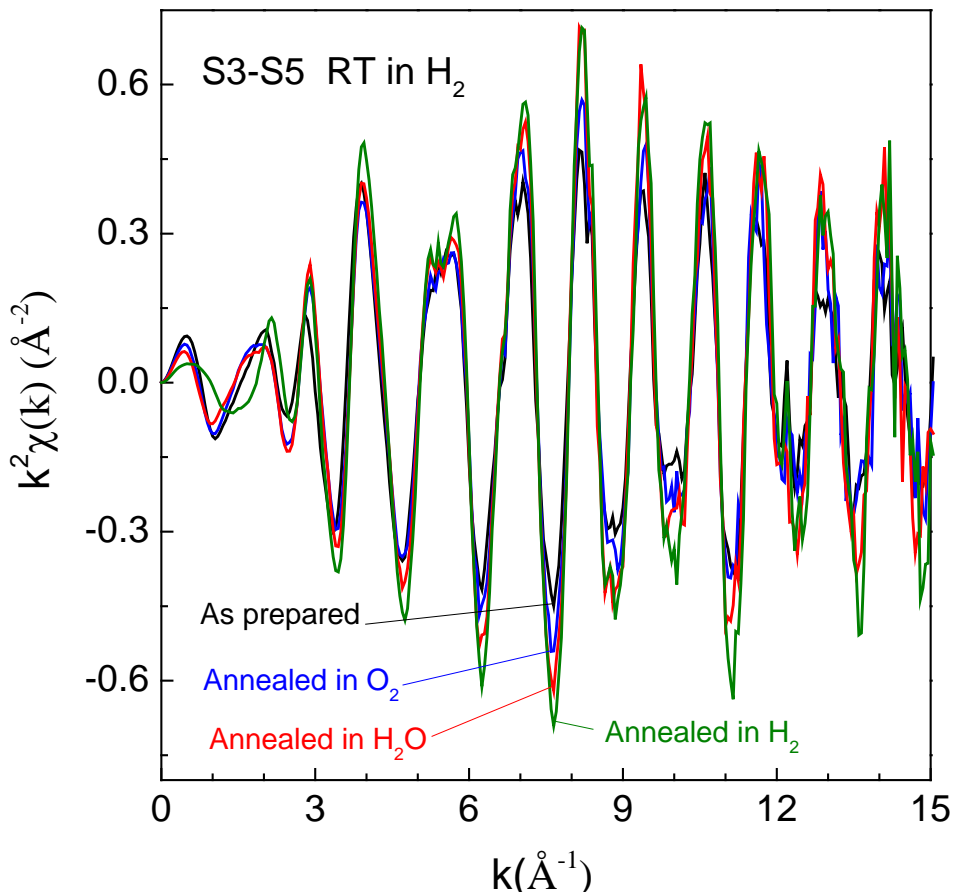


Fig. 33:  $k^2$ -weighted EXAFS in  $k$ -space of similarly prepared samples acquired at RT in  $H_2$  after annealing at  $450^\circ C$  for 3 hours in different environments:  $O_2$  (S4),  $H_2O$  (S5), and  $H_2$  (S6).

After reduction in  $H_2$  at  $375^\circ C$ , the as-prepared samples were characterized by  $NN1 = 6.5 \pm 0.4$ . Annealing in oxygen for several hours at  $450^\circ C$  did not induce any clear changes in the average NN1, with  $NN1 = 6.9 \pm 0.4$  (S4), indicating the stability of the NPs in the oxidizing environment. When the same sample (a different portion of the same sample) was pre-dosed with water vapor and annealed in a water-containing environment (in He), a small change in the overall NP size was observed via EXAFS,



with NN1=  $7.3 \pm 0.3$  (S5). In contrast, an identical thermal treatment in H<sub>2</sub> was found to lead to clear NP sintering, with NN1=  $8.3 \pm 0.4$  (S6).

Nanoparticle sizes can also be estimated based on the EXAFS NN1 coordination numbers (Table 3), following the method presented in Ref. 82 that provides a relation between the NP's weighted average size and the EXAFS 1<sup>st</sup> NN coordination number. Such data are included and compared to volume-weighted STEM diameters in Table 3. An overall good agreement between the EXAFS and STEM NP sizes is observed.

Table 3: First nearest neighbor coordination numbers (NN1), Pt-Pt distances (R), atomic disorders ( $\sigma^2$ ), and NP sizes extracted from EXAFS and STEM data (diameter) after sample exposure to different *in situ* thermal treatments in O<sub>2</sub> (S4), H<sub>2</sub>O (S5), and H<sub>2</sub> (S6).

<b>SAMPLE Pt NPs/<math>\gamma</math>-Al<sub>2</sub>O<sub>3</sub></b>	<b>NN1</b>	<b>R (Å)</b>	<b><math>\sigma^2</math> (Å<sup>2</sup>)</b>	<b>TEM NP Diameter (nm)</b>	<b>TEM volume- weighted NP Diameter (nm)</b>	<b>NP Size from EXAFS (nm)</b>
S4-S6 in H <sub>2</sub> at RT after reduction in H <sub>2</sub> at 375°C	6.5(4)	2.749(4)	0.0078(4)	0.5(2)	0.6(2)	0.9(1)
S4 in H <sub>2</sub> at RT, after annealing at 450°C in O <sub>2</sub> +He	6.9(4)	2.750(3)	0.0073(3)	0.6(2)	0.8(3)	1.0(1)
S5 in H <sub>2</sub> at RT, after annealing at 450°C in H <sub>2</sub> O+He	7.3(3)	2.752(2)	0.0066(2)	0.8(3)	1.2(4)	1.1(1)
S6 in H <sub>2</sub> at RT, after annealing at 450°C in H <sub>2</sub> +He	8.3(4)	2.743(2)	0.0068(2)	1.2(3)	1.4(3)	1.4(2)
Pt foil	12	2.763(1)	0.0050(1)			

This study revealed a clearly distinct coarsening behavior of three identical samples after annealing in different environments (S4 in O<sub>2</sub>, S5 in H<sub>2</sub>O, S6 in H<sub>2</sub>).

Fig. 34 shows XANES data of S5 acquired during the thermal treatment at 450°C in H<sub>2</sub>O vapor. The progressive increase in the intensity of the Pt-L<sub>3</sub> absorption peak (white line) with increasing annealing time demonstrates the gradual oxidation of the NPs, which might explain their partial stabilization, as was the case of the NPs in S4 after a similar treatment in oxygen. While platinum oxide species are unstable at high temperature (~450°C) under ultrahigh vacuum (UHV) or reducing atmospheres, they could be formed and stabilized at such temperatures in oxygen environments.

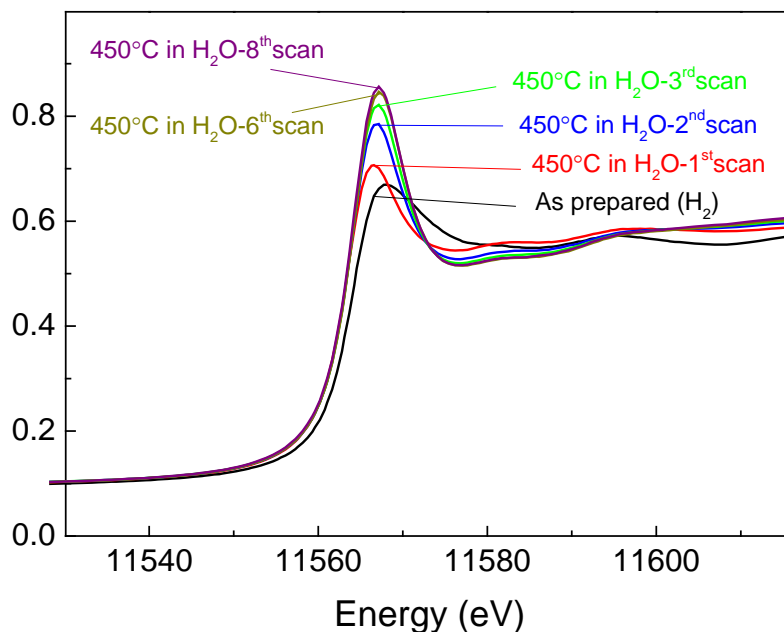


Fig. 34: Pt-L<sub>3</sub> XANES absorption peak of sample S5 acquired *in situ* during a thermal treatment at 450°C in H<sub>2</sub>O vapor+He. The progressive increase in the intensity of the absorption peak (or white line) with increasing annealing time (together with changes in the EXAFS region) reveal the gradual oxidation of the NPs under this environment. For reference, the data of the as-prepared sample after reduction in H<sub>2</sub> at 375°C are shown.

Fig. 35 shows the XANES and EXAFS data obtained at 450°C for samples S4, S5, and S6 under O<sub>2</sub>, H<sub>2</sub>O, and H<sub>2</sub> environments, respectively. From both, the increase in the white line intensity, Fig. 35(a), and appearance of a Pt-O contribution in the EXAFS spectra at ~2 Å, Fig. 35(b), the formation of stable PtO<sub>x</sub> species on our samples is concluded. Although the increase in the XANES white line intensity in Fig. 35(a) upon annealing in O<sub>2</sub> or H<sub>2</sub>O might also be indicative of the presence of chemisorbed oxygen, and not PtO<sub>x</sub>, the presence of PtO<sub>x</sub> in samples S4 and S5 is evident in the EXAFS spectra from the decrease in the Pt-Pt contribution (coordination numbers) concomitant with an increase in the Pt-O component.

Fig. 36 shows the EXAFS spectra, fitted with Pt-Pt and Pt-O components. The fit results are shown in Table 4.

Table 4: First-nearest neighbor coordination number (NN1), interatomic distance (R) and disorder ( $\sigma^2$ ) parameters of the Pt-Pt and Pt-O contributions extracted from *in situ* EXAFS measurements acquired during thermal treatments in O<sub>2</sub> (S4), H<sub>2</sub>O (S5), and H<sub>2</sub> (S6) at 450°C.

SAMPLE Pt NPs/ $\gamma$ -Al <sub>2</sub> O <sub>3</sub>	Pt-Pt			Pt-O		
	NN1	R (Å)	$\sigma^2$ (Å <sup>2</sup> )	NN1	R (Å)	$\sigma^2$ (Å <sup>2</sup> )
S4 at 450°C in O <sub>2</sub>	2.2(2.2)	2.69(3)	0.012(1)	2.1(0.5)	2.03(2)	0.001(3)
S5 at 450°C in H <sub>2</sub> O	5.0(2.1)	2.68(3)	0.016(5)	1.2 (0.3)	2.03(2)	0.001(3)
S6 at 450°C in H <sub>2</sub>	8.1(0.8)	2.716(7)	0.013(1)	-	-	-

From this analysis, the largest oxide content was obtained for S4 (O<sub>2</sub>) followed by S5 (H<sub>2</sub>O), while no significant Pt-O contribution was observed for S6 (H<sub>2</sub>).

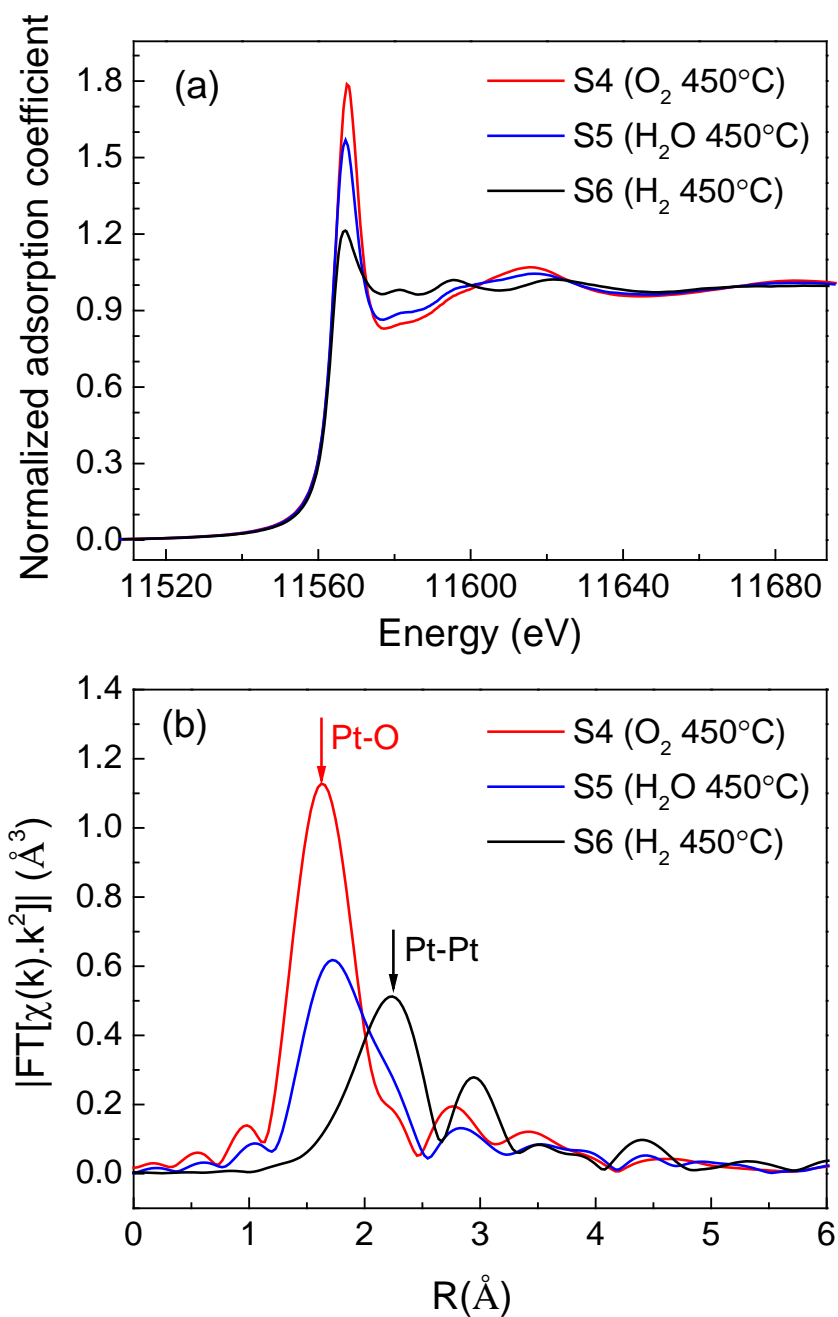


Fig. 35: (a) Normalized absorption coefficient corresponding to the Pt-L<sub>3</sub> edge and (b) k<sup>2</sup>-weighted Fourier transform magnitudes of Pt L<sub>3</sub>-edge EXAFS spectra of samples S4-S6 acquired at 450°C in O<sub>2</sub>, H<sub>2</sub>O and H<sub>2</sub>.

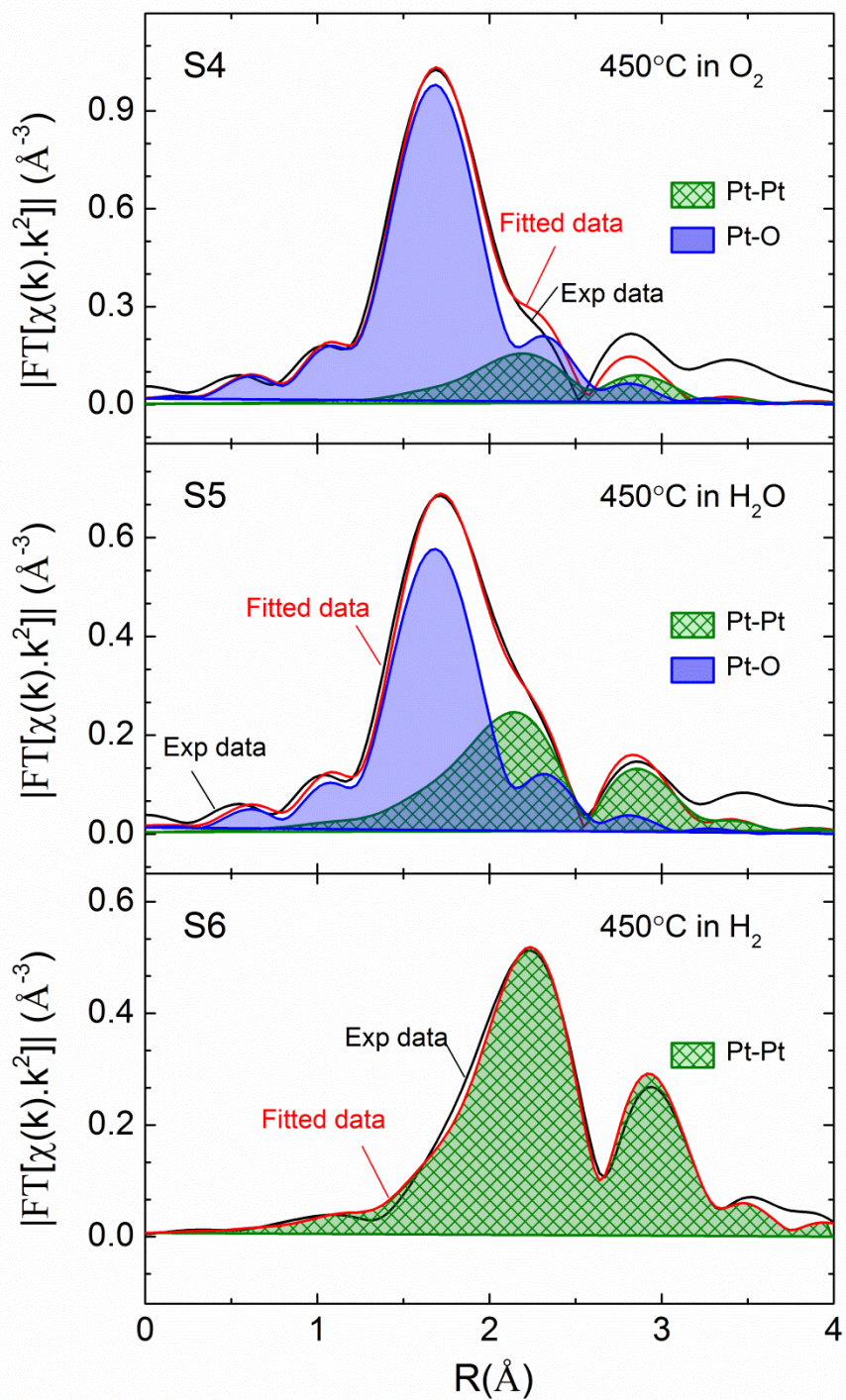


Fig. 36:  $k^2$ -weighted Fourier transform magnitudes of Pt L<sub>3</sub>-edge EXAFS spectra acquired for samples S4, S5 and S6 at 450°C under different environments. The data were fitted with two components: a Pt-Pt scattering path (hatched area) and a Pt-O path (filled area). The fit results are shown in Table 4.

## 4.5 Discussion

### 4.5.1 STM observations

The data shown above reveal clear changes in the stability of Pt NPs as a function of the preparation method, with micellar Pt NPs being significantly more stable than UHV-evaporated NPs on TiO<sub>2</sub>(110). In addition, in agreement with previous literature<sup>55-57, 78, 91-93, 95</sup>, the coarsening of evaporated Pt NPs appears to be affected by the pre-treatment underwent by the support, which leads to drastic changes in its morphology and stoichiometry (surface reduction). For Pt NPs evaporated in UHV, we have observed enhanced coarsening when the NPs were deposited on the polymer pre-coated TiO<sub>2</sub> surface (S2), as compared to pristine (sputtered/annealed) TiO<sub>2</sub> (S1), indicating weaker NP/support binding in S2. This effect could be partially attributed to the distinct pretreatment that the TiO<sub>2</sub> support in S2 underwent prior to the evaporation of Pt NPs, since due to the initial polymer-coating of the TiO<sub>2</sub> surface in S2, the Pt NPs were not able to nucleate on stable binding sites such as O-vacancies. In addition, the O<sub>2</sub>-plasma pre-treatment conducted on S2 after Pt evaporation might have affected the initial stability of the NPs. As will be discussed below, the O<sub>2</sub>-treatment does not only modify the surface of the TiO<sub>2</sub> support, but also that of the Pt NPs, including their oxidation state. NP coarsening has been explained in the past due to the formation of volatile PtO<sub>x</sub> species and their re-deposition on the support surface.<sup>59</sup> Although the larger (~3 nm) micellar Pt NPs (S3) were exposed to the same O<sub>2</sub>-plasma treatment as S2 but did not display any mobility, smaller Pt clusters (S2) are known to experience a more facile oxidation and stronger oxygen binding<sup>5, 76</sup>, and are therefore expected to be more affected by the oxygen pre-treatment. Nevertheless, the above arguments can

only be used to explain the higher coarsening rate of the Pt NPs on the polymer-coated sample below 930°C, but not within the temperature regime employed here to monitor coarsening (930°C-1060°C). At such elevated temperatures, the Pt NPs and the TiO<sub>2</sub> surface are reduced for all three samples.

We consider that the different coarsening trends observed when comparing S1 and S2 after annealing above 930°C are due to either strong metal support interactions and/or to morphological (rather than chemical) changes induced on TiO<sub>2</sub> by the pre-treatment. It is known that Pt NPs are more prone to become encapsulated by TiO<sub>2</sub> on a reduced TiO<sub>2</sub> substrate<sup>93</sup>, and it is possible that the higher extent of TiO<sub>x</sub> encapsulation on the pristine sample (strongly reduced, S1) as compared to the polymer-coated sample (more oxidized up to 800°C, S2) is partially responsible for the higher stability against coarsening of S1.<sup>93</sup> The morphological differences between the TiO<sub>2</sub> surfaces in S1 and S2 mentioned above are related to the fact that step edges, known to stabilize NPs<sup>18, 96, 97</sup>, are available on S1 (pristine TiO<sub>2</sub>) before Pt deposition, while they only form on the polymer-coated and O<sub>2</sub>-plasma treated S2 after high temperature annealing.

Jak<sup>55-57</sup> reported a higher growth rate and decoration of steps for Pd NPs evaporated on mildly reduced TiO<sub>2</sub>(110), while Pd evaporation on strongly reduced TiO<sub>2</sub> surfaces gave rise to smaller NPs distributed over the terraces. On the latter surface, the NP mobility was so low that a significant fraction of the NPs were not able to reach the energetically favorable step sites. Analogous findings were reported for Pt<sup>78</sup>, Au<sup>94</sup>, Cu and Ni on TiO<sub>2</sub>(110)<sup>96</sup>. We observed a similar behavior in our samples, since some clusters were still seen on the terraces for the Pt/pristine-TiO<sub>2</sub> sample at 1060°C (S1).

Datye et al.<sup>59</sup> explained the enhanced sintering behavior of Pt NPs in air as compared to that under reducing conditions based on the formation of volatile PtOx species leading to more favorable interparticle mass transport. Nevertheless, other studies have shown enhanced stability of Pt NPs supported on Y-Al<sub>2</sub>O<sub>3</sub> under oxygen environment for temperatures below 650 °C when the PtO<sub>x</sub>/oxide support interfaces are formed.<sup>82</sup> Additionally, the work by Goeke and Dayte's<sup>69</sup> on the mobility of large Pd clusters deposited on SiO<sub>2</sub> and Al<sub>2</sub>O<sub>3</sub> revealed an enhanced rate of sintering for Pd/Al<sub>2</sub>O<sub>3</sub>, even though that system is characterized by stronger metal/support interactions than Pd/SiO<sub>2</sub>. A NP/support combination, where strong metal/support interactions are expected (Pt/pristine-TiO<sub>2</sub>), does not necessarily lead to more stable NPs. To the contrary, in such cases, the support may assist the mobility of NPs and atoms, leading to more pronounced coarsening patterns at least through the Ostwald-ripening pathway.

Fig. 37 shows the percentage of NPs found on terraces and at step edges for all Pt NP samples (S1-S3). Both evaporated samples show an increase in the percentage of NPs at step edges with increasing annealing temperature, while the micellar sample showed the opposite trend. As was discussed before, the micellar NPs are not mobile, but their presence on the TiO<sub>2</sub> surface leads to changes in its morphology, as for example the presence of narrower terraces or formation of TiO<sub>2</sub> nanostripes.<sup>28, 82</sup>

With increasing annealing temperature, wider terraces and a lower density of step edges are observed in all samples, but the mobile evaporated Pt NPs can still reach those sites, while the immobile micellar NPs won't follow the changes in the support morphology.



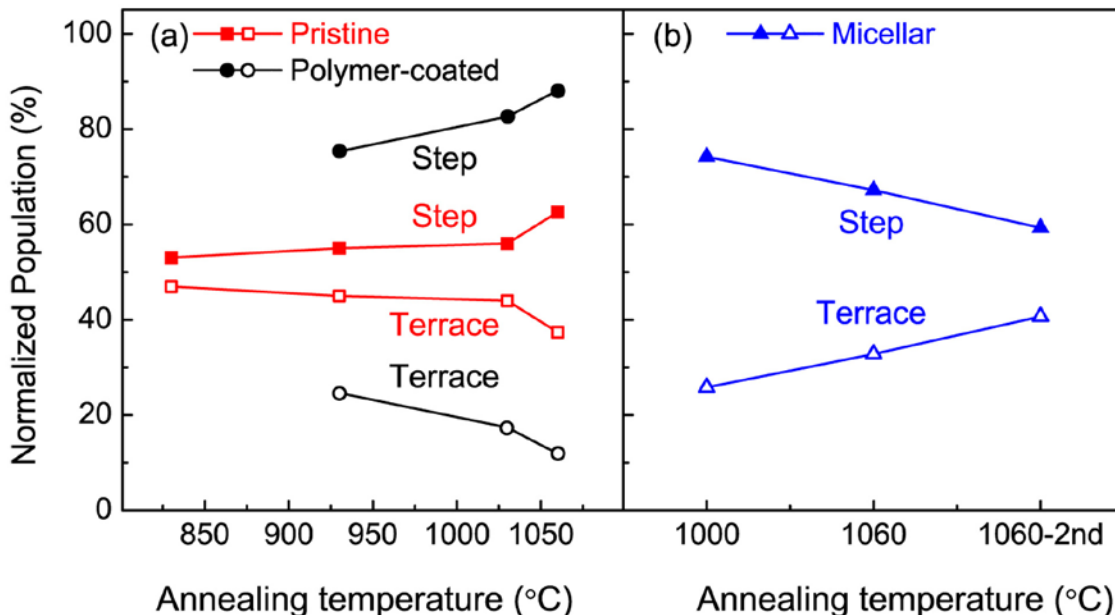


Fig. 37: Thermal evolution of the number of Pt NPs present on terraces and at step edges for (a) PVD-grown and (b) micellar NP samples..

Despite the lower number of step edges available, the increase in the number of evaporated NPs (S1 and S2) decorating steps after annealing at high temperature is a signature of coarsening. Both coarsening mechanisms could result in NP step-edge decoration. In an Ostwald-ripening model, the step edges would stabilize the NPs and therefore reduce the rate of departing atoms, and eventually favor the growth of NPs at those sites in detriment of those at terraces. On the other hand, in a diffusion-coalescence model, the step edge stabilization would diminish the diffusion of the NPs decorating the steps, and therefore, more mobile NPs (e.g. those at terraces) would eventually coalesce with the stationary (pinned) NPs at the step edges. Therefore, at the elevated temperatures investigated here, coarsening by either Ostwald-ripening,

diffusion-coalescence, or a combination of both processes, could be held responsible for the step edge decoration of PVD NPs.

Although the shape of the size histograms has been used in the past to differentiate the two fundamental coarsening models (Ostwald-ripening versus diffusion-coalescence), this approach has been questioned by many authors.<sup>59, 60, 69, 98</sup> Howard et al.<sup>98</sup> have studied the mobility of Pd NPs on TiO<sub>2</sub>(110) using high temperature STM. Although the size histogram obtained after 240 min annealing in UHV at 750 K was skewed toward larger sizes (as expected from the diffusion-coalescence mechanism), they did not observe a clear evidence for diffusion-coalescence via STM. Instead, their real-time STM measurements at 750 K demonstrated that the Ostwald-ripening pathway was the main coarsening mechanism. Similar experiments on Au/TiO<sub>2</sub>(110) by Mitchell et al.<sup>60</sup> revealed that both coarsening mechanisms are responsible for the sintering observed, even though their size histograms displayed a bimodal distribution not resembling any of the skewed normal distribution expected for either model.

In addition, although we see fewer and larger NPs in the polymer-coated sample as compared to the pristine sample after annealing, it cannot be necessarily concluded that there is less coarsening for the pristine sample within the range of temperatures shown in Fig. 25 and Fig. 27. One must also consider that even though the same amount of Pt was evaporated on both samples, it is likely that the initial NP size distribution before annealing was different. In particular, the presence of the polymer on the TiO<sub>2</sub> surface of S2 could have led to an initial larger average size distribution which could have propagated after annealing, leading to the size differences between S1 and S2 observed at 930°C (see Table 1). In addition to the possible distinct nucleation of Pt

atoms and Pt NP growth on reduced TiO<sub>2</sub> (pristine sample, S1) as compared to polymer-coated TiO<sub>2</sub> (S2), coarsening might also have occurred during the subsequent O<sub>2</sub>-plasma treatment underwent by S2 due to the formation of volatile PtO<sub>x</sub> species. Due to the enhanced roughness of the TiO<sub>2</sub> support after the latter treatment, the NPs could not be resolved, and the coarsening behavior of all samples is only compared after annealing at high temperature.

It should be noted that the initial sample pre-treatment is expected to affect the nucleation and growth dynamics of the PVD NPs and therefore, their initial size distribution. Nevertheless, the comparison and conclusions drawn here regarding their coarsening behavior are not related to their initial size and substrate distribution just after RT deposition or after a RT O<sub>2</sub>-plasma treatment, but after annealing cycles at elevated temperature (>930°C). Under those circumstances, the TiO<sub>2</sub> substrate was strongly reduced in all cases. Therefore, regardless of the initial NP size distribution, we have followed its evolution for all samples after annealing at high temperature using as starting point for the comparison STM data acquired at/above 930°C. Although theoretically ideal, it is not possible experimentally to obtain identical initial NP size distributions and NP densities on the TiO<sub>2</sub> surface after the different surface functionalizations described here. To overcome this issue, the simulation approach described here could be useful, since the effect of the distinct initial NP size and NP density have already been implicitly taken into account within the simulation models. Therefore the coarsening behavior of samples with different initial size distributions and NP densities could be compared via the fitting parameters  $E_{tot}$  and  $K_S$ . For instance, large  $E_{tot}$  and small  $K_S$  values are indicative of a higher resistance towards coarsening.

To the best of our knowledge, real-time (live) STM or TEM measurements of NP coarsening at the elevated temperatures employed here (>900°C) have not been reported due to instrumentation limitations. The above discussion demonstrates the need of having a more reliable method to understand the main coarsening mechanism underlying our experimental observations and to obtain coarsening rates. The dominant coarsening mechanism is determined here based on simulations of the size histograms following two different sintering models.

Lastly, the enhanced thermal stability of micellar Pt NPs could be attributed to possible small amounts of carbon (not detectable by XPS), present underneath the NPs or at the NP/support perimeter in the form of TiC compounds. Furthermore, in contrast to UHV evaporated NP samples, our size-selected 3D-like spherical NPs samples have relatively large interparticle distances, and Pt atoms or small Pt seeds are not present between larger NPs, making Ostwald ripening processes less favorable. Also the good size distribution of Pt NPs and their large interparticle distances could also hinder certain coarsening pathways. As discussed before, the size-dependent heat of sublimation is the driving force for the Ostwald ripening pathway. A narrower NP size distribution would result in a smaller difference between the rate of atomic detachment as compared to that of incoming atoms for any given NP. In addition, the large interparticle distances make it more difficult for either NPs (diffusion-calescence pathway) or isolated atoms (Ostwald ripening pathway) to diffuse on the surface and find another NP. In such case, the rate limiting step in the Ostwald ripening model would be the diffusion of atoms across the surface, rather than the detachment of atoms from the NPs. This requires a modified simulation model.<sup>65, 67</sup>

## 4.5.2 Simulation of coarsening mechanisms

### 4.5.2.1 Ostwald ripening

Fig. 38 displays simulations of the evolution of the NP radius for Pt NPs evaporated on (a) pristine TiO<sub>2</sub> and (b) polymer-coated TiO<sub>2</sub> following the Ostwald-ripening model described in the theoretical methods section above. Each simulation uses an experimental size distribution as starting point and calculates the evolution of such distribution during a given annealing treatment. Since the NPs are assumed to be hemispherical, the values of R in eq. (1) are identical to the NP height (shown in the plots). Each experimental thermal treatment consists of three segments: (i) a ramp to the target annealing temperature (1030°C or 1060°C) with a rate of 1.5 °C/s, (ii) annealing at a constant target temperature for 10 min, and (iii) a second ramp to decrease the sample temperature to RT with the same rate as in (i). Each graph in Fig. 38 shows the initial experimental histogram (full curve with hatched-pattern filled area) and the subsequent experimental NP size distribution after the thermal treatment (full curve with solid filled area), together with the results from the simulation at 1030°C (a,b) and 1060°C (c,d) (red solid curves).

The only fitting parameter was the total energy barrier of the system  $E_{tot}$ , varied within the range of 100 to 600 kJ/mol. The best fit was selected as such having the same NP surface density (number of NPs/surface area) than the experimental data after the annealing cycle.

Although the peak positions of the simulated histograms are similar to the experimental data, a common feature in all simulations is their narrower size distribution as compared to the experimental results.

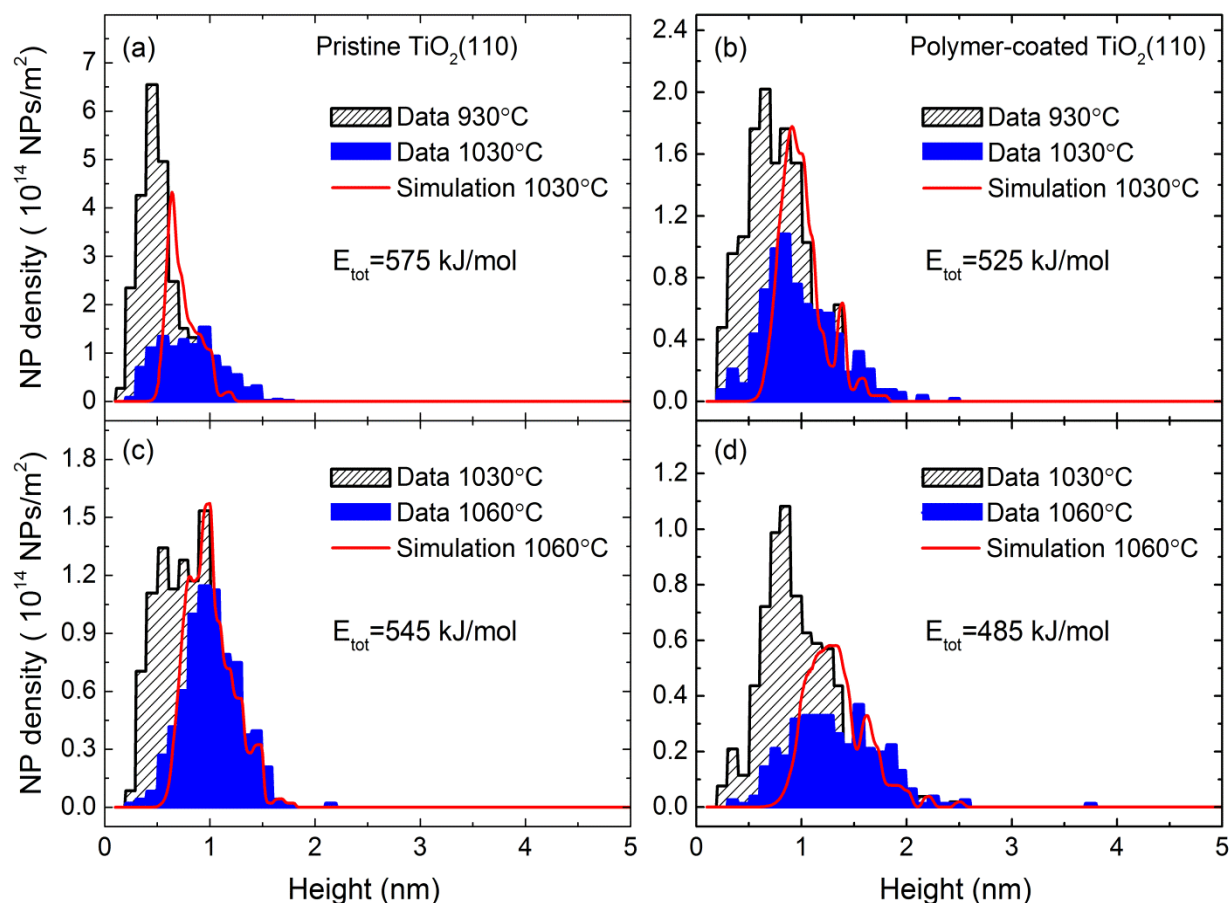


Fig. 38: Best fits obtained from Ostwald-ripening simulations of the pristine (a,c) and polymer-coated (b,d) Pt/TiO<sub>2</sub>(110) samples. The hatched and solid filled areas are the initial and the final experimental size distributions, respectively. The solid line displays the simulated final size distribution obtained after annealing treatments in UHV at 1030 °C (a,b) and 1060 °C (c,d).

The best  $E_{tot}$  values extracted from our simulations are shown in Table 2. The error bars were defined as the deviation in  $E_{tot}$  needed to obtain a 10 % change in the NP surface density with respect to the experimental value. The total energy barrier obtained for the Pt NPs evaporated on the polymer-coated sample was found to be ~50 kJ/mol lower than that of the pristine sample, demonstrating a higher coarsening rate. Another interesting result is the ~30-40 kJ/mol decrease in  $E_{tot}$  for these samples after

the second annealing cycle (1060° C). This result is in agreement with the increase in the aspect ratio described in the previous section with increasing annealing temperature, leading to a decreased NP/support interaction (dewetting) and to a weaker support effect for the larger NPs formed at the highest temperatures.

Table 5: Total energy barrier ( $E_{tot}$ ), support effect ( $K_S$ ), and diffusion coefficient ( $D_C$ ) obtained from the best fit of the Ostwald-ripening and diffusion-coalescence models to our experimental NP size distributions. The experimental data correspond to UHV evaporated Pt NPs deposited on pristine and polymer-coated TiO<sub>2</sub>(110). The estimated errors are given within parenthesis.

	Annealing temperature (°C)	Pristine TiO <sub>2</sub> (S1)	Polymer-coated TiO <sub>2</sub> (S2)
Ostwald-ripening $E_{tot}$ (kJ/mol)	1030	575 (10)	525 (15)
	1060	545 (20)	485 (10)
Diffusion-coalescence $K_S$ ( $10^{-3}$ ) $D_C$ ( $\times 10^{-26}$ m <sup>2</sup> /s)	1030	1.3×(1.3±1) 5.5	4×(1.5±1) 5.8
	1060	1.7×(1.7±1) 4.6	13×(1.3±1) 18.0

Considering the heat of sublimation of platinum (563 kJ/mol)<sup>99</sup> and the adsorption energy of Pt monomers on TiO<sub>2</sub>(110)<sup>100, 101</sup> (~3.5 eV on O-vacancy sites and ~2.1 eV on hollow sites with an average value of ~2.8 eV or 272 kJ/mol) and the diffusion barrier of Pt on TiO<sub>2</sub>(110)<sup>100, 101</sup> (~2.1eV for the [100] direction and ~0.9 eV for  $[1\bar{1}0]$ ), with an average value of ~1.5 eV or 147 kJ/mol) we could estimate  $E_{tot}$  from:

$$E_{tot} = \Delta H_{sub} + H_m^S - E_{ad}^S \quad (24)$$

, where  $\Delta H_{sub}$  is the bulk heat of sublimation and  $H_m^S$  and  $E_{ad}^S$  are the diffusion barrier and adsorption energy of metal atoms on the support, respectively. According to

eq. (24), a typical value for the total energy barrier of Pt on the TiO<sub>2</sub> surface is 438 kJ/mol, and in comparison, all of the  $E_{tot}$  values obtained from our simulations are larger. It should be however noted that the overall agreement between simulated and experimental data is not good for this model.

#### 4.5.2.2 Diffusion-coalescence

The same thermal treatment described in the previous section was used for the diffusion-coalescence simulations. The following constant parameters were used in the simulations:  $D=10^{-7}$  m<sup>2</sup>/s for Pt monomers on Pt(111)<sup>99, 102</sup> and  $\rho_0=1.5\times 10^{19}$  m<sup>-2</sup>. In this case, the calculations were done using the NP volume distribution since the volume is the independent variable in eq. (19) (see Fig. 39). The volumes were obtained from STM measurements of the NP height assuming a hemispherical NP shape.

In Fig. 40, the simulation results were rescaled from NP volume to NP height to be consistent with the STM measurements as well as to allow the direct comparison with the results of the Ostwald ripening simulations. The results of the best fits (solid curves), together with the initial (full curves with filled hatched area) and final (full curves with solid filled area) experimental histograms, are also shown in Fig. 40. The only fit parameter used in the simulation is  $K_S$ . The simulation results are in good agreement with the experimental data for both samples, especially after the second annealing treatment. The  $K_S$  values obtained for the pristine and polymer-coated samples are shown in Table 2. Since the parameter  $K_S$  entails support effects (NP pinning and step-edge stabilization), which normally lead to decreased diffusion rates, it is expected to be smaller than 1, as obtained in our simulations ( $\sim 10^{-3}$ , Table 2). Despite the initial larger



average NP size (at 930 °C), and similar to our findings based on the Ostwald-ripening model, a more pronounced coarsening was evidenced for the polymer-coated sample as compared to the pristine sample. In addition, a higher diffusion rate was also observed during the second annealing cycle (1060° C).

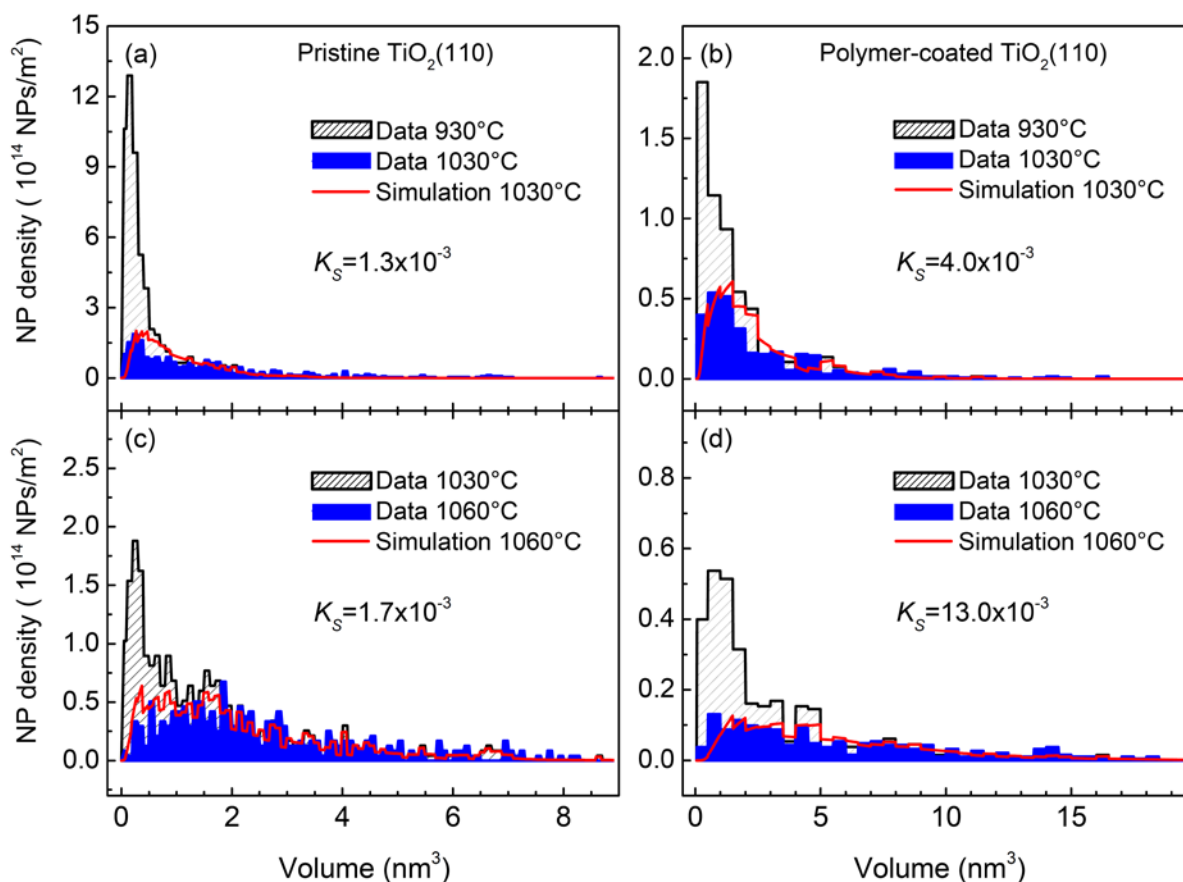


Fig. 39: Best fits obtained from a diffusion-coalescence simulation for pristine (a,c) and polymer-coated (b,d) Pt/TiO<sub>2</sub>(110) samples. The hatched and solid filled areas are the initial and the final experimental size distributions, respectively. The solid line displays the simulated final size distribution obtained after annealing treatments in UHV at 1030 °C (a,b) and 1060 °C (c,d). Since the independent parameter in the diffusion-coalescence model is the NP volume [eq. (19)], the calculations were done using NP volume histogram (graph above) and were subsequently rescaled to display the NP height in Fig. 40.

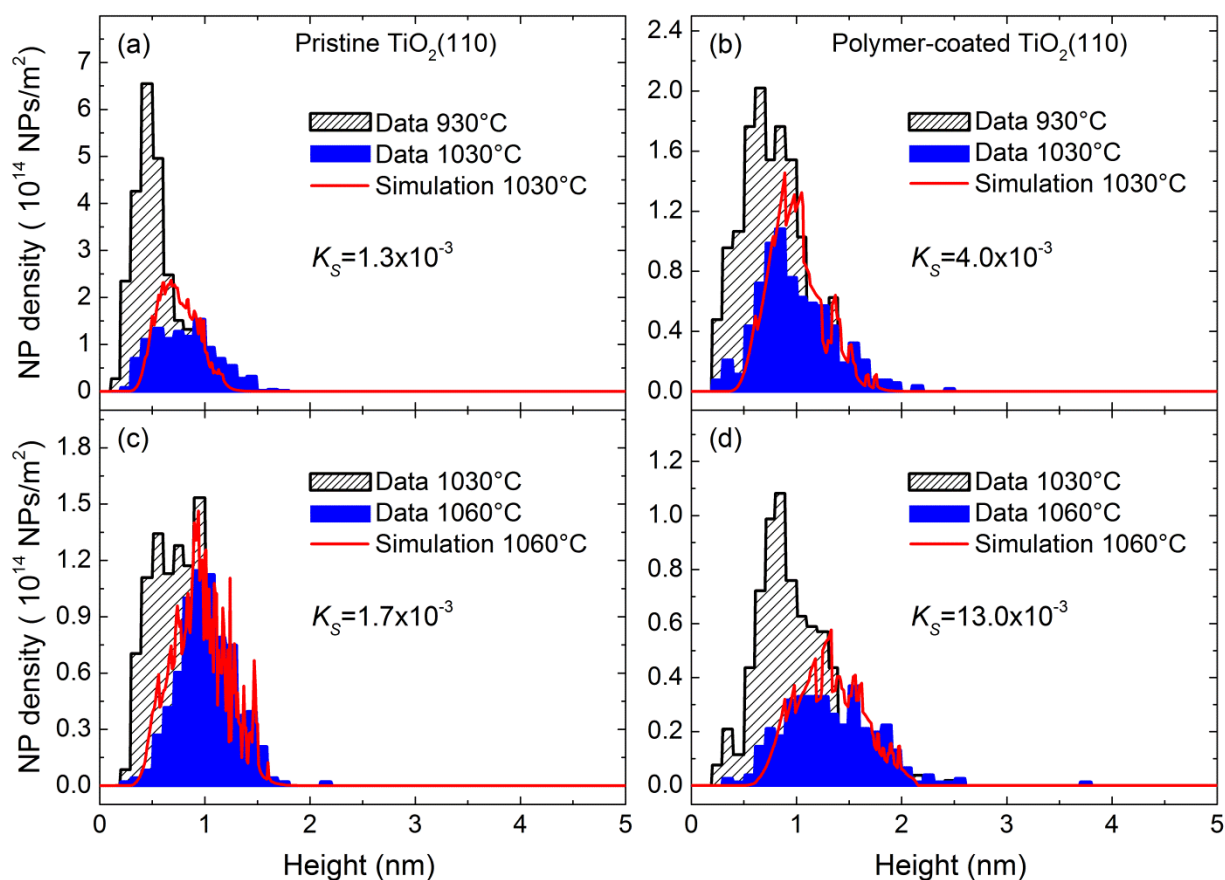


Fig. 40: Best fits obtained from a diffusion-coalescence simulation for pristine (a,c) and polymer-coated (b,d) Pt/TiO<sub>2</sub>(110) samples. The hatched and solid filled areas are the initial and the final experimental size distributions, respectively. The solid line displays the simulated final size distribution obtained after annealing treatments in UHV at 1030 °C (a,b) and 1060 °C (c,d).

In order to conclude which coarsening pathway better describes our experimental data, a fit quality parameter (Q) must be defined. Efron's pseudo-R<sup>2</sup> parameters ( $R^2_{\text{pseudo}} = Q$ ) were used to evaluate the goodness of the fit of the simulated histograms to the experimental data.<sup>103</sup> However, due to statistical fluctuations in both, simulated and experimental histograms, data smoothing (spline fit) was conducted before the comparison.

The Efron's pseudo- $R^2$  ( $R^2_{pseudo}$ ) parameter was used as a quantitative representation of the goodness of the fit of our coarsening simulations (fit quality parameter, Q) to the experimental STM data. This description is an extension of the regression model based on a “percent variance” interpretation, as described in Ref. 103 and the equation below:

$$Q = R^2_{pseudo} = 1 - \frac{\sum_i (y_i - f_i)^2}{\sum_i (y_i - \bar{y})^2} \quad (25)$$

The  $R^2_{pseudo}$  parameter differs from  $R^2$  in linear regressions in the fact that it is not constrained between 0 and 1, since in nonlinear models there is no lower limit for  $R^2$ . However, the closer the value of  $R^2_{pseudo}$  to 1, the better the fit quality.

Due to statistical fluctuations in the experimental data, data smoothing (spline fit) is needed prior to the comparison of the simulation results to the experimental data. An example of the procedure used for the calculation of the fit quality parameter (Q, Table 3) is illustrated in Fig. 41. First, the experimental and simulated histograms are fitted with spline curves (data smoothing), Fig. 41(a,b).

Subsequently, the spline curves representative of the experimental and simulated histograms are compared, Fig. 41(c), and  $R^2_{pseudo}$  (Q-factor) obtained following eq. (25). The resulting fit quality factors, Q, are given in Table 3 with larger Q values representing better agreement between the simulation and experimental data (perfect agreement for Q=1).

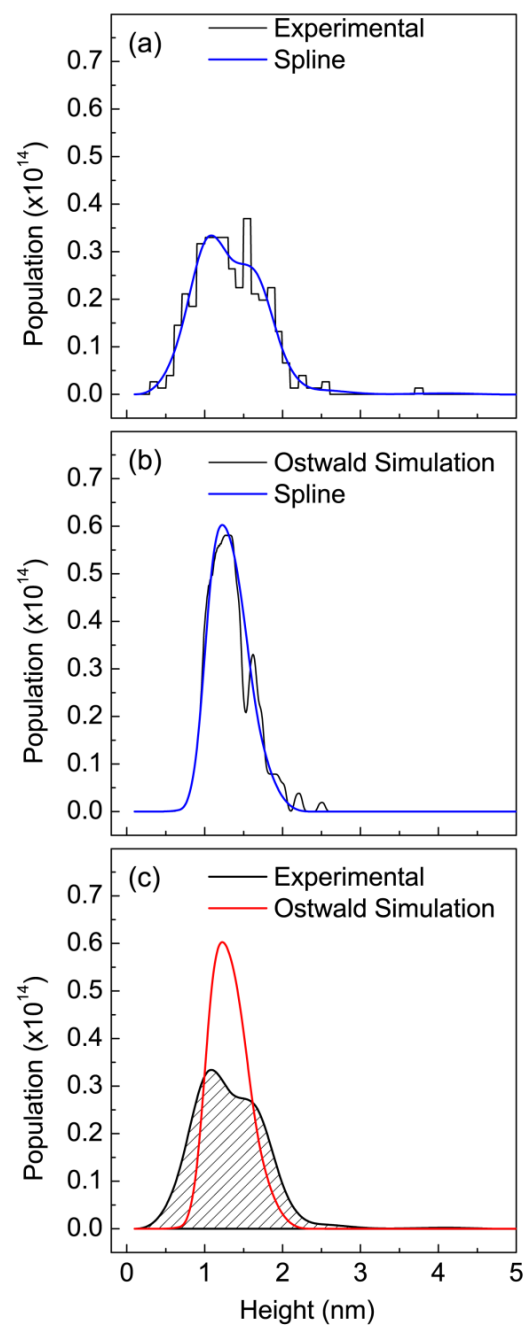


Fig. 41: Spline fits to the experimental STM data (a) and to the Ostwald ripening simulation results (b) for a polymer pre-coated sample (S2) annealed at 1060°C. The graph in (c) compares the smoothed (spline-fit) Ostwald-ripening simulation histogram to the smoothed experimental histogram. From the latter comparison, the fit quality parameter  $Q$  is obtained.

Table 6: Simulation quality factors (Q) for pristine (S1) and polymer pre-coated (S2) samples obtained for the Ostwald-ripening and diffusion-coalescence coarsening models.

Sample	Temperature (°C)	Q Diffusion- coalescence	Q Ostwald ripening
Pristine (S1)	1030	0.57	-0.33
	1060	0.92	0.90
Polymer pre-coated (S2)	1030	0.86	0.18
	1060	0.96	0.31

For the polymer pre-coated sample (S2), the quality of the simulation is considerably better for the diffusion-coalescence model as compared to the Ostwald ripening model during both thermal treatments. This is mainly due to the fact that size distributions narrower than those in the experimental data result from the Ostwald ripening simulations. Therefore, we conclude that the diffusion-coalescence pathway is the dominant coarsening mechanism underwent by the NPs in this sample. A similar conclusion can be drawn for the first thermal treatment (1030°C histogram) of the NPs supported on the pristine TiO<sub>2</sub>(110) surface (S1). Nevertheless, for the second thermal treatment (1060°C histogram), good agreement between the simulation and experimental data was observed for both models.

However, in this case the total energy barrier obtained from the Ostwald ripening model ( $E_{tot} = 545$  kJ/mol) is too large and unphysical as compared to the expected theoretical value ( $E_{tot} \approx 438$  kJ/mol). Therefore, the Ostwald ripening pathway can be ruled out. Additionally, the fitting parameters obtained for the diffusion coalescence model ( $K_S$ ) are reasonable for all samples and similar to those obtained by Jak et al.<sup>56</sup>

for the Pd/TiO<sub>2</sub> system. Accordingly, the diffusion-coalescence pathway is assigned as the dominant sintering mechanism during all thermal treatments carried out on PVD-grown NPs.

Considering the average NP height (Table 1),  $K_S$  (Table 2), and the adatom formation energy barrier (Fig. 24), the NP diffusion coefficient [ $D_C$  in eq. (21)] was obtained for S1 and S2 for both annealing treatments and reported in Table 2. The smallest  $D_C$  value was found for the pristine sample (S1) during the second thermal treatment (1030 °C to 1060°C), indicating reduced NP mobility. Interestingly, the values of the coarsening parameters obtained from the simulations after annealing at 1030°C [support effect ( $K_S$ )] indicate the higher stability of our Pt NPs as compared to model hemispherical NPs. Nevertheless, a decrease in their stability, approaching the theoretical values, was observed with increasing annealing temperature. The latter effect correlates with the increase in the NP aspect ratio (height to radius) and can be understood in terms of substrate de-wetting leading to NP de-stabilization. Carrey et al.<sup>104</sup> showed that small NPs which were trapped by surface defects were released after they had grown to larger sizes.

In order to directly observe and determine the coarsening mechanism, *in situ* real-time microscopic data at temperatures exceeding 900°C will be needed. However, such studies cannot be implemented experimentally to date due to instrumentation limitations (large drift), justifying thus the present approach.

### 4.5.3 *In situ* investigation of coarsening phenomena: environmental effects

As was shown in the results section, the evolution of the morphology of Pt NPs supported on nanocrystalline  $\gamma$ -Al<sub>2</sub>O<sub>3</sub> was investigated via *ex situ* TEM and *in situ* EXAFS. It should be mentioned that EXAFS is a complementary method to TEM, also presenting certain valuable advantages: (i) it can be used to extract information on the evolution of the NP size (via the atomic coordination numbers) during a given thermal or chemical treatment. (ii) EXAFS not only can provide insight into the NP size at a given temperature and under a given chemical environment, but also on the structure of the NPs<sup>5, 105</sup> (e.g. fcc or icosahedral). (iii) EXAFS can provide information on Pt-Pt bond lengths for very small NPs<sup>5, 106</sup>, whose structure cannot be resolved via *ex-situ* TEM. Even *in situ* bright field TEM measurements on reduced NPs (e.g. in H<sub>2</sub>) are extremely challenging for NPs within this size range (<1 nm), and have not been reported for the material system at hand. (iv) EXAFS can also provide information on the degree of internal atomic disorder of the NPs via the “static disorder” parameter.<sup>5</sup> (v) EXAFS can provide insight into the presence of adsorbates on the NP surface as well as on the formation of oxidic species.<sup>79, 107, 108</sup> Such information would not be detected via *ex situ* TEM for very small NPs, especially if such oxide shells are highly disordered (amorphous). (vi) EXAFS provides ensemble-averaged values from the entire sample, while TEM provides local information.

As can be seen in Table 3, due to the overall small final average size of the NPs in our samples (< 1.2 nm according to TEM), the Pt-Pt distances obtained are smaller than those of bulk Pt, a contraction which is expected for small NPs. Further, the latter effect is observed even though all samples were measured in H<sub>2</sub>, which has been shown to

relax the Pt-Pt bonds<sup>5, 79, 106, 109</sup>. Additionally, a correlation between the final NP size and the magnitude of the EXAFS disorder was observed, with the largest values obtained for the as-prepared and O<sub>2</sub>-annealed samples (0.0073-0.0078 Å<sup>2</sup>), and the smallest values for the H<sub>2</sub>O and H<sub>2</sub> annealed samples (0.0066-0.0068 Å<sup>2</sup>). For comparison, a value of 0.005 Å<sup>2</sup> was obtained from the fit of a bulk Pt foil.

For NPs in S4, no sintering was detected at least up to 450°C in O<sub>2</sub> for 3 hours. An initial O<sub>2</sub>-mediated NP redispersion might contribute to this effect, since coalescence phenomena have been shown to be less favorable when the NPs are widely spaced<sup>110</sup>. The presence of PtO<sub>x</sub> species might contribute to strengthening the binding between the Pt NPs and the Al<sub>2</sub>O<sub>3</sub> support, as suggested for O<sub>2</sub>-annealed Au NPs on SiO<sub>2</sub><sup>71</sup> and Pd on Al<sub>2</sub>O<sub>3</sub><sup>111</sup>. Interestingly, Goeke and Datye<sup>69</sup> previously reported smaller NP sizes for Pd NPs synthesized by electron beam evaporation when annealed in O<sub>2</sub> at 700°C as compared to identical samples pre-annealed in an inert atmosphere. This effect was also assigned to the formation of PdO<sub>x</sub> species. The same explanation is valid when the distinct stability of samples S4 (annealed in O<sub>2</sub>) and S6 (annealed in H<sub>2</sub>) is considered, with reducing annealing environments favoring the sintering of the inverse micelle prepared NPs above 375°C. This oxide formation and NP growth are schematically depicted in Fig. 42.

More importantly, the pre-treatment in O<sub>2</sub> is likely to affect the structure, chemical state, and density of defects in the Al<sub>2</sub>O<sub>3</sub> surface, which are also expected to influence the stability of the NPs. In fact, the presence of hydroxyl groups on Pt NP/γ-Al<sub>2</sub>O<sub>3</sub> samples below 580°C has been reported,<sup>80, 112</sup> and OH species may act as anchoring sites for the Pt NPs, as previously suggested for Pd/Al<sub>2</sub>O<sub>3</sub><sup>111</sup> and Au/MgO.<sup>113</sup>



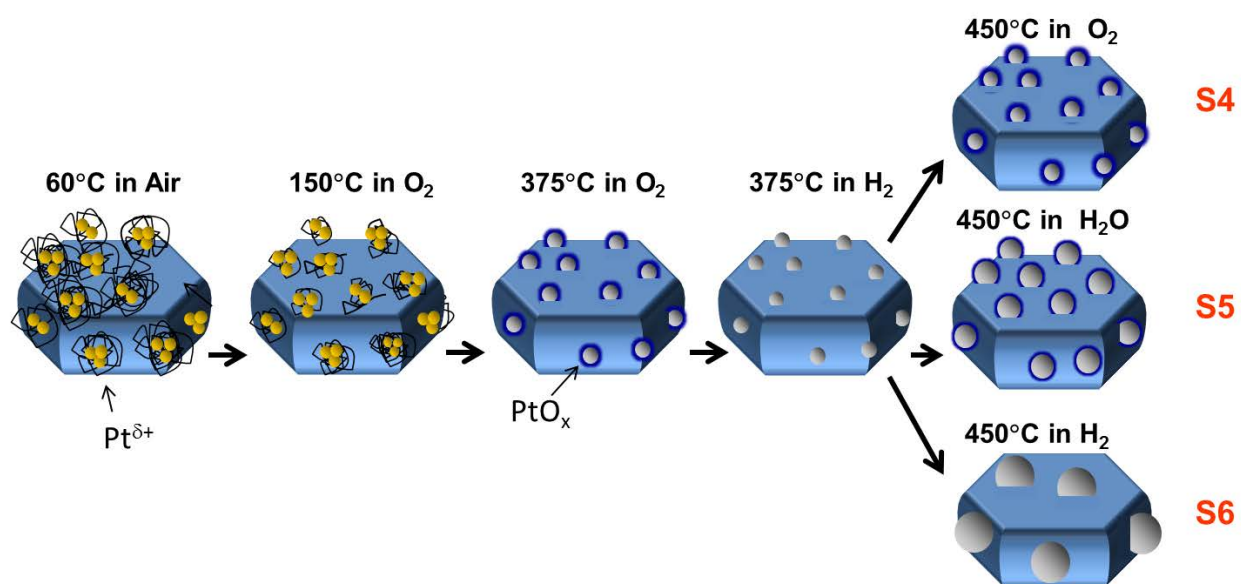


Fig. 42: Schematic representation of the evolution of the structure and chemical state of our inverse micelle prepared Pt/ $\gamma$ -Al<sub>2</sub>O<sub>3</sub> samples (S4-S6) under various thermal and chemical treatments inferred from the analysis of *in situ* EXAFS and *ex situ* STEM data.

For sample S6 this effect adds to the additional partial de-stabilization of the Pt NPs expected to occur after reduction of the PtO<sub>x</sub> species by the H<sub>2</sub> treatment at 400°C, since weaker NP/support bonding has been reported for metallic NPs on oxides, as for example reduced Pd on Al<sub>2</sub>O<sub>3</sub>.<sup>111</sup> Therefore, our results indicate that pre-treatments in O<sub>2</sub> might be valid alternatives to stabilize as well as to regenerate coarsened catalysts via catalysts redispersion, although the possible loss of Pt through the formation of volatile PtO<sub>x</sub> species must also be taken into account.<sup>80</sup> Regarding the stabilizing effect of hydroxyl groups against NP sintering,<sup>113, 114</sup> our EXAFS and TEM data of the sample pre-dosed with water and annealed in water vapor at 450°C (S5) demonstrate that such pre-treatment contributes to the partial stabilization of the NPs (as compared to S6 annealed in H<sub>2</sub>), although it is less efficient than the pre-treatment or annealing in an O<sub>2</sub> atmosphere (S4).

Although NP redispersion has been reported for the Pt/ $\gamma$ -Al<sub>2</sub>O<sub>3</sub> system after annealing in oxygen at temperatures below 600°C<sup>115-117</sup>, treatments at higher temperature in the same environment were shown to result in NP sintering<sup>115, 116, 118, 119</sup>. Furthermore, redispersion of metal NPs was only observed for systems characterized by strong interactions between the metal oxides formed on the NPs and the oxide support. Such phenomenon was found to involve the detachment of metal oxide species from the NPs and their subsequent migration to trap sites on the support surface. The stronger binding of PtO<sub>x</sub> to Al<sub>2</sub>O<sub>3</sub>, as opposed to metallic Pt, and better wetting of the  $\gamma$ -Al<sub>2</sub>O<sub>3</sub> surface, is expected to underlie the enhanced thermal stability of our Pt NPs during coarsening treatments in oxygen at 450°C (S4 as compared to S6). It should also be noted that low metal loadings and high surface area supports are crucial for this phenomenon to occur,<sup>120</sup> which might be related to the need of available defect sites on the support surface to stabilize the redispersed clusters. Sample annealing in reducing environments (e.g. hydrogen) leads to the reduction of the oxidized metal species, the concomitant weakening of the NP/support bond, and the release of the trapped oxide species, resulting in NP sintering<sup>115, 116, 121</sup>. The latter is observed for samples S6.

The work described above emphasizes the importance of *in situ* investigations for the understanding of coarsening phenomena at the nanoscale. Furthermore, we have illustrated that EXAFS is a powerful technique for monitoring the *in situ* evolution of the structure and size of small NPs under real industrial operation conditions, e.g. under high temperature and in the presence of adsorbates. TEM is a great complementary technique to EXAFS for these types of studies.

## 4.6 Conclusions

The thermal stability, mobility, and coarsening of Pt NPs supported on  $\text{TiO}_2(110)$  was investigated by combining STM measurements with simulations based on Ostwald ripening and diffusion-coalescence models. The effect of the substrate pre-treatment, roughness, and degree of reduction on the coarsening of metallic NPs deposited on oxide supports was discussed. Evaporated Pt NPs show a stronger binding to the strongly reduced pristine  $\text{TiO}_2(110)$  as compared to polymer-coated and  $\text{O}_2$ -plasma treated  $\text{TiO}_2(110)$ . Furthermore, the support-induced stability appears to be stronger for the smaller NPs.

Modifications to the traditional mathematical description of the diffusion-coalescence coarsening model were implemented to better describe the temperature dependence of the diffusion constant as well as to incorporate physically meaningful energetics for adatom formation in NPs. In addition, more efficient computational methods to simulate coarsening phenomena following the Ostwald ripening and diffusion-coalescence models were developed. The efficiency of such simulation methods is essential in order to be able to follow industrially relevant sintering processes that are likely to occur over extended periods of time. Our mathematical description facilitates the comparison of coarsening phenomena occurring on NP samples supported on distinct substrates. Our simulations revealed that the diffusion-coalescence model provides a considerably better description of our experimental data for evaporated NPs (S1, S2) as compared to the Ostwald-ripening model. On the other hand, no changes in the NP size distribution were observed for the larger micellar Pt NPs after identical thermal treatments. The advantages of the stabilization of NPs within

the size range of our micellar Pt NPs (~3 nm at ~1060 °C) should be recognized, since such sizes have been reported to be active for certain catalysis applications.<sup>122</sup> Thus, micellar-based NP fabrication methods may be considered excellent candidates for the production of rationally-engineered active and durable nanocatalysts.

At last, we investigated the thermal stability of inverse micelle prepared Pt NPs supported on  $\gamma$ -Al<sub>2</sub>O<sub>3</sub> and demonstrated the applicability of EXAFS as a tool for studying NP coarsening at high temperature and under gaseous environments. We found that for samples annealed at 450°C under different chemical atmospheres, reducing environments (H<sub>2</sub>) lead to drastic NP sintering, while slight or no coarsening was observed upon annealing in water vapor and oxygen, respectively. The formation of PtO<sub>x</sub> species upon O<sub>2</sub> annealing and the associated increase in the strength of the NP/support bond, possibly involving Pt-OH species, are considered likely explanations for the observed effects. Our findings might be of relevance for high temperature industrial catalysis applications, since sintered NPs with low surface-to-volume ratios have been generally shown to display decreased chemical reactivity.

## CHAPTER 5: SHAPE DETERMINATION OF NANOPARTICLES AND EPITAXIAL RELATION WITH THE UNDERLYING SUPPORT

### 5.1 Introduction

Metal nanoparticles are currently being used in a variety of applications in the fields of plasmonics, magnetism, and catalysis.<sup>1, 3, 5</sup> Since many of the unusual electronic, optical, magnetic, and chemical properties of NPs have been shown to be size-, shape-, and strain-dependent,<sup>5-11</sup> control of these parameters could be used to optimize NP performance in a range of applications.<sup>10, 19</sup> For example, a good epitaxial relationship would lead to significant improvements in the photocatalytic performance of the Pt/TiO<sub>2</sub> system through the facilitation of electron transfer processes from the substrate to the NPs<sup>10</sup>. Additionally, for small (few-nm) NPs, an epitaxial relationship with the substrate could lead to a degree of lattice strain that could otherwise not be obtained, which in turn may affect catalytic activity.<sup>10, 11</sup> Finally, different epitaxial relationships could also affect the faceting of the NPs and thus potentially enhance the performance of the nanocatalysts. Therefore, determining and ultimately having the ability to tune such orientations could lead to major breakthroughs in this field. However, the preparation of high density 3D epitaxial NPs homogeneously dispersed over large substrate areas, presents a challenge for most materials systems grown via physical vapor deposition, sputtering, and other *in situ* or *ex situ* synthesis methods, with most systems producing highly anisotropic or island-like structures.

In addition to fabrication challenges, the investigation of epitaxial NPs presents significant characterization challenges. Several attempts have been made to solve the

structure of supported metallic NPs via ensemble-averaging methods<sup>5, 123, 124</sup>. For example, using angle-resolved x-ray photoelectron spectroscopy (AR-XPS)<sup>123</sup>, low-energy electron diffraction (LEED),<sup>123, 125</sup> and x-ray photoelectron diffraction (XPD) techniques<sup>126</sup>, the dominant orientation of PVD-deposited Pt NPs on TiO<sub>2</sub>(110) was found to be {111}. However, in order to evaluate different NP/support epitaxial orientations which might coexist within the same sample, spatially resolved non-averaging techniques such as TEM or STM are required. STM can routinely provide atomically-resolved images on flat surfaces<sup>127</sup> and large 2D NPs with flat top facets.<sup>88, 128, 129</sup> However, when three dimensional nano-sized features are present on a surface, a larger fraction of the tip apex is involved in the imaging process, and tip convolution effects smear out the geometrical features of the NPs. In the present work, the use of ultra-sharp tips enables partial imaging of select side facets of small (2-6 nm) 3D NPs, allowing the determination of their shape.

Our study illustrates how an *ex situ* chemical synthesis method, namely, inverse micelle encapsulation, can be used to achieve well-defined and tunable 3D NP shapes with epitaxial NP/support interfaces, and how the size of the micellar NPs can be used to control their final shape and their epitaxial orientation on the underlying support. Furthermore, we demonstrate that this method can produce NP shapes that significantly deviate from the common bulk-like Wulff equilibrium structures defined for unsupported clusters.

## 5.2 Experimental

Self-assembled size-selected Pt NPs were synthesized by micelle encapsulation<sup>40</sup>. Polystyrene-block-poly(2-vinylpyridine) [PS(x)-P2VP(y)] with different molecular weights were dissolved in toluene to form reverse micelles. To prepare NPs with a variety of sizes, different polymers with atomic weights (x:y) of (27700:4300), (81000:14200), and (81000:21000) were used. Subsequently, H<sub>2</sub>PtCl<sub>6</sub> or HAuCl<sub>4</sub> was added at a metal salt/P2VP concentration ratio ranging from 0.01 to 0.6. The NP size is controlled by the length of the polymer head (P2VP) and the metal-salt/P2VP concentration ratio, while the interparticle distance is determined by the length of the polymer tail (PS)<sup>40, 130</sup>. Planar samples were prepared using a dip-coating method resulting in a monolayer-thick film of self-assembled micellar NPs on the substrate. Two Pt and one Au samples were investigated. Prior to the NP deposition, single crystal TiO<sub>2</sub>(110) substrates were cleaned in ultrahigh vacuum (UHV) by cycles of Ar<sup>+</sup> sputtering (1 keV) at RT and annealing at 1000°C. The encapsulating polymer was removed *in situ* by an O<sub>2</sub>-plasma treatment (4×10<sup>-5</sup> mbar, 120 min). XPS measurements of the C-1s core level region corroborated the complete removal of the organic ligands. Subsequently, the sample was isochronally annealed in UHV in 100°C intervals for 20 min from 300°C to 900°C, and for 10 min from 1000°C to 1060°C. This treatment resulted in the reduction of the PtO<sub>x</sub> species formed upon O<sub>2</sub>-plasma exposure. By varying the molecular weight of the encapsulating polymer, metal salt loading and thermal treatment (temperature and time), a variety of final NP volumes could be obtained, while keeping individual NPs well separated from each other on the TiO<sub>2</sub> surface. Fig. 43 describes schematically the NP synthesis process.

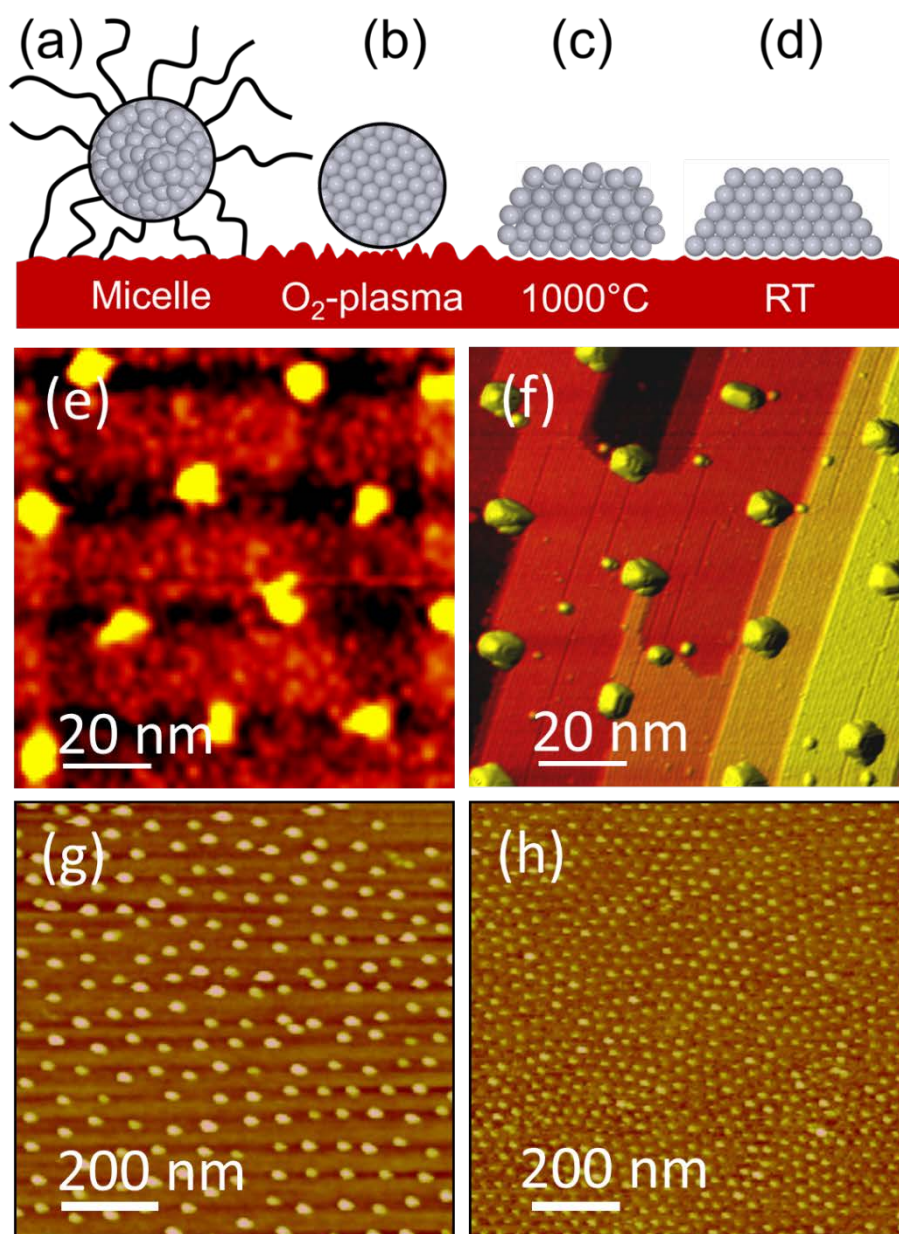


Fig. 43: Schematic representation of the evolution of the structure of micellar NPs supported on TiO<sub>2</sub> after different chemical and thermal treatments. STM images of polymer-free micellar Pt NPs on TiO<sub>2</sub>(110) acquired at RT after annealing at (e) 150°C and (f) 1000°C are also shown. The hexagonal NP arrangement is observed in (e), but also significant roughness of the TiO<sub>2</sub> support. A flatter and atomically-resolved TiO<sub>2</sub> surface with shape-resolved Pt NPs is evident in (f). Typical large scale AFM images of micellar NPs prepared using two different PS(x)-P2VP(y) polymers with (x: 53000, y: 43800) in (g) and (x: 27700, y: 4300) in (h).



Different steps in NP synthesis are shown: (a) micelle-encapsulated spherical NPs without contact with the support; (b) ligand-free long-range-ordered single grain NPs resulting from the exposure to an O<sub>2</sub>-plasma in UHV. Exposure to air and also O<sub>2</sub>-plasma also results in an increase in the roughness of the support. At this stage, the NPs make contact with the support but their shape remains spherical.<sup>29, 131</sup> (c) Reduction and flattening of the TiO<sub>2</sub> support after high temperature annealing (1000°C) accompanied by enhanced mobility of metal atoms within the NPs allowing them to rearrange and obtain a good interfacial matching. (d) Well faceted NPs with an epitaxial relation with the support obtained upon cooling to RT.

All STM images were acquired at RT after sample annealing at temperatures above 1000°C. The chemically-etched tungsten tips used were cleaned *in situ* via Ar<sup>+</sup> sputtering.

### 5.3 Results and discussion

STM images demonstrating four main NP shape categories are shown in Fig. 44. These shapes were observed on TiO<sub>2</sub>(110) after the micellar NP formation and subsequent high temperature annealing. All NPs show pronounced faceting and a clear orientation relative to the substrate's crystalline directions. Based on the observed relative angles of the various facets, the orientation of the free and interfacial Pt surfaces could be identified, as shown in Fig. 44(e-h). Type A (TA), type B (TB) and type D (TD) NPs have flat top facets while type C (TC) has a wedge on top. The interfacial facets of each NP category are: {111} for TA, {100} for TB, and {110} for TC and TD.

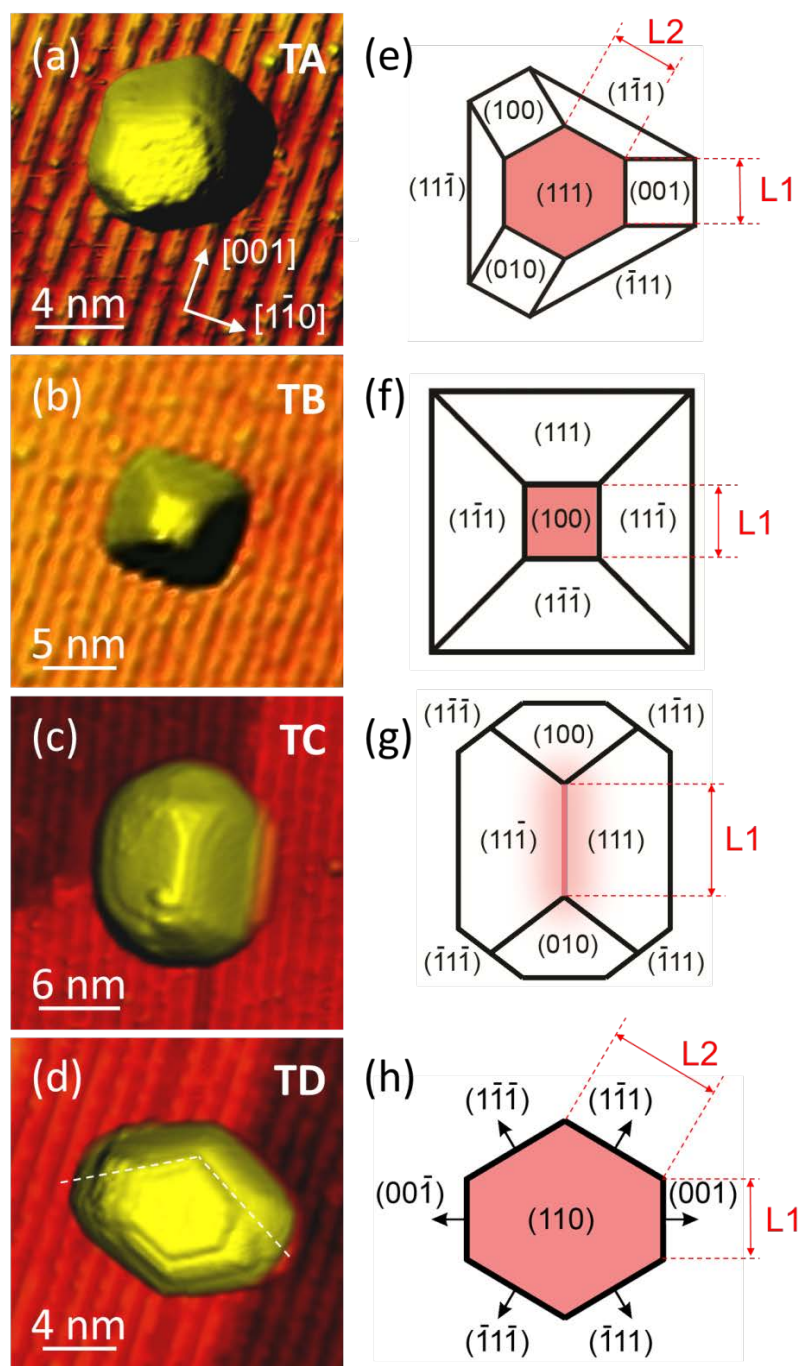


Fig. 44: STM images of micellar Pt NPs supported on TiO<sub>2</sub>(110) acquired at RT after annealing at 1000°C. Four main categories of NP shapes are displayed (a-d) with the corresponding models (e-h). The facets at the perimeter of TD NPs are perpendicular to the NP/support interface. The apparent slopes observed around them in (d) are due to tip convolution effects.

Although TA and TD NPs have in common a hexagonal top facet, the angles between the edges on the top facet are  $\sim 125^\circ$  and  $\sim 110^\circ$  for TD NPs, in contrast with  $120^\circ$  for TA NPs. In addition, TD NPs have 2-fold rotational symmetry, while TA NPs have 3-fold symmetry. NP shapes of TA and TB, although with a much smaller height/diameter aspect ratio, were also observed for large NPs synthesized via PVD following a seeding growth method along the crystalline orientation of the seed.<sup>88, 128</sup>

Nevertheless, to the best of our knowledge, TC and TD NPs have not been previously reported. Large Pt NPs ( $\sim 30$ - $100$  nm) of TC shape were however fabricated via electron beam lithography on  $\text{SrTiO}_3(110)$  substrates.<sup>7</sup>

The observations made in Fig. 44 can be understood by the structural evolution of the NPs schematically depicted in Fig. 43(a-d). Since the largely metallic core of the micelles is originally surrounded by polystyrene (PS) groups, there is no contact between the NP core and the oxide support after deposition. Therefore, no preferential decoration sites on the support surface are initially available for the micellar NPs. This is evidenced by the persistence of the hexagonal NP arrangement obtained after dip-coating, with an interparticle spacing determined by the length of the encapsulating PS groups<sup>28</sup>, Fig. 43(e),(f). This is in clear contrast with the observations made for PVD metal NPs on  $\text{TiO}_2$ , which are known to preferentially nucleate at defect sites such as step edges or vacancy sites<sup>18, 132</sup>. After the removal of the polymer ( $\text{O}_2$ -plasma in UHV), the NPs come in contact with the  $\text{TiO}_2(110)$  substrate. Subsequent annealing above  $1000^\circ\text{C}$  leads to surface- and/or bulk-melting of the NPs, and the minimization of their surface energy results in thermodynamically stable shapes. Our STM study, carried out

at RT after the former treatment, demonstrates the stabilization of isolated faceted single grain Pt and Au NPs with an epitaxial relation with the  $\text{TiO}_2(110)$  support, Fig. 44.

The NPs shapes, facet configurations, and epitaxial relationship with the  $\text{TiO}_2$  support shown here for micellar NPs are not limited to the Pt/ $\text{TiO}_2$  system, which is known for its strong metal-support interaction (SMSI) effect.<sup>123, 133</sup> To illustrate this, Fig. 45 shows similar faceting and epitaxial orientation for identically prepared (micelle-synthesis) Au NPs on  $\text{TiO}_2(110)$ .

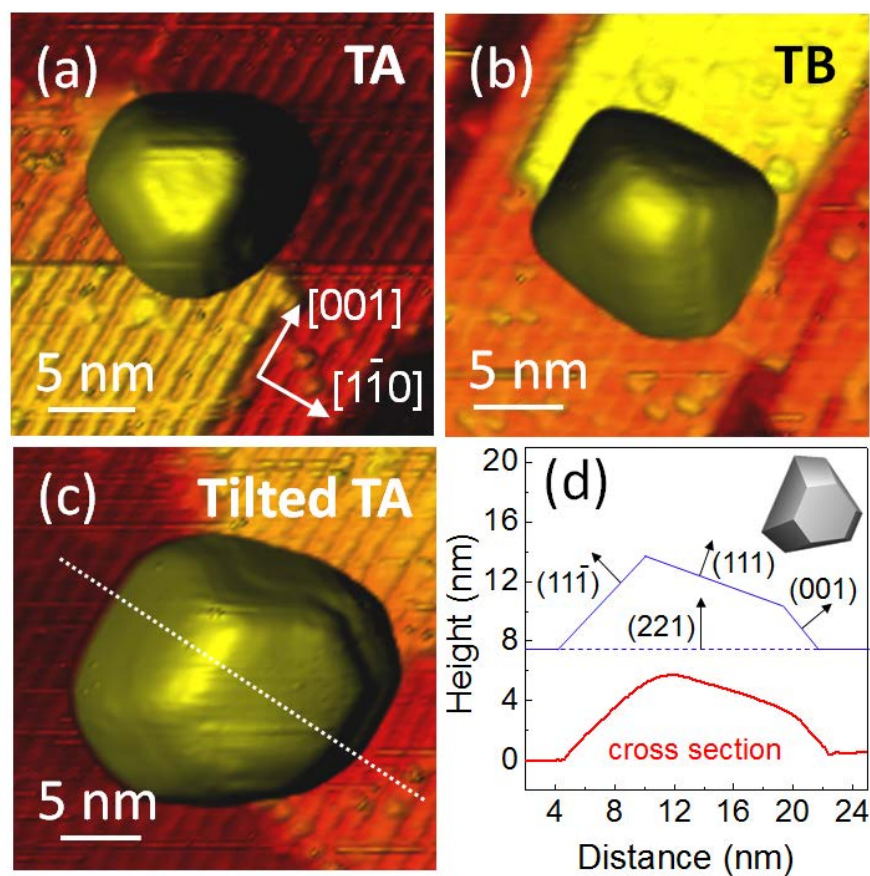


Fig. 45: STM images of micellar Au NPs on  $\text{TiO}_2(110)$  acquired at RT after sample annealing at  $1000^\circ\text{C}$ . The following NP shapes are shown: (a) TA, (b) TB, and (c) tilted TA. The STM cross section of the NP in (c) (along the dotted line) and a schematic of the corresponding facets are shown in (d). A Au(211) facet was found at the NP/support interface. The inset in (d) shows a model of the reconstructed NP shape.

Au NPs of TA and TB shapes, similar to the shapes observed for the Pt NPs are shown in Fig. 45(a) and Fig. 45(b) respectively. However, Au NPs of type C show a different shape than those observed for Pt, namely, they were found to be  $\sim 19^\circ$  tilted along the  $\text{TiO}_2(110)$ -[001] axis, as shown in Fig. 45(c). The direction in which these NPs were sidewise tilted was found to be random and independent from the scanning direction selected. The cross section profile of the latter STM image is shown in Fig. 45(d) (bottom) together with the corresponding model of the NP configuration and facet in contact with the  $\text{TiO}_2$  support, in this case {221}. Another high-index Miller lattice orientation, {211}, was previously determined for Au/ $\text{TiO}_2$  using electron backscattered diffraction techniques,<sup>124</sup> but not for Pt/ $\text{TiO}_2$ .

Variations in the ratio of {100}/{111} facet areas ( $A_{100} / A_{111}$ ) within each category of NP shapes were observed, and examples are shown in Fig. 46. For instance, the {100} top facet in TB square NPs, Fig. 44(b) is absent for some NPs, leading to a truncated octahedron shape, Fig. 46(b).

The tip convolution effect is the main obstacle for obtaining reliable information about the size, diameter, contact area with the support, or free surface area of small NPs using scanning probe microscopy methods such as AFM and STM. Only the size/shape information that is obtained from the highest points of the NPs using SPM techniques can be considered reliable since they are the least likely to be affected by artifacts related to tip convolution effects. The morphological features which can be accurately resolved in our four different NP categories are marked by shading in the schematics of Fig. 47 (left column) and Fig. 44 (right column).

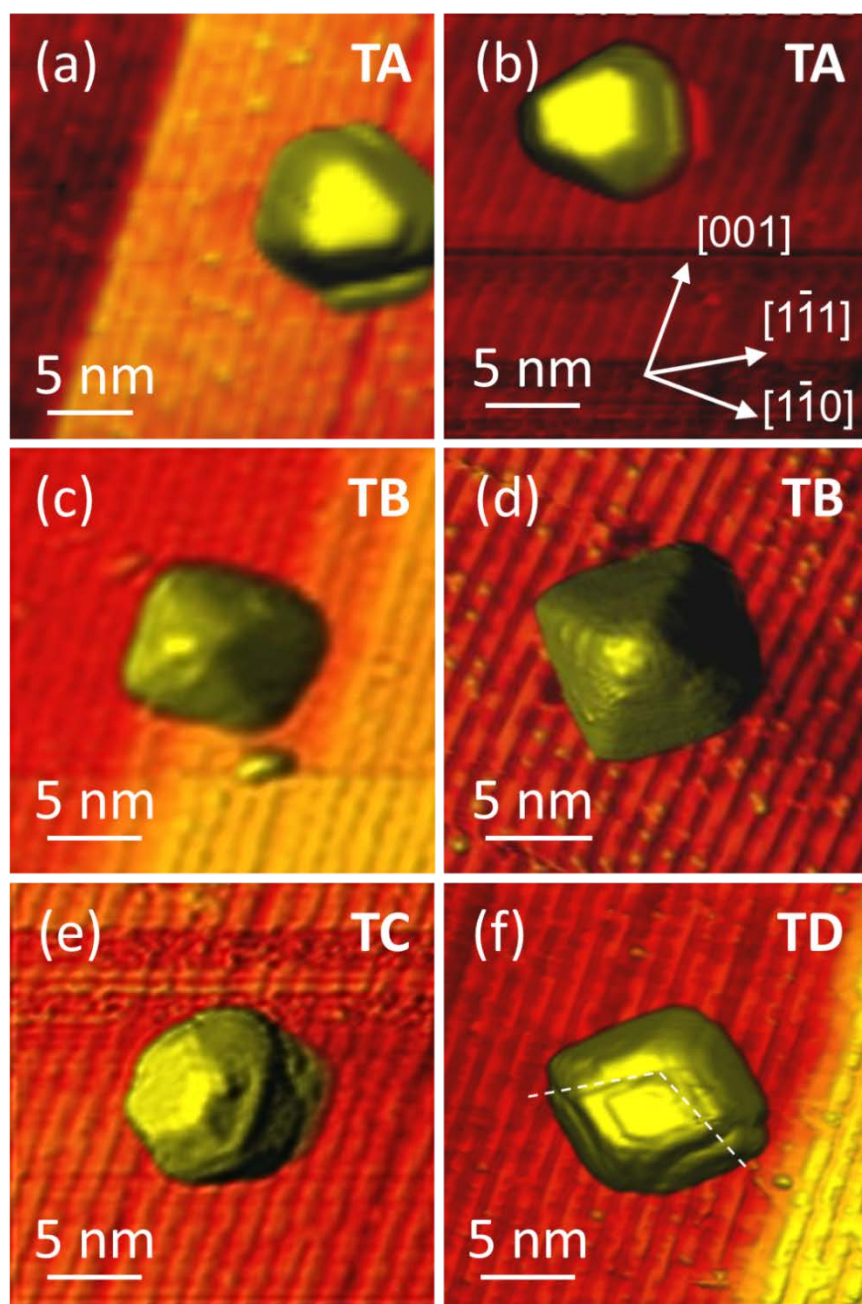


Fig. 46: STM images of micellar Pt NPs on  $\text{TiO}_2(110)$  acquired at RT after annealing at  $1000^\circ\text{C}$ . Examples of variations in the shapes of NPs within a given category (TA-TD) based on distinct  $A_{100}/A_{111}$  ratios are shown (a,c,e,f). NPs of TA and TD in (a, c, f) have a lower  $A_{100}/A_{111}$  ratio than those in Fig. 44(a, b, d), respectively. In rare cases, some NPs were found to be rotated by (b)  $30^\circ$  (TA) and (d)  $45^\circ$  (TB) with respect to the  $\text{TiO}_2(110)$ -[001] direction.

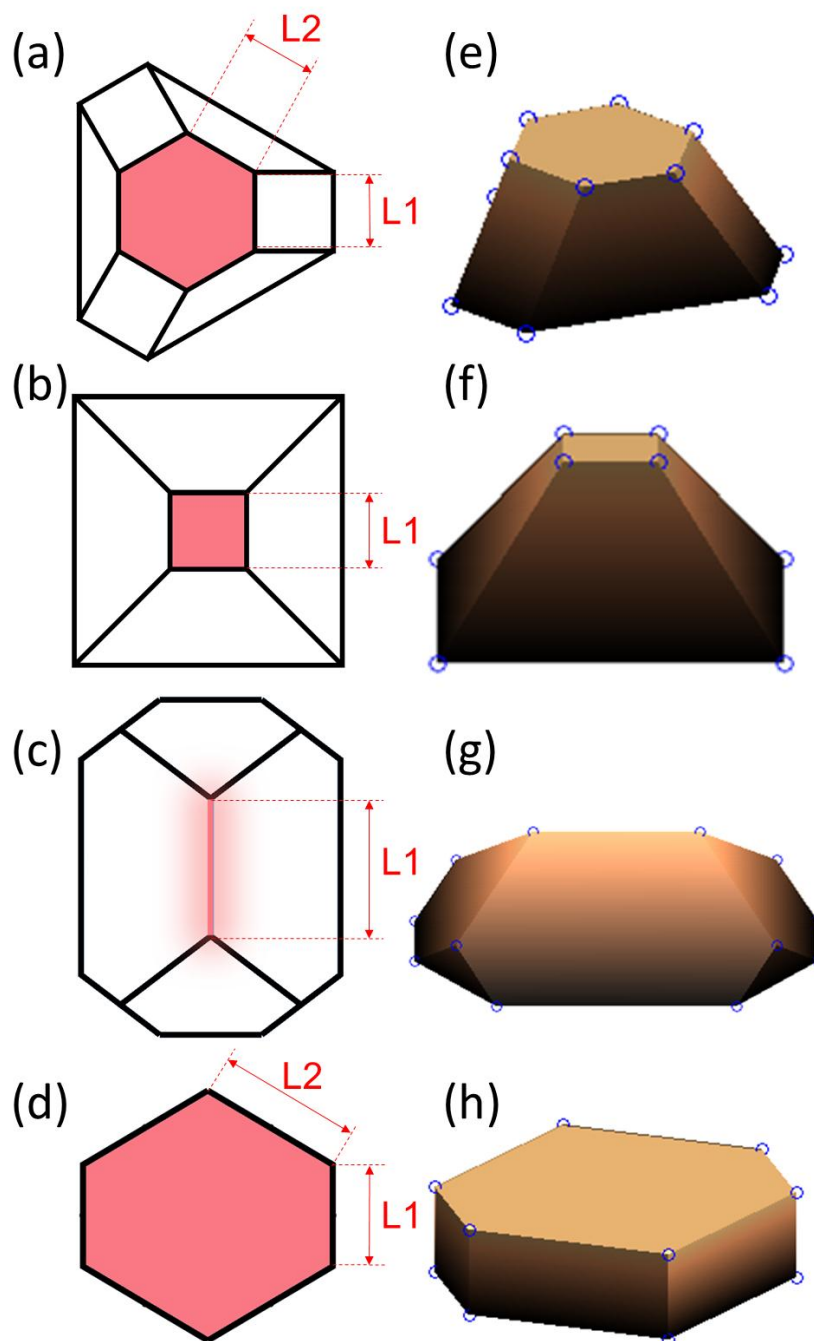


Fig. 47: Morphological features within different types of NP shapes which are not affected by tip-convolution effects are shown in (a-d) and highlighted in pink. The height of the NPs and the dimensions of the top facet ( $L1$  and  $L2$ ) in (a-d) are used to reconstruct the 3D shape of the NPs (e-h) using a MATLAB code.

For NPs in categories TA, TB and TD with a flat top facet, these features include the NP height and the lengths of the sides of the top facet (L1 and L2), Fig. 47(a-c). For TC, the artifact-free STM data are the NP height and the length of the top wedge, Fig. 47(d). Using this information and knowing the NP facet orientations, it is possible to reconstruct the shape of each NP and obtain relevant geometrical information such as the number of atoms and different facets area in each NP. Based on the former experimental parameters, a MATLAB code was written to reconstruct the 3D shape of our NPs.

Our first assumption is the absence of high Miller index facets (e.g. {330}, {221}, {441}, etc) on the free surface of the NPs due to their high surface energy as well as the fact that these facets have not been reported for small Pt NPs (<10 nm) elsewhere. This leaves us with only {100}, {110} and {111} facets on free surface of NPs.

Examples of the calculated shapes are provided in Fig. 47(e-h). From the reconstructed shapes, information regarding the NP volume, number of atoms, and the area of different facets (substrate interface, {111}, {100} and {110}) was obtained.

It should be however noted that despite the finite degree of shape heterogeneity reported in Fig. 44, Fig. 45 and Fig. 46 including STM data acquired on three differently synthesized Au and Pt NP samples, a single initial narrow NP size distribution was found to lead to a relatively well defined particle shape distribution.

Following Wulff's theory,<sup>134</sup> a variety of equilibrium shapes can be obtained for unsupported NPs depending on the surface energy ( $\gamma$ ) ratio of different facets (i.e.  $\gamma_{100}/\gamma_{111}$ ), since distinct facets are characterized by different surface energies. These



shapes include octahedron, cuboctahedron, truncated cuboctahedron and cubic shapes. An example of bulk like Wulff shapes (truncated cuboctahedron) is shown in Fig. 48(a) for a surface energy ratio of 1.15.

Although the Wulff theorem determines the distance of each facet from the center of the NP based on the surface energy ratios, it does not provide directly the surface area ratios. Fig. 48(a) also shows the  $A_{100}/A_{111}$  ratio versus the respective  $\gamma_{100}/\gamma_{111}$  surface energy ratios obtained from numerical calculations. It should be noted that these shapes are obtained based on Wulff's reconstruction model without considering the support effect.

Fig. 48(b) (left axis) shows the experimental  $A_{100}/A_{111}$  surface area ratio as a function of the number of atoms in each NP for the three categories of shapes most commonly observed via STM. Accordingly, Fig. 48(a) can be used to extract the  $\gamma_{100}/\gamma_{111}$  ratio of the STM-resolved NPs. This is shown in Fig. 48(b) (right axis).

Since the majority of the experimental TiO<sub>2</sub>-supported Pt NPs display shapes analogous to those theoretically predicted for unsupported Wulff model NPs but truncated in half, the experimental surface area ratios are expected to be similar to those of the Wulff structures.

The  $A_{100}/A_{111}$  ratio is 0.25 for a truncated cuboctahedron NP (bulk-like Wulff shape typical of large NPs).<sup>87, 135, 136</sup> However, different geometrical characteristics were observed here for the micellar Pt NPs, with  $A_{100}/A_{111} < 0.25$  for TB NPs and  $> 0.25$  for TA and TC. The corresponding surface energy ratios are  $\gamma_{100}/\gamma_{111} > 1.4$  for TB NPs, and  $\gamma_{100}/\gamma_{111} < 1.1$  for TA and TC.

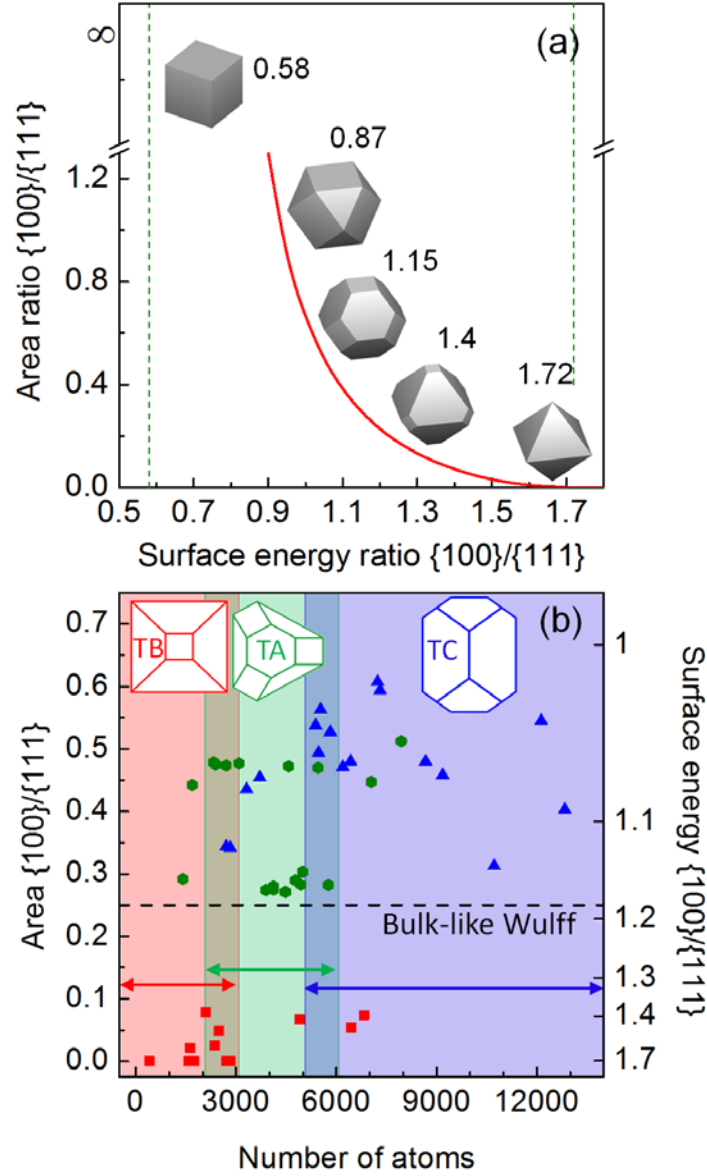


Fig. 48: (a) Ratios of  $\{100\}/\{111\}$  surface areas ( $A_{100}/A_{111}$ ) as a function of the corresponding surface energy ratios ( $\gamma_{100}/\gamma_{111}$ ) following the Wulff theorem. Representative model NP shapes are shown as inset. For  $\gamma_{100}/\gamma_{111} > 1.7$ , no  $\{100\}$  facets are present, and the NPs adopt octahedron shapes. For  $0.87 < \gamma_{100}/\gamma_{111} < 1.15$ , the NPs adopt cuboctahedron and truncated cuboctahedron shapes. For  $\gamma_{100}/\gamma_{111} > 0.58$ , cubic shapes are found. (b) STM-resolved  $A_{100}/A_{111}$  ratios (left axis) and corresponding  $\gamma_{100}/\gamma_{111}$  ratios (right axis) obtained from (a) plotted versus the number of atoms within each NP. Schematics of the NP shapes observed are included as insets in (b).

Since these shapes were obtained for NPs pre-annealed above 1000°C, they are considered to be the most thermodynamically stable shapes for this system. The observed deviations from bulk-like Wulff structures ( $\gamma_{100} / \gamma_{111} = 1.18$ )<sup>135-137</sup> might be due to finite size effects, interface-induced stress, and adsorbate effects<sup>138, 139</sup>.

Fig. 48(b) demonstrates that the majority of TB NPs (>75 %) have less than 3000 atoms, while the majority of TA NPs (> 75 %) contain 2000 to 6000 atoms. Type C NPs are the largest among these three categories, with 75 % of the NPs having more than 5000 atoms. The range of NP sizes (or number of atoms) giving rise to NPs of TA is highlighted by green shading, those of TB by red, and TC by a blue background. These data reveal that the dominant shape of the NPs formed via the present micellar synthesis method on a given substrate can be controlled by tuning their size distribution. Such shape transition was predicted for Pt NPs on MgO with increasing the NP size<sup>140</sup>.

Interestingly, all of our NPs have an epitaxial relationship with the underlying substrate, since one of the NPs' symmetry axes is always parallel to the TiO<sub>2</sub>(110) rows. As demonstrated in Fig. 43(e), such epitaxial relation does not exist after NP deposition and moderate annealing (150 °C), and should have been developed as a result of the high temperature annealing (1000 °C). Although in most cases the NPs have two edges parallel to the TiO<sub>2</sub>(110)-[100] rows [Fig. 44 and Fig. 46(a, c, d)], a few examples of NPs rotated by 30° [Fig. 46(b)] or 45° [Fig. 46(d)] without any edge parallel to the TiO<sub>2</sub>(110)-[100] direction can also be found. However, even for these rare cases, one of the symmetry axes of the NPs is parallel to the TiO<sub>2</sub>(110)-[100] rows, demonstrating the existence of an epitaxial relation with the support. Such exceptions were not found for

TC Pt NPs, with the top edge being always parallel to the TiO<sub>2</sub> rows. Type D Pt NPs were very rare and insufficient statistics could be obtained for this category.

A major difference between our micellar NPs and PVD NPs is the growth mechanism. While micellar NPs are deposited on the substrate pre-formed, the evaporated NPs grow on the surface via the adsorption of diffusing metal adatoms. Therefore, in the latter case, the anisotropy of the substrate surface plays a crucial role in determining the growth kinetics and final NP shape. For example, the lowest diffusion coefficient for Pt adatoms on stoichiometric TiO<sub>2</sub>(110) has been found to be along the [001] direction<sup>100</sup>. The latter might be responsible for the more asymmetric NP shapes of PVD-prepared NPs, which appear elongated along [001]<sup>88, 128</sup> in contrast to symmetric shapes observed for our micellar NPs. Metal NPs have been shown to affect the surface segregation of oxygen vacancies in TiO<sub>2</sub> substrates<sup>141</sup>. The possible existence of different vacancy concentrations underneath the NPs in NP samples prepared by PVD versus our micellar method might result in different NP/support binding energies and consequently different NP shapes.

Several procedures have been developed in the past in order to gain control over the shape of NPs based on altering the growth rate of different facet orientations<sup>6, 142, 143</sup>. Although good shape-selection results from some of these methods, the morphologies obtained are mainly dominated by growth kinetics, and such structures are not thermodynamically stable. Therefore, they cannot withstand the environmental conditions that some applications might require (e.g. high-temperature catalytic reactions).<sup>47</sup> Micellar Pt NPs show an enhanced stability against coarsening and no mobility after severe thermal treatments (>1000°C).<sup>28</sup> Therefore, the shapes adopted by

these NPs are expected to be the most thermodynamically favored geometries. Moreover, since in theoretical calculations the clusters are allowed to relax and to find the energy minima, the equilibrium shapes obtained for the micellar NPs are expected to be much better models for comparison with theoretical calculations of fcc clusters.<sup>144</sup>

As was mentioned in the introduction, not just their epitaxial relation but also the specific orientation of the NPs on the support is important for their application in catalysis and other fields<sup>10</sup>. For this reason, the lattice matching and interfacial strain was also obtained. In order to explain the epitaxial orientation of the annealed micellar NPs on TiO<sub>2</sub>(110), for a given interfacial Pt plane, the corresponding facets were superimposed to the TiO<sub>2</sub> surface lattice and rotated about an axis perpendicular to the interface. This procedure follows the “coincidence of reciprocal lattice points” method (CRLP)<sup>145</sup>, but has been modified to describe real-space 2D lattices found at the NP/support interface.

A MATLAB code was written to evaluate the overlap of different interfacial Pt facets [e.g. (111), (100), (110), etc.] and the TiO<sub>2</sub> (110) surface after taking into consideration the possible strain of the first Pt interfacial layer. In the calculation of the overlap between the Pt atoms and the TiO<sub>2</sub> primitive cell, each atom is considered a sphere with a radius of  $r$ . The overlap between two spheres of radius  $r$  located at a distance  $d$  can be obtained following:

$$V_{overlap} = \frac{2\pi}{3}(2r^3 - 3r^2d + d^3) \quad (26)$$

,where  $d < r$ . Therefore, the total overlap is given by:  $V = \sum V_{overlap}$ .

For any desired Pt facet, the MATLAB code rotates the facet along an axis perpendicular to the TiO<sub>2</sub> surface from  $\theta = 0$  to  $180^\circ$  in steps of  $0.1^\circ$ . After each rotation, the Pt lattices is strained (expanded or contracted) by  $\varepsilon_x$  and  $\varepsilon_y$  percent ( $-14 < \varepsilon_x, \varepsilon_y < 14$  in 0.1 steps) along the [001] and  $[1\bar{1}0]$  directions of TiO<sub>2</sub>(110), respectively. The strain ( $\varepsilon$ ) is defined as:

$$\varepsilon = \frac{L_{Bulk} - L_{Relaxed}}{L_{Bulk}} \quad (27)$$

, where  $L_{relaxed}$  and  $L_{Bulk}$  are the dimensions of the 2D unit cells of the relaxed (strained) and bulk-like Pt interfacial facets. An expansion in the interfacial Pt lattice is indicated by  $\varepsilon_x, \varepsilon_y < 0$ , while positive values represent lattice contraction. The x and y directions are parallel to the [001] and  $[1\bar{1}0]$  directions of TiO<sub>2</sub>(110), respectively. For all combinations of  $\varepsilon_x, \varepsilon_y$ , and  $\theta$ , the total overlap of the interfacial Pt lattice and the unreconstructed TiO<sub>2</sub> surface was calculated. These calculations were performed using the lattice points lying in the range of  $R < 7a$ , and the sphere of radius  $r=0.15a$ , where  $a$  is the lattice constant. The lattice constants of Pt and Au are 3.92 Å and 4.08 Å respectively.

Examples of the results of this procedure are given in Fig. 49 and Fig. 50 for Pt(100) and Pt(111) facets, respectively. A Pt(100) interfacial facet is representative of type B NPs while Pt(111) is representative of hexagonal NPs of type A.

The parameter R determines the radius of the area of the desired facet used in these calculations, and it is shown as a large blue circle surrounding the Pt lattice in Fig. 49(b, d) and Fig. 50(b, d). It should be noted that the results obtained here are not

sensitive to the choice of  $R$  and  $r$ . For example, a larger (smaller) value of  $r$  will only result in broader (sharper) peaks in the total overlap curves shown in Fig. 49(a,c) and Fig. 50(a,c), but the peak positions would remain the same.

The optimum rotation angles were found to be zero for all configurations, resulting in one edge of the NPs being parallel to the  $\text{TiO}_2(110)$ -[001] direction, as observed in our experiments.

A positive (negative) value of  $\epsilon$  represents the contraction (expansion) of the interfacial Pt lattice in contact with  $\text{TiO}_2$ . The optimum strain values and rotation angle ( $\theta$ ), e.g. those leading to the maximum interfacial overlap of Pt (or Au) and  $\text{TiO}_2$  lattices, are shown in Table 7 and Table 8.

An analogous analysis carried out for the rotated TA NP in Fig. 46(b) is shown in Fig. 49(c,d) and Fig. 50(c,d). Here the rotation angle was fixed to the observed value of  $30^\circ$  for TA and  $45^\circ$  for TB NPs and the strain values were varied.

As can be seen, the rotated type A and B NPs display a lower total overlap as compared to the regular NPs and are not favorable, although they may show lower lattice strain in one or both directions.

For instance, in Fig. 49(c),  $\epsilon_x$  is smaller for the rotated NP as compared to the regular NP, Fig. 49(b), but the maximum overlap obtained, which is equal to the number of Pt atoms marked in blue in (d) (37 atoms) is much smaller than the overlap obtained for not-rotated TB NPs (61 atoms) (b). The latter explains the rare occurrence of rotated NPs of type A and B. Analogous data for the Au NPs investigated are included in Table 8.

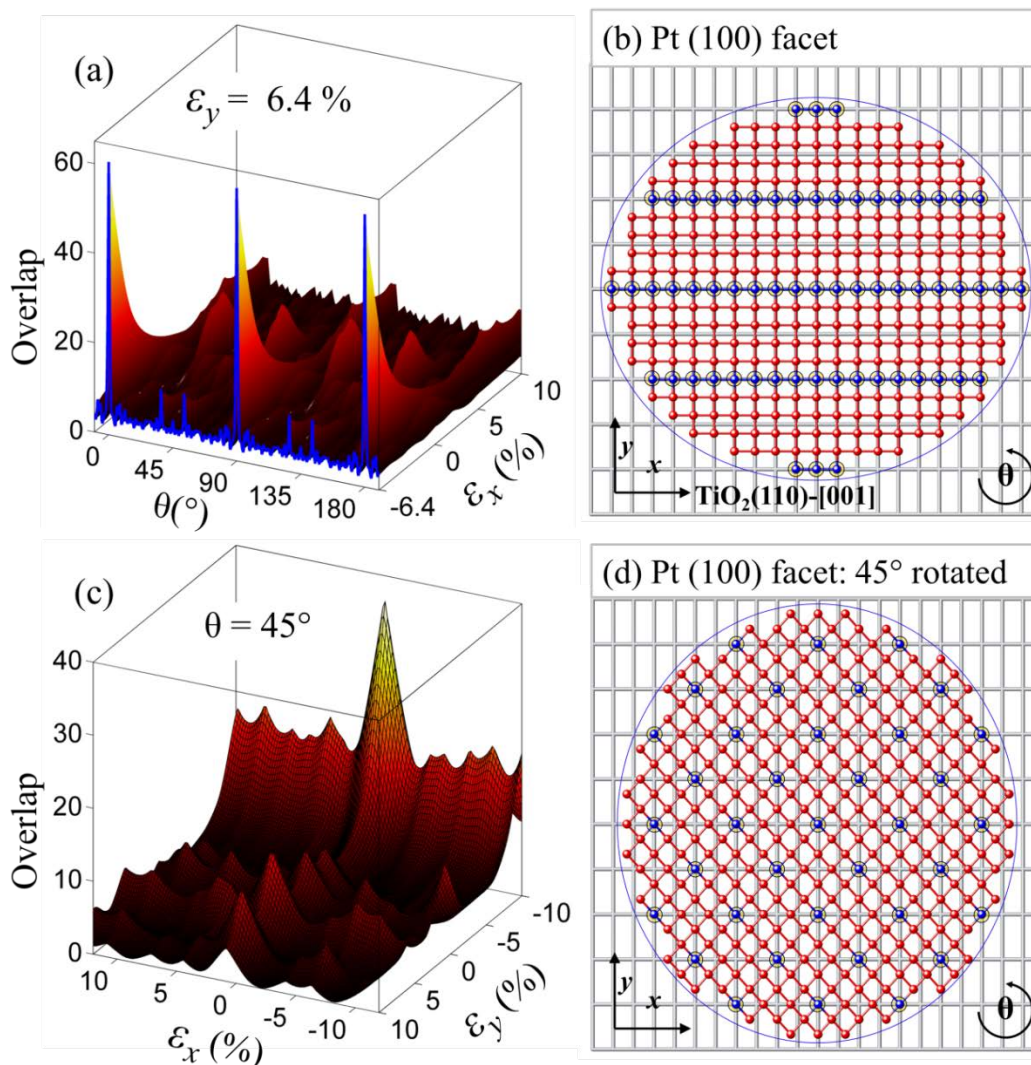


Fig. 49: Total overlap between different strained interfacial Pt facets and the  $\text{TiO}_2(110)$  surface. In the schematics of (b, d), the  $\text{TiO}_2$  lattice is shown as grey rods separated by  $2.94 \text{ \AA}$  in the  $[001]$ -direction and  $6.48 \text{ \AA}$  in  $[1\bar{1}0]$ . The maximum overlap was found by changing the values of the strain parameters  $\epsilon_x$ ,  $\epsilon_y$  and in-plane rotation angle ( $\theta$ ) for a Pt(100) facet. For the purpose of display,  $\epsilon_y$  was fixed in (a) to its calculated optimum value (6.4%). For the Pt(100) facet, the rotational angles giving rise to the optimum interfacial match were  $0^\circ$ ,  $90^\circ$ , and  $180^\circ$  for  $\epsilon_x = -6.4\%$ . These orientations are in agreement with our STM observations. To investigate the epitaxial relation of the rotated NPs, the rotation angle ( $\theta$ ) was fixed to the value observed via STM, i.e.  $45^\circ$  for the TB NP in (c), Fig. 46(d). The strain coefficients  $\epsilon_x$  and  $\epsilon_y$  were then varied until the maximum overlap between the Pt and  $\text{TiO}_2$  lattices was obtained. The maximum overlap for the  $45^\circ$  rotated TB NP was achieved for  $\epsilon_x = -0.3\%$  and  $\epsilon_y = -10.0\%$ .



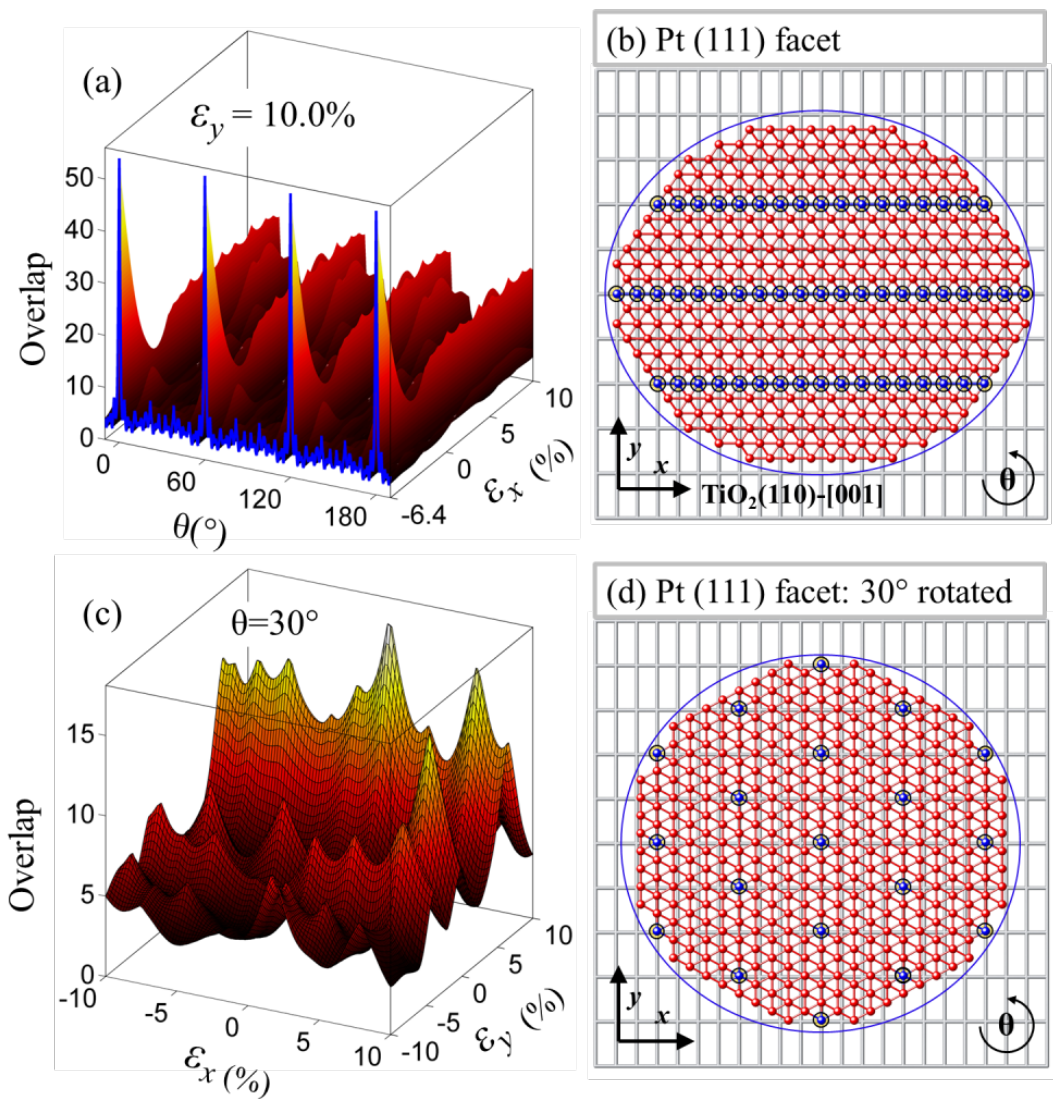
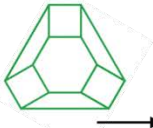
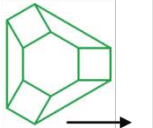
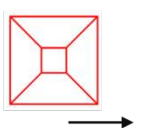
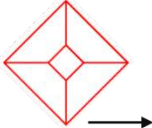
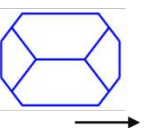
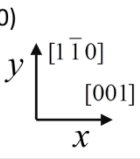
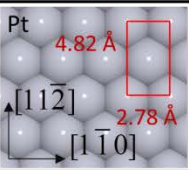
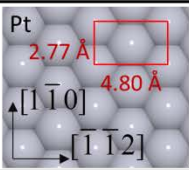
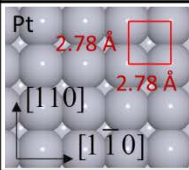
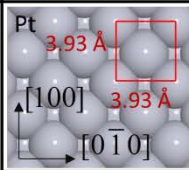
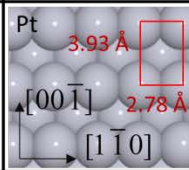


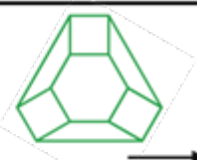
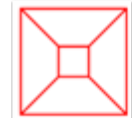
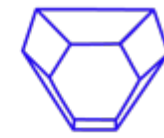
Fig. 50: (a,c) Calculations of the epitaxial relationship between Pt(111) interfacial facets in TA NPs and the  $\text{TiO}_2(110)$  support. Pt atoms overlapping with the  $\text{TiO}_2(110)$  surface unit cell are drawn in blue and highlighted by open black circles. The remaining Pt atoms are drawn in red. The data in (a) and (b) correspond to Pt NPs analogous to those in Fig. 44(a) and Fig. 46(a) (TA, not rotated). Due to the 6-fold symmetry of the Pt(111) facet, the best overlap between both lattices was found at  $0^\circ$ ,  $60^\circ$ ,  $120^\circ$  and  $180^\circ$ . For better visibility, only a cross sectional view of the complete plot is shown in (a). The overlap corresponds to a Pt(111) interfacial layer expanded by 6.4% in the [001] direction of  $\text{TiO}_2(110)$  and contracted by 10.0% along  $[\bar{1}\bar{1}0]$ , as shown in (b). For the rotated TA NP in (c), the rotation angle was kept fixed to the STM-observed value ( $\theta=30^\circ$ ), and the strain parameters ( $\epsilon_x$ , and  $\epsilon_y$ ) were varied until a maximum overlap of the Pt(111) interfacial facet and the substrate lattice was obtained for  $\epsilon_x=1.7\%$  and  $\epsilon_y=6.5\%$  (c).

Table 7: Epitaxial relation between different strained interfacial Pt facets and the TiO<sub>2</sub>(110) surface, including the corresponding lattice mismatch. The number of TiO<sub>2</sub> and Pt unit cells giving rise to the obtained overlap is represented by the parameter  $n_{\text{TiO}_2}:n_{\text{Pt}}$ . For example,  $n_{\text{TiO}_2}:n_{\text{Pt}} = 3:2$  reflects that the overlap between the Pt and TiO<sub>2</sub> lattices occurs every 3 surface unit cells of TiO<sub>2</sub> and 2 of Pt.

Pt NP type & orientation					
	TiO <sub>2</sub> (110)-[001]	TiO <sub>2</sub> (110)-[001]	TiO <sub>2</sub> (110)-[001]	TiO <sub>2</sub> (110)-[001]	TiO <sub>2</sub> (110)-[001]
TiO <sub>2</sub> (110) 					
Pt interface facet	Pt(111)	Pt(111)	Pt(001)	Pt(001)	Pt(110)
Pt direction    x	Pt [1 $\bar{1}$ 0]	Pt [ $\bar{1}$ 1 $\bar{2}$ ]	Pt [1 $\bar{1}$ 0]	Pt [0 $\bar{1}$ 0]	Pt [1 $\bar{1}$ 0]
$n_{\text{TiO}_2}:n_{\text{Pt}}$	1:1	8:5	1:1	4:3	1:1
$\epsilon_x$	-6.4 %	1.7 %	-6.4 %	-0.3 %	-6.4 %
Pt direction    y	Pt [11 $\bar{2}$ ]	Pt [1 $\bar{1}$ 0]	Pt [110]	Pt [100]	Pt [001]
$n_{\text{TiO}_2}:n_{\text{Pt}}$	3:2	5:2	2:5	2:3	2:3
$\epsilon_y$	+10.0 %	6.5 %	+6.4 %	-10.2 %	-10.2 %
Total overlap	55	19	61	37	81

The strain values reported here are based on the assumption that the TiO<sub>2</sub> substrate is completely rigid, and only the lattice of the Pt or Au (see Table 7 and Table 8) overlayer is allowed to relax in order to match the TiO<sub>2</sub> structure. The strain values obtained from our calculations are physically reasonable, since similar relaxations in the Pt lattice (up to ~10 %) were observed via TEM for small Pt NPs supported on Al<sub>2</sub>O<sub>3</sub> interfaces.<sup>146</sup> Interestingly, no deformation of the Al<sub>2</sub>O<sub>3</sub> support underneath the NPs was detected via TEM.<sup>146</sup> However, if a non-rigid TiO<sub>2</sub> interface is considered, significantly smaller strain values would be obtained for Pt. In fact, the deformation of the TiO<sub>2</sub> lattice in contact with Pt NPs has been suggested based on TEM data.<sup>10</sup>

Table 8: Epitaxial relation between different strained interfacial Au facets and the TiO<sub>2</sub>(110) surface, including the corresponding lattice mismatch.

Au NP type & orientation			
	TiO <sub>2</sub> (110)-[001]	TiO <sub>2</sub> (110)-[001]	TiO <sub>2</sub> (110)-[001]
TiO <sub>2</sub> (110) y [1̄10] x [001]			
Au interface facet	Au (111)	Au (001)	Au (221)
Au direction    x	Au[1̄10]	Au[1̄10]	Au[1̄10]
n <sub>TiO<sub>2</sub></sub> :n <sub>Au</sub>	1:1	1:1	1:1
ε <sub>x</sub>	-2.3 %	-2.3 %	-2.3 %
Au direction    y	Au [112̄]	Au [110]	Au [114̄]
n <sub>TiO<sub>2</sub></sub> :n <sub>Au</sub>	2:3	1:2	No match
ε <sub>y</sub>	13.5 %	-12.3 %	--
Total overlap	55	163	55

In any case, assuming a flexible or rigid TiO<sub>2</sub> support would only affect the absolute value of the strain coefficients obtained, but not the rest of the general trends discussed above.

Previous calculations by Muller et al.<sup>147</sup> predicted that interfacial strain could affect the area of specific facets in small NPs. Furthermore, in some cases, a slight change in the NP size was found to lead to discontinuities in the surface energy and unusual relative contributions of different facets. Such effect might explain the shape variations observed within a given NP category for NPs with nearly identical volume (or total number of atoms), Fig. 48. For small supported NPs, interfacial stress likely extends

throughout the NP, resulting in a change of the energy of surface facets having a component parallel to the direction of the stress vector. Accordingly, top NP facets parallel to the interface should be the most affected by the former effect. Similar tensile stresses (~6 %) in the TiO<sub>2</sub>(110)-[001] direction were obtained for the four NP shape categories resolved here via STM. Since the lattice of the free Pt surface is naturally under tensile stress,<sup>148</sup> the addition of interface-induced tensile stress is expected to increase the surface energy, and therefore, to decrease the area of the top facets parallel to the NP/support interface. This might explain why NPs of type A and C with top (111) facets are characterized by  $A_{100}/A_{111}$  ratios higher than the bulk-like Wulff structures, while type B NPs with (100) top and interfacial facets show smaller relative  $A_{100}/A_{111}$  ratios. In Fig. 48, the  $A_{100}/A_{111}$  ratios of TA NPs are centered around 0.3 ( $\gamma_{100}/\gamma_{111}=1.15$ ) and 0.5 ( $\gamma_{100}/\gamma_{111}=1.05$ ). Based on ab-initio calculations, Iddir et al.<sup>136</sup> explained variations in this ratio for Pt NPs supported on SrTiO<sub>3</sub> due to a {100} hexagonal surface reconstruction. Such surface reconstruction is likely sensitive to environmental fluctuations (e.g. presence of adsorbates or encapsulation effects of the NPs by the underlying substrate), and reconstructed and non-reconstructed NP surfaces could co-exist on one sample, resulting in a category of shapes (TA) with two different  $A_{100}/A_{111}$  ratios. The one with a higher fraction of {100} facets might correspond to the reconstructed (or support-encapsulated) surface with the minimum surface energy<sup>136</sup>.

The Pt/TiO<sub>2</sub> system is known to display SMSI effects<sup>93</sup> and therefore, Pt NPs might be subjected to TiO<sub>x</sub><sup>123, 149, 150</sup> encapsulation or surface alloying effects<sup>133</sup> (e.g.

Pt<sub>3</sub>Ti) after annealing at high temperature. However, we do not believe that the shapes reported here for Pt NPs can be attributed to SMSI, since similar NP shapes were also observed for our micellar Au NPs on TiO<sub>2</sub>(110) (Fig. 45), even though the latter system does not show SMSI.

The energy barrier between different crystalline configurations is expected to increase with increasing NP size, and therefore, smaller NPs are expected to adopt their equilibrium shapes at lower temperature.<sup>151</sup> Within the size and temperature ranges of this study (2 nm < NPs < 6nm, ~1000°C), the energy barrier appears to be small enough to let the NPs stabilize in only a few geometrical configurations, but not small enough to allow them to adopt the shape with the interfacial facet that has the minimum interfacial energy.

## 5.4 Conclusions

In conclusion, we have shown that geometrically well-defined faceted and epitaxial Pt and Au NPs can be obtained on TiO<sub>2</sub>(110) via inverse micelle encapsulation methods followed by annealing in vacuum above 1000°C. Despite the existence of significant anisotropic interfacial strain, our NPs were found to be symmetric and of single crystal nature. The micellar NPs adopt shapes that have not been previously observed for analogous but physical vapor deposited NPs. The epitaxial orientation of the interfacial facets observed and rare occurrence of rotated NPs were explained based on calculations of lattice mismatch. Moreover, the surface area and related surface energy ratios ( $A_{100}/A_{111}$  and  $\gamma_{100}/\gamma_{111}$ ) in the micellar NPs was found to be different from conventional bulk-like Wulff structures. Some of our Pt NPs displayed higher Miller

index surfaces such as {110}, and tilted Au NPs with {221} interfacial facets were observed.

Our study demonstrates that the shape of micellar NPs and their interfacial epitaxy can be controlled by tuning the NPs size. Such control over the size, shape, homogeneous dispersion on the support and interfacial epitaxy represents a significant advance in our ability to engineer active elements at the nanoscale such as tunable nanoelectronic devices and nanocatalysts. Furthermore, the thermodynamically stable morphology of our NPs guarantees the stability of bottom-up-built nanodevices under extreme operation conditions, including elevated temperatures, and provides an excellent platform for theoretical calculations based on equilibrium NP shapes.

## CHAPTER 6: NANOPARTICLE-SUPPORT INTERACTIONS

### 6.1 Introduction

The unusual structural, electronic, magnetic, and chemical properties of metallic nanostructures have been proven useful for numerous applications in technologically important areas such as catalysis, molecular electronics, nanomedicine, energy conversion and plasmonics<sup>12-17</sup>. Nevertheless, in order to take advantage of these new material systems in an industrial setting, a thorough understanding of how those properties are affected by their environment (support and surrounding adsorbates) as well as operation condition (e.g. elevated temperature) is needed.

Strong metal-support interactions<sup>88, 123</sup> are believed to be a key factor determining the reactivity of heterogeneous catalysts such as Pt NPs supported on TiO<sub>2</sub>. The present study provides insight into the interaction of micellar metal NPs with oxide supports. There are numerous studies showing how different supports could affect the shape, electronic structure, catalytic properties and coarsening behavior of NPs.<sup>1-3, 29, 56, 152</sup> However, less is known about the changes brought about by the presence of the NPs on the support itself, including its reconstruction and patterning. Here we demonstrate that micellar Au and Pt NPs can serve as nucleation centers for the growth of [001]-oriented TiO<sub>2</sub> nanostripes on the surface of TiO<sub>2</sub>(110) upon annealing in UHV at and above 1000°C. Such surfaces are expected to display a modified reactivity, since [001] step edges have been recently shown to give rise to higher photocatalytic activity for certain photodegradation reactions as compared to  $[1\bar{1}1]$  steps edges<sup>153</sup>. Therefore, surface engineering methods that provide the ability to tune the density of certain step

edges are desirable. The realization of this idea in an easily scalable manner is presented here.

## 6.2 Experimental

Size-selected Pt and Au NPs were prepared by a reverse micelle encapsulation method<sup>2, 28, 29, 39, 79</sup> using two commercial diblock copolymers, polystyrene-*block*-poly(2-vinylpyridine) [P1: PS(27700)-PVP(4300) and P2: PS(81000)-P2VP(14200)]. Metal salts, H<sub>2</sub>AuCl<sub>4</sub>·3H<sub>2</sub>O and H<sub>2</sub>PtCl<sub>6</sub>·6H<sub>2</sub>O, were added to separate polymeric solutions previously obtained by dissolving 50 mg of the PS-P2VP in 10 ml of toluene. Using this synthesis method, the NP size as well as their interparticle distance can be controlled independently.<sup>2, 28, 29, 39, 79</sup> The length of the diblock-copolymer core (P2VP) and the metal-salt/P2VP concentration ratio determines the NP size, while the interparticle distance can be tuned by modifying the length of the PS tail. In the present case, P2 is expected to result in NPs spaced by larger distances as compared to P1, as seen in Fig. 51(a) and Fig. 51(b). We have prepared three different samples: samples S1 and S2 contain Pt NPs and were synthesized using polymers P1 and P2, respectively, while S3 includes Au NPs encapsulated by P2. The metal loadings (metal/P2VP ratio) used were 0.6 for S1 and 0.3 for S2 and S3. A self-assembled monolayer of NPs on the TiO<sub>2</sub>(110) substrate was obtained by dip-coating the single crystal into the Au or Pt polymeric solutions at a speed of 200 μm/s.

Upon *ex situ* NP deposition, the removal of the encapsulating polymer was carried out in UHV by an oxygen-plasma treatment (O<sub>2</sub> pressure = 4×10<sup>-5</sup> mbar, 90-120 min). No residual C signal was detected by XPS after this treatment,<sup>2, 28, 29, 39, 79</sup> but the NP



surface becomes oxidized. Subsequently, the micellar samples were isochronally annealed in UHV in 100°C intervals from 300°C to 800°C for 20 min, a treatment which stabilizes the NPs against coarsening, followed by isochronal annealing at/above 900°C for 10 min, and in 10°C increments from 1000°C to 1060°C. STM images were measured at RT after several of the annealing treatments. The tunneling voltage was set to 1.2 V and the tunneling current to 0.1 nA.

### 6.3 Results and discussion

Fig. 51 displays STM images of TiO<sub>2</sub>-supported micellar NPs in (a, c-f) S1 and (b) S2 acquired after annealing in UHV above 1000°C. The average size of the Pt NPs in S1 is ~3.0 nm and their interparticle distance ~ 30 nm, and both parameters remained nearly constant after annealing in UHV from 1000°C to 1060°C, Fig. 51(a). Further details on the enhanced stability of the Pt/TiO<sub>2</sub>(110) system are reported in Ref. 28. The superior thermal stability of micellar Pt NPs as compared to PVD-grown clusters might be assigned to the following factors: (i) coarsening phenomena based on diffusion-coalescence processes might be minimized for the micelle-based samples due to their large and homogeneous interparticle distances and relatively low NP density on the support; (ii) the narrower initial NP size distribution in the micellar samples might inhibit Ostwald-ripening pathways in which large clusters grow at the expense of smaller NPs; (iii) the micellar NPs are exposed to atomic oxygen at RT prior to the thermal treatment, which leads to NP oxidation. Even though the PtO<sub>x</sub> species formed are expected to be decomposed at the high annealing temperatures employed here<sup>29, 80</sup>, the former

treatment might contribute to strengthening the initial binding between the Pt NPs and the TiO<sub>2</sub> support, leading to their subsequent stabilization.

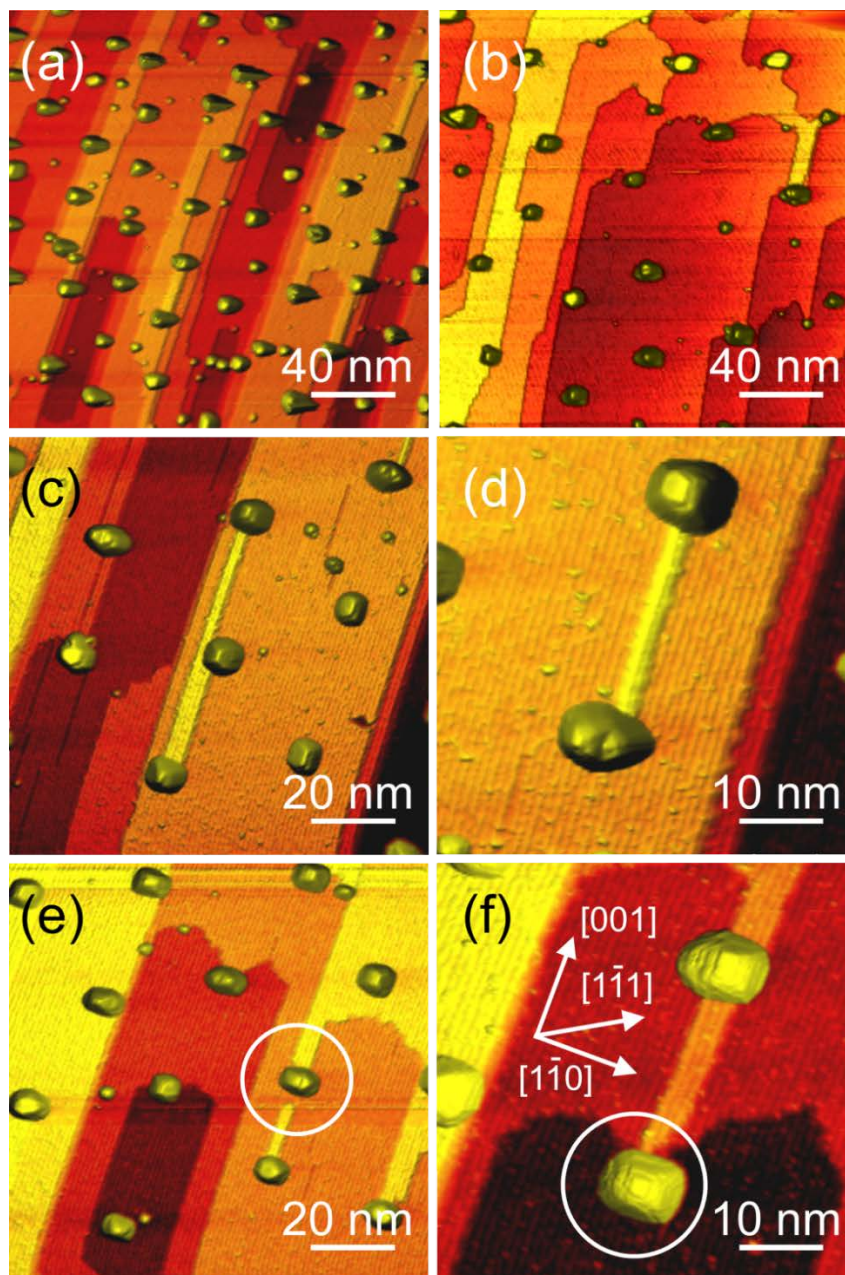


Fig. 51: RT STM images of micellar NPs in S1 (a,c-f) and S2 (b), deposited on TiO<sub>2</sub> (110) and acquired after polymer removal by an *in situ* O<sub>2</sub>-plasma treatment and subsequent isochronal annealing in UHV at 1010 °C (a,b), 1020 °C (c,d), 1060 °C (e,f).

Although our Pt NPs are mostly oxidized after the initial O<sub>2</sub>-plasma treatment, XPS measurements have shown their reduction after annealing in UHV at temperatures above 450°C.<sup>29, 80</sup> Nevertheless, due to the low NP coverage in our samples and the limitations in the sensitivity of XPS, we cannot rule out the presence of PtO<sub>x</sub> at the NP/support interface. Such species might influence the coarsening behavior of the micellar NPs.

It is also worth mentioning that the present high temperature annealing treatments result in surface/bulk melting of our NPs, as evidenced by the faceted shapes and epitaxial NP/TiO<sub>2</sub> relationship adopted by the NPs upon cooling, Fig. 51f and Ref. 39.

Since the polymer used in the synthesis of S2 had longer head and tail lengths, the resulting Pt NPs were characterized by larger average sizes (~3.7 nm) and larger interparticle distances (~40 nm), Fig. 51(b).

Interestingly, the STM images in Fig. 51 and Fig. 53 reveal the formation of TiO<sub>2</sub> nanostripes on the Pt NP-coated TiO<sub>2</sub>(110) surface upon annealing. This is in striking contrast with the behavior observed on NP-free TiO<sub>2</sub> surfaces<sup>28, 72</sup> or those decorated by PVD NPs after annealing at RT<sup>94</sup>, moderate temperatures (400 °C-730 °C)<sup>56, 78</sup> or similar conditions to our experiment<sup>41</sup>.

Our TiO<sub>2</sub> nanostripes were found to be attached to the NPs and have a preferential growth direction along the [001] orientation of the TiO<sub>2</sub>(110) substrate. The width of these nanostripes was found to be similar to the NP diameter (3-5 nm) and their length to be as large as 80 nm. Interestingly, at the highest annealing temperatures employed (1040°C and 1060°C), the TiO<sub>2</sub> nanostripes start to become detached from

the Pt NPs [see white circles in Fig. 51(e) and Fig. 51(f)]. Further annealing lead to the growth of wider TiO<sub>2</sub> terraces in detriment of the narrow TiO<sub>2</sub> nanostripes.

Such narrow terraces or nanostripes are not observed when the NP-free substrate is subjected to the same thermal treatment, Fig. 52(b).

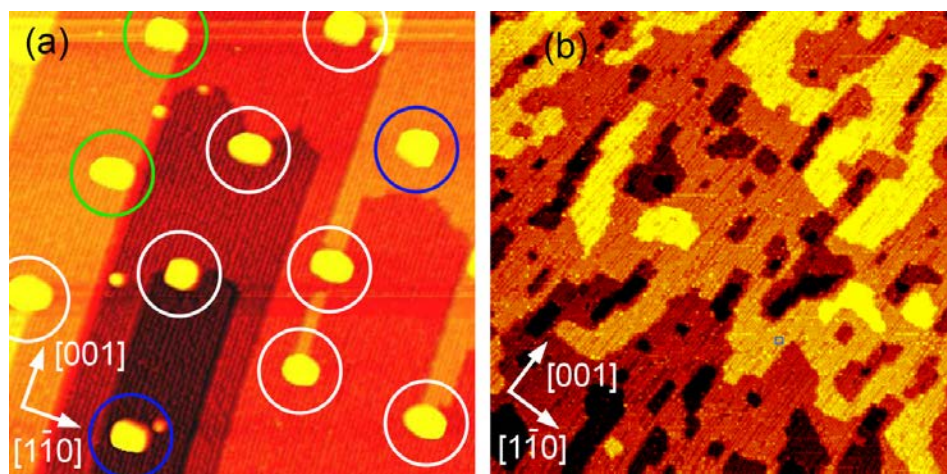


Fig. 52: (100 x 100 nm) *In-situ* STM images obtained on (a) micellar Pt NPs deposited on TiO<sub>2</sub>(110) and (b) the pristine TiO<sub>2</sub>(110) substrate after annealing at 1060°C and 1030°C for 10 min, respectively. The TiO<sub>2</sub> substrate appears atomically resolved. The circles in (a) highlight the presence of NPs at different substrate sites: (1) NPs on the center of TiO<sub>2</sub> terraces [blue circles]; (2) NPs on steps parallel to the [001] direction [green circles]; (3) NPs at the end of TiO<sub>2</sub> nanostripes, at [1  $\bar{1}$  0] steps [white circles].

The average width of the TiO<sub>2</sub> terraces on the Pt-decorated samples was ~16 nm at 1010°C, ~23 nm at 1060°C (10 min), and increased to ~47 nm at 1060°C (20 min). For comparison, at 1030°C, a larger average terrace width of ~ 80 nm was measured for the Pt-free TiO<sub>2</sub>(110) support.

In addition, the ratio of the length of [001] to [1  $\bar{1}$  0] steps was much higher for the Pt-decorated surface (~11) as compared to pristine TiO<sub>2</sub> (~2.4), Fig. 52. From the analysis of multiple 200 x 200 nm STM images of our Pt/TiO<sub>2</sub> system, a strong decrease

in the total length of the steps parallel to [001] was observed with increasing annealing temperature. Measured lengths ranged from ~2430 nm at 1010°C to ~1730 nm and ~853 nm for the 10 min and 20 min annealing treatments at 1060°C, respectively. A similar analysis revealed significantly shorter lengths for the steps parallel to  $[1\bar{1}0]$ , with ~227 nm at 1010°C, ~130 nm at 1060°C (10 min), and ~236 nm at 1060°C (20 min).

Surprisingly, the TiO<sub>2</sub> stripes and steps were found to be rather straight, and a large population of the TiO<sub>2</sub> stripes was found to have one NP at the end. Statistics of the location of the Pt NPs in our samples after annealing (averaging 340-690 NPs at each temperature) revealed that 45 % of the NPs are located at the end of stripes at steps parallel to  $[1\bar{1}0]$  at 1000°C [white circles in Fig. 52(a)], while at 1060°C (20 min) they tend to be located on the middle of terraces (40 % versus 25% at this location at 1000°C). Since the initial NP arrangement was preserved, this result is not attributed to the migration of Pt NPs to those step sites, but to the mobility of Ti-O molecules or Ti and O atoms in the support. Berko et al.<sup>154</sup> reported that Pt atoms activate the separation of Ti<sub>x</sub>O<sub>y</sub> compounds, and a preferential atomic diffusion along [001] was described. Besides, our data reveal that the bonding between Pt atoms and the TiO<sub>2</sub> substrate is strongest at step sites<sup>154</sup>. It is noteworthy that sample annealing at our highest temperature (1060°C, 20 min) resulted in a rupture of the connection between many of our NPs and the TiO<sub>2</sub> nanostripes, leading to the increase in the TiO<sub>2</sub> terrace width.

The Pt/TiO<sub>2</sub> system is characterized by strong metal-support interactions (SMSI)<sup>123, 133, 149, 150</sup>. This includes support-induced changes in the electronic properties of the

Pt NPs and Pt encapsulation by ultrathin  $\text{TiO}_x$  layers. Therefore, the formation of the  $\text{TiO}_2$  nanostripes observed here for the Pt/ $\text{TiO}_2$  system could be intuitively attributed to some degree of SMSI effect. However, this possibility is disregarded, since identical trends were observed for Au/ $\text{TiO}_2$ , a system which does not show the SMSI effects, Fig. 53(c,d).

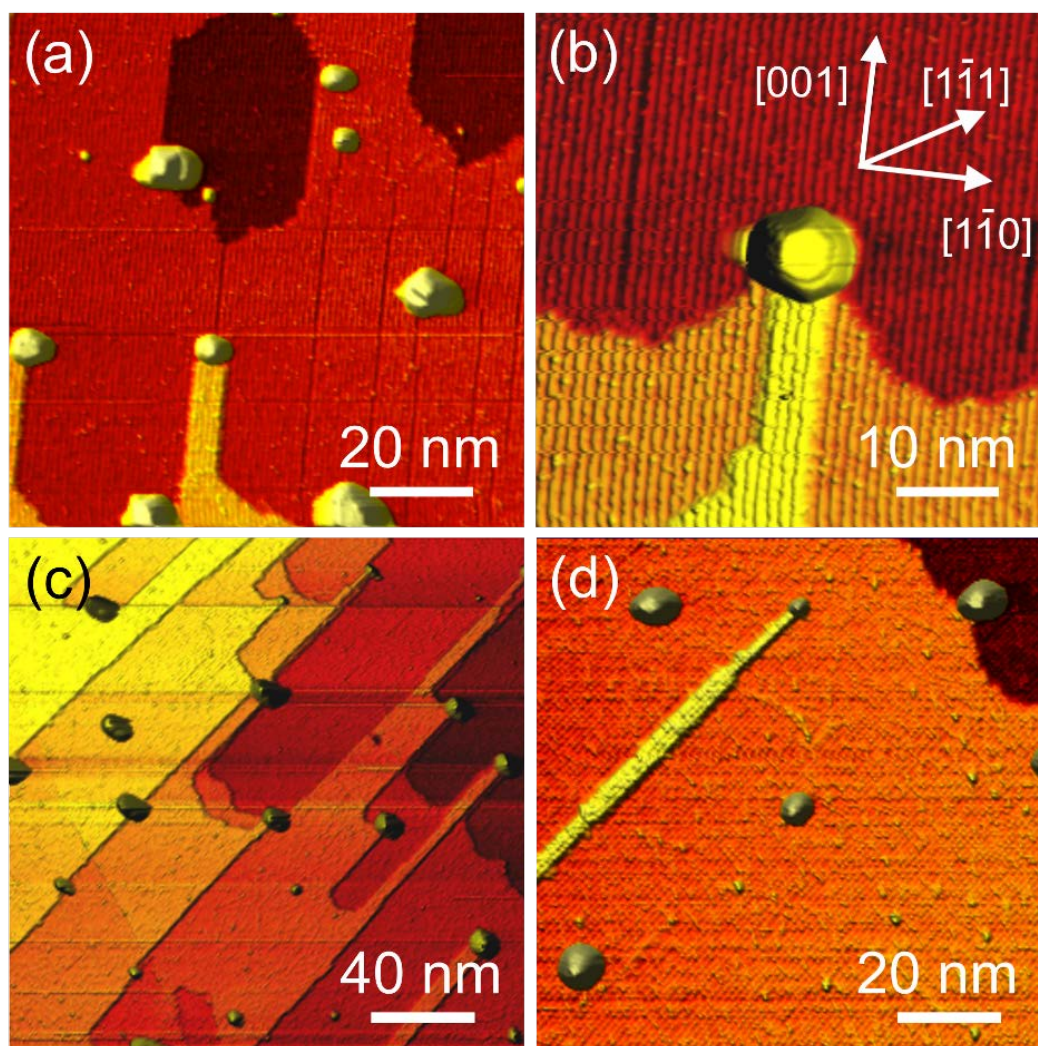


Fig. 53: RT STM images of Pt NPs in S2 (a,b), and Au NPs in S3 (c,d) on  $\text{TiO}_2(110)$  acquired after annealing in UHV at  $1000^\circ\text{C}$  for 10 min.

The main difference between our micellar Au and Pt NPs on TiO<sub>2</sub>(110) is the fact that due to the lower melting temperature of Au, the initial hexagonal NP arrangement<sup>28, 39</sup> is lost for the Au NPs after annealing at elevated temperatures (>1000°C, Fig. 53(c,d)), and therefore, the spacing between the TiO<sub>2</sub> nanostripes formed is not uniform, as is the case for Pt/TiO<sub>2</sub>.

Different mechanisms have been reported in the past as responsible for the reconstruction of NP-decorated oxide surfaces. For example, by annealing in oxygen environments, TiO<sub>2</sub> islands were found to grow around PVD Pt and Pd NPs on TiO<sub>2</sub>(110).<sup>155, 156</sup> In the former examples, oxygen was found to spill-over from the NPs to the support, resulting in the segregation of Ti interstitials from the bulk to the surface of the TiO<sub>2</sub> crystal and the formation of TiO<sub>x</sub> islands around the NPs. Nevertheless, nanostripes such as those shown in Fig. 51 and Fig. 53 were never obtained, and the former effects were observed upon annealing at lower temperatures (< 500°C), and in the presence of oxygen. In fact, even in oxygen environments, higher annealing temperatures (>550°C), such as those employed in our experiments, were reported to inhibit this effect.<sup>157</sup> Vapor-liquid-solid (VLS) growth processes<sup>158, 159</sup> mediated by the metal NPs can also not be held responsible for the growth of the TiO<sub>2</sub> nanostripes observed here, since such growth requires the presence of titanium vapor, which was not available in our experiments. On the other hand, preferential diffusion of TiO<sub>x</sub> species activated by the metal NPs<sup>160</sup> cannot explain the formation of our nanostripes, since such phenomenon should have led to the formation of stripes on both sides of the NPs, which is not observed here.

Before discussing the actual growth mechanism of our nanostripes we would like to point out the distinct properties of our micellar NPs as compared to more conventionally synthesized NPs. While mobile PVD-grown NPs are known to preferentially decorate at vacancies and TiO<sub>2</sub> step edges,<sup>41, 56, 78, 94</sup> the same does not apply to the micellar NPs. This is due to the fact that the micellar NPs are surrounded by polymeric ligands upon initial deposition on the TiO<sub>2</sub> surface, and that the TiO<sub>2</sub> surface is roughened during the *ex situ* (air) NP deposition.<sup>39</sup> Nevertheless, as can be seen in Fig. 51 and Fig. 53 and Ref. 28, a large fraction of the micellar NPs were located at step edges after high temperature annealing treatments. Since we have shown that the micellar Pt NPs are resistant against diffusion even after extreme thermal treatments,<sup>28, 39</sup> and since their hexagonal arrangement is still preserved [see Fig. 51(a,b)], it can be concluded that rather than the NPs moving toward the step edges of TiO<sub>2</sub>, the step edges moved toward the NPs. To understand this phenomenon, the diffusion of Ti and O species in TiO<sub>2</sub> and the effect of the bulk and surface stoichiometry of our single crystal oxide support should be considered. It has been shown that the bulk reduction state of TiO<sub>2</sub> plays an important role in the resulting surface reconstruction.<sup>161</sup> After numerous cycles of Ar<sup>+</sup> sputtering and annealing (900-1000°C) in vacuum, the degree of reduction of our TiO<sub>2</sub> single crystal was very high, as evidenced by its dark blue color and (1×2) surface reconstruction before NP deposition.<sup>72, 157, 161</sup> The subsequent dip-coating of the micellar NPs in air followed by the *in situ* O<sub>2</sub>-plasma treatment (polymer removal) results in the oxidation of the TiO<sub>2</sub> surface. Nevertheless, the succeeding annealing treatments in UHV at high temperature (>900°C) are expected to lead to the desorption of surface oxygen, while Ti cations



(Ti<sup>3+</sup>) diffuse inward from the surface to the bulk of the crystal.<sup>157, 161, 162</sup> At this time, significant changes in the morphology of our TiO<sub>2</sub> surface were found to occur, in particular, the formation of TiO<sub>2</sub> nanostripes.

Two key aspects of our experimental observation should be considered in order to understand the NP-mediated growth mechanism of the TiO<sub>2</sub> nanostripes. First, in most cases the nanostripes are attached to only one side of the NPs, while conventional TiO<sub>2</sub> growth/reconstruction mechanisms such as those based in spillover effects result in islands surrounding the NPs<sup>157, 163</sup>. If nanostripes were to be obtained from such spillover processes, they should have been observed on both sides of a given NP, which is not the present case. Second, if the TiO<sub>2</sub> nanostripe growth would result from the diffusion of Ti adatoms on the TiO<sub>2</sub>(110) surface, the extremely large aspect ratio of the nanostripes observed here would require a very large diffusion anisotropy constant. As mentioned before, the width of our nanostripes follows very closely the diameter of the NPs, their length reaches several tens of nm in the [001] direction, but there is almost no nanostripe growth along [1 $\bar{1}$ 0].

Due to tip-convolution effects inherent to all scanning probe microscopy techniques, an exact evaluation of the NPs' lateral dimensions is not feasible. This is especially relevant to the analysis of small NPs with 3D shapes, as some of the ones presented here<sup>39</sup>. Therefore, a quantitative claim regarding the correlation between the diameter of our NPs and the width of the stabilized TiO<sub>2</sub> nanostripes cannot be made. However, the majority of our images suggest that the nanostripe width is either equal to or smaller than the diameter of the NPs attached to them.

The former trends would suggest a one-dimensional diffusion phenomenon along [001]. Nevertheless, previous *ab initio* calculations<sup>164</sup> and also experimental results<sup>165</sup> do not support this hypothesis. In fact, due to the existence of different diffusion mechanisms, the barrier for Ti diffusion was found to be lower along  $[1\bar{1}0]$  than in the [001] direction<sup>164</sup>. In addition, it was shown that interstitial Ti atoms are more energetically favorable than adatoms on the surface,<sup>166</sup> and that the energy barrier to go subsurface should be easily overcome during our high temperature annealing treatments. Therefore, any Ti adatoms which might be present on our surface would not have a tendency to diffuse on the surface, but would rather go subsurface instead.

The above arguments justify our conclusion that neither spill-over effects nor preferential diffusion of Ti adatoms on the TiO<sub>2</sub> surface are responsible for the growth of nanostripes observed here. Instead, we propose a mechanism based on diffusion/mass transfer perpendicular to the surface, also involving the stabilization of certain TiO<sub>2</sub> step edges by the micellar NPs. Previous high temperature (~730°C) STM snapshots of pristine TiO<sub>2</sub>(110) had shown the loss of material upon annealing in vacuum, evidenced by the observation of receding step edges.<sup>157, 161</sup>

In the previous studies, the gradual disappearance of the top-most TiO<sub>2</sub> terraces was assigned to the desorption of oxygen to vacuum and the migration of the titanium that is left behind into the bulk.<sup>157, 161</sup> Interestingly, this gradual disappearance of TiO<sub>2</sub> rows starts at  $[1\bar{1}0]$  step edges and follows a chain reaction that proceeds along TiO<sub>2</sub> rows in the [001] direction<sup>157</sup>. This phenomenon, illustrated in Fig. 54, is the most likely mechanism behind the nanostripe formation observed in our study.

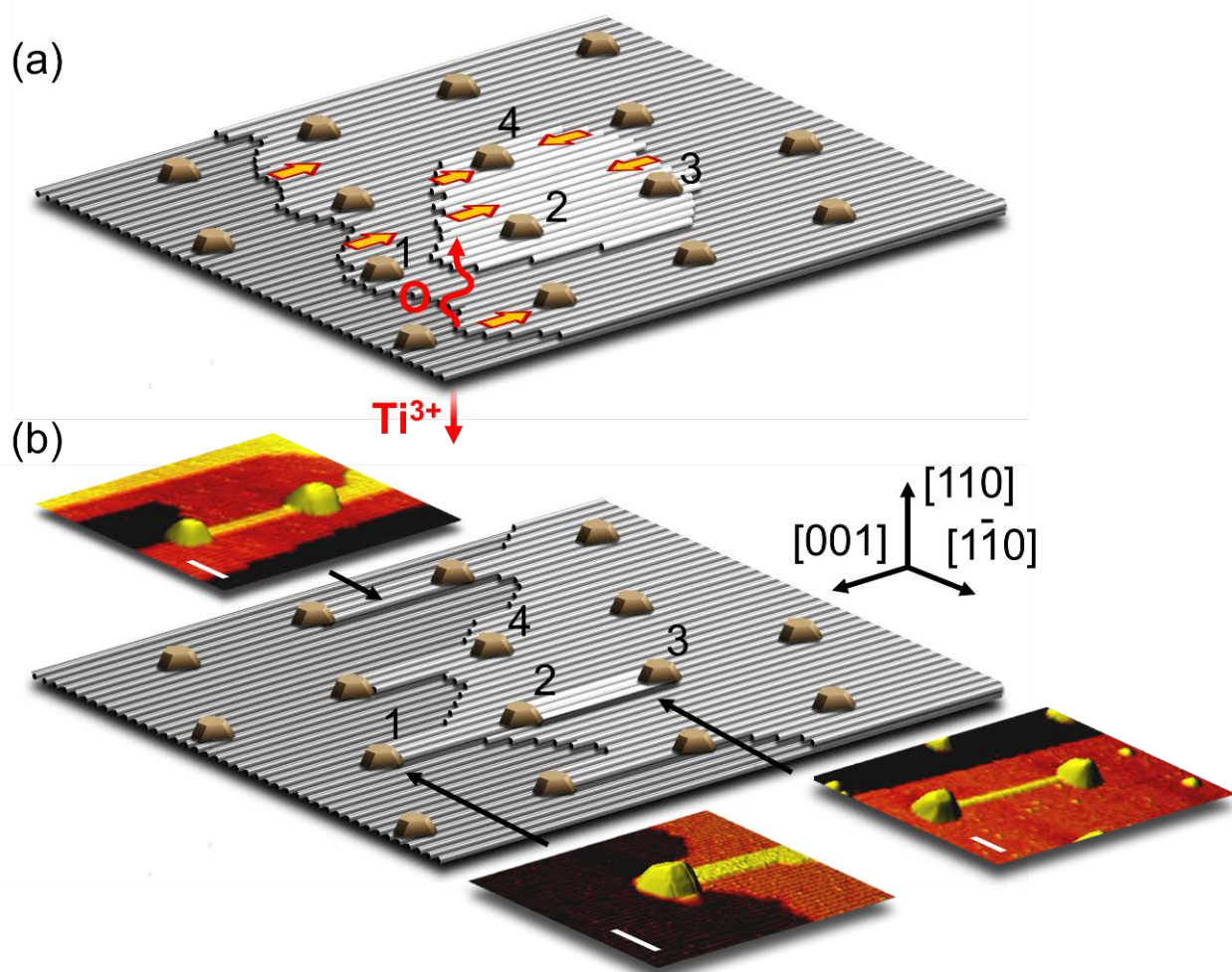


Fig. 54: Schematics showing the formation of nanostripes attached to micellar NPs. Upon sample annealing above 1000°C in UHV, oxygen desorbs from the  $\text{TiO}_2(110)$  surface to vacuum and  $\text{Ti}^{3+}$  goes into the bulk of the crystal.  $\text{TiO}_2$  rows along the  $[001]$  direction shrink in length and in some cases disappear. However, the stabilization of  $[1\bar{1}0]$   $\text{TiO}_2$  step edges by micellar NPs prevents the disruption of the rows attached to the NPs, resulting in the formation of nanostripes. The insets in (b) correspond to STM images representative of this process. The white scale bars in the STM images correspond to 10 nm.

Micellar Pt or Au NPs stabilize low coordinated atoms at  $\text{TiO}_2(110)$ - $[1\bar{1}0]$  step edges and therefore, prevent the disintegration of the  $\text{TiO}_2$  structure that is in contact with the NPs along  $[1\bar{1}0]$  steps. While the majority of the top-most  $\text{TiO}_2(110)$ - $[1\bar{1}0]$  step

edges retreat [see arrows in Fig. 54(a)], those attached to NPs remain stable due to the passivation of the oxygen desorption sites. The remaining stable TiO<sub>2</sub> rows give rise to TiO<sub>2</sub> nanostripes with a width similar to the diameter of the NPs.

Interestingly, this is also in agreement with the observation that most of the nanostripes are attached just to one side of the NPs, in contrast to spillover mechanisms that should have resulted in growth on both sides. A few different nanostripe formation possibilities, based on the relative locations of the NPs on the TiO<sub>2</sub> surface, are highlighted in Fig. 54(b). The TiO<sub>2</sub> terrace underneath the NP labeled as 1 has no step edge on its right hand side and therefore, the desorption of oxygen only happens on the left side through the  $[1\bar{1}0]$  step edge. This results in the formation of a nanostripe on the right side of the NP. In some cases, a few TiO<sub>2</sub> rows are protected at both ends by NPs, as it is shown between NPs 2 and 3 in Fig. 54(b). Also, the terraces with  $[1\bar{1}0]$  step edges on both sides of a NP may disappear completely and not result in stripe formation, since both step edges would move toward the NP and vanish entirely, as NP4 in Fig. 54(b). This mechanism could also explain the large aspect ratio of the nanostripes. In this scenario, the length of the nanostripes is not limited by diffusion anisotropy, and only depends on the configuration of the TiO<sub>2</sub> terraces in the vicinity of the NPs.

A similar *in situ* atomic oxygen treatment followed by high temperature heating in UHV recently conducted on small PVD-grown Pt NPs (~1.3 nm) did not result in the nanostripe formation demonstrated here.<sup>41</sup> A possible explanation might be size-dependent cluster mobility. The small PVD clusters may be partially stabilized by step edges, reducing their mobility along certain substrate orientations, while at the high

annealing temperatures required for the TiO<sub>2</sub> reconstruction and nanostripe formation (>900°C), PVD cluster mobility along the step edges might still occur. This would limit the step edge pinning needed for the formation of nanostripes. For the larger (~3 nm) micellar particles, the particle mobility is expected to be reduced, enabling step edge pinning at the high temperatures used here. This interpretation is supported by the fact that the nanoparticle diffusion coefficient is inversely proportional to its radius ( $D \sim 1/r^4$ ), making the larger micellar particles significantly less mobile.<sup>41, 56</sup> Additionally, intrinsic differences in the shape of the micellar<sup>39</sup> (mainly 3D-like) and PVD NPs (mainly 2D-like) after our *in situ* treatments might also influence their ability to stabilize certain steps edges. Since our preliminary data on PVD-grown NPs targeted smaller NP sizes as compared the typical average micellar NP size investigated here, it cannot be ruled out that analogously pre-treated but larger PVD NPs might also produce similar nanostripe patterns.

#### 6.4 Conclusions

TiO<sub>2</sub> step edges are known to stabilize metal NPs. Here we have shown that the opposite trend also occurs, namely, immobile NPs can stabilize step edges. The enhanced thermal stability of micellar NPs against coarsening and diffusion have allowed us to observe the changes in the underlying support surface around the micellar NPs. In contrast to metal surfaces in which the surface reconfiguration/reconstruction occurs mainly through surface diffusion of adatoms<sup>167</sup>, the present example illustrates the diffusion of Ti cations perpendicular to the surface into the bulk of TiO<sub>2</sub>(110) upon oxygen desorption at elevated annealing temperatures. The former effect is responsible

for the drastic morphological changes observed on our  $\text{TiO}_2(110)$  surface, in particular, for the formation of  $\text{TiO}_2$  nanostripes along [001] stabilized by the micellar NPs. Our findings open the possibility of using metallic micellar NPs to pattern oxide surfaces, generating uniform arrays of oxide nanostripes with tunable width (related to NP diameter), orientation, and inter-stripe distance (related to interparticle distance). Finally, it should be noted that our  $\text{TiO}_2$  nanostripes are highly reduced, since they display a  $(1\times 2)$  reconstruction typical of reduced  $\text{TiO}_2$  surfaces. Since oxygen desorption occurs at the  $\text{TiO}_2$  surface, a lower degree of reduction is expected for the bulk of the  $\text{TiO}_2$  substrate. Although a quantification of the sub-surface conductivity cannot be carried out based on the experimental tools at hand, a higher electrical conductivity is expected for the  $\text{TiO}_2$  layers closer to the surface as well as for the nanostripes<sup>168</sup>. Since our synthesis method can lead to NPs interconnected by reduced  $\text{TiO}_2$  nanostripes [Fig. 1(c,d)], they might hold promise as self-organized NP contacts on higher bandgap  $\text{TiO}_2$  substrates.

## CHAPTER 7: THERMODYNAMIC PROPERTIES OF $\gamma$ - $\text{Al}_2\text{O}_3$ SUPPORTED Pt NANOPARTICLES: SIZE, SHAPE, SUPPORT, AND ADSORBATE EFFECTS

### 7.1 Introduction

Metal NPs display anomalous electronic and thermodynamic properties, including metal to non-metal transitions,<sup>9, 122</sup> superheating,<sup>19</sup> and negative thermal expansion<sup>20-23</sup>. For free NPs, phonon confinement effects and strong modifications of the phonon density of states as compared to bulk materials have been reported<sup>24-27, 29, 81</sup>. In addition, for most experimental conditions, there are other factors contributing to this unusual behavior (e.g., NP interaction with the support, encapsulating ligands, and/or adsorbates), but they are normally discussed in isolation. Furthermore, while it is recognized that environmental effects do contribute to the thermodynamics of small systems<sup>32</sup>, very little is known on how to sort out and control such complex interactions at the nanoscale.

Consensus exists regarding the strong influence of the NP size on the thermal properties of nanoscale materials<sup>169</sup>, but further investigations are required in order to understand specific size-dependent trends. It has been suggested that NPs within different size regimes must be treated differently. For example, non-monotonic variations in the melting point ( $T_m$ ) of small (< 200 atoms) size-selected clusters have been observed,<sup>33, 34</sup> and assigned to the interplay of electronic and geometric effects.<sup>9</sup> However, the relative contribution of such effects could not be separated. For larger NPs (> 200 atoms), monotonic size-dependent trends in  $T_m$  were observed.<sup>170</sup> For a given material system, the specific thermal behavior was found to be drastically affected

by environmental influences such as the presence of a support, an encapsulating matrix, the internal defect density within a NP, the structural and chemical nature of the NP/support interface, and the presence of ligands or surface adsorbates<sup>171-176</sup>.

Recent EXAFS experiments revealed two peculiarities in the thermal properties of certain supported metal NPs: (i) a contraction in their nearest neighbor bond lengths at elevated temperatures, and (ii) an increase in their Einstein (and, hence, Debye,  $\theta_D$ ) temperature with respect to bulk<sup>177, 178</sup>.

For some NP systems, changes in the electronic properties (e.g. discretization of the energy levels) of small NPs together with the interaction with the NP support, were held responsible for a size-dependent crossover from positive to negative thermal expansion observed with decreasing NP size,<sup>21, 22, 31</sup> or with increasing sample temperature for a given NP size.<sup>179</sup> However, most of the experimental data reported thus far were collected on NPs exposed to a certain environment, for example, in the presence of hydrogen,<sup>180</sup> and the role of such adsorbates on their thermodynamic properties is yet to be fully understood. It is well known that hydrogen lifts the contraction that the bonds of Pt NPs undergo because of low coordination either partially<sup>5, 22, 37, 181</sup> or almost totally.<sup>182</sup> On the other hand, the effective hydrogen coverage on the NP surface might vary in the course of an experimental thermal cycle. Interestingly, while Pt(111) can be saturated with hydrogen at 85 K and nearly complete H desorption has been observed in vacuum above 400 K,<sup>183</sup> Pt NPs on Al<sub>2</sub>O<sub>3</sub> have been reported to become free of H only above 550 K.<sup>181</sup> An in-depth investigation of the role of H desorption from NPs in the thermal expansion or contraction observed experimentally under constant H<sub>2</sub> flow is still lacking. This study aims to address this



issue and to help evaluate the changes in the bond lengths brought about by the adsorption of H and their contribution to the negative thermal expansion observed for small Pt NPs.

In addition, reduced melting and Debye temperatures with respect to bulk have been generally reported for free-standing as well as supported NP systems.<sup>31, 170, 184-190</sup> By contrast, an increased  $\Theta_D$  relative to the bulk has been reported for a variety of supported NP systems<sup>175-178, 191</sup> and unsupported nanocrystalline agglomerates.<sup>171, 173, 192</sup> The wide discrepancy observed for  $\Theta_D$  suggests that many factors are at play. In free clusters, enhanced surface energy and the concomitant increase in the surface stress causes a lattice contraction at the NP surface, softening of interatomic force constants, and a suppression of  $\Theta_D$  and the melting temperature.<sup>24</sup> On the other hand, the increased  $\Theta_D$  observed for certain systems has been attributed to *structural stiffening* and *inhomogeneous internal stress* correlated to the NP size, surroundings (e.g. adsorbates/surface ligands<sup>171, 173, 174</sup>, a matrix encapsulating the NPs, or a support<sup>23, 175, 176</sup>), and to the presence of structural defects and multiple grains in large NPs<sup>192</sup>.

In addition, a correlation between  $T_m$  and the NP diameter has been commonly observed, with decreasing  $T_m$  with decreasing NP size.<sup>19</sup> Since for bulk systems  $T_m$  is proportional to  $\Theta_D^2$  (Lindemann's criterion<sup>193</sup>), the Debye temperature is also expected to decrease in clusters relative to the bulk<sup>194</sup>. Nevertheless, increased  $\Theta_D$  and superheating have been observed via a variety of methods (e.g. TEM, X-ray diffraction, differential scanning calorimetry, EXAFS, etc.) for several nanoscale material systems, including supported or embedded Pt<sup>21, 22, 37, 191</sup>, Ag<sup>176</sup>, and Ge NPs<sup>175, 195, 196</sup>, as well as unsupported nanocrystalline agglomerates such as Ag<sup>192</sup>, Au<sup>192</sup>, ZnS<sup>171</sup>, and thiol-

capped CdS<sup>172</sup> and CdTe<sup>173</sup> nanocrystals. A comparison between the different references is challenging due to the distinct sample preparation and characterization conditions, and in some cases, the lack of detail on the specific structure of the systems investigated. However, some interesting trends could be extracted from the literature. Enhanced thermal stability and superheating was detected for faceted NP shapes with good crystallinity and coherent or semi-coherent (nearly epitaxial) interfaces around the embedded NPs, or when NPs were coated by a high melting-point matrix.<sup>175, 197, 198</sup> On the other hand, reduced  $T_m$  values were found for NPs randomly embedded (e.g. without epitaxial relationships) in similar matrixes. According to previous studies, internal defects within the NPs or at the NP/support interface, voids, impurities, grain boundaries, as well as low-coordinated surface atoms (for NPs not fully embedded in a support matrix) act as nucleation sites for the onset of heterogeneous melting.<sup>19</sup> Therefore, a global understanding of the thermodynamic properties of nanoscale materials requires in-depth insight into their geometrical structure, including its modifications in the presence of an environment (support and/or adsorbate).

It is evident that the understanding of thermal, structural, and electronic properties of this system is hindered by its complexity, due to the multiple competing factors that define its behavior, and a detailed atomic-scale investigation of the origin of these anomalies is yet to be undertaken.

This study focuses on the investigation of the influence of the NP geometry (size and shape) and environment (adsorbate and support) on the thermal properties of structurally well-defined, free and  $\gamma$ -Al<sub>2</sub>O<sub>3</sub>-supported Pt NPs.

For this purpose, we have taken advantage of state-of-the-art nanostructure fabrication (micelle encapsulation) and characterization methods (EXAFS, TEM, and cluster shape modeling). In particular, we investigated the relationship between thermodynamic quantities ( $\theta_D$  and thermal expansion coefficient) and geometrical properties of ligand-free, homogeneous, size- and shape-selected Pt NPs supported on  $\gamma$ -Al<sub>2</sub>O<sub>3</sub> using EXAFS.

## **7.2 Experimental and theoretical methods**

### **7.2.1 Sample preparation**

Size- and shape-selected Pt NPs were prepared by inverse micelle encapsulation methods using poly(styrene)-block-poly(2vinylpyridine) [PS-P2VP] diblock copolymers. Briefly, commercially available PS-P2VP diblock-copolymers were dissolved in toluene to form inverse micelles, with the P2VP head groups constituting the micelle core. Size-selected Pt NPs are created by dissolving H<sub>2</sub>PtCl<sub>6</sub> into the polymeric solution. Subsequently, the nanocrystalline  $\gamma$ -Al<sub>2</sub>O<sub>3</sub> support (average size ~40 nm) is added. After drying, the encapsulating ligands are eliminated by annealing in O<sub>2</sub> at 375°C for 24 hours.

Our micellar synthesis normally leads to 3D-like NP structures. Nevertheless, the NP shape can be changed from 3D to 2D by decreasing the metal loading into the initially spherical polymeric micelles. Further details on the sample preparation method and synthesis parameters can be found in Refs. 5, 28, 29, 36, 37, 81 and Table 13.

Description of synthesis parameters and size information of micellar Pt NPs supported on nanocrystalline  $\gamma$ -Al<sub>2</sub>O<sub>3</sub> are summarized in Table 13. The parameter “L” represents the metal-salt to polymer head (P2VP) ratio used in the NP synthesis.

### 7.2.2 Morphological characterization (TEM)

The NP sizes (diameter) are obtained by HAADF STEM. TEM measurements were carried out by our collaborators at the University of Pittsburgh (Prof. Judith Yang’s group in the Department of Chemical and Petroleum Engineering). The TEM samples were prepared by making an ethanol suspension of the Pt/ $\gamma$ -Al<sub>2</sub>O<sub>3</sub> powder and placing a few drops of this liquid onto an ultrathin C-coated Cu grid, and allowing the sample to dry in air. HAADF images of the Pt/ $\gamma$ -Al<sub>2</sub>O<sub>3</sub> samples were acquired under scanning mode within a JEM 2100F TEM, operated at 200 kV. The probe size of the STEM is about 0.2 nm. The Pt NP diameters were determined by measuring the full width at half maximum of the HAADF intensity profile across the individual Pt NPs. The TEM images shown here were acquired after the EXAFS measurements. Nanoparticle sintering did not take place in the course of the EXAFS measurements, since the samples were previously stabilized by a 24-h annealing treatment at the maximum temperature of the EXAFS thermal cycle (648 K).

Fig. 55a shows a representative TEM image of Pt NPs in S1. The corresponding NP diameter histogram is displayed in Fig. 55b, and average values for the rest of the samples are given in Table 13. Additional TEM images of other samples included in this study could be found in Refs. 38, and 5. All of our samples containing small NPs are characterized by narrow size distributions according to in-depth TEM analysis, while

wider size distributions were observed for some of the larger clusters. Histograms of the TEM NP diameters for other samples are shown in Ref. 38.

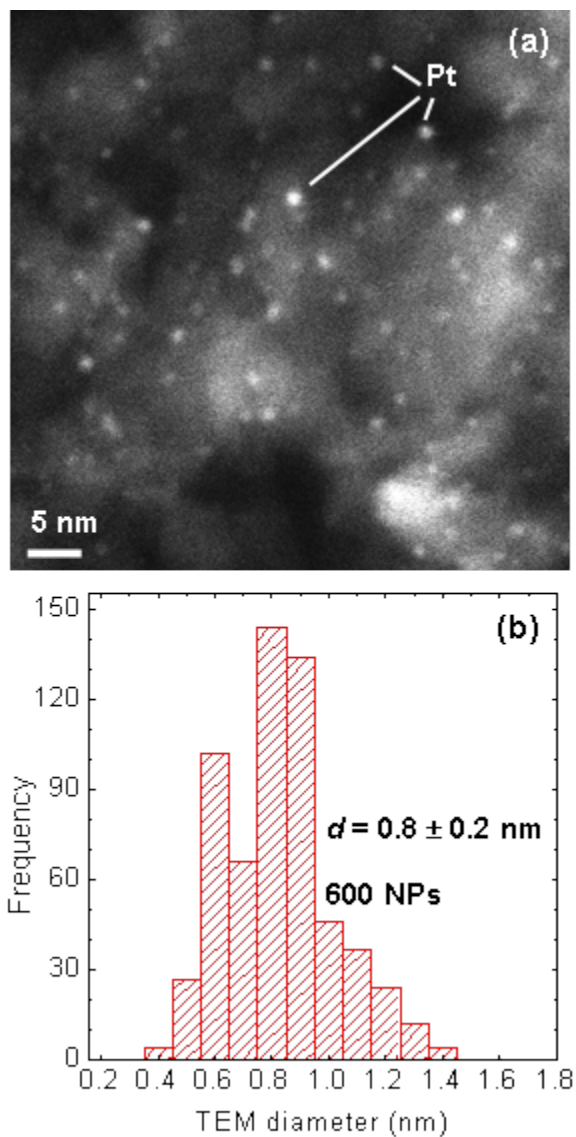


Fig. 55: (a) HAADF STEM image of micellar Pt NPs on  $\gamma$ -Al<sub>2</sub>O<sub>3</sub> (S1) obtained by L. Li, and Z. Zhang (Prof. Judith Yang's group) at the University of Pittsburgh. (b) Histogram of the NP diameter distribution.

### 7.2.3 Structural and vibrational characterization (EXAFS)

EXAFS data were acquired at beamline X18B of the NSLS at Brookhaven National Laboratory in transmission mode using the Pt-L<sub>3</sub> edge. The EXAFS samples were prepared by pressing the Pt/γ-Al<sub>2</sub>O<sub>3</sub> powders into thin pellets which were mounted in a sample cell that permitted sample heating, liquid nitrogen cooling via an external PID controller, as well as the continuous flow of gases during data acquisition and on-line mass spectrometry analysis.

A bulk Pt foil was measured simultaneously with all samples (in reference mode) for energy alignment and calibration purposes. Multiple scans (up to 6) were collected at each temperature of interest and averaged in order to improve the signal-to-noise ratio. Measurements were done at different temperatures under H<sub>2</sub> (50 % H<sub>2</sub> balanced with He for a total flow rate of 50 ml/min, samples S1-S9 in Table 13) and He (S2) atmospheres.

Data processing and analysis with the IFEFFIT package<sup>199</sup> was conducted by analyzing the first shell Pt-Pt contribution for data acquired at all temperatures concurrently, as described in Refs. 178 and 200, with the exception that the EXAFS Debye-Waller factors were found following the Correlated Debye Model (CDM)<sup>201</sup> instead of the Einstein model.

The total bond length disorder,  $\sigma$ , includes configurational, or static ( $\sigma_s$ ) and dynamic ( $\sigma_d$ ) contributions:  $\sigma^2 = \sigma_s^2 + \sigma_d^2$ . The CDM was used to extract both the dynamic and static mean-square relative bond length disorders from the analysis of temperature-dependent EXAFS data, and through that,  $\theta_D$ . In the high-temperature

approximation,  $\sigma_d^2 = \frac{k_B T}{k} \sim \frac{T}{\theta_D^2}$ , with  $k$  being the effective force constant, and  $k_B$  the Boltzmann constant<sup>202, 203</sup>. Hence, the slope of the temperature dependence of  $\sigma_d^2$  is inversely proportional to  $\theta_D^2$ .

The static disorder values ( $\sigma_s^2$ ) shown in Table 13 are considered a measure of the degree of anisotropy in the internal structure of the NPs (distribution of bond lengths), which for small clusters can be intrinsic<sup>204</sup> but are also strongly influenced by the underlying support.<sup>205</sup>

The following parameters were varied in the EXAFS analysis: the corrections to the photoelectron energy origin, the nearest neighbor bond lengths, the coordination numbers, the third cumulant of the 1NN pair distribution function, and the values of  $\theta_D$  and  $\sigma_s^2$ .<sup>200</sup>

We carefully investigated the effect of the energy origin ( $E_0$ ) on the values of the structural parameters (distances and third cumulants) extracted from the fits, since they correlate. In most of the samples the x-ray absorption near edge structure (XANES) portion of the absorption coefficient exhibits a small shift (ca. 1-1.5 eV, depending on the sample) toward lower energies with increasing temperature. The same effect was observed earlier by Sanchez et al.<sup>178</sup> To compensate the effect of this shift on the change of the phase of the EXAFS signals we compared two different fitting procedures: 1) the correction to the energy origin was varied independently for each temperature, and 2) all the data were aligned in energy before extracting the EXAFS signals, and subsequently the energy origin correction (same for all data that were

analyzed concurrently), was varied during the fitting routine. The best fit results for these two approaches were very close (within the uncertainties).

The Fourier transform parameters used during the EXAFS data analysis are as follows: k-range from 2 to 13-19 Å<sup>-1</sup> (depending on the sample and temperature), Hanning window sills ( $\Delta k$ ) for all samples 2 Å<sup>-1</sup>. In the inset of Fig. 57 (fit to EXAFS data of S2) the k-range and the r-range used in the fit were 2-19 Å<sup>-1</sup> and 1.5-5.9 Å, respectively. k<sup>2</sup>-weighting was used in all Fourier transforms.

Table 9 contains details of the fitting parameters, including the number of relevant independent data points and variables used for the analysis of EXAFS spectra acquired at different temperatures presented in our article, as well as fit quality factors.

Table 9: Number of relevant independent data points and variables in the fits of temperature-dependent EXAFS data, as well as the values of the reduced  $\chi^2$  and r-factor obtained from the fits.

<b>Sample</b>	<b>Number of data points</b>	<b>Number of variables</b>	<b>Reduced <math>\chi^2</math></b>	<b>r-factor</b>
<b>S1</b>	61.8	14	13.5	0.020
<b>S2 He</b>	49.2	12	13.7	0.009
<b>S2 H<sub>2</sub></b>	59.6	12	24.8	0.02
<b>S3</b>	50.8	12	11.5	0.009
<b>S4</b>	60.7	17	11.7	0.017
<b>S5</b>	73.6	18	4.2	0.017
<b>S6</b>	56.6	14	2.7	0.016
<b>S7</b>	65.3	17	1.6	0.014
<b>S8</b>	80.0	17	7.6	0.007
<b>S9</b>	71.8	13	40.8	0.035

Chi-square ( $\chi^2$ ) is evaluated by adding the squares of the difference between the experimental data and the theory. The reduced  $\chi^2$  parameter is obtained by dividing  $\chi^2$



by the number of unused datapoints (number of data points minus number of variables, e.g 47.8 for S1 in Table 9). The r-factor is the sum over the absolute difference between the data and theory divided by the data value at each point.

The values of the third cumulants obtained from multiple-data-set fits at different temperatures are shown in Table 10.

Table 10: The best fit values of the third cumulants (in Å<sup>3</sup>) obtained from multiple-data-set fits at different temperatures.

Sample	173-188 K	298 K	408 K	473 K	528 K	648 K
<b>S1</b>	-0.00009(6)	0.00005(7)	-0.00000(9)	---	0.0001(1)	0.0008(2)
<b>S2 He</b>	-0.00003(3)	-0.00006(4)	---	0.00004(7)	---	0.0004(2)
<b>S2 H<sub>2</sub></b>	-0.00007(3)	-0.00016(5)	---	-0.0002(1)	---	-0.0001(2)
<b>S3</b>		0.0000(3)	0.00001(4)	---	0.00005(6)	0.00019(8)
<b>S4</b>	0.00005(8)	-0.0001(1)	0.0000(1)	---	0.000(1)	0.000(2)
<b>S5</b>	-0.00005(6)	-0.0001(1)	-0.00002(8)	---	-0.0000(1)	0.0000(1)
<b>S6</b>	-0.00007(3)	-0.00002(6)	---	0.00003(8)	---	0.0002(1)
<b>S7</b>	-0.00006(5)	0.00006(6)	0.00001(7)	---	0.0001(1)	-0.0001(1)
<b>S8</b>	-0.00003(2)	-0.00000(3)	0.00000(3)	---	0.00009(4)	0.0001(1)
<b>S9</b>	-0.00005(2)	-0.00002(4)	0.00004(7)	---	-0.00005(7)	0.00004(11)

Quantitative determination of the NP shape was carried out by analyzing low temperature EXAFS data up to the 4<sup>th</sup> nearest neighbor contribution, including multiple scattering (MS), as described in Ref. 36 and references therein. Degeneracy of single and multiple-scattering paths in EXAFS analysis is simply related to the coordination number of the nearest neighbors, and can be obtained from the non-linear least squares fit of the theoretical EXAFS equation<sup>199</sup>. Physically reasonable constraints between the fitting variables were applied to maximize the number of degrees of freedom in the fits.

The passive electron reduction factor was fixed to that found for the Pt foil reference: 0.861. Only the most important single and collinear multiple-scattering paths were used in the fits through the 4<sup>th</sup> coordination shell. Among the multiple-scattering paths we used double- and triple-scattering paths to the 4<sup>th</sup> nearest neighbor (4NN) through the intervening atom (1<sup>st</sup> neighbor, or 1NN) along the same line. The total Debye-Waller values ( $\sigma^2$ ) for these paths were constrained to be the same as that of the 4NN Pt-Pt pair. In addition, a double-scattering path connecting the central atom, its 1NN, and another 1NN in the opposite direction was used in the fit. The disorder parameter of this path was varied independently from the others. Distance corrections were constrained to vary in accordance with the isotropic lattice expansion or contraction for all paths except for the first one, for which the third cumulant of the pair distribution function accounting for its asymmetry was varied as well. This approximation is justified by the apparent strong structural order in all particles, evident by comparing raw data in R-space for all the samples and the reference bulk Pt foil (Fig. 57a). Coordination numbers of all single scattering paths were varied independently; those of the multiple-scattering paths were constrained to those of the single scattering paths to the 4NN or 1NN, depending on the geometry of a particular path. Finally, the same energy correction ( $E_0$ ) was used for all paths.

As an example, Table 11 displays coordination numbers and distances of each coordination shell to the absorbing atom obtained from the multiple scattering analysis of EXAFS data acquired for sample S2.

The possibility of morphological changes in our samples as a function of temperature has not been accounted for in our analysis. This approach decreases the

number of fitting parameters and is justified by the following arguments: (i) the behavior of our raw EXAFS data throughout the entire temperature range is not consistent with a size or shape change, (ii) our samples were measured under a hydrogen atmosphere that passivates the NPs and stabilizes their shapes, and (iii) the analysis of the vibrational properties of our NPs was conducted up to a maximum annealing temperature of 375°C, which is the same temperature used for sample calcination (for 24 hours) prior to the EXAFS measurements.

Table 11: Coordination numbers (N), distances of each coordination shell to the absorbing atom (r), and bond length disorder parameters ( $\sigma^2$ ) obtained from the multiple scattering analysis of EXAFS data acquired in H<sub>2</sub> on reduced micellar Pt NPs supported on  $\gamma$ -Al<sub>2</sub>O<sub>3</sub> (sample S2) at 173 K. Uncertainties are shown in parentheses. More examples of similar data obtained for some of the other samples and bulk Pt are included in Ref. 36. The best fit value for the energy origin correction  $E_0$  was 9.9 (4) eV, the third cumulant was 0.00000 (2) Å<sup>3</sup>, and the disorder parameter of the double-scattering path to the 1NN was 0.0033(22) Å<sup>2</sup>. Only the distance correction to the 1NN was varied independently from the others, the rest were constrained with the isotropic lattice expansion/contraction factor,  $\epsilon$ . The best fit value of  $\epsilon$  was 0.0000(7), and its uncertainty was used to evaluate the error bars of the distances to 2NN through 4NN.

Sample S2	Coordination numbers of 1st through the 4th nearest neighbor shells, N			
	Distance to each shell, r (Å)			
	Bond length disorder, $\sigma^2$ (Å <sup>2</sup> )			
T=173 K	<b>N<sub>1</sub></b> 7.7 (4)	<b>N<sub>2</sub></b> 3.2 (1.0)	<b>N<sub>3</sub></b> 8.6 (1.7)	<b>N<sub>4</sub></b> 5.8 (1.1)
	<b>r<sub>1</sub>(Å)</b> 2.765 (4)	<b>r<sub>2</sub>(Å)</b> 3.920 (3)	<b>r<sub>3</sub>(Å)</b> 4.801(3)	<b>r<sub>4</sub>(Å)</b> 5.544 (4)
	<b><math>\sigma_1^2</math>(Å<sup>2</sup>)</b> 0.0040 (1)	<b><math>\sigma_2^2</math>(Å<sup>2</sup>)</b> 0.0049 (11)	<b><math>\sigma_3^2</math>(Å<sup>2</sup>)</b> 0.0044 (6)	<b><math>\sigma_4^2</math>(Å<sup>2</sup>)</b> 0.0040 (16)

If any changes in the NP morphology (size and/or shape) were to occur at 375°C, they should have already taken place before the EXAFS measurements. Evidence of the lack of NP sintering at this annealing temperature can be found in the TEM images of analogous samples depicted in Ref. 36.

#### **7.2.4 Nanoparticle shape modeling**

The shapes of our Pt NPs have been resolved by matching structural information obtained experimentally via EXAFS (coordination numbers up to the 4<sup>th</sup> nearest neighbor,  $N_1$ - $N_4$ ) and TEM (NP diameter,  $D$ ) to analogous data extracted from a database I generated, containing ~4000 model fcc NP shapes. Only closed shell clusters were considered in the models. In our analysis, after taking into consideration the error bars in the EXAFS coordination numbers as well as the TEM diameters, we have found on average only 3 model fcc cluster shapes consistent with all five experimental parameters ( $N_1$ ,  $N_2$ ,  $N_3$ ,  $N_4$ , and  $D$ ).

In order to determine the most representative NP shape, we have used volume-weighted TEM diameters. In general, the use of the volume-weighted diameters is preferred when comparing TEM and EXAFS structural information, since EXAFS is a volume-weighted technique. Examples of the NP shapes typical of similarly prepared but larger micellar Pt NPs resolved by STM can be found in Refs. 5, 38.

Table 12 shows examples of the best three model shapes for S2-S5, with information on the total number of atoms, the ratio of the number of Pt atoms at the NP surface and perimeter to  $N_t$  ( $N_s/N_t$ ), the ratio of the number of Pt atoms in contact with the support to  $N_t$  ( $N_c/N_t$ ), and a factor ( $Q$ ) indicating how much each of the specific

model shapes deviates from the experimentally measured EXAFS coordination numbers and volume-weighted TEM NP diameter. The shapes with the best Q-factors are depicted in a darker color in Table 12 and also in Table 13. The Q- factor has been obtained following eq. (28):

$$Q = \sqrt{\frac{NE_1^2 + NE_2^2 + NE_3^2 + DE^2}{4}} \quad (28)$$

, where  $NE_1$ ,  $NE_2$  and  $NE_3$  are normalized errors of the experimental 1<sup>st</sup>, 2<sup>nd</sup> and 3<sup>rd</sup> coordination numbers, and  $DE$  is the normalized error of the TEM diameter. The latter errors are calculated following eqs. (29) and (30):

$$NE = \frac{\text{Experimental CN} - \text{Model CN}}{\text{Experimental error of CN}} \quad (29)$$

$$DE = \frac{\text{Experimental } D - \text{Model } D}{\text{Experimental error of } D} \quad (30)$$

, where  $D$  is the NP diameter and  $CN$  are the respective coordination numbers ( $N_1$ ,  $N_2$  or  $N_3$ ). In the calculation of the Q factor we have not considered the 4<sup>th</sup> coordination number extracted from EXAFS. As shown by A. Jentys<sup>206</sup>, either  $N_3$  or  $N_4$  can be used interchangeably to estimate the particle shape, but since  $N_3$  is generally larger than  $N_4$  for most shapes of fcc particles (e.g., 24 vs. 12 in the bulk), the former number has greater impact on the shape determination.

A low Q factor indicates a good fit between experimental and model CN and  $D$ . As can be seen in the Table 12, only one shape provides a Q factor  $\leq 1$  for samples S2 and S4, while as few as 3 shapes satisfy that constraint for S3 and S5, indicating the low

degeneracy in the determination of the cluster shape for samples containing NPs in our size range (~0.8-1 nm). For S3, two shapes with identical Q factor were obtained.

Table 12: Model polyhedron shapes for fcc-Pt NPs providing the best fit to the experimental coordination numbers (EXAFS) and volume-weighted NP diameters (TEM). The average and volume-weighted TEM diameters, the total number of atoms in each NP ( $N_t$ ), the ratio of the number of Pt atoms at the NP surface and perimeter to  $N_t$  ( $N_s/N_t$ ), and the ratio of the number of Pt atoms in contact with the support to  $N_t$  ( $N_c/N_t$ ) are given. A factor (Q) representing the deviations of the coordination numbers and diameter of each of the model shapes with respect to the experimental samples are also included.



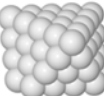



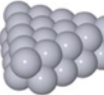


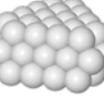
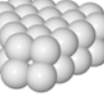

Sample 2 - weighted diameter: 0.9 (2) nm					Sample 3 - weighted diameter: 1.2 (2) nm				
	$N_t$	$N_s/N_t$	$N_c/N_t$	Q		$N_t$	$N_s/N_t$	$N_c/N_t$	Q
	44	0.84	0.23	0.3 ✓		85	0.74	0.18	0.8 ✓
	70	0.72	0.26	1.1		79	0.72	0.15	0.8 ✓
	67	0.72	0.27	1.1		75	0.75	0.12	1.0 ✓
Sample 4 - weighted diameter: 1.1(2) nm					Sample 5 - weighted diameter: 1.2(3) nm				
	$N_t$	$N_s/N_t$	$N_c/N_t$	Q		$N_t$	$N_s/N_t$	$N_c/N_t$	Q
	33	0.82	0.55	0.8 ✓		55	0.75	0.16	0.9 ✓
	46	0.78	0.54	1.2		70	0.77	0.26	1.0 ✓
	43	0.76	0.58	1.2		66	0.72	0.24	1.0 ✓

Table 13: Parameters used for the synthesis of micellar Pt NPs, including polymer type (PS-PVP) and the ratio (L) between the metal salt loading and the molecular weight of the polymer head (P2VP). Also included are the mean and the volume-weighted TEM diameters. By comparing structural information obtained via EXAFS (1<sup>st</sup>-4<sup>th</sup> NN CNs) and TEM (NP diameters) with a database containing fcc-cluster shapes, the ratio of the number of surface atoms to the total number of atoms in a NP ( $N_s/N_t$ ) and the ratio of the number of atoms in contact with the substrate to the total number of atoms ( $N_c/N_t$ ) were obtained. The largest facets within each NP were selected as facets in contact with the support: (111) for S1-S4, S6, and (100) for S5. The static disorders ( $\sigma_s^2$ ) obtained from the analysis of EXAFS data are also shown. The largest values of  $\sigma_s^2$  were generally observed for the samples with the largest NP/support interface (S1 and S4).

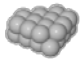





Sample Name	Polymer	L	TEM diameter (nm)	Volume-weighted TEM diameter (nm)	$\sigma_s^2$ (Å <sup>2</sup> )	Model cluster shapes	$N_t$	$N_s/N_t$	$N_c/N_t$
S1	PS(27700)-P2VP(4300)	0.06	0.8 (0.2)	0.9 (0.3)	0.0023(2)		22	0.86	0.55
S2	PS(27700)-P2VP(4300)	0.1	0.8 (0.2)	0.9 (0.2)	0.0013(2)		44	0.84	0.23
S3	PS(27700)-P2VP(4300)	0.2	1.0 (0.2)	1.2 (0.2)	0.0010(3)		85	0.74	0.18
S4	PS(16000)-P2VP(3500)	0.05	1.0 (0.2)	1.1 (0.2)	0.0028(3)		33	0.82	0.55
S5	PS(16000)-P2VP(3500)	0.1	1.0 (0.2)	1.2 (0.3)	0.0019(2)		55	0.75	0.16
S6	PS(16000)-P2VP(3500)	0.2	1.0 (0.2)	1.1 (0.3)	0.0015(2)		140	0.64	0.13
S7	PS(16000)-P2VP(3500)	0.4	1.8 (1.5)	5.7 (2.2)	0.0015(2)				
S8	PS(27700)-P2VP(4300)	0.3	3.3 (1.5)	6.0 (2.8)	0.0016(1)				
S9	PS(27700)-P2VP(4300)	0.6	5.4 (3.0)	15.0 (10.0)	0.0012(1)				

Table 13 contains information on the total number of atoms within each NP ( $N_t$ ), the ratio of the number of Pt atoms at the NP surface and perimeter to the total number of atoms ( $N_s/N_t$ ), and the ratio of the number of Pt atoms in contact with the support to the total number of atoms within a NP ( $N_c/N_t$ ) extracted from the selected model NP shapes.

Shape determination was not carried out for samples S7-S9 due to the large shape degeneracy for NPs with large coordination numbers.

The distinction between 2D- and 3D-like NPs obtained from the former analysis is in agreement with the general trends observed here for the EXAFS static disorders, with the highest values corresponding to the 2D NPs (S1 and S4, 0.0023 and 0.0028 Å<sup>2</sup>, respectively), i.e. those with the highest relative number of atoms in contact with the support.

### 7.3 Results

Examples of EXAFS spectra in k-space measured at different temperatures in He (S2) and H<sub>2</sub> (S3-S5) are shown in Fig. 56. The decrease in the oscillation magnitude is due to the increase in the dynamic disorder at higher temperatures. Also by increasing the temperature, the data become noisier at higher k values and therefore, a smaller k-range must be used for data analysis.

Fourier-transformed EXAFS spectra from ligand-free micellar Pt NP samples supported on  $\gamma$ -Al<sub>2</sub>O<sub>3</sub> acquired in H<sub>2</sub> at RT (S1, S2, S8) as well as a bulk Pt sample are shown in Fig. 57a.



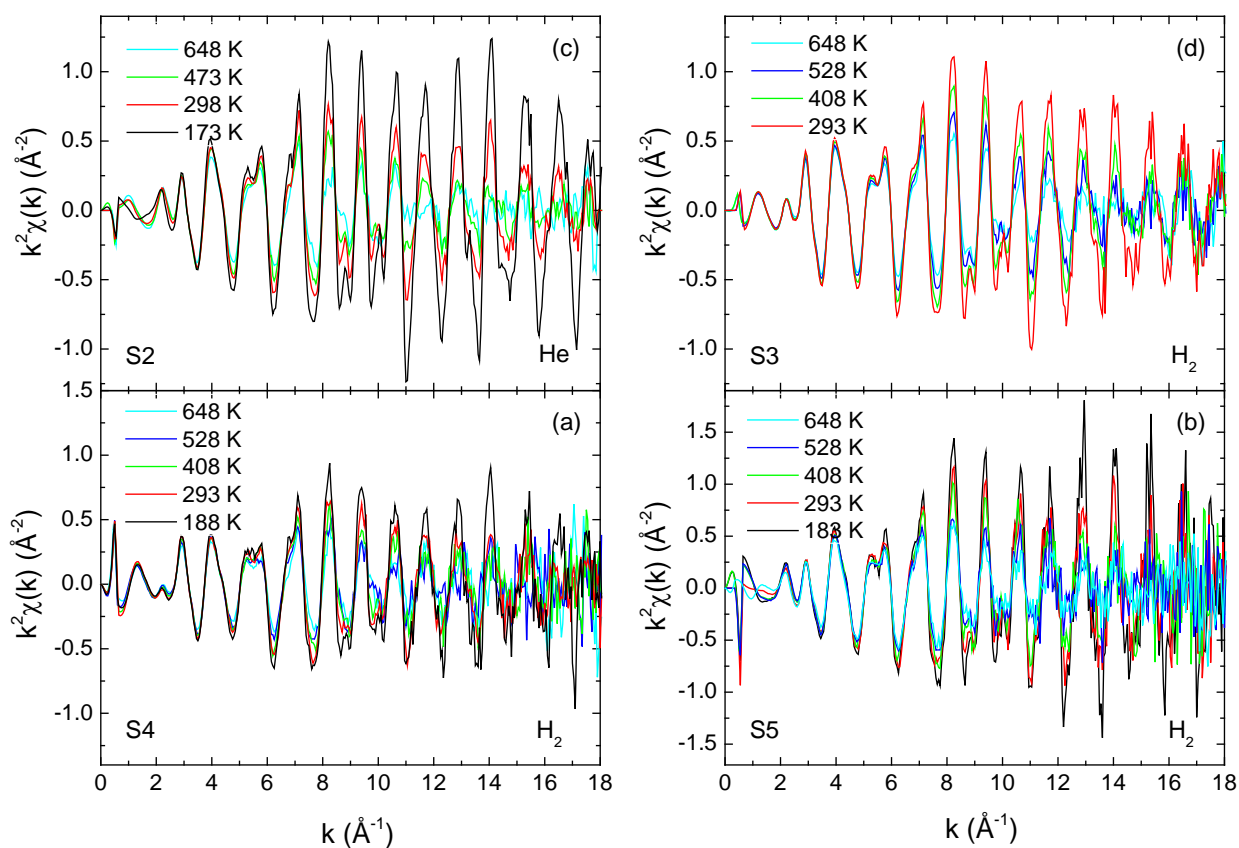


Fig. 56:  $k^2$ -weighted EXAFS data in  $k$ -space for reduced Pt NPs on  $\gamma$ - $\text{Al}_2\text{O}_3$  measured in  $\text{He}$ : (a) S2 and in  $\text{H}_2$ : (b) S3, (c) S4, (d) S5 at different temperatures (from 173 to 648 K).

The smaller magnitude observed for smaller NPs (e.g. S2 as compared to S8) is due to both lower coordination numbers and higher disorder expected for smaller NPs. The effect of temperature on the EXAFS data is shown in Fig. 57b for sample S2 at temperatures ranging from 173 K to 648 K. A decrease in the intensity of the EXAFS signals with increasing temperature is evident. Such effect can be attributed to an increase in the bond length disorder in the framework of Pt atoms, to a decrease in the Pt-Pt first nearest neighbor coordination number due to changes in the NP size and/or shape, or to both.

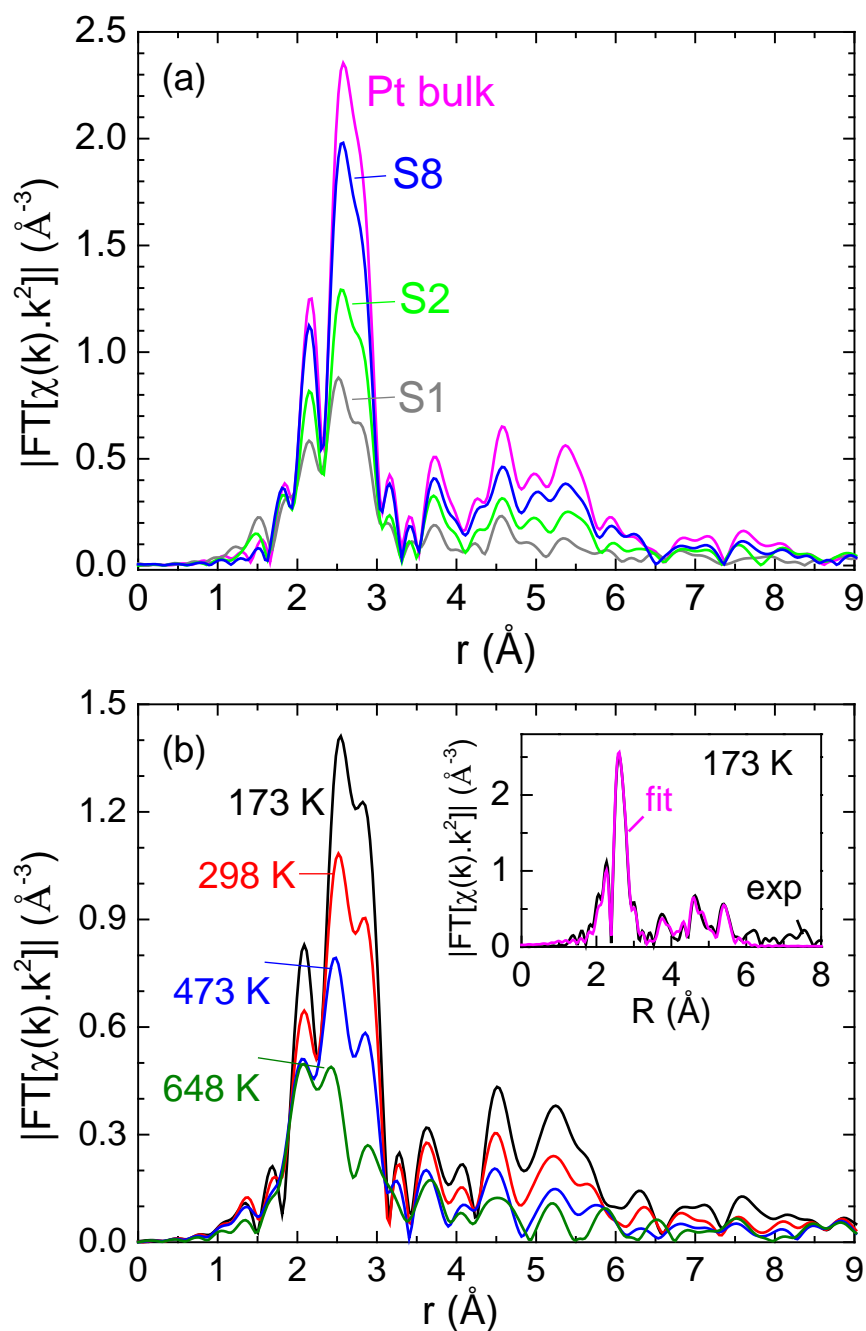


Fig. 57: (a)  $k^2$ -weighted EXAFS data in  $r$ -space of Pt NPs supported on  $\gamma$ - $\text{Al}_2\text{O}_3$  in samples S1, S2, S8 and a bulk Pt foil. All samples were measured in a  $\text{H}_2$  atmosphere at RT after NP reduction. The range of the Fourier transform is 2-11  $\text{\AA}^{-1}$ . (b) Temperature-dependent EXAFS data in  $r$ -space of S2 measured in  $\text{H}_2$ . The inset displays the experimental data acquired at 173 K together with the corresponding multiple-scattering fit.

We can single out the disorder as the dominant factor responsible for this behavior when we examine the k-space data, Fig. 56. If the NP size and/or shape were changing with temperature, the coordination number effect would be visible for all k-values, since it affects the EXAFS signal as a constant multiplicative factor. However, the decrease in the intensity of our k-space data is more prominent at the end of the k-range than at the beginning. Such observation is in agreement with the disorder effect, since it is expected to increase with increasing k.

A representative multiple-scattering fit of the 173 K spectrum is included as inset in Fig. 57b. However due to lower quality of the data at higher temperatures, only first-shell analysis was done for the temperature-dependent study. Representative fits in r-space to temperature-dependent data from S5 are shown in Fig. 58. Pt-Pt distances (R) in the temperature range of 150 K to 700 K are shown in Fig. 59a for samples S1, S2, S7, S8 and for a reference bulk-like Pt foil<sup>37</sup>. All measurements were carried out under a continuous H<sub>2</sub> flow, with the exception of sample S2, for which He and H<sub>2</sub> environments were used [Fig. 59b].

The data in Fig. 59a, and Fig. 59b correspond to the best fit results of the experimental EXAFS spectra obtained for the first nearest neighbor (1NN) Pt-Pt bond lengths (R, averaged over all bonds within one NP) at different temperatures.

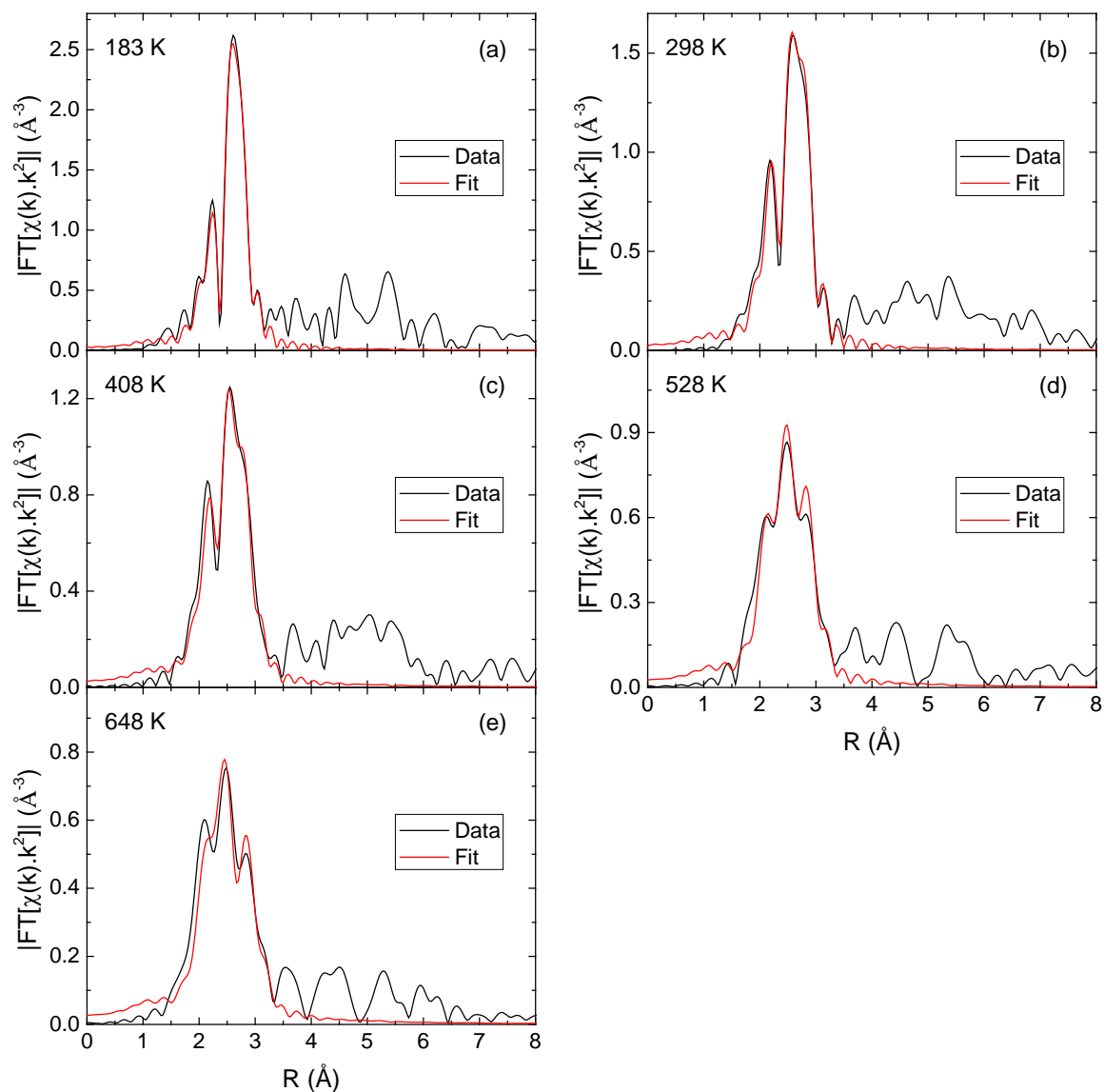


Fig. 58: Fourier transform magnitudes of  $k^2$ -weighted EXAFS data and 1<sup>st</sup>-shell multiple-data-set fit for sample S5 measured in  $\text{H}_2$  at 183 K (a), 293 K (b), 408 K (c), 528 K (d), and 648 K (e).

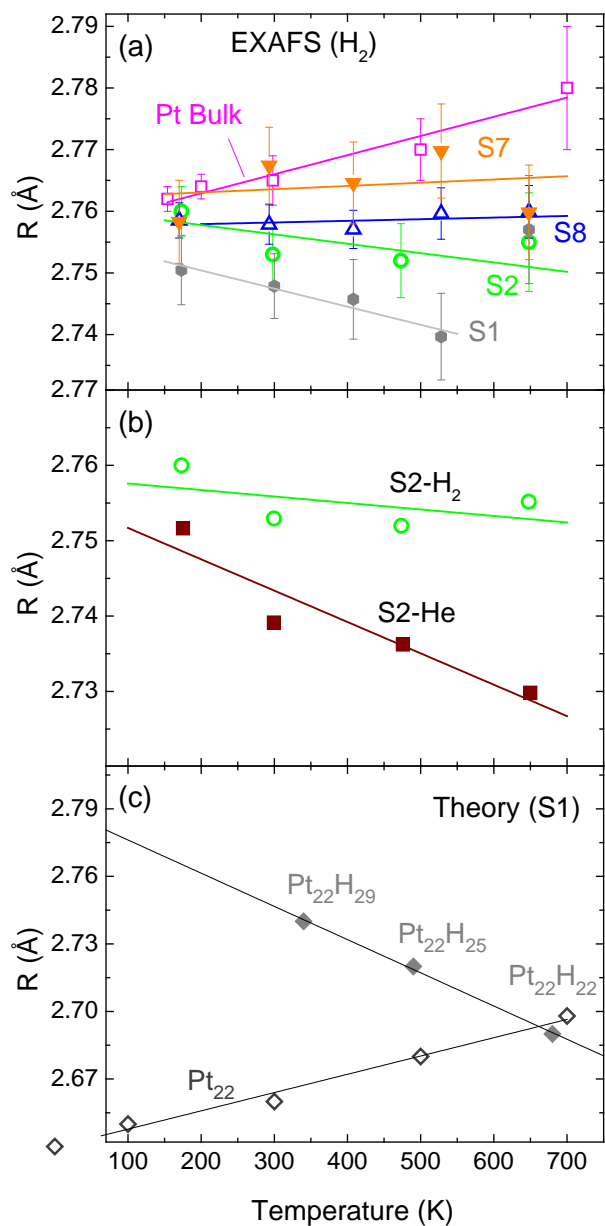


Fig. 59: (a) Temperature-dependent Pt-Pt bond lengths ( $R$ ) obtained from EXAFS measurements on samples S1, S2, S7, S8 and a bulk Pt foil. All samples were measured in  $H_2$ . (b) Pt-Pt distances from S2 measured in He and  $H_2$ . In (a) and (b) solid lines represent linear fits to the experimental data. (c) Calculated median of the Pt-Pt bond-lengths of an unsupported clean  $Pt_{22}$  NP (open symbols, *ab initio* MD calculations) and a H-covered  $Pt_{22}H_M$  NP (solid symbols, model for S1) plotted as a function of temperature. Calculations were performed by M. Alcántara Ortigoza and G. Shafai in Prof. Talat Rahman's group at the University of Central Florida. Additional details on the calculations can be found in Ref. 38.

The solid lines in Fig. 59a, b represent a linear fit to the experimental data. From the slope of such fit, the average thermal expansion coefficient ( $\alpha$ ) can be extracted from equation below:

$$\alpha = \frac{1}{R_0} (\partial R / \partial T) \quad (31)$$

, where  $R_0$  is the Pt-Pt distance obtained for each sample at the lowest measurement temperature. Due to the enhanced noise of the experimental data of sample S1 at high temperature, the Pt-Pt distance shown in Fig. 59a at ~700 K was not included in the linear fit.

*Ab initio* MD calculations (performed by Dr. M. Alcántara Ortigoza and G. Shafai in Prof. Talat Rahman's group at UCF, Ref. 38) are shown in Fig. 59c. The solid symbols in (c) correspond to hydrogen coverages that are thermodynamically stable at the given temperature, and the empty symbols show the bond lengths of a clean Pt<sub>22</sub> cluster at different temperatures. Table 14 shows the experimental and theoretical (DFT) normalized average Pt-Pt bond length for different samples. The experimental values were obtained at low temperature (172-188 K) as well as RT (300 K), while the theoretical values were obtained at 0 K.

The thermal expansion coefficients,  $\alpha$ , for all samples are shown in Fig. 60a as a function of the average 1<sup>st</sup> NN EXAFS coordination number and in Fig. 60b as a function of the average TEM NP diameter. In general, large coordination numbers (close to 12 for bulk Pt) are associated with large NPs, and small values with small NPs, although NPs with different shapes will also display distinct coordination numbers<sup>5</sup>.

Our data reveal a size-dependent trend in the thermal expansion coefficient, namely, a cross-over from positive (S3, S5-S9) to negative (S1, S2, S4) thermal expansion with decreasing NP size. The effect of hydrogen chemisorption in the thermodynamic properties of our NPs will be discussed in more detail in the following section.

Table 14: Experimental (EXAFS) and theoretical (DFT) average 1<sup>st</sup>-NN bond lengths of Pt NPs with different sizes and shapes given as a fraction of the respective bulk values. All experimental samples but S2 were H<sub>2</sub>-passivated and supported on  $\gamma$ -Al<sub>2</sub>O<sub>3</sub>. S2 was also measured in He. The NPs analyzed theoretically were unsupported and free of adsorbates, with the exception of S1, which was also investigated with different H coverages. The experimental bulk Pt-Pt reference distances are 2.762 (2) Å at 154 K, 2.765 (4) Å at 300 K, and 2.78 (1) Å at 700 K. The calculated bulk Pt-Pt distance is 2.805 Å at 0 K. The DFT calculations were only carried out on Pt NPs containing less than 100 atoms.

Sample Name	Pt-Pt bond lengths relative to bulk (EXAFS)			Pt-Pt bond lengths relative to bulk (DFT)
	172-188 K	300 K	648 K	0K
S1	0.996	0.994	0.992	0.943 (Pt <sub>22</sub> ) 0.960 (Pt <sub>22</sub> H <sub>22</sub> ) 0.969 (Pt <sub>22</sub> H <sub>25</sub> ) 0.979 (Pt <sub>22</sub> H <sub>29</sub> )
S2	0.999 (H <sub>2</sub> ) 0.996 (He) <sup>37</sup>	0.996 (H <sub>2</sub> ) 0.991 (He)	0.991 (H <sub>2</sub> ) 0.982 (He)	0.964 (Pt <sub>44</sub> )
S3		0.999	0.995	0.975 (Pt <sub>85</sub> )
S4	0.994	0.991	0.986	0.943 (Pt <sub>33</sub> )
S5	0.996	0.993	0.990	0.968 (Pt <sub>55</sub> )
S6	0.997	0.997	0.992	
S7	0.999	1.001	0.993	
S8	0.999	0.997	0.993	
S9	0.998	0.997	0.993	

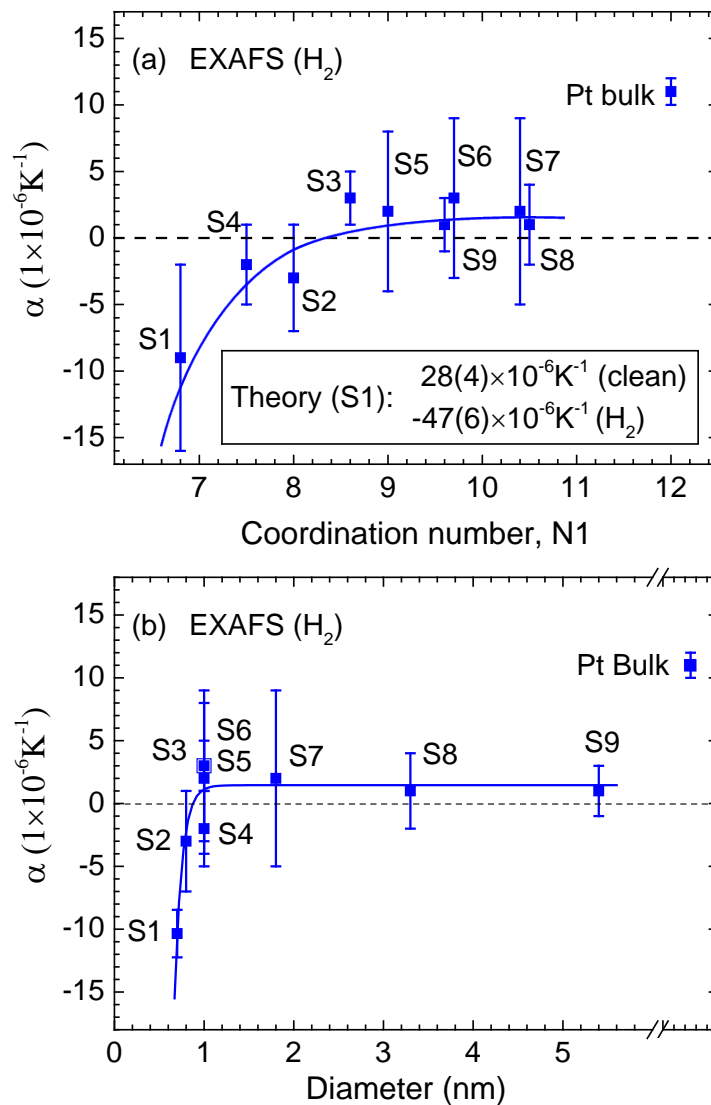


Fig. 60: Average thermal expansion coefficient ( $\alpha$ ) extracted from the linear fit of the EXAFS data shown in Fig. 59a and those from additional samples described in Table 13, plotted as a function of (a) the 1<sup>st</sup> NN coordination number, and (b) the average TEM NP diameter. The inset in (a) displays calculated thermal expansion coefficients for an unsupported clean (adsorbate-free) Pt<sub>22</sub> NP (model of S1) and a H-covered Pt<sub>22</sub> NP.

The dynamic correlated mean-square bond length disorders ( $\sigma_d^2$ ) obtained from the fits of the experimental EXAFS data following the correlated Debye model (CDM)<sup>201</sup>



are shown in Fig. 61a. The slope of the temperature dependence of  $\sigma_d^2$  in the high temperature regime (e.g. >100 °C) is inversely proportional to  $\Theta_D^2$ . Above 100 K, our experimental data display a good linear dependence at least up to our maximum measurement temperature of ~650 K. Deviations from the linear behavior of  $\sigma_d^2$  might be found in the proximity of the melting temperature<sup>207</sup>, which, even for small Pt NPs,<sup>189</sup> is expected to be significantly higher than 650 K.

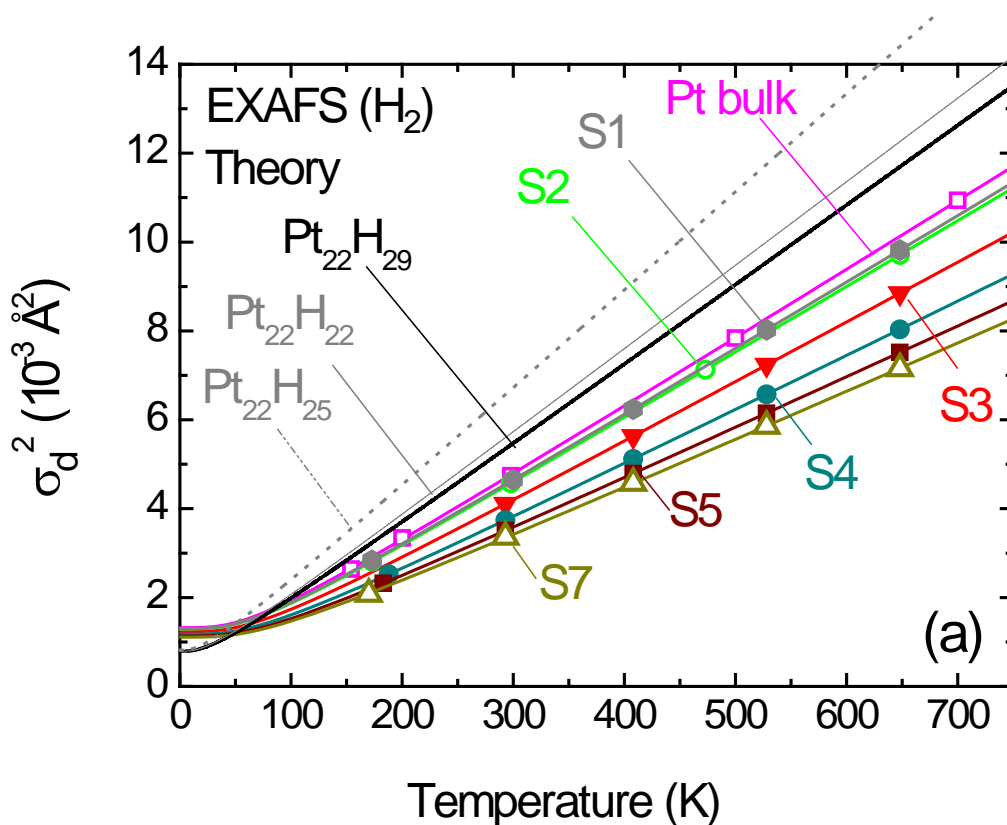


Fig. 61: Dynamic contribution ( $\sigma_d^2$ ) to the total EXAFS Debye-Waller factor obtained for micellar Pt NPs on  $\gamma$ -Al<sub>2</sub>O<sub>3</sub> (S1-S5, S7) under H<sub>2</sub> flow and analyzed with the CDM (solid lines). Symbols correspond to the temperatures at which the EXAFS data were measured. For reference, analogous data of a bulk-like Pt foil are also shown. In addition, the calculated thermal evolution of the mean square bond-projected bond-length fluctuations ( $\sigma_d^2$ )<sub>th</sub> of a H-covered Pt<sub>22</sub> NP (model of S1) for several thermodynamically stable states (Pt<sub>22</sub>H<sub>22</sub>, Pt<sub>22</sub>H<sub>25</sub> and Pt<sub>22</sub>H<sub>29</sub>) are also included.

Our results indicate that the majority of Pt atoms in our NPs are characterized by smaller bond-projected bond-length fluctuations (correlated displacements) than those in bulk Pt samples.

The Debye temperatures obtained from the CDM analysis of our EXAFS data are displayed in Fig. 62a as a function of the TEM NP diameter, and in Fig. 62b as a function of the total number of atoms in the NP normalized by the number of atoms at the NP surface and perimeter ( $N_t/N_s$ ). All data correspond to samples passivated by H<sub>2</sub> under identical conditions. Fig. 62b does not include data from the large NPs (S7-S9) due to the degeneracy in the model shapes obtained for those samples.

A bimodal trend in  $\theta_D$  as a function of the NP diameter is observed in Fig. 62a. For NPs  $\leq 1$  nm, an overall decrease of  $\theta_D$  was found with decreasing NP size (Fig. 62a) or decreased  $N_t/N_s$  (Fig. 62b).

Nevertheless, relative differences were observed for NPs with the same TEM diameter but different shape ( $\sim 0.8$  nm S1 and S2, and  $\sim 1$  nm, S3-S6). For larger NPs ( $> 1$  nm), decreasing Debye temperatures were observed with increasing NP size (TEM diameter), approaching the bulk  $\theta_D$  value for sizes above 5 nm. Interestingly,  $\theta_D$  of all experimental NP samples was found to exceed that of bulk-Pt. A detailed description of possible origins for these intriguing size- and shape-dependent trends is given in the discussion section.

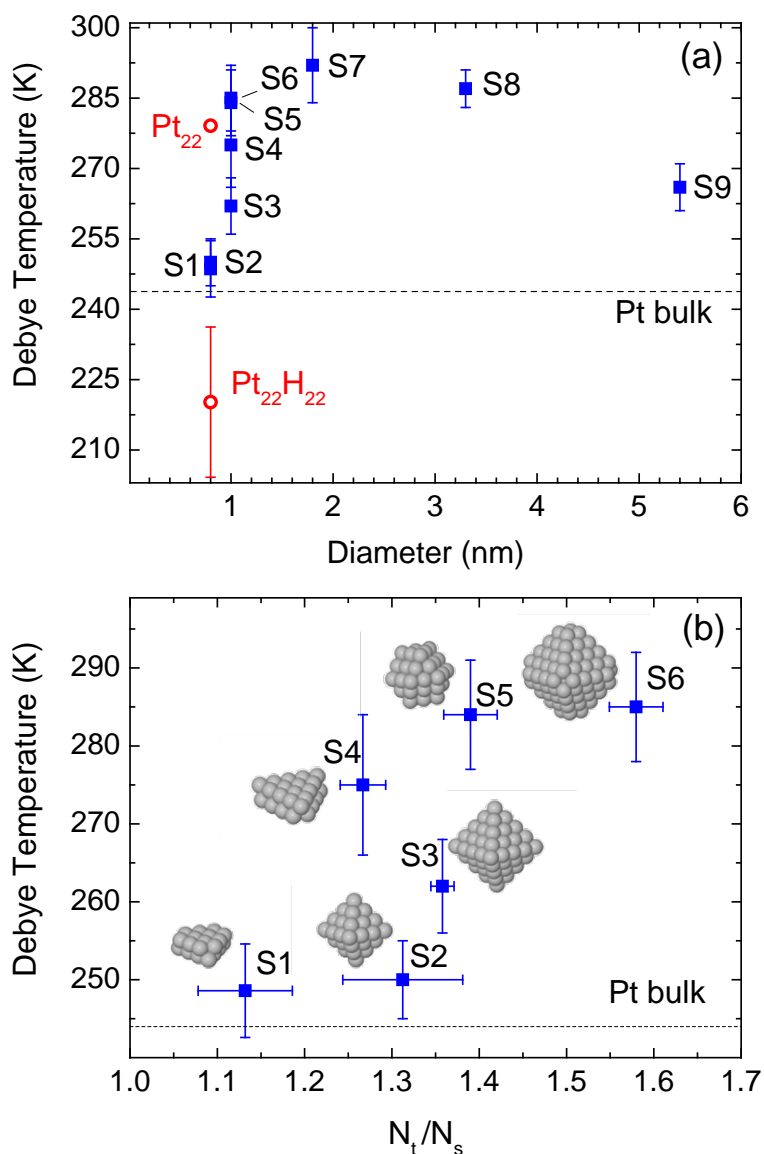


Fig. 62: Debye temperature extracted from the CDM fit of EXAFS data displayed in Fig. 61 as a function of (a) the TEM NP diameter, and (b) the total number of atoms in a NP ( $N_t$ ) normalized by the number of surface atoms ( $N_s$ ),  $N_t/N_s$ . The values in (b) were obtained for the model NP shapes that best fitted the coordination numbers extracted from the MS analysis of low-temperature EXAFS data and the measured TEM NP diameters. The insets in (b) display the model NP shapes representative of each sample. The error margins reported for the  $N_t/N_s$  values reflect the degeneracy of NP shapes obtained as best representation of each experimental sample. The Debye temperature of a bulk-like Pt foil is also shown for reference (dashed line). In (a), the Debye temperatures calculated for  $Pt_{22}H_{22}$  and  $Pt_{22}$  (models for S1) are also shown.

Table 15: First nearest-neighbor coordination number ( $N_1$ ), thermal expansion coefficient ( $\alpha$ ), and Debye temperature ( $\Theta_D$ ) of samples S1–S9 and of a bulk-like Pt foil. All samples were measured in H<sub>2</sub>. S2 was also measured in He.

Sample	$N_1$	$\alpha$ ( $10^{-6} \text{ K}^{-1}$ )	$\Theta_D$ (K)
S1(H <sub>2</sub> )	6.8	-9 (7)	249 (6)
S2 (H <sub>2</sub> )	8.0 (2)	-3 (4)	250 (5)
S2 (He)	7.8 (3)	-15 (4)	240 (6)
S3 (H <sub>2</sub> )	8.6 (3)	3 (2)	262 (6)
S4 (H <sub>2</sub> )	7.5 (3)	-2 (3)	275 (9)
S5 (H <sub>2</sub> )	9.0 (3)	3 (2)	284 (7)
S6 (H <sub>2</sub> )	9.7 (4)	3(6)	285 (7)
S7 (H <sub>2</sub> )	10.4 (4)	2(7)	292 (8)
S8 (H <sub>2</sub> )	10.5 (2)	1(3)	287 (4)
S9 (H <sub>2</sub> )	9.6 (3)	1(2)	266 (5)
Pt bulk	12	11 (1)	244 (3)

## 7.4 Discussion

### 7.4.1 Anomalous lattice dynamics and thermal properties of supported, size- and shape-selected Pt nanoparticles

The thermal expansion coefficients ( $\alpha$ ) of the Pt NP samples were estimated from the slope of the linear interpolation of the bond length as a function of temperature (Fig. 59a) and are summarized in Table 15.

As expected, the Pt foil displays positive thermal expansion. However, all of our NP samples were found to have smaller thermal expansion coefficients than bulk Pt [ $\alpha \sim 11 \times 10^{-6} \text{ K}^{-1}$  is the reference value extracted from EXAFS measurements of a Pt foil, or  $8.8 \times 10^{-6} \text{ K}^{-1}$  from Ref. 208]. This effect can be partially assigned to the influence of

the NP/support interface, since  $\gamma\text{-Al}_2\text{O}_3$  is characterized by a smaller  $\alpha$  of  $\sim 4.5 \times 10^{-6} \text{ K}^{-1}$ .<sup>209</sup> The latter has also been held responsible for the reduced coefficient of thermal expansion measured for superheated Al NPs in  $\text{Al}_2\text{O}_3$ <sup>210</sup>. Furthermore, for identically synthesized NPs, Fig. 60 constitutes a clear example of the influence of the NP size and geometry on their thermal properties. Interestingly, Fig. 60b reveals a cross-over from positive to negative thermal expansion at/below 1 nm. This result is in agreement with data from Kang et al.<sup>21</sup> and Sanchez et al.<sup>22</sup> obtained for 0.9-1.1 nm Pt NPs supported on  $\gamma\text{-Al}_2\text{O}_3$  prepared by impregnation-precipitation. According to previous DFT calculations for  $\text{Pt}_{13}$  on dehydrated  $\gamma\text{-Al}_2\text{O}_3$  (with relatively strong metal/support interactions),<sup>62</sup> the impregnation-precipitation preparation method is likely to result in 2D-shaped NPs.

In our study, the three samples displaying negative thermal expansion coefficients include the smallest NPs (S1 and S2,  $\sim 0.8$  nm with 2D and 3D shape, respectively) and a sample with slightly larger NP size but 2D shape ( $\sim 1$  nm, S4). In fact, the largest negative thermal expansion coefficient obtained for our micellar Pt NPs in  $\text{H}_2$  was for the 2D NPs in S1 ( $-9 \times 10^{-6} \text{ K}^{-1}$ ), which is comparable with that reported by Kang et al.<sup>21</sup> for 0.9 nm Pt NPs ( $-13 \times 10^{-6} \text{ K}^{-1}$ ), also measured in  $\text{H}_2$ .

Since other samples with average NP size of  $\sim 1$  nm but 3D shape did not show such effect (S3, S5, S6), both, the NP/support interface, and the relative ratio of Pt surface atoms with adsorbed H ( $N_s$  sites) must be key parameters responsible for the anomalous thermodynamic behavior observed.

Interestingly, Fig. 59b demonstrates that larger negative  $\alpha$  values were measured for the 3D NPs in S2 on  $\gamma\text{-Al}_2\text{O}_3$  under He ( $-15 \times 10^{-6} \text{ K}^{-1}$ , Table 15) as compared to  $\text{H}_2$

( $-3 \times 10^{-6} \text{ K}^{-1}$ , Table 15), clearly confirming that adsorbates on the surface of small NPs influence their thermal expansion significantly.

DFT calculations have shown that clean and unsupported Pt NPs display an overall bond length contraction (averaged over all bonds within a NP) of about 6% at 0 K for Pt<sub>22</sub> with respect to bulk Pt.<sup>38</sup> However, for the smallest experimental NPs measured in H<sub>2</sub> (S1), the contraction measured at 172-188 K is only 0.4% (Table 14). This cannot be assigned to the difference in the experimental and theoretical temperatures, but rather to the presence of H<sub>2</sub> (dissociative adsorption) on the experimental Pt NPs.

*Ab initio* MD calculations conducted by our collaborators (Dr. M. Alcántara Ortigoza and G. Shafai in Prof. Talat Rahman's group at UCF, Ref. 38) had shown that the large negative  $\alpha$  is not *intrinsic* to the NPs, since for support- and adsorbate-free Pt NPs (e.g. Pt<sub>22</sub>), a large positive thermal expansion coefficient was obtained.<sup>38</sup> The *extrinsic* contribution of H-desorption to the bond-length contraction observed experimentally for small Pt NPs with increasing measurement temperature was demonstrated theoretically in Fig. 59c<sup>38</sup>. Since hydrogen lifts the intrinsic contraction (due to size effects), any reduction in hydrogen coverage at higher temperatures would result in Pt-Pt bond contraction. In other words, due to the hydrogen effect, the Pt-Pt bond is expanded at low temperature, and increasing the temperature results in two competing phenomena: (i) the increase in Pt-Pt bond length due to intrinsic thermal expansion, accompanied by (ii) the decrease in Pt-Pt bond length due to the lower hydrogen coverage, expected on the NP surface with increasing temperature. It has been shown<sup>38</sup> that the effect of the decrease in the hydrogen coverage is ~5 times

larger than the standard thermal expansion and therefore, the net effect appears as a negative thermal expansion (e.g. in  $\text{Pt}_{22}\text{H}_x$ , Fig. 59c). More specifically, without taking into account the stiff substrate, the temperature-dependent desorption of hydrogen already resulted in a calculated *negative* thermal expansion coefficient about five times larger ( $\sim -47 \times 10^{-6} \text{ K}^{-1}$  extracted from Fig. 59c closed symbols) than that measured via EXAFS for the supported NPs in S1 ( $\sim -9 \times 10^{-6} \text{ K}^{-1}$ ), Fig. 60a. With both contributions at hand, one could see that the two effects combined can account qualitatively for the observed negative  $\alpha$ , at least once the onset temperature for H desorption has been reached.

In addition to adsorbate effects and size-dependent changes in the geometry (and therefore, electronic properties) of small NPs, NP/support interactions (not included in theoretical calculations) also appear to be of significance for the understanding of their thermal properties. From our experimental results, it seems that the observed negative thermal expansion cannot be explained only based on the reduction in hydrogen coverage, and that other factors are involved. As an example, higher negative thermal expansion is observed for S2 in the He environment (where no adsorbate effect is expected) as compared to the  $\text{H}_2$  environment, Fig. 59b and Table 15. Such behavior may originate from NP-support interactions. An alternative mechanism proposed to explain negative thermal expansion for materials characterized by strong bonding anisotropy relates to enhanced atomic displacements in the transverse direction to the bond<sup>211</sup>. Another possibility is the effect of minute oxygen contamination that might be present in the He stream (due to small leaks in the tubing not detectable by mass

spectrometry), resulting in chemisorbed oxygen on the surface and therefore a change in Pt-Pt bond length and thermal expansion coefficient.

Previous calculations by Vila et al.<sup>23</sup> on H-free Pt<sub>10</sub> clusters deposited on dehydrated  $\gamma$ -Al<sub>2</sub>O<sub>3</sub> revealed a small but negative thermal expansion trend attributed to changes in the bond lengths as the NP diffuses on the substrate, which is in clear contrast with our collaborator's MD results<sup>38</sup> for the larger, adsorbate-free, but unsupported Pt<sub>22</sub> NP. The latter emphasizes the important role of the substrate. At the same time, these calculations reported significantly smaller Pt-Pt contractions (~3 times smaller) than those measured experimentally by the same group,<sup>23</sup> which we assign to the adsorbate effect described above. Our experimental data also provide evidence for the important role of the  $\gamma$ -Al<sub>2</sub>O<sub>3</sub> substrate. For example, sample S4, with similar surface/volume ratio and NP/support contact area as S1 ( $N_s/N_t = 0.82$ - $0.86$  and  $N_c/N_t = 0.55$  for these two samples), but larger average size (~0.8 nm for S1 and ~1 nm for S4), showed a lower but still negative thermal expansion coefficient. When samples containing small NPs with the same size and analogous surface area for H<sub>2</sub>-chemisorption are compared (e.g. S1 and S2, ~0.8 nm,  $N_s/N_t = 0.84$ - $0.86$  Table 13), the negative thermal expansion effect was found to be more pronounced for sample S1, with the highest NP/support contact area ( $N_s/N_t = 0.55$  for S1, versus  $N_s/N_t = 0.23$  for S2). A recent EXAFS study by Sanchez et al.<sup>22</sup> revealed clear changes in the thermal expansion behavior of Pt NPs prepared by the deposition-impregnation method and supported on  $\gamma$ -Al<sub>2</sub>O<sub>3</sub> and carbon substrates, with positive  $\alpha$  values reported for the clusters deposited on the more weakly interacting C support, and negative  $\alpha$  on  $\gamma$ -Al<sub>2</sub>O<sub>3</sub>.



The specific role of the NP support is yet to be determined, since the calculations of our collaborators at UCF (Prof. Rahman's group)<sup>38</sup> were carried out on unsupported NPs, and only one support ( $\gamma$ -Al<sub>2</sub>O<sub>3</sub>) was used for all experiments.

#### 7.4.2 Debye temperature

The dynamic bond length disorders ( $\sigma_d^2$ ) obtained from the fits of the experimental EXAFS data following the CDM<sup>201</sup> are shown in Fig. 61. Analysis of the EXAFS data obtained for the Pt-foil via the CDM lead to a Debye temperature,  $\theta_D$  of  $244 \pm 3$  K, which is in agreement with literature reports<sup>174</sup>. Significantly higher values (249 K-292 K) are obtained for samples S1-S9. The data in Fig. 61 reveal a striking behavior of our NPs in this regard, which will be discussed in greater detail below. The best fit values of static disorder,  $\sigma_s^2$  are shown in Table 13 and the best fit results for the first nearest-neighbor coordination numbers ( $N_1$ ) and Debye temperature,  $\theta_D$  are shown in Table 15.

Compressive strains might be partially responsible for the enhanced  $\theta_D$ , due to the asymmetry of the effective pair potential, where the short distance branch is steeper than the long distance branch (due to the hard-core repulsion), and therefore the Pt-Pt bond stiffness should be large in the systems having bonds with large compressive strain. It should also be mentioned that the compressive strain present in supported NP systems might have different origins, as for example the presence of ligands on the NP surface (not the present case), adsorbates, or a support ( $\gamma$ -Al<sub>2</sub>O<sub>3</sub>). However, the

explanation of the enhanced  $\Theta_D$  observed appears to be more complex than a direct correlation with a contraction of Pt-Pt distance.

This result can be explained to some extent by the fact that EXAFS measurements underestimate the relative contribution of low-energy vibrational modes to the total  $\sigma_d^2$ , an effect that theoretically has been demonstrated to be significant for small unsupported NPs<sup>38</sup>. EXAFS is only sensitive to the changes in the bond length, and therefore, position fluctuations perpendicular to the bonds are neglected. Hence, the bond length disorder obtained by EXAFS,  $\sigma_d^2$ , corresponding to the correlated motion of atom pairs is essentially different than the crystallographic Debye-Waller factor  $\langle x^2 \rangle$ , which is the mean-square displacement of individual atoms about their equilibrium position. Therefore clear differences exist between the calculated  $\langle x^2 \rangle_{th}$  and  $(\sigma_d^2)_{th}$ , as it is considered in the theory of EXAFS<sup>212</sup>.

It has been also shown that the temperature dependence obtained for  $(\sigma_d^2)_{th}$  are clearly different from those of the “real” (uncorrelated) atomic mean square displacements,  $\langle x^2 \rangle_{th}$ . More specifically, smaller slopes of the  $(\sigma_d^2)_{th}$  versus temperature plots were observed for the majority of the clean NPs as compared to bulk Pt (exp.), which is in qualitative agreement with the experimental data in Fig. 61a. However, the contrary is true for  $\langle x^2 \rangle_{th}$ , with larger atomic displacements and slopes for the NPs as compared to bulk Pt. It was shown that for all different NPs,  $(\sigma_d^2)_{th}$  and its slope are significantly smaller than  $\langle x^2 \rangle_{th}$  and its slope<sup>38</sup>.

Based on the slope of  $\langle x^2 \rangle_{th}$  or  $(\sigma_d^2)_{th}$ , a parameter,  $\Theta^{slope}$ , is defined in correspondence with the Debye temperature of bulk Pt:

$$\Theta^{slope} = \Theta_D^{bulkPt} \sqrt{\frac{\Delta^{bulkPt}}{\Delta^{NP}}} \quad (32)$$

,where  $\Theta_D^{bulkPt}$  is the Debye temperature of bulk Pt (244 K),  $\Delta^{bulkPt}$  is the slope of  $\sigma_d^2$  for bulk Pt derived from EXAFS measurements ( $1.528 \times 10^{-5} \text{ \AA}^2/\text{K}$ )<sup>22</sup>, and  $\Delta^{NP}$  is the slope of  $(\sigma_d^2)_{th}$  calculated for the NP.

Fig. 62a displays,  $\Theta^{slope}$ , extracted from the slope of the theoretical  $(\sigma_d^2)_{th}$  versus T plots of clean Pt<sub>22</sub> (S1) and Pt<sub>22</sub>H<sub>22</sub>. The Pt<sub>22</sub>H<sub>22</sub> coverage was selected because it is stable at the highest temperature investigated (T > 600 K). The error bar corresponds to the variations of  $\Theta^{slope}$  with H coverage, considering only those that are thermodynamically stable. Overall, the adsorption of hydrogen was found to lead to a reduction of  $\Theta^{slope}$  for all H coverages studied. Nevertheless, the observed changes were non-monotonic, being largest for Pt<sub>22</sub>H<sub>29</sub> ( $\Theta^{slope} = 226$  K) and smallest for Pt<sub>22</sub>H<sub>25</sub> ( $\Theta^{slope} = 203$  K), with Pt<sub>22</sub>H<sub>22</sub> ( $\Theta^{slope} = 220$  K) in between, Fig. 62a.

It is useful to point out that since a number of low-energy vibrational modes correspond to shear perturbations of surface atoms<sup>213</sup>, if the NPs are strongly bound to a stiff substrate, the corresponding boundary condition might eliminate some of those modes.<sup>26, 214</sup> In addition, the presence of a strongly binding support might lead to an increase in the phonon gap present for small NPs.<sup>54</sup> For instance, the vibrational gap increased from 0.2 to 4.2 meV for free versus pseudomorphic Ru(0001)-supported single-layer Au<sub>13</sub>.<sup>214, 215</sup> Therefore, for NPs supported on stiff substrates, in which the low-energy VDOS might be suppressed, the differences between  $\langle x^2 \rangle$  and  $\sigma_d^2$

measured via EXAFS might not be as significant as those for the unsupported theoretical NPs. Thus, quantitative agreement between theoretical and experimental data requires also the consideration of the support in the calculations, which for the various NP sizes and shapes investigated in Ref. 38 is beyond computational possibilities based on first principle calculations. Moreover, it should be noted that the calculation results shown in Fig. 61a of  $\sigma_d^2$  versus T curves for Pt<sub>22</sub>H<sub>22</sub>, Pt<sub>22</sub>H<sub>25</sub> and Pt<sub>22</sub>H<sub>29</sub> intend to single out the effect of the limited sensitivity of EXAFS to low-E vibrational modes, but do not take into consideration the expected changes upon gradual desorption of H<sub>2</sub> with increasing temperature, since they correspond to a constant hydrogen coverage.

From the slope of the  $\sigma_d^2$  versus T plot of the EXAFS data in Fig. 61a, a Debye temperature was obtained for NPs in the size range of 0.8 to 5.4 nm, Fig. 62. As already mentioned, the behavior of the Debye temperature signifies here only the trends in the mean square bond length fluctuations. It neither validates nor refutes the Debye model for the vibrational density of states, which has been noted to be unsuitable for accurately describing the vibrational properties of small unsupported NPs (< 500 atoms,<sup>63</sup> <2 nm) due to the 3N-discretization of the vibrational energies<sup>214, 216</sup> and the observation of an excess vibrational density of states (VDOS) at low phonon energies<sup>25</sup>. The following observations are made based on the analysis of the EXAFS data shown in Fig. 62: (i) an overall increase in the Debye temperature of all NP samples with respect to bulk Pt; (ii) the distinct thermal properties of small and large Pt NPs. For NPs  $\leq 1$  nm, a decrease in  $\Theta_D$  is observed with decreasing NP size, while for larger NPs (> 1 nm), the Debye temperature was found to decrease with increasing NP diameter, Fig.

62(a). The  $\Theta_D$  value of bulk Pt was not reached for the largest NPs investigated here (~5.4 nm). The size-dependency displayed by the NPs with sizes > 1.5 nm is in agreement with that reported for superheated NPs with well-ordered (epitaxial) NP/support interfaces.<sup>19</sup> (iii) For NPs < 1.5 nm, a decrease in  $\Theta_D$  is also obtained with increasing relative number of atoms at the NP surface ( $N_s$ ), Fig. 62b. It should be taken into consideration that  $N_s$  here includes surface and perimeter atoms (the latter in contact with the support). A plausible explanation for this observation is the consideration of the low-coordinated surface atoms as defects leading to a suppression of  $\Theta_D$ , while the perimeter atoms in contact with the support might have the contrary effect. In fact, if the interaction of Pt atoms with  $\gamma$ -Al<sub>2</sub>O<sub>3</sub> is responsible for the large experimental  $\Theta_D$ , increasingly large 3D NPs will have a smaller fraction of atoms in contact with the support, which would lead to the disappearance of the  $\Theta_D$ -enhancement (bulk limit). This trend is observed here for the largest NPs investigated (S9).

Although we did not measure the melting temperature of our NPs directly, according to eq. (3), similar size-dependent trends are expected for  $T_m$  and  $\Theta_D$ <sup>194</sup>:

$$T_m = \frac{2\pi mc^2 R^2 \Theta_D^2 k_B}{h^2} \quad (33)$$

, with  $m$  being the atomic mass,  $c$  Lindemann's constant,<sup>193</sup>  $R$  the bond length,  $k_B$  the Boltzmann constant, and  $h$  the Planck constant.

In the literature<sup>19</sup>, the following factors have been discussed to contribute to the  $\Theta_D$  (or  $T_m$ ) enhancement reported for some nanoscale systems: (i) the presence of a matrix (e.g.  $\gamma$ -Al<sub>2</sub>O<sub>3</sub>) with a higher melting temperature than that of the NPs (e.g. Pt) or a

high melting-temperature coating around the NPs, and/or a support that binds strongly the NPs, (ii) a low density of structural defects within the NPs, good crystallinity, and NP faceting, (iii) a NP/support interface with a low defect density and if possible, an epitaxial relation between the NP/support, and (iv) the absence of a significant number of grain boundaries, twinning and other related structural defects. The sample preparation method is a key factor controlling the structural features affecting this anomalous thermodynamic behavior. Our large NPs ( $> 1.5$  nm) display a trend for the Debye temperature analogous to that reported for the melting temperature of melt-spun superheated In NPs embedded in Al<sup>197</sup> or Pb NPs in Al<sup>217</sup>, namely, increasing  $\Theta_D$  with decreasing NP size. Interestingly, for the same experimental systems, differently prepared samples (ball-milled) with incoherent NP/matrix interfaces displayed the opposite trend, namely, decreasing  $T_m$  with decreasing NP size.<sup>197, 217</sup> These effects were explained in terms of an enhanced internal disorder and non-coherent NP/support interface for the latter set of samples. Cahn<sup>198</sup> attributes superheating effects to a constraint in the amplitude of the vibration of atoms at the NP/support interface, highlighting the importance of an epitaxial relation between the metal NPs and the coating, matrix, or support material. In our case, Fig. 61a might suggest an overall stiffening of our NPs because of the reduced bond-projected bond length fluctuations, although the data shown correspond to the entire NP, not only to atoms at the NP/support interface. On the other hand, it should be kept in mind that our calculations suggest that H reduces the slope of  $(\sigma_d^2)_{th}$ , but they do not include the  $\gamma$ -Al<sub>2</sub>O<sub>3</sub> substrate, which is expected to increase it and thus play a pivotal role in the thermodynamic behavior of supported NPs.

Following the preceding ideas, the enhanced Debye temperatures observed for our large NPs ( $1.5 \text{ nm} < d < 5 \text{ nm}$ ) and their size dependency appears typical of well ordered, faceted NPs with coherent or semi-coherent NP/support interfaces surrounded by a high melting-temperature matrix (or support in our case). The crystallinity of our large NPs can be seen in the EXAFS spectra included in Fig. 57a (4-6 Å range) (S8) as compared to a bulk Pt reference. On the other hand, our small NPs (S1-S6  $\leq 1 \text{ nm}$ ) behave similarly to disordered NPs, for which a decreasing melting temperature was observed with decreasing NP size<sup>197</sup>. Furthermore, when small NPs are considered, not just the NP size, but also their shape might strongly affect their Debye temperature. For example, we obtained different Debye temperatures for NPs of identical size ( $\sim 1 \text{ nm}$  TEM diameter, S3-S6), and a correlation was observed between the number of low coordinated atoms at the NP surface and  $\Theta_D$ , with lower  $\Theta_D$  values for the NPs with the highest surface-to-volume ratio, Fig. 62b. This trend can also be explained by the adsorbate effect, since the higher the surface-to-volume ratio, the stronger the adsorbate effect will be. Our theoretical results on unsupported  $\text{Pt}_{22}\text{H}_M$  revealed that the adsorption of hydrogen increases the mean square bond length fluctuations and its slope [ $(\sigma_d^2)_{\text{th}}$  versus T] with respect to the corresponding values of adsorbate-free  $\text{Pt}_{22}$ , leading to a smaller  $\Theta_D$ , Fig. 62a. Nevertheless, it should be noted that the support, which is expected to have the opposite effect, still needs to be taken into account. Experimentally, it was observed that the flat NPs in S4 displayed a higher  $\Theta_D$  than analogously-sized 3D clusters (S3) with a lower contact area with the  $\gamma\text{-Al}_2\text{O}_3$  substrate. This effect reveals the important role played by the NP/support interface in the thermodynamic properties of small NPs.

Summarizing, our data provide insight into the influence of the geometric structure (size and shape) and environment (adsorbates and substrate) in the thermodynamic properties of metal nanoparticles. In particular, the important role of H<sub>2</sub> desorption in the negative thermal expansion experimentally observed for small supported metal clusters is discussed. Furthermore, size-dependent changes in the Debye temperature observed via EXAFS are explained in terms of the NPs geometrical structure and NP/support interface, but also as a function of intrinsic limitations of the experimental technique used.

## 7.5 Conclusions

A synergistic combination of EXAFS, TEM, NP shape modeling, *ab initio* total energy and molecular dynamics calculations based on DFT have allowed us to gain insight into the structure and thermal properties of Pt NPs supported on  $\gamma$ -Al<sub>2</sub>O<sub>3</sub>. Our main experimental findings are: (i) a size-dependent cross-over from positive to negative thermal expansion with decreasing NP size; (ii) the observation of enhanced experimental Debye temperatures for small Pt NPs bound to  $\gamma$ -Al<sub>2</sub>O<sub>3</sub>; (iii) the different vibrational behavior of large and small metal NPs. Small NPs ( $\leq 1.5$  nm) show a general decrease in the Debye temperature with decreasing NP size associated with the increase in the number of atoms at the NP surface. For large NPs ( $> 1.5$  nm), decreasing Debye temperatures are observed with increasing NP size. For the latter samples, the existence of a decreasing number of atoms within the NPs in contact with the support appears to contribute to the suppression of the matrix-induced  $\theta_D$ -enhancement.



Our computational investigations revealed that the negative thermal expansion of the smallest NPs is not intrinsic, and qualitatively suggests that thermal desorption of chemisorbed hydrogen is at least partially responsible for this effect. The comparison of the calculated bond-projected  $(\sigma_d^2)_{th}$  (based on the Correlated Debye Model) and the total mean squared atomic displacement,  $\langle x^2 \rangle_{th}$  for unsupported and adsorbate-free NPs revealed smaller slopes in the  $(\sigma_d^2)_{th}$  vs. T plots. Hence, the relatively small experimental  $\sigma_d^2$  slopes, and therefore, the unusually large Debye temperatures obtained experimentally, can be partially assigned to the nature of the experimental probe used for its determination, since fluctuations in the bond length perpendicular to the bond, which might be present at low energies, are not accessible to EXAFS. Furthermore, our calculations traced the observed decrease in the mean square atomic displacements or bond-length fluctuations to the possible elimination of low energy vibrational modes of the NPs. We have shown that this might occur due to specific detection limits of the experimental technique used, by the presence of large gaps in the vibrational density of states of the NPs, or due to NP/support interactions.

In this work we have demonstrated that the lattice dynamics and thermal behavior of NPs is affected by their geometric properties and adsorbates. Our experimental data provide important validation for nanothermodynamics theories that, as we have shown qualitatively in this work, should incorporate geometrical effects (size and shape) and environmental interactions (e.g., adsorbate and support) to adequately describe thermal properties at the nanoscale.

## CHAPTER 8: ELECTRONIC PROPERTIES AND CHARGE TRANSFER PHENOMENA IN Pt NANOPARTICLES SUPPORTED ON $\gamma$ -Al<sub>2</sub>O<sub>3</sub>: SIZE, SHAPE, SUPPORT, AND ADSORBATE EFFECTS

### 8.1 Introduction

Striking changes in the physical and chemical properties of small metal NPs have been reported<sup>9, 19-21, 30, 31, 122</sup>, and in some cases assigned to size-dependent modifications of their electronic properties, including metal/non-metal transitions, the discretization of energy levels, and rehybridization of *spd* orbitals.<sup>9, 18</sup> Nevertheless, in addition to intrinsic changes in the NP properties brought about by specific geometrical features (e.g. NP size and shape), the role of external influences such as adsorbate and support effects must also be taken into consideration.

Although significant effort has been dedicated to the investigation of geometric and environmental effects on the electronic properties of metal NPs<sup>23, 204, 218-224</sup>, some discrepancies still remain in the literature regarding the interpretation of certain experimental trends<sup>223, 225-228</sup>. These are due in part to the challenge of synthesizing geometrically well-defined target material systems, the difficulty of separating the different influences to a given electronic property (since some correlations exist among them), and the complexity of real-world experimental NP supports, making related modeling descriptions difficult.

In situ XANES measurements have been proven valuable for the study of intrinsic and extrinsic effects on the electronic properties of NPs,<sup>23, 182, 204, 218-223, 226, 229-233</sup> since this technique is sensitive to unoccupied electronic states. The following differences have been observed when comparing XANES data from nanoscale and bulk systems: (i) modifications in the intensity of the absorption edge peak (or white line, WL), (ii) an

increase/decrease in the width of the WL, and (iii) a shift in the energy of the absorption edge. The extent of these modifications was found to be strongly influenced by extrinsic effects. More specifically, changes in  $L_3$  and  $L_2$  XANES spectra of metals upon chemisorption can be explained in terms of orbital hybridization, charge transfer, and metal-adsorbate scattering.

Although general agreement exists on the correlation between the integrated area of the adsorption peak and the amount of chemisorbed hydrogen<sup>223, 225-228</sup>, it is still unclear whether the peak energy is influenced by the number of H adsorption sites on the NP surface, the presence of co-adsorbates, and the NP size/shape. In the absence of adsorbed hydrogen, a narrowing of the electron density of states (DOS) and a shift of the d-band center towards the Fermi level ( $E_F$ ) have been theoretically described by comparing unsupported  $Pt_6$  NPs and Pt(111), highlighting that intrinsic effects must also be considered.<sup>223</sup>

In addition to adsorbate effects, the interaction of the NPs with the underlying support must also be addressed. This is, however, a difficult task, since due to specifics of the most common NP synthesis approaches used, a direct comparison of the influence of different supports on NPs of identical geometry (same size and shape) cannot normally be conducted, leading to a convolution of support (extrinsic) and size/shape (intrinsic) effects. Some groups report a lack of correlation between the intensity of the absorption peak, integrated area or energy, and the type of NP support<sup>182, 229, 234</sup>, exclusively assigning the changes observed to adsorbate chemisorption. On the other hand, a theoretical study of a  $Pt_6$  cluster in a zeolite-LTL pore revealed a broadening of the WL for the supported cluster with respect to bare  $Pt_6$

and a concomitant decrease in the WL intensity in order to maintain the overall density of d-states constant<sup>204</sup>.

For Pt NPs on carbon nanotubes, the smaller WL of the NPs as compared to bulk Pt was assigned to charge redistribution between C-2p and Pt-5d states, which did not lead to the loss of charge<sup>219</sup>. For Pt NPs on SiO<sub>2</sub>, the observed increase in the WL intensity was assigned to charge transfer from Pt to SiO<sub>2</sub><sup>219</sup>. This is another controversial aspect in the literature, since some groups explain the observed changes in the XANES data (e.g. energy shift) based on charge transfer phenomena (to/from adsorbates or the support), while others on the formation of metal-adsorbate or metal/support bonds (charge redistribution) leading to changes in the electron density of states near the Fermi level.<sup>226, 235</sup> Furthermore, theoretically predicted fluctuating cluster-substrate interactions and charge transfer phenomena for Pt<sub>10</sub> on  $\gamma$ -Al<sub>2</sub>O<sub>3</sub> were correlated with the positive energy shifts experimentally observed with decreasing NP size and decreasing measurement temperature.<sup>23</sup>

The present study takes advantage of state-of-the-art nanostructure fabrication, and characterization methods to gain deep insight into the role played by the geometrical structure of NPs (size and shape), support, and surface adsorbates, on their electronic properties. Specifically, we used size- and shape-selected Pt NPs (produced via inverse micelle encapsulation methods) supported on  $\gamma$ -Al<sub>2</sub>O<sub>3</sub> combined with *in situ* XANES, and cluster shape modeling. The ability of tuning the d-electron density in supported NPs via a rational geometrical design is key for the ultimate control of catalytic properties, since reactivity is strongly influenced by the interaction of d-orbitals of metals with valence orbitals of reactants.

## 8.2 Experimental and theoretical methods

### 8.2.1 Sample preparation

Size- and shape-selected Pt NPs were prepared via micelle encapsulation. Poly(styrene)-block-poly(2vinylpyridine) [PS-P2VP] diblock copolymers were dissolved in toluene to form inverse micelles. Size-selected Pt NPs are created by dissolving  $\text{H}_2\text{PtCl}_6$  into the polymeric solution. Subsequently, the nanocrystalline  $\gamma\text{-Al}_2\text{O}_3$  support (Alfa Aesar, average crystalline size  $\sim 40$  nm) is added. The Pt loading is 1 % by weight. The encapsulating ligands are eliminated by heating in 50 %  $\text{O}_2$  balanced by He at 648 K for 24 hours. Different NP sizes can be obtained by changing the molecular weight of the head (P2VP) of the encapsulating polymer, the metal/P2VP ratio (micelle loading), and the post-preparation annealing treatment and atmosphere<sup>5</sup>. Our micellar synthesis normally leads to 3D-like NP structures. Nevertheless, the NP shape can be changed from 3D to 2D by decreasing the metal loading into the initially spherical polymeric micelles. Further details on the sample preparation, synthesis parameters, and TEM characterization can be found in Refs. 5, 28, 29, 41, 81 and Table 16.

### 8.2.2 Structural, and electronic characterization (XAFS)

Pt  $L_3$ -edge XAFS data were acquired at beamline X18B of the NSLS at BNL in transmission mode. The XAFS samples were prepared by pressing the Pt/ $\gamma\text{-Al}_2\text{O}_3$  powders into thin pellets which were mounted in a cell described previously,<sup>236, 237</sup> that permitted sample heating via an external PID controller, liquid nitrogen cooling, as well as the continuous flow of gases during data acquisition. A Kapton window in the cell allows both in situ x-ray transmission and fluorescence measurements. A bulk Pt foil

was measured simultaneously with all samples for energy alignment and calibration purposes. Multiple scans were collected at each temperature of interest and averaged in order to improve the signal-to-noise ratio. Measurements were made at different temperatures under H<sub>2</sub> (50 % H<sub>2</sub> balanced with He for a total flow rate of 50 ml/min, S1-S9) and He (S2) atmospheres. The sample measured in He was first reduced in H<sub>2</sub> at 648K. Subsequently, the H<sub>2</sub> environment was replaced by He and XAFS data were acquired at different temperatures during cooling from 648 K to 173 K.

Quantitative determination of the average NP shape was carried out by analyzing low temperature (166-188 K) EXAFS data up to the 4<sup>th</sup> nearest neighbor contribution, including multiple scattering paths as described in Refs. 5, 41 and references therein. The  $r$  fitting range was 1.8 Å to 5.7 Å. The shapes of our Pt NPs have been resolved by matching structural information obtained experimentally via EXAFS (coordination numbers up to the 4<sup>th</sup> nearest neighbor, N<sub>1</sub>-N<sub>4</sub>) and TEM (NP diameter,  $d$ ) to analogous data extracted from a self-generated database containing ~4000 model fcc NP shapes<sup>5, 41</sup>. The shape selection procedure is described in chapter 7.

All of our small NP (diameter < 1.5 nm) samples are characterized by narrow size distributions according to in-depth TEM analysis, while wider size distributions were observed for the larger clusters (Table 16 and Ref. 41). In order to determine the most representative NP shape for each of the samples, we have used volume-weighted (small NPs, S1-S6) TEM diameters. In general, the use of the volume-weighted diameters ( $d_{\text{average}} = \sum (d \cdot w) / \sum w$ , where the weighting factor  $w$  is the NP volume which is proportional to  $d^3$ ) is preferred when comparing TEM and EXAFS structural







information, since EXAFS is a volume-weighted technique. Detailed structural characterization of the present samples is given in Ref. 5, 41, and 5.

Table 16 shows the shapes that best fitted the EXAFS and TEM data for each of the samples investigated and contains information on the ratio of the number of Pt atoms at the NP surface and perimeter to the total number of atoms within each NP ( $N_s/N_t$ ) and that of the number of Pt atoms in contact with the support to the total number of atoms within a NP ( $N_c/N_t$ ) extracted from the selected model NP shapes. As it is described in more detail in Ref. 5, for each of the samples containing small Pt NPs, only 2-3 similar shapes were in good agreement with the EXAFS coordination numbers and TEM diameter (including the experimental error margins). No shapes are displayed in this manuscript for the samples containing large NPs (S7-S9), since a large number of cluster shapes are in agreement with the EXAFS coordination numbers and TEM diameters<sup>200</sup>.

Changes in the morphology of our samples as a function of temperature have not been accounted for in our analysis since our EXAFS measurements were conducted up to a maximum temperature of 648 K, which is the same temperature used for sample calcination (24 h) prior to the *in situ* spectroscopy analysis. If any changes in the NP morphology (size and/or shape) were to occur at 648 K, they should have already taken place before the XAFS measurements.

In order to gain insight into the electronic properties of Pt NPs, we present here XANES spectra from the Pt L<sub>3</sub> absorption edge. These data provide information on the binding energies of 2p electrons (2p<sub>3/2</sub> initial state) and the unoccupied “d” electron density of states near the Fermi level (d<sub>5/2</sub> + d<sub>3/2</sub> states).

Table 16: Parameters used for the synthesis of micellar Pt NPs, including polymer type (PS-PVP) and the ratio ( $L$ ) between the metal salt loading and the molecular weight of the polymer head (P2VP). Also included are the mean TEM diameters from Ref. 41. By comparing structural information obtained via EXAFS (1<sup>st</sup>-4<sup>th</sup> nearest neighbor coordination numbers) and TEM (NP diameters) with a database containing fcc-cluster shapes, the ratio of the number of surface atoms to the total number of atoms in a NP ( $N_s/N_t$ ) and the ratio of the number of atoms in contact with the substrate to the total number of atoms ( $N_c/N_t$ ) were obtained (see details in Ref. 41). The NP shapes obtained for large NPs in S7-S9 are not shown in this table due to the large shape degeneracy for the obtained coordination number and TEM diameter.

Sample Name	Polymer	$L$	TEM diameter (nm)	Model cluster shapes	$N_t$	$N_s/N_t$	$N_c/N_t$
S1	PS(27700)-P2VP(4300)	0.06	$0.8 \pm 0.2$		22	0.86	0.55
S2	PS(27700)-P2VP(4300)	0.1	$0.8 \pm 0.2$		44	0.84	0.23
S3	PS(27700)-P2VP(4300)	0.2	$1.0 \pm 0.2$		85	0.74	0.18
S4	PS(16000)-P2VP(3500)	0.05	$1.0 \pm 0.2$		33	0.82	0.55
S5	PS(16000)-P2VP(3500)	0.1	$1.0 \pm 0.2$		55	0.75	0.16
S6	PS(16000)-P2VP(3500)	0.2	$1.0 \pm 0.2$		140	0.64	0.13
S7	PS(16000)-P2VP(3500)	0.4	$1.8 \pm 1.5$				
S8	PS(27700)-P2VP(4300)	0.3	$3.3 \pm 1.5$				
S9	PS(27700)-P2VP(4300)	0.6	$5.4 \pm 3.0$				

Since the intensity and integrated area of the Pt-L<sub>3</sub> absorption peak are considered to be proportional to the density of unoccupied 5d electronic states, they can



be used to extract information on d-level electronic charge redistributions<sup>238</sup>. It should be noted that our experimental set-up, along with our calibration procedures, allows us to discern relative energy shifts in the XANES peak position with sensitivity of about 0.1 eV. In order to obtain the peak position, the experimental data were fitted with a spline curve. In the following section, we will also provide information on the changes of the area of the Pt-L<sub>3</sub> absorption peak. Different methods have been used in the literature to calculate this area before and after NP/adsorbate exposure<sup>182, 222, 223, 226, 227, 229, 239-242</sup>. Some authors first aligned all the spectra and subsequently calculated their respective difference, while others<sup>241, 242</sup> used the area of the second feature (peak B in Fig. 69) observed in raw (not artificially aligned)  $\Delta$ XANES spectra as the representative parameter.<sup>182, 222, 223, 226, 227, 229, 239, 240</sup> We have followed the second approach for the calculation of the  $\Delta$ XANES areas shown within the main text of this manuscript.

In particular,  $\Delta$ XANES areas were obtained by subtracting the XANES spectrum of the NPs at 648 K from that of the same sample measured at a given lower temperature, both in hydrogen. In the literature, some authors have shown similar  $\Delta$ XANES plots using as reference spectra from the Pt foil<sup>182, 223</sup>, or NPs measured under He<sup>223, 226, 239</sup> or in vacuum<sup>182, 222, 227-229, 231</sup>. Due to the inherent experimental difficulty of preventing the effect of trace oxygen and moisture possibly leading to the oxidization of small Pt NPs in conventional XAFS-compatible cells in the absence of H<sub>2</sub>, we decided to use as reference of the adsorbate-free NP state, our highest temperature XANES spectra measured under H<sub>2</sub>,<sup>227</sup> since a minimum H coverage on the NP surface is expected under those conditions, and lack of chemisorbed oxygen and/or NP oxidation is ensured under the continuous H<sub>2</sub> flow employed here.

### 8.3 Results

The effects of the Pt NP size, shape, support, and chemical environment (adsorbates) on its electronic properties were investigated *in situ* via Pt-L<sub>3</sub> edge XANES. Fig. 63 shows the normalized absorption coefficient corresponding to the Pt-L<sub>3</sub> edge of Pt NPs with different sizes supported on  $\gamma$ -Al<sub>2</sub>O<sub>3</sub> measured in H<sub>2</sub> at RT and also low temperature (LT) after *in situ* NP reduction at 648K. Two main differences were observed for the samples containing small NPs with respect to bulk Pt: (i) an increase in the width of the absorption peak, (ii) a shift in the absorption peak to higher energy.

The effect of size and shape of the NPs are shown in Fig. 64, and Fig. 65. The insets correspond to the model shapes that best represent the NPs in samples S1-S4. By comparing the NPs with the same TEM diameter, the energy shift was found to be more significant for the NPs with 2D shape (S1 as compared to S2 and S4 as compared to S3), Fig. 64. In particular, for samples containing NPs of identical average size (TEM diameter)<sup>5, 41</sup> but different shape, the following energy shifts were measured:  $\Delta E = +0.5$  eV for S1 with respect to S2 ( $0.8 \pm 0.2$  nm), and  $+0.7$  eV for S4 with respect to S3 ( $1.0 \pm 0.2$  nm) (Fig. 64).

In addition by comparing the NPs with similar shape but different TEM diameter it was found that smaller NPs show larger energy shift (Fig. 65). For instance, S2 and S3 have the same octahedron shape but different sizes. The energy shift and peak broadening are larger for S2 as compared to S3 due to smaller size of S2 as compared to S3.

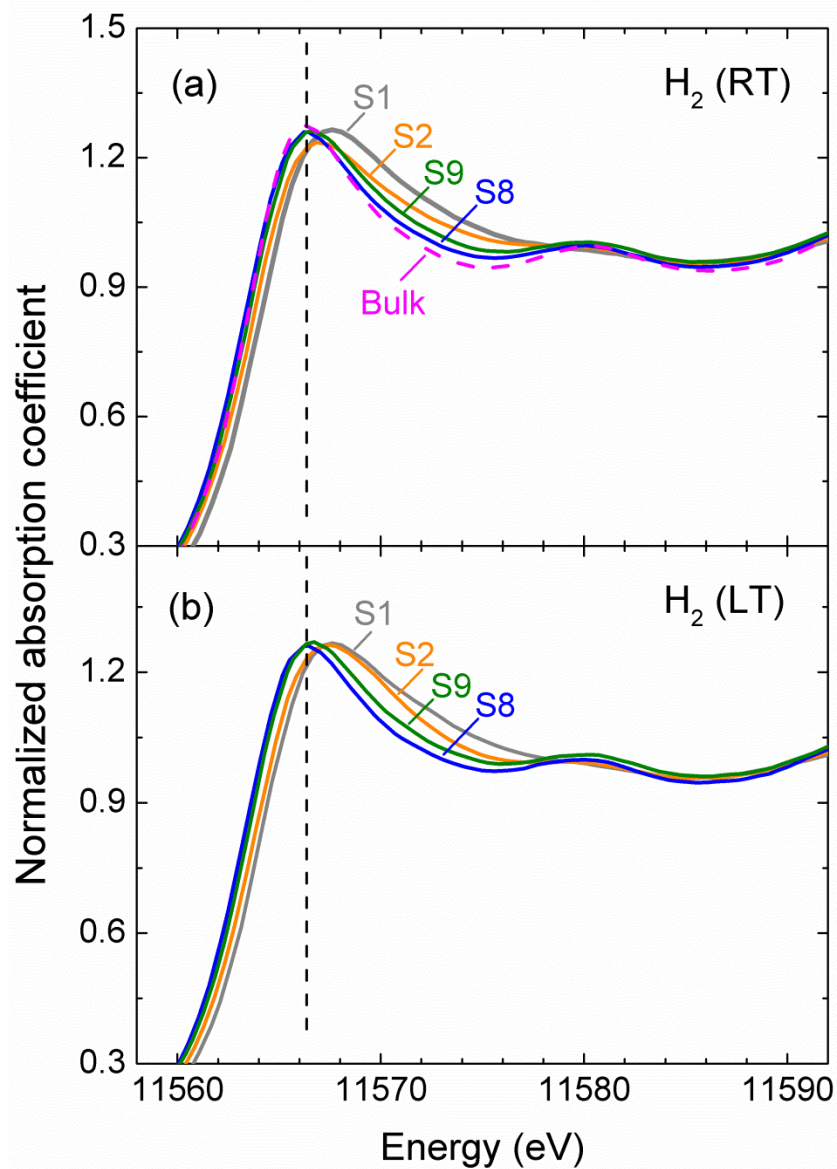


Fig. 63: Normalized absorption coefficient,  $\mu(E)$ , versus energy (XANES region) for the Pt- $L_3$  edge of Pt NPs. The samples were measured at (a) RT and (b) low temperature (173 K for S1 and S2, 180 K for S8 and S9) in  $H_2$  after reduction. Similar data from a Pt foil (bulk) are also displayed for reference in (a).

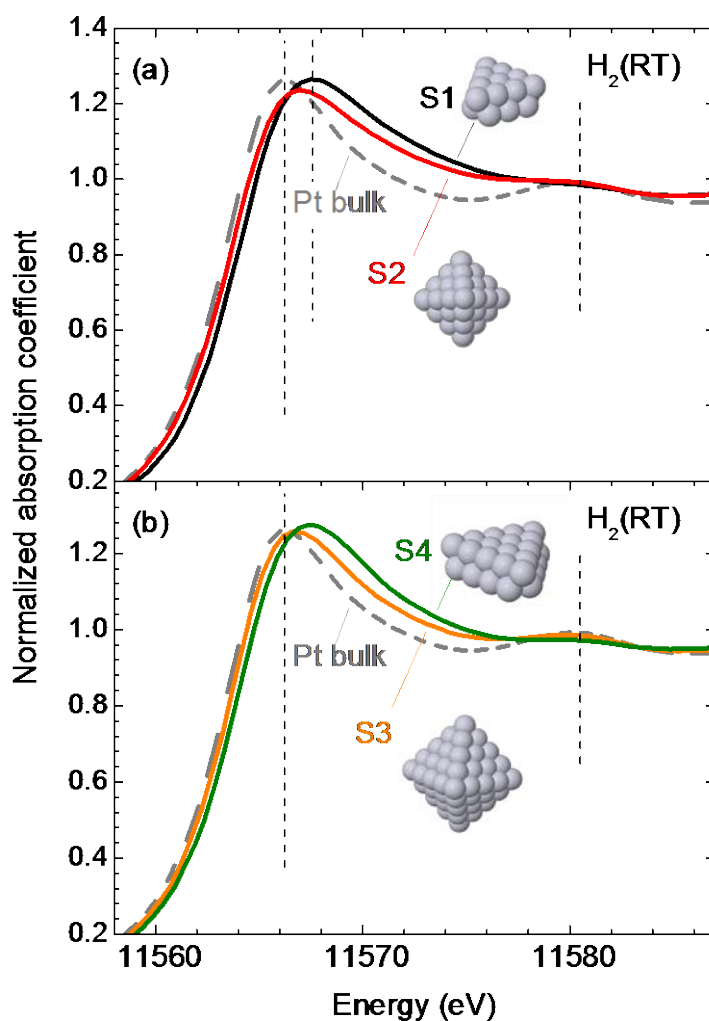


Fig. 64: Normalized absorption coefficient,  $\mu(E)$ , versus energy (XANES region) for the Pt-L<sub>3</sub> edge of Pt NPs (~0.8 nm for S1 and S2, ~1 nm for S3 and S4) on  $\gamma$ -Al<sub>2</sub>O<sub>3</sub>. Samples were measured at RT in H<sub>2</sub> after reduction. Similar data from a Pt foil (bulk) are also shown for reference.

Furthermore, for samples of identical shape (2D) but different size, e.g.  $0.8 \pm 0.2$  nm NPs in S1 and  $1.0 \text{ nm} \pm 0.2$  in S4, Fig. 65(a), an increase in the width of the absorption peak was observed with decreasing NP size. The same was observed for the 3D NPs in Fig. 65(b). As expected, no drastic changes were observed in the XANES spectra of the samples containing large Pt NPs (S8, S9 > 3 nm) as compared to bulk Pt, Fig. 65(c).

In order to gain insight into the role of the adsorbate, the same sample S2 was measured in H<sub>2</sub> and He at low temperature (173 K). As can be seen in Fig. 65(d) in H<sub>2</sub>, a broader absorption feature, higher WL intensity, and a larger energy shift with respect to the He data were observed. Complete saturation of the NP surface with H<sub>2</sub> is expected under these measurement conditions.

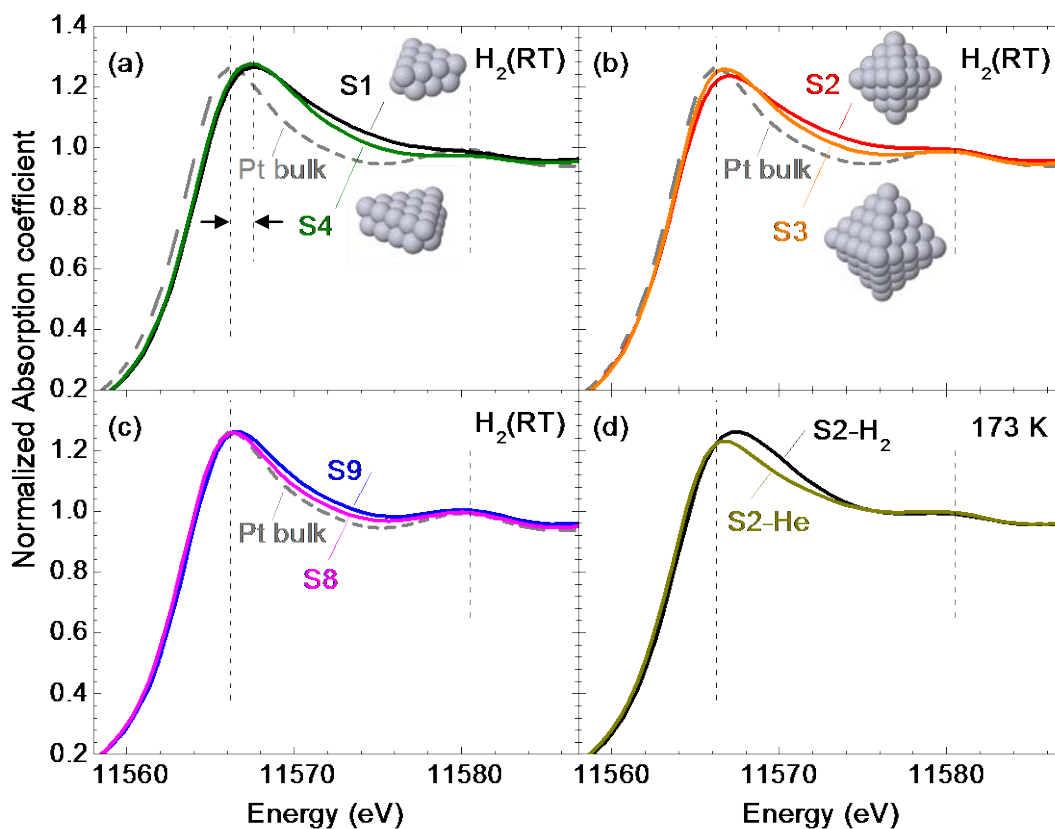


Fig. 65: Normalized absorption coefficient,  $\mu(E)$ , versus energy (XANES region) for the Pt-L<sub>3</sub> edge of Pt NPs on  $\gamma$ -Al<sub>2</sub>O<sub>3</sub>. The samples in (a-c) were measured at RT in H<sub>2</sub> after reduction (S1-S4). Similar data from a Pt foil are also displayed for reference. Sample S2 was measured in H<sub>2</sub> and He at 173 K (d).

Fig. 66 displays temperature-dependent XANES data from Pt NPs with different sizes and shapes measured under an identical H<sub>2</sub> atmosphere: ~ 0.8 nm (S1, S2), ~ 1.0 nm (S3, S4), ~ 3.3 nm (S8), and ~ 5.4 nm (S9).

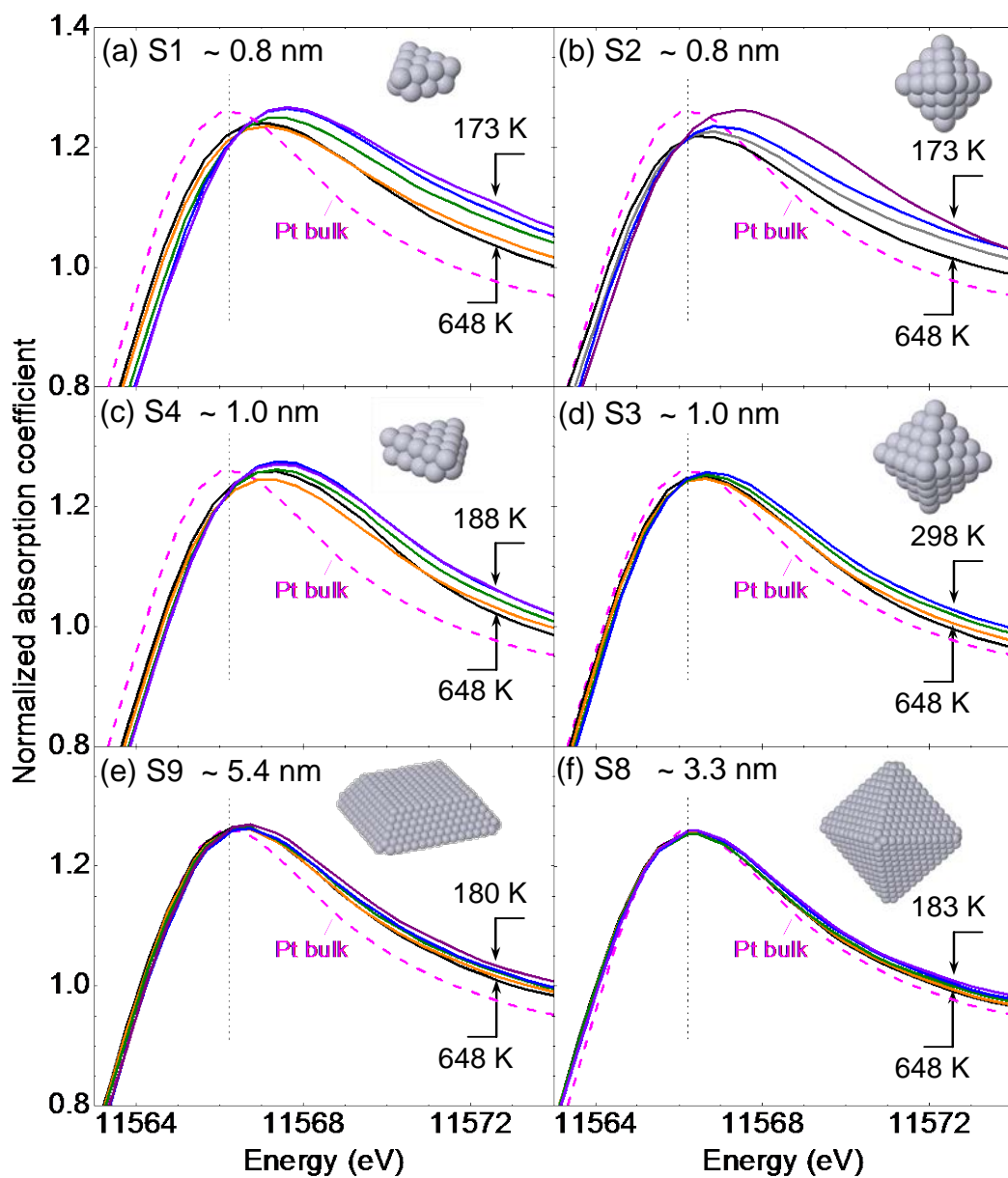


Fig. 66: Normalized absorption coefficient,  $\mu(E)$ , versus energy (XANES region) for the Pt- $L_3$  edge of Pt NPs on  $\gamma$ - $Al_2O_3$ : (a) S1, (b) S2, (c) S4, (d) S3, (e) S9, (f) S8. Temperature dependent data acquired in  $H_2$  from 173 K to 648 K are shown for all samples. The insets correspond to model NP shapes representative of the NPs in each of the samples. For the large NPs (S8 and S9), a large degeneracy of shapes was obtained, and the models shown in (e,f) are only a guide of the possible NP structures.

The insets correspond to the model NP shapes extracted from the analysis of low-temperature (173-188 K) EXAFS data. With increasing temperature from 173 K to 648 K, a decrease in the WL intensity, a shift towards lower energy, and a decrease in the line width were observed.

A linear correlation between the energy shift of the absorption edge peak (with respect to bulk Pt) and its total area and the first nearest neighbor coordination number ( $N_1$ ) was observed at RT: decreasing values with increasing  $N_1$ , Fig. 67(a),(b), respectively.

The blue shift of the WL observed for the NP samples relative to the Pt foil is most noticeable for S1 (+1.35 eV) but also present for the other samples (+1.25 eV for S4 and +0.8 for S2). A similar trend was observed when the former energy shifts are plotted versus the TEM NP diameter, Fig. 67(c), corroborating that the smallest NPs are the most affected by intrinsic (size and shape) as well as extrinsic (adsorbate and support) effects. It should be noted that the overall trend is the same if one uses the TEM diameter as representative size parameter, Fig. 67(c), or the EXAFS NP size [e.g. 1<sup>st</sup> NN CN, Fig. 67(a)], although the dependence is slightly different, with a more abrupt change observed as a function of the NP diameter for NPs below ~1.5 nm. The difference is attributed to the fact that the EXAFS data ( $N_1$ ) also contain structural information about the NP shape (not only its diameter), which, as will be discussed in more detail below, might play a role in the effect observed, via for example NP-support charge transfer phenomena for clusters with a large fraction of atoms in contact with the support. Analogous XANES data acquired at low-temperature (166 K-188 K) in H<sub>2</sub> are presented in Fig. 68.

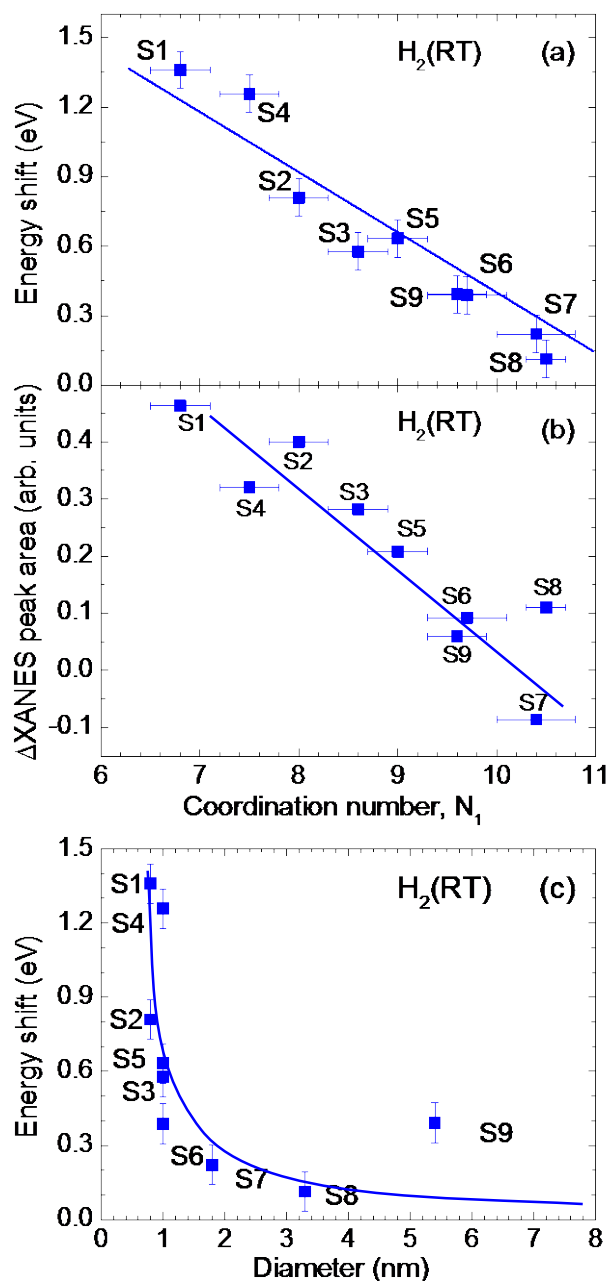


Fig. 67: Shift in the energy of the Pt-L<sub>3</sub> absorption edge of Pt NPs on  $\gamma$ -Al<sub>2</sub>O<sub>3</sub> with respect to a bulk Pt reference as a function of: (a) the 1<sup>st</sup> nearest neighbor coordination number ( $N_1$ ), (c) the TEM NP diameter from Ref. 41 (b) Evolution of the  $\Delta$ XANES area (peak B) of NPs with different sizes as a function of  $N_1$ . The  $\Delta$ XANES plots were obtained by subtracting XANES spectra measured under H<sub>2</sub> at 648 K (nearly adsorbate-free) from those measured at RT under H<sub>2</sub> (nearly H-saturated).



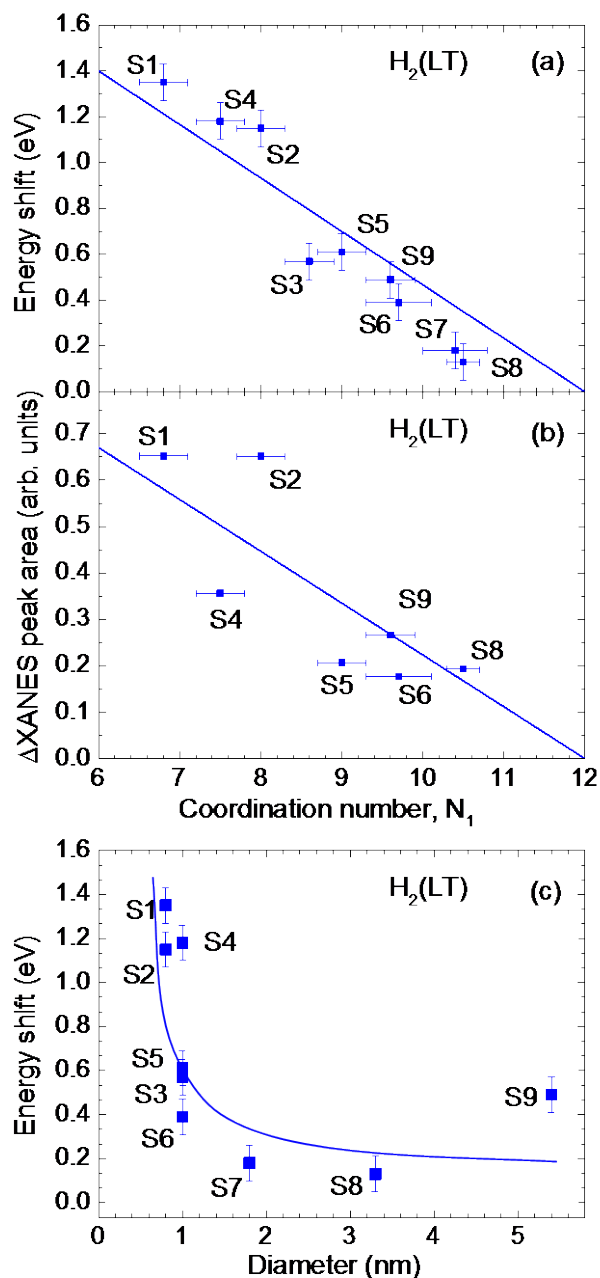


Fig. 68: Shift in the energy of the Pt-L<sub>3</sub> absorption edge of Pt NPs on γ-Al<sub>2</sub>O<sub>3</sub> with respect to a bulk Pt reference as a function of: (a) the 1<sup>st</sup> nearest neighbor (NN) coordination number ( $N_1$ ) and (c) the TEM NP diameter from Ref. 41 (b) Evolution of the ΔXANES area (peak B) of NPs with different sizes as a function of  $N_1$ . The ΔXANES plots were obtained by subtracting XANES spectra measured in H<sub>2</sub> at 648 K (nearly adsorbate-free) from those measured at low temperature under H<sub>2</sub> (H-saturated). The minimum low temperature achieved in our experimental setup was slightly different for different samples: 173K (S1, S2), 188K (S4), 183K (S5, S6), 166 K (S7), 180 K (S8,S9).

In order to gain further insight into the role of adsorbed hydrogen on the electronic properties of our small fcc Pt NPs,  $\Delta$ XANES plots were constructed. Fig. 69(a) displays XANES data from NPs with different sizes measured in H<sub>2</sub> at RT after subtraction of the 648 K spectrum of the respective NP sample. As was shown in our recent work<sup>41</sup>, significant H<sub>2</sub> desorption was predicted above 450 K (upon heating in an H<sub>2</sub> atmosphere), and therefore, it is reasonable to assume that the XANES data measured at 648 K are the ones least affected by chemisorbed hydrogen, and can therefore be used as reference as the state of the NPs with the minimum hydrogen coverage. Fig. 69(a) provides information on the H<sub>2</sub> effect and effective hydrogen coverage on the surface of NPs of different sizes, with increasing spectral area with decreasing NP size. Quantitative analysis of these data will be shown later. Similar  $\Delta$ XANES plots are included in Fig. 69(b) and (c), but in those cases the 648 K XANES spectra were subtracted from the data acquired in H<sub>2</sub> at different temperatures for samples S1 (b) and S9 (c) (the smallest and largest NPs). It should be noted that although the spectral features change drastically with temperature in the EXAFS region, XANES data are not strongly affected by thermal effects<sup>204</sup>, and therefore, comparisons such as the one described above are justified.

For the small NPs in S1, a clear trend of increasing spectral area with decreasing measurement temperature was detected, which correlates with the higher hydrogen coverage at the lowest measurement temperatures. As expected, due to the significantly lower surface to volume ratio of the NPs in S9, the adsorbate effect in Fig. 69(c) is small.

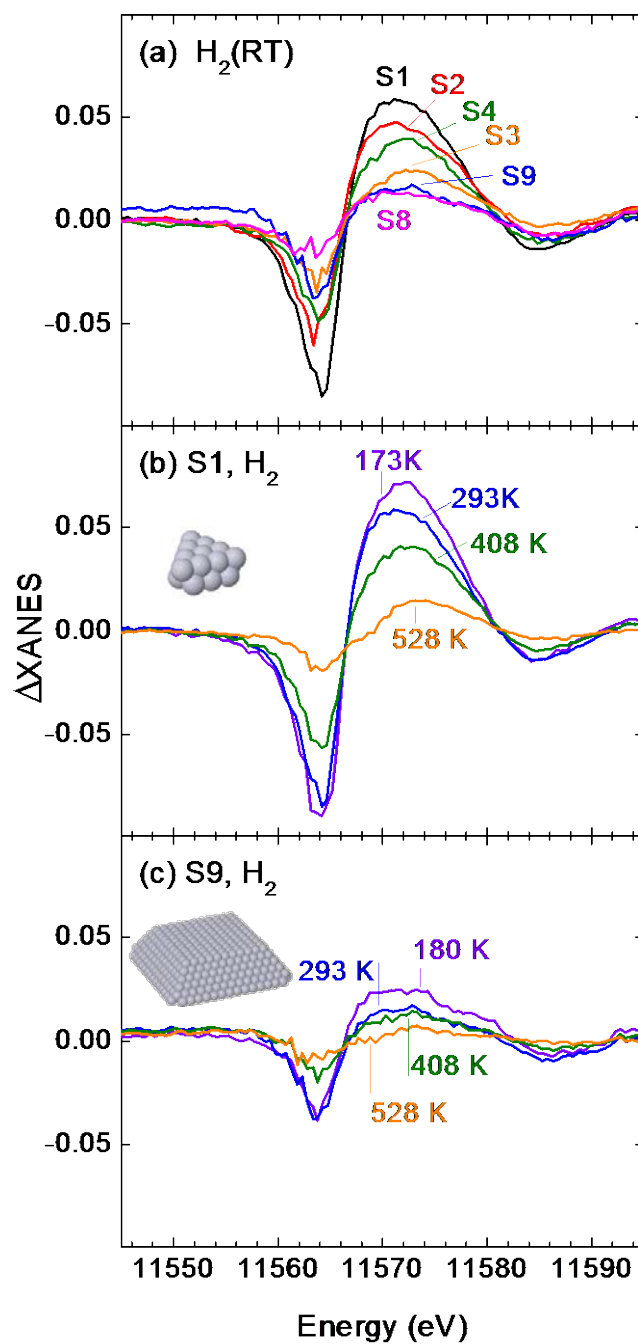


Fig. 69: Difference XANES spectra ( $\Delta$ XANES) from the Pt-L<sub>3</sub> absorption edge of Pt NPs on  $\gamma$ -Al<sub>2</sub>O<sub>3</sub> displayed as a function of the NP size (a), and the measurement temperature for NPs in S1 (b) and S9 (c). All measurements were conducted in a H<sub>2</sub> environment. In all plots, the 648 K data are subtracted from those acquired at lower temperatures [RT in (a) and variable temperatures in (b) and (c)] in order to deconvolute the adsorbate effect, since no significant H<sub>2</sub> effect is expected at 648 K.

To evaluate the relative contribution of NP-adsorbate and NP-support charge transfer and redistribution phenomena, we have used structural information obtained from the model NP shapes that best represent our samples (see Table 16). In particular, the relative number of atoms at the NP surface ( $N_s/N_t$ ) and that of atoms in contact with the support ( $N_c/N_t$ ) are considered. Fig. 70(a) summarizes the evolution of the absolute energy of the absorption peak with increasing measurement temperature for several of our samples. The decrease in the energy shift observed for the small NPs (e.g. S1, S2, S4) with increasing annealing temperature is at least partially assigned to the loss of  $H_2$ . The difference in the energy of the Pt-L<sub>3</sub> XANES absorption peak of our Pt NPs at RT with respect to the measurement at 648 K (lowest H coverage) versus  $N_s/N_t$  is shown in Fig. 70(b). The highest relative energy shifts were obtained for the NPs with the largest number of low-coordinated surface atoms (S1, S2). Analogous energy shift data comparing low-temperature (166 K-188 K) spectra and 648 K spectra measured in  $H_2$  are included in Fig. 71a. A similar result is obtained when the integrated  $\Delta$ XANES peak area is considered, Fig. 71b.

As was mentioned before, the energy shifts observed at 648 K for the NP samples with respect to bulk Pt might be considered nearly independent of adsorbate effects (lowest effective residual hydrogen coverage due to the low sticking coefficient of hydrogen at this temperature), allowing us to decouple two extrinsic environmental factors, adsorbate and support effects.

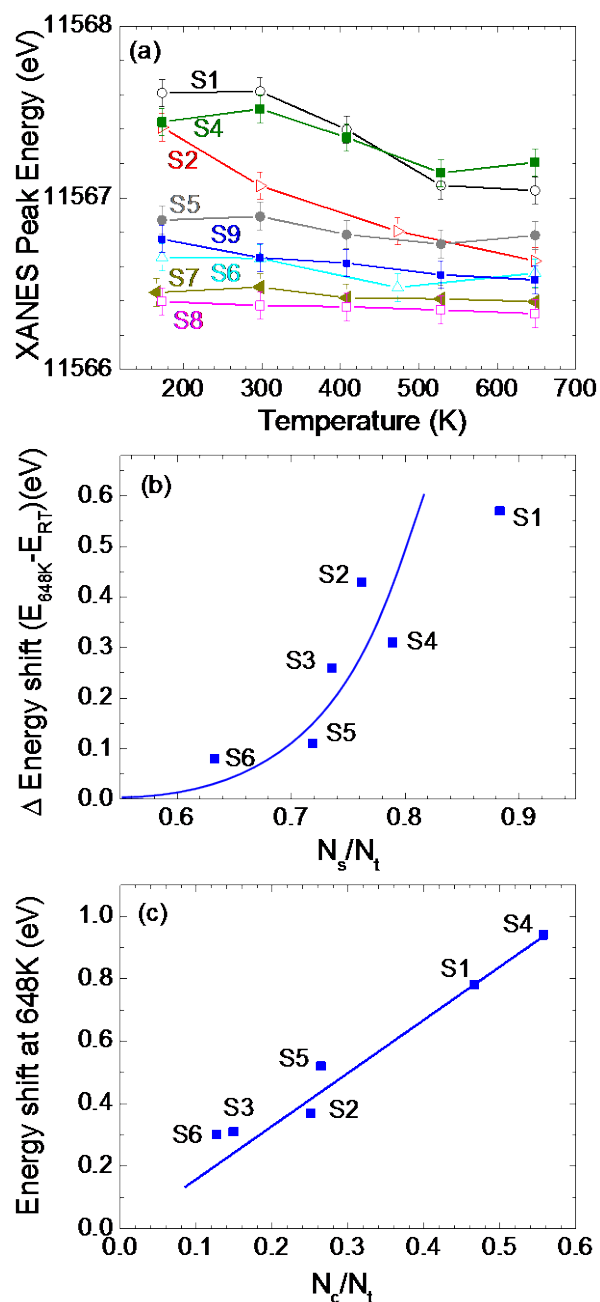


Fig. 70: (a) Temperature dependence of the absorption peak energy (Pt-L<sub>3</sub>) of a selected set of Pt NPs on  $\gamma$ -Al<sub>2</sub>O<sub>3</sub> samples: S1, S2, S4-S9. All samples were measured in H<sub>2</sub> after reduction. (b) Shift in the Pt-L<sub>3</sub> absorption peak energy of NPs with different sizes measured in H<sub>2</sub> at RT with respect to data from the same samples acquired at 648 K plotted versus the relative number of surface atoms in each NP ( $N_s/N_t$ ). A bulk Pt foil has been used as reference. (c) Energy shift of the Pt-L<sub>3</sub> absorption edge of Pt NPs measured at 648 K with respect to bulk Pt (RT) versus the relative number of atoms within the NPs in contact with the NP support ( $N_c/N_t$ ). All samples were measured in H<sub>2</sub> after NP reduction.

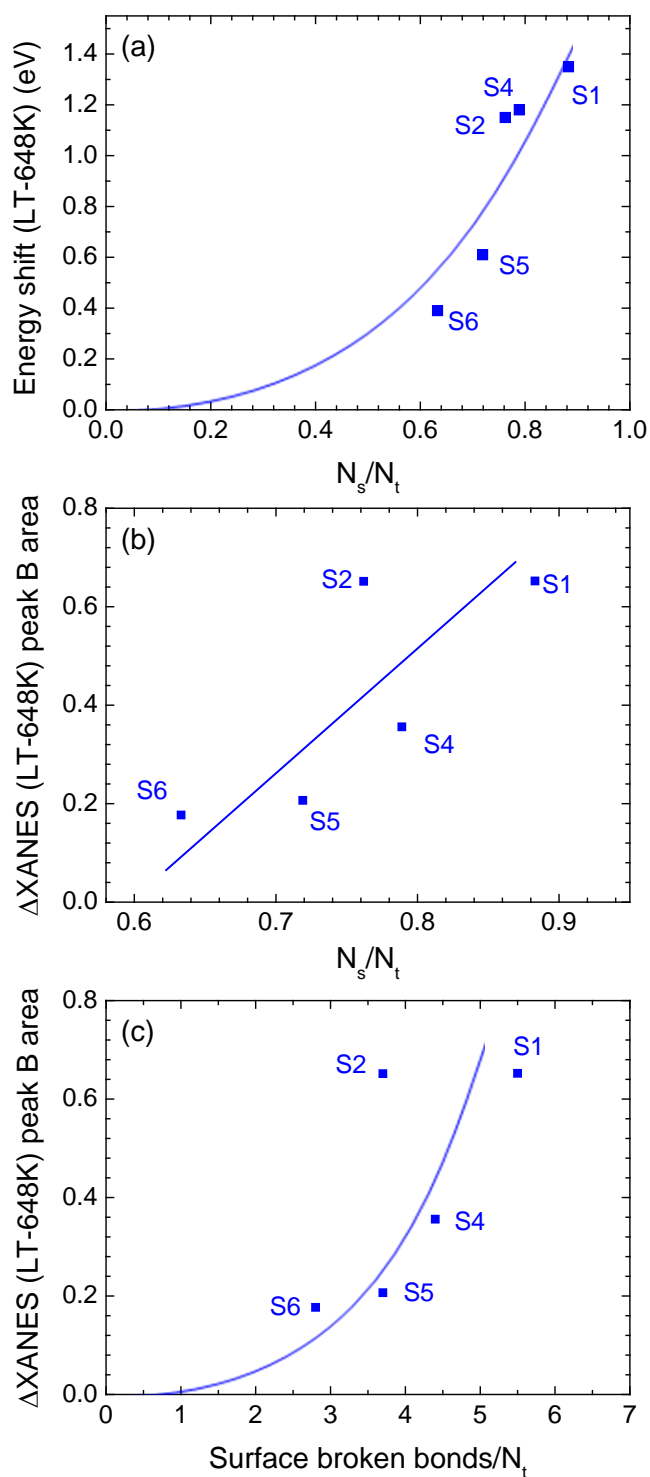


Fig. 71: (a) Energy shift (LT-648 K) versus  $N_s/N_t$ . (b)  $\Delta$ XANES (LT-648 K) peak B area versus  $N_s/N_t$ , and (c) versus the number of broken bonds at the NP surface normalized by the total number of atoms within the NP ( $N_t$ ) for S1-S6.

When the high temperature energy shifts (with respect to the Pt foil) are plotted versus the relative number of atoms within our NPs in contact with the support ( $N_c/N_t$ ), Fig. 70(c), a linear correlation is observed, with the largest shifts being associated to the samples with 2D shapes, e.g., those with the largest interfacial areas (S1, S4).

To extract additional information on the adsorbate (hydrogen) effect, the evolution of the  $\Delta$ XANES area of our Pt NP samples with increasing annealing temperature is shown in Fig. 72(a). The peak areas displayed here correspond to the feature labeled as “peak B” in the inset of Fig. 72(a). A linear trend was observed for all samples, with decreasing area with increasing temperature, i.e., with decreasing H coverage. In addition, a size-dependent trend was also observed, since different slopes were obtained for NPs with different average size, with the largest slopes corresponding to the smallest NPs (S1, S2). An analogous linear trend was observed when the former areas were normalized by the relative number of atoms at the NP surface ( $N_s/N_t$ ). Fig. 72(b) displays the former peak B area of samples S1-S5 normalized by  $N_s/N_t$  and by the peak B area of S6 (largest NPs available with well-defined shape) measured at 183 K to ensure the maximum initial H<sub>2</sub> coverage. After the former normalization, (carried out only for the narrowly size distributed NPs with well-defined average shape) the data sets corresponding to samples of different geometry do not overlap. For example, even at the lowest measurement temperature, when complete saturation of the NP surface with hydrogen is expected, three different normalized areas corresponding to three different maximum hydrogen saturation coverages were obtained. The different maximum hydrogen saturation coverages are associated to samples with different total number of atoms according to our model shapes, with the largest NPs shown (S5 with

85 atoms and S6 with 140 atoms) having the lowest maximum H coverage, namely one hydrogen atom per surface Pt atom for S6.

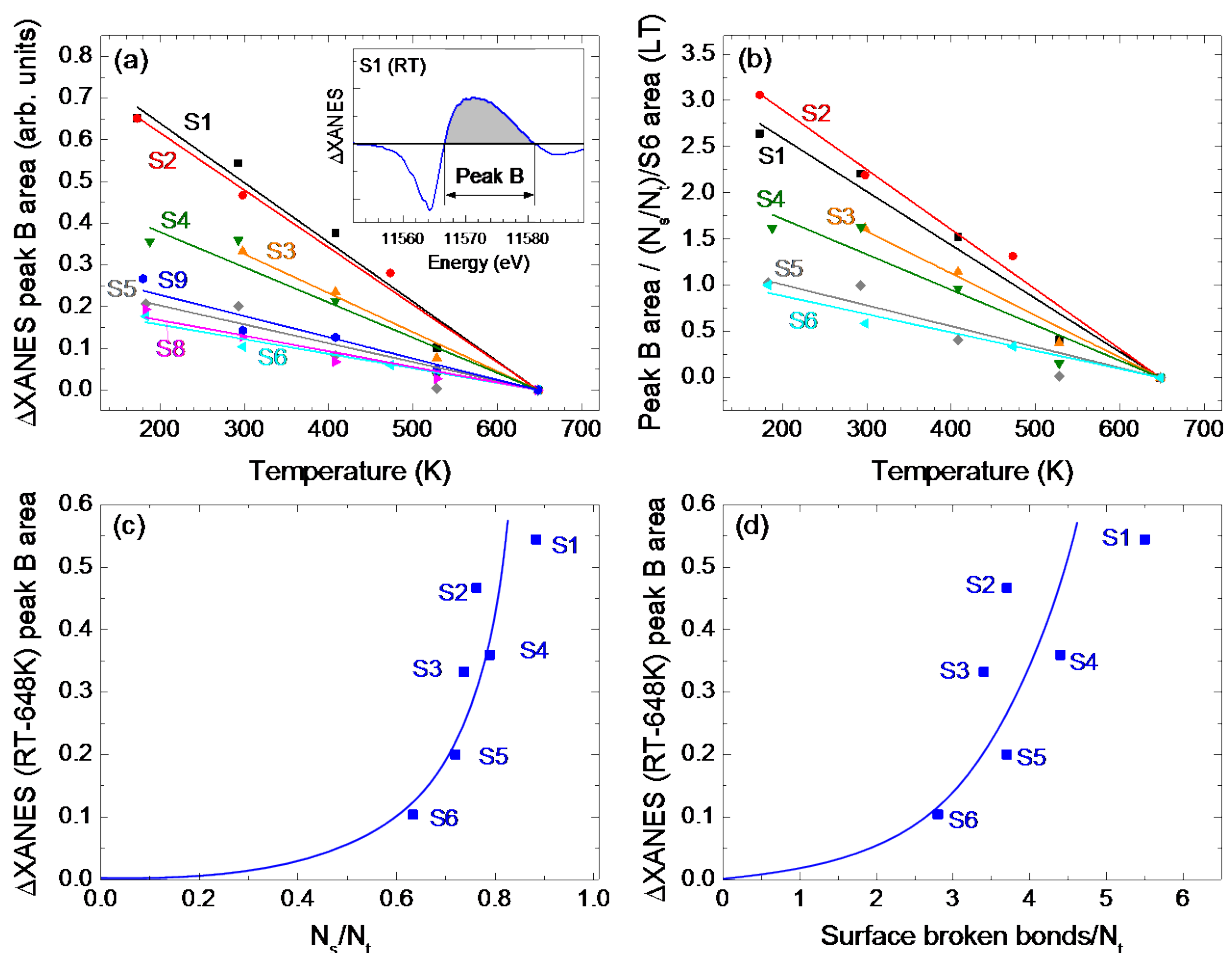


Fig. 72: (a) Evolution of the  $\Delta$ XANES peak B area (see inset for definition of peak B) of NPs with different sizes as a function of temperature. All samples were measured in  $H_2$  after NP reduction. (b) the area of the  $\Delta$ XANES peak B normalized by  $N_s/N_t$  and by the area of peak B of S6 measured at 183 K (1H for each surface Pt atom for larger NPs). The  $N_s/N_t$  normalization compensates for the fact that larger NPs have a lower number of atoms at their surface affected by H adsorption.  $\Delta$ XANES (RT – 648 K) peak B area versus (c) the relative number of atoms at the NP surface ( $N_s/N_t$ ), and (d) the relative number of broken bonds at the NP surface (broken/ $N_t$ ). The broken bonds reflect the presence of Pt atoms at the NP surface with coordination less than 12. The inset in (a) displays a typical  $\Delta$ XANES spectra and the shaded area corresponds to peak B.



The same size-dependent trend is observed at higher temperatures, when partial H desorption sets in. Our normalized data suggest up to about 3 times higher H per Pt ratios for the smallest NPs investigated (S1 and S2) as compared to the larger clusters (S5 and S6), and extended Pt surface.

Furthermore, if the area of peak B in  $\Delta$ XANES plots comparing RT to 648 K H<sub>2</sub> data is plotted versus  $N_s/N_t$  [Fig. 72(c)] or versus the normalized number of broken bonds at the NP surface [ $12 - (\text{total number of Pt-Pt bonds} / \text{total number of Pt atoms})$ ], Fig. 72(d), a progressive increase in the area is observed with increasing number of surface atoms and with decreasing coordination of the atoms at the NP surface (or increasing number of broken bonds).

Since by subtracting data from the same NPs in H<sub>2</sub> at high temperature from low or RT data we can gain insight into the role of the adsorbate, the findings in Fig. 72 unveil a direct correlation not only between the maximum hydrogen coverage and the number of atoms at the NP surface, Fig. 72(a), but also indicate that samples with specific shapes characterized by low average atomic coordination at the surface, i.e. with a larger fraction of broken bonds, are able to stabilize higher hydrogen coverages, Fig. 72 (b) and Fig. 72(d). These results are in agreement with previous theoretical calculations and will be discussed in more detail below.<sup>219, 243-245</sup>

## 8.4 Discussion

Clear changes in the electronic properties of our Pt NPs as compared to bulk Pt could be experimentally observed via XANES, in particular, a positive shift in the peak energy and an increase in the integrated intensity of the absorption peak. The origin of

these effects has been the subject of intense debate in the literature<sup>204, 222, 225, 229, 231, 233, 234, 241, 246-250</sup>. While some references attribute the former effects mainly to the interaction of atoms in the Pt NPs with hydrogen, others also involve the NP support. We suggest that some of this discrepancy is due to the difficulty of separating the different contributions to the XANES spectra in the absence of geometrically well-defined NPs with good crystallinity and narrow size distributions, as well as to the challenge of using a unique synthesis approach to generate small NPs with either 2D or 3D shape on the same support in order to evaluate the role of the NP/support interface. Our micellar synthesis has been proven ideal for the generation of size- and shape-selected metal NPs in the sub-2 nm size regime with tunable shape, being thus suitable for the above investigations and subsequent direct comparison with first principle theories.

A difference between analogously-sized NPs with different shape (e.g. S1 and S2) is the strength of the peak observed at 11.58 keV (marked with a dashed vertical line in Fig. 64), being stronger for the flatter NPs. A correlation between such feature and the internal degree of crystalline order in NPs of different sizes has been discussed in the literature<sup>204, 251</sup>, and it was found to be strongly suppressed in poorly ordered NPs or in NPs of very small size.

It should be noted that in our study the WL intensity was found to only minimally change with decreasing NP size (see Fig. 63). This is in contrast to the results of Lei et al.<sup>223</sup> for Pt NPs with sizes ranging from 1.4 to 9 nm, but in agreement with Ankudinov et al.<sup>204</sup>, since the latter only reported strong WL intensity variations for very small NPs ( $\leq 5$  atoms), while our smallest NPs have about 22 atoms. Nevertheless, a small difference in the WL intensity was observed when comparing NPs of roughly the same TEM

diameter (e.g. S1 and S2 or S3 and S4) but different shape (2D versus 3D). In particular, planar structures were found to show slightly higher WL intensities. This is in accord with previous theoretical predictions<sup>204</sup>. The same group also observed nearly constant WL intensities for 3D close-packed and polytetrahedral NPs of different sizes (Pt<sub>13</sub>, Pt<sub>19</sub>, Pt<sub>43</sub>), which was assigned to a fixed Pt-5d charge count.<sup>204, 225</sup>

#### 8.4.1 Adsorbate effects

Strong correlations are expected for size- and adsorbate-effects, since with decreasing NP size there is an increase in the number of surface atoms available for hydrogen chemisorption. Temperature-dependent XANES data can be used to decouple these effects, as for a given NP size, high temperature data (e.g. our 648 K data) are expected to be only minimally influenced by adsorbate effects due to the much lower onset temperature for hydrogen desorption<sup>41</sup>. It should be noted that under our experimental conditions (1 atm, 50% H<sub>2</sub> + 50 % He) the presence of trace amounts of hydrogen at 648 K cannot be completely ruled out. However, as can be seen in Fig. 70(a), the position of the XANES peak of the small NPs does not change above 528 K, suggesting that the possible residual hydrogen coverage on the NP surface (if any) has already reached its minimum value at that temperature, which is below the 648 K used in our study as reference for the adsorbate-free state of the NPs.

As illustrated in Fig. 67, positive energy shifts as well as an increase in the total integrated XANES peak area beyond the edge were observed with decreasing NP size (TEM diameter) or decreasing 1<sup>st</sup> NN coordination number (EXAFS). Moreover, there is a correlation between the relative energy shift of the XANES peak at RT, Fig. 70(b) [as

well as at 173-188 K for H-saturated NPs, Fig. 71(a)] with respect to 648 K and the number of atoms at the NP surface ( $N_s/N_t$ ). The latter finding illustrates that at least part of the energy shift and peak area enhancement are not intrinsic to the specific NP sizes, but due to the chemisorption of hydrogen. This aspect is corroborated based on the comparison of S2 measured in He and H<sub>2</sub> at 173 K, Fig. 65(d). Since S2 is characterized by 3D NPs with a large number of surface atoms ( $N_s/N_t = 0.84$ ), it constitutes a good example of a NP geometry where adsorbate effects are expected to be dominant. A much smaller spectral area and nearly no energy shift ( $\Delta E \sim 0.1$  eV, within our error margin) were observed in He, while an energy shift of +0.8 eV with respect to bulk Pt was measured under H<sub>2</sub>, emphasizing the extrinsic nature of the effect observed. Our data thus reveal that the H<sub>2</sub> effect dominates the trends observed.

Regarding the hydrogen effect on Pt NPs and XANES, it is known that hydrogen adsorption relaxes the Pt-Pt lattice, the effect can be thought of consisting of two parts: (i) geometrical relaxations of Pt NPs induced by H<sub>2</sub>, and (ii) electronic structure changes caused by the formation of H-Pt bonds. Both of these effects may lead to energy shifts of the XANES absorption features.

The effect of tensile strain (an expansion of Pt-Pt bond length) on the d-DOS is characterized by a shift in the occupied d-DOS center away from  $E_F$  and a suppression of the unoccupied portion near  $E_F$ <sup>252</sup>. However, it has been shown that the effect of H<sub>2</sub> is mostly of electronic nature (extrinsic effect) rather than an intrinsic effect based on the expansion of the Pt-Pt lattice<sup>252</sup>. The blue shift obtained for the *unoccupied* d-band center due to hydrogen adsorbates has been found to depend on the NP size, with

larger shifts obtained for smaller NPs.<sup>252</sup> This is in agreement with the observed relative energy shift of the XANES absorption peaks of S1 and S2, Fig. 67(a).

Theoretically, the increased peak area and positive energy shift described above for the small Pt NPs in hydrogen reflect a decrease in the density of electronic states near the Fermi level, e.g. the transfer of charge from the NPs to either the support,<sup>227, 246, 253-255</sup> to hydrogen for the formation of Pt-H bonds (via the creation of anti-bonding states above  $E_F$ ),<sup>222, 223, 229, 234</sup> or to both. DFT calculations have shown that there is a net charge transfer from Pt to hydrogen atoms<sup>252</sup>. Thus, the remarkable hydrogen effect on the electronic structure of Pt NPs can be attributed to charge transfer from the Pt NPs to hydrogen. However, not all hydrogen atoms receive electrons from the Pt atoms, but primarily those adsorbed at corner and edge sites<sup>252</sup>. Additionally, the calculated hydrogen adsorption energy has been found to be larger for lower hydrogen coverages, since fewer low coordination sites are available for the higher hydrogen coverages. By comparing similar hydrogen coverages, the hydrogen adsorption energy has been found to strongly depend on the NP size, with stronger binding of hydrogen to the smaller NPs<sup>252</sup>. This has been assigned to the presence of a larger number of sites with low coordination in the smaller NPs<sup>252</sup>.

Quantitative information on the amount of adsorbed hydrogen on Pt NPs has been extracted from the integrated area of the  $\Delta$ XANES absorption peak<sup>182, 222, 226, 229, 234, 255</sup>, and a linear correlation between the peak area and the H/Pt ratio established. In the present work, the evolution of the absorption peak energy and integrated  $\Delta$ XANES (peak B) area with temperature shows a marked size-effect, Fig. 70(a) and Fig. 72(a). For all samples measured in  $H_2$ , a progressive decrease in the spectral area was

observed with increasing temperature for the small NP sizes ( $\leq 1$  nm), while such effect was found to be much less pronounced for the larger clusters. Charge transfer phenomena should be more prominent at low temperature due to the overlap of metal, adsorbate, and support orbitals. The larger WL intensity observed at low temperature for the small NPs, constitutes an indication of a decrease in the total charge within the NPs, which has been transferred to either the hydrogen adsorbate or the support. As can be seen in Fig. 69, Fig. 70(b), and Fig. 72(a),(b), the adsorbate effect is dominant. In particular, for the samples measured in  $H_2$ , the increase in the measurement temperature is expected to lead to a decrease in the effective  $H_2$  coverage on the NP surface, which in turn results in a decrease in the energy shifts, height of the absorption peak WL, and integrated area. As shown in the theory section, higher charge transfer is expected from metal to hydrogen for Pt atoms with lower coordination numbers. Also, a larger amount of charge transfer should affect the XANES region by inducing larger energy shifts and broadening. Therefore, the smaller NPs would be more affected by hydrogen adsorbates due to: (i) their higher surface/bulk ratio, (ii) larger number of H adsorbate atoms per surface Pt atom, and (iii) larger amount of charge transfer between each H and Pt atom.

Additional information on the role of the NP geometry (size and shape) on the binding of hydrogen can be extracted from Fig. 72(c),(d). The correlation observed between the number of surface atoms and the  $\Delta$ XANES peak B area comparing H-covered NPs (RT data) to nearly adsorbate-free NPs (648 K) of different structures, Fig. 72(c), reveals higher hydrogen coverages at RT on the NPs with the highest number of surface atoms ( $N_s/N_t$ ). The same trend was observed at all investigated temperatures,

including 165-175 K, where the complete saturation of the NP surface with hydrogen is expected. After the normalization of the integrated peak areas by the relative number of surface atoms in each sample and the peak B area of the largest NPs investigated with well-defined geometry (S6), Fig. 72(b), clear size-dependent differences can be seen. In particular, the maximum hydrogen coverage stable on the NPs at any given temperature was found to be strongly dependent on the NP geometry. Our data also suggest that the one H per one Pt atom normalization factor based on H saturation coverages on Pt(111) surfaces, commonly used to describe dispersion in NP samples<sup>226</sup>, cannot be reliably used to extract quantitative information of the absolute hydrogen coverage per surface atom within small NPs. Indeed, up to 3 H atoms per Pt atom at the NP surface were obtained at the lowest investigated temperatures [166-188 K, Fig. 72(b)]. Previous groups reported saturation of the NP surface with 1.2 H per Pt atom at RT<sup>15,23</sup>, and others used the integrated  $\Delta$ XANES area at RT in He as normalization factor in the calculation of relative fractional hydrogen coverages at higher temperatures.<sup>226</sup> Nevertheless, our data indicate that higher H saturation coverages might be obtained at and below RT, and that the 1:1 H/Pt ratio commonly used in Langmuir adsorption measurements<sup>256</sup> likely underestimates the amount of H that can be stabilized on the surface of a small Pt NP ( $\leq 1$  nm) with a large fraction of low-coordinated sites (e.g. steps, corners and edges). This observation is in agreement with experimental data from Bus et al.<sup>228</sup> reporting H/Pt ratios higher than 1 for Pt NPs and Kip et al.<sup>257</sup> for Pt, Rh and Ir NPs on Al<sub>2</sub>O<sub>3</sub> and SiO<sub>2</sub> (from RT measurements). It is worth mentioning that in the former references the H/Pt ratios were obtained based on the total number of Pt atoms in a NP and not the actual number of surface atoms, as it

is considered here. Therefore, even higher H/Pt ratios are expected for the surface atoms. Furthermore, our experimental data also demonstrate that the maximum H saturation coverage is strongly size-dependent, and so is the strength of the Pt-H bond upon sample heating. In addition, the largest  $\Delta$ XANES areas (e.g. largest H coverage) were not only measured for the NP shapes with the highest number of low coordinated surface atoms, Fig. 72(c), but also for those with the largest number of broken bonds at the NP surface, Fig. 72(d). This indicates that more hydrogen atoms can be adsorbed on corner and edge atoms within a NP as compared to higher-coordinated atoms on a Pt(111) surface. Theoretically, H/Pt saturation ratios of up to 4:1 have been predicted for small Pt NPs with different structures<sup>243, 244</sup>, and higher average hydrogen adsorption energies were obtained for small clusters as compared to bulk. Upon hydrogen saturation, Pt<sub>12</sub>H<sub>30</sub> structures were reported on a NaY zeolite<sup>258</sup> based on DFT calculations. Furthermore, a decrease in the hydrogen desorption energy with increasing coverage was observed, reflecting the lower reactivity of the clusters with higher surface hydrogen coverages.<sup>243, 252</sup> A size-effect was also described in the literature, with a nearly linear increase in the number of H atoms chemisorbed on small Pt NPs with increasing NP size (<10 atoms).<sup>224, 252</sup> Simple theoretical models such as the Langmuir model could not reproduce the hydrogen coverage dependence displayed by our experimental system, Fig. 72(a). This is assigned to three important factors: (i) we do not have a single hydrogen desorption site (e.g. corners, faces, edges), and therefore, not a single desorption energy in our complex nanoscale system, (ii) the desorption energy at a given site might be different for NPs of different sizes, (iii) the desorption energy might be coverage dependent, and adsorbate-adsorbate interactions



must be considered. These aspects will require future theoretical work and is beyond the scope of the present study.

#### **8.4.2 Support effects**

In our experimental work, the relative contribution of the NP support to the electronic properties of our NPs can be inferred from the comparison of samples with identical TEM diameter but different shape (2D versus 3D), Fig. 65(a,b). As was described before, larger energy shifts were observed for the flatter NPs, which are the ones with the highest contact area with the support. It should be mentioned that contrary to the case of NPs prepared by conventional impregnation-precipitation synthesis methods, where the final NP geometry is strongly influenced by the nature of the support, our micellar synthesis allows us to create different NP geometries on the same substrate ( $\gamma\text{-Al}_2\text{O}_3$ ) by changing the metal loading within a given micellar cage. This allows us to compare the electronic properties of 2D and 3D NPs on the same substrate and to separate size from support effects.

Even though with the data at hand we cannot completely exclude the presence of any residual H atoms on the NP surface at 648 K under our experimental conditions, we can still gain insight into the support effect by comparing samples with nearly the same  $N_s/N_t$  ratio (same adsorbate effect) but clearly distinct  $N_c/N_t$ . For a given NP diameter, the samples with the highest energy shifts (S1 and S4) are also the ones with the highest  $N_c/N_t$  ratio (0.55 for S1 and S4 versus 0.18-0.23 for S2 and S3), suggesting a correlation between the NP/support contact area and the magnitude of the XANES peak shift and charge transfer or charge redistribution effect. For example, since the  $N_s/N_t$

ratios (relative number of surface atoms) for S1 and S2 are nearly identical (0.84-0.86), a similar NP/adsorbate interaction is expected, and the energy shift difference observed while comparing these two samples ( $\Delta E \sim 0.5$  eV) must be largely attributed to distinct NP/support interactions. This trend is also illustrated in Fig. 70(c), where the energy shifts measured at high temperature are shown versus  $N_c/N_t$ . As discussed before, this high temperature data are expected to be the least influenced by adsorbate effects.

To explain the blue shift observed at high temperature where the NPs are almost adsorbate free, the support effect should be taken into account. Assuming that a support such as  $\gamma\text{-Al}_2\text{O}_3$  may induce a charge transfer similar to that induced upon hydrogen adsorption (from the Pt NP to  $\gamma\text{-Al}_2\text{O}_3$ ), larger blue shifts would be expected for NPs with a larger fraction of atoms in contact with the support. The correlation between the Pt-L<sub>3</sub> peak energy shift of our samples with respect to bulk Pt at 648K and  $N_c/N_t$  (contact area with the support) is demonstrated in Fig. 70(c). This postulation suggests that the experimental trends are not intrinsic to the specific NP geometries, but strongly influenced by environmental effects, in the latter case, by support effects.

In the literature, electronic effects underlying metal-support interactions have been described based on different models. For example, for Pt NPs supported on LTL zeolite and on  $\text{SiO}_2$ , no net charge transfer was reported.<sup>239, 240, 255</sup> Instead, modification of the valence orbitals of the metal by the Madelung potential of the support had to be considered.<sup>239, 240, 255</sup> On the other hand, the transfer of charge from interfacial Pt atoms to defects in  $\text{Al}_2\text{O}_3$  was proposed in Refs. 255, 259. Furthermore, *ab initio* calculations by Cooper et al.<sup>253</sup> for Pt(111) films on  $\alpha\text{-Al}_2\text{O}_3$  revealed the transfer of charge from Pt to the support when the surface is O-terminated, and in the opposite direction when it is

Al-terminated. Due to the sample pre-treatment used in our study (prolonged annealing in O<sub>2</sub>), an oxygen-terminated (hydroxyl) Al<sub>2</sub>O<sub>3</sub> surface is expected, and the direction of the charge transfer inferred here based on the XANES data of the 2D NPs (from Pt to Al<sub>2</sub>O<sub>3</sub>) is in agreement with the previous calculations for Pt thin films. A broadening of the Pt-L<sub>3</sub> WL due to the interaction of small Pt NPs with LTL-zeolite supports was also previously shown.<sup>204</sup> Nevertheless, other groups reported no support effects on the peak area<sup>229</sup>. In our study, the support effect is evident in the extent of the energy shifts (with respect to bulk Pt).

Our experimental and theoretical findings illustrate the crucial role of not just geometrical effects, but also environmental influences such as adsorbates and the NP support in the electronic properties of small Pt NPs. This level of understanding might be leveraged in order to tune related material properties, as for example, catalytic reactivity. For instance after evaluating how the support affects a desired catalytic reaction, the shape of the NPs could be tuned to be 2D or 3D in order to maximize or minimize the NP interface with the support and therefore to optimize the reactivity or selectivity. Also by increasing the number of atoms at corners and edges, the binding energy and also the coverage of adsorbates could be increased, affecting both the reaction onset temperature and the turn over frequency. The approach used in this study provides a comprehensive mean to evaluate the size and shape of NPs as well as to deconvolute different effects induced by support or the particular shape of the NPs.

## 8.5 Conclusions

A synergistic combination of XANES and NP shape modeling based on EXAFS data has allowed us to gain insight into the correlations between the structure (size and shape) and environment (adsorbate and support) of  $\gamma$ -Al<sub>2</sub>O<sub>3</sub>-supported Pt NPs (XANES). Our data reveal that the size-dependent trends observed in the electronic properties of Pt NPs are not exclusively intrinsic due to the specific NP geometry, but largely due to extrinsic parameters such as the chemisorption of H<sub>2</sub> and NP/support interactions, which are strongly affected by the NP shape and NP/support contact area.

# CHAPTER 9: EVOLUTION OF THE STRUCTURE AND CHEMICAL STATE OF Pd NANOPARTICLES DURING THE *IN SITU* CATALYTIC REDUCTION OF NO WITH H<sub>2</sub>

## 9.1 Introduction

Although in the last two decades significant progress has been made towards the understanding of the structure and chemical composition of supported NPs in the as-prepared state and after reaction state,<sup>2, 5, 12, 138, 260-267</sup> much less is known about their *in situ* (*operando*) structural and chemical features, and how they evolve in the course of a chemical reaction.<sup>108, 139, 268-274</sup> Reaction-induced morphological changes in NPs need to be considered, since they might lead to a decrease/increase in the relative area of the most catalytically active surface sites, as well as to changes in the chemical state of the active metal catalysts.<sup>269-274</sup>

The present study targets the *in situ* catalytic reduction of NO. This structure-sensitive reaction is of enormous industrial and environmental relevance, since NO<sub>x</sub> emissions have significant adverse effects on the environment (acidification of rain and the generation of smog), as well as on humans (respiratory infections) and therefore, remediation through catalysis is critical.<sup>275-281</sup> The most common routes for the removal of NO are the selective catalytic reduction (SCR) with ammonia, CO, H<sub>2</sub> and hydrocarbons, as well as the direct decomposition.<sup>261, 279, 282-307</sup>

The present work focuses on the reduction of NO with H<sub>2</sub> (H<sub>2</sub>-SCR).<sup>308-310</sup> This reaction is not as selective for N<sub>2</sub> as, for instance, ammonia, but has potential technological applications due to its lower onset temperature, and the fact that H<sub>2</sub> is readily available in exhaust streams (from the water-gas-shift reaction or from

hydrocarbons).<sup>284</sup> Noble metal-based catalysts are generally preferred for the H<sub>2</sub>-SCR of NO because of their high selectivity and reduced operation temperatures.<sup>302, 311-314</sup> Although Rh is overall catalytically better than Pd for NO-SCRs, the lower cost, higher abundance, and low-temperature activity of Pd have made it a material of choice in industrial applications.<sup>312, 315-322</sup> A vast amount of literature is available describing the conversion and selectivity of various combinations of metal catalyst, support, and reducing agent.<sup>261, 279, 282-284</sup> However, much less attention has been paid to the optimization of the structure and oxidation state of the active catalysts, its evolution under reaction conditions, and its influence on catalytic performance.<sup>323, 324</sup> Nevertheless, previous work has revealed the important role of the oxidation state of metal catalysts in their activity, selectivity, and stability for NO-SCRs. For example, oxidized Rh catalysts are more active for H<sub>2</sub>-SCR than metallic Rh,<sup>325</sup> and NO adsorption on Cu catalysts is faster on the oxidized surface, contrary to the faster adsorption reported on the reduced surfaces of other materials such as chromia or manganese oxides.<sup>261</sup> Additional examples discussing the reactivity of oxidized Pd species formed under reaction conditions can be found for CH<sub>4</sub>-SCR reactions carried out in the presence of oxygen.<sup>304, 326, 327</sup> The nature of the support has also been found to influence catalytic performance either by stabilizing the NPs against coarsening, by providing additional active reaction sites, or by influencing the chemical state of the supported catalysts.<sup>113, 320-322</sup> On acidic supports, oxidative redispersion of PdO over the support was observed, while larger PdO clusters were found on non-acidic substrates.<sup>304, 326</sup> Dispersed Pd<sup>2+</sup> cations were reported to constitute the active phase in CH<sub>4</sub>-SCR NO reduction in the presence of O<sub>2</sub>,<sup>327-329</sup> while NO was found to dissociate

on Pd<sup>0</sup> sites during H<sub>2</sub>-SCR NO reduction with O<sub>2</sub> in the reactant stream.<sup>330</sup> Furthermore, enhanced selectivities were observed when the Pd nanocatalysts were deposited on acidic zeolites or sulfated ZrO<sub>2</sub> supports.<sup>331</sup> In addition, exposure of zeolite and perovskite-supported Pd NPs to O<sub>2</sub> and NO was found to result in the formation of highly mobile cationic Pd species.<sup>326, 332-334</sup> Finally, the size of the NPs was also shown to affect their reactivity.<sup>335-341</sup> For example, N<sub>2</sub>O was not formed over small Pd NPs on SiO<sub>2</sub>, but was present when larger clusters were used as catalysts.<sup>340</sup>

It is evident from the above description that a detailed knowledge of the correlation between the structure (size, shape, and dispersion on a support), chemical state of the active species, and their reactivity is indispensable for the rational design of efficient and highly selective nanocatalysts. In the present work, the H<sub>2</sub>-SCR NO reduction over ZrO<sub>2</sub>-supported Pd NPs has been investigated *in situ* via XAFS spectroscopy and mass spectrometry, complemented with *ex situ* TEM. XAFS allows element-specific structural and chemical analysis under *operando* conditions, and is therefore the ideal technique to investigate the microscopic morphology of the catalysts *at work*, and to gain insight into the structure and reaction mechanisms guiding the reduction of NO.

## 9.2 Experimental

### 9.2.1 Sample preparation and characterization

The Pd NPs were synthesized by inverse micelle encapsulation. Micellar nanocages were prepared by dissolving a non-polar/polar diblock copolymer [polystyrene-block-poly(2-vinylpyridine), PS-P2VP] in toluene and subsequently loaded with a metal precursor (C<sub>4</sub>H<sub>6</sub>O<sub>4</sub>Pd) to create encapsulated NPs. Adjusting the polymer

head length (P2VP) and metal precursor-polymer head ratio (L) enables the control of the particle size. The Pd NPs in our investigation were prepared by loading PS(16000)-P2VP(3500) copolymers with a metal precursor/P2VP ratio L of 0.05. Subsequently, the NPs were impregnated on commercially available nanocrystalline (powder) ZrO<sub>2</sub> supports (~ 20 nm average grain size) by dissolving the support in the polymeric solution. The polymeric ligands are removed by annealing in an O<sub>2</sub> environment at 375°C for 24 h. After this treatment, the NPs are free of carbon as verified by XPS. The Pd loading was 1% by weight. TEM measurements were carried out by our collaborators, Prof. Judith Yang's group, in the Department of Chemical and Petroleum engineering, at the University of Pittsburgh. For the TEM measurements, the Pd/ZrO<sub>2</sub> powders were dissolved in ethanol and subsequently drop-coated onto a carbon-coated Cu grid and dried in air.

### **9.2.2 Reactivity data**

The catalytic performance of our ZrO<sub>2</sub>-supported Pd nanocatalysts for the reduction of NO was determined using a packed-bed mass flow reactor interfaced to a quadrupole mass spectrometer. The reactants (1% NO, 1% H<sub>2</sub>) were introduced employing low flow mass flow controllers and were balanced with He to provide a total flow of 25 ml/min. The catalyst bed was stepwise annealed up to 240°C in order to determine the temperature dependent conversion of NO and reaction selectivity via mass spectrometry. Reactivity data were acquired at each temperature under steady-state conditions. Prior to exposing the Pd NPs to the reactants, they were reduced for 1 h in a hydrogen atmosphere (40 % H<sub>2</sub> balanced with He) at 240°C.



### 9.2.3 Structural and chemical analysis (EXAFS, XANES)

EXAFS and XANES spectroscopy measurements were performed at the NSLS at BNL (beamline X18B). The experimental set-up consisted of a home-built packed-bed mass flow reactor cell compatible with *in situ* transmission XAFS measurement and interfaced to a quadrupole mass spectrometer for the evaluation of catalytic reactivity.

A minimum of three Pd K-edge EXAFS spectra were acquired before and after the *in situ* reduction of the Pd catalysts as well as at various temperatures during the H<sub>2</sub>-SCR reaction (25-240°C). The ATHENA software was used for averaging and aligning the spectra with the simultaneously-acquired bulk Pd foil reference spectra. The smooth isolated atom background was removed using the AUTOBK algorithm.<sup>83, 84, 342</sup> The Fourier transformation of the ( $k$ ,  $k^2$ ,  $k^3$ )-weighted EXAFS data was performed via the Artemis software package, and the resulting radial distributions were fitted (first shell) with a theoretical model calculated for fcc-palladium with the FEFF6 code.<sup>86, 343</sup> Typical  $k$ -ranges were 2.5-10 Å<sup>-1</sup> and  $r$ -ranges 1.5-3.0 Å. The best fit for the passive electron reduction factor of the bulk Pd reference spectrum, was 0.84 and was kept constant during the analysis of all NP samples. The structural parameters extracted from the fits of the EXAFS data of our Pd/ZrO<sub>2</sub> catalysts under different reaction conditions are summarized in the Table 17 together with fit quality factors.

## 9.3 Results

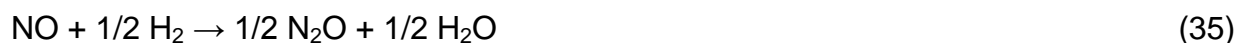
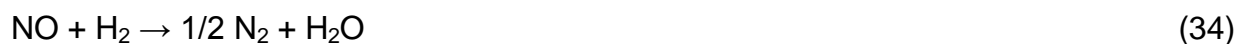
### 9.3.1 Structure, and morphological (TEM)

TEM measurements were carried out by our collaborators Prof. Judith Yang's group, at the University of Pittsburgh on our ZrO<sub>2</sub>-supported Pd NPs after (a) O<sub>2</sub>-

annealing at 375°C (as-prepared), and (b) the H<sub>2</sub>-SCR NO reduction reaction up to 240°C<sup>108</sup>. Detailed statistics of the average NP size and size distribution of this sample could not be carried out via HAADF STEM due to the poor Z-contrast between the Pd NPs and the nanocrystalline ZrO<sub>2</sub> support. However, based on the analysis of a small set of particles (~20-30) observed in bright field images, the average size of the NPs was estimated to be 5.3 ± 1.5 nm before the reaction (as-prepared sample), and 6.5 ± 2.3 nm after the reaction. Overall, the particles were found to be rather flat, with an average width/height ratio of ~2.2 before the reaction, and ~2.6 after the reaction, suggesting a strong NP-support interaction after our initial annealing pre-treatment at 375°C.

### 9.3.2 Catalytic reactivity

The temperature dependence of the conversion of NO over the ZrO<sub>2</sub>-supported Pd NPs under steady-state reaction conditions is shown in Fig. 73. The onset reaction temperature (defined as the 50% conversion temperature, T<sub>50</sub>) was found to be 140°C, and a 100% conversion was reached at 150°C. The reaction products observed for the H<sub>2</sub>-SCR of NO are nitrous oxide (N<sub>2</sub>O), nitrogen (N<sub>2</sub>), ammonia (NH<sub>3</sub>), and water. These products are obtained through the following pathways:



No traces of nitrogen dioxide ( $\text{NO}_2$ ) were detected in the course of the reaction. The product selectivity is presented in Fig. 73. At the onset of the  $\text{NO}$  conversion, a high selectivity ( $>70\%$ ) toward  $\text{N}_2\text{O}$  is observed, but it rapidly decreases with increasing temperature to a saturation level of about 15%.

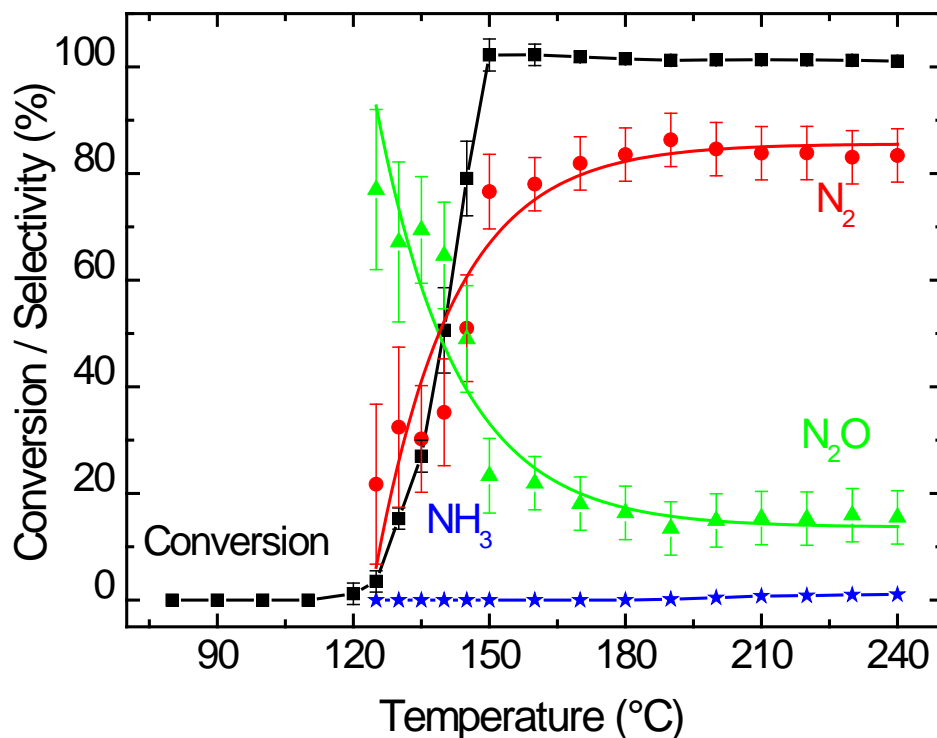


Fig. 73: Conversion and selectivity data as a function of temperature for the steady state  $\text{H}_2$ -SCR  $\text{NO}$  reduction over micellar Pd NPs supported on  $\text{ZrO}_2$ .

Simultaneously, the selectivity toward  $\text{N}_2$  shows the opposite trend; a strong increase from less than 30% at the onset temperature for  $\text{NO}$  conversion to a maximum saturation level of  $\sim 85\%$  at  $150^\circ\text{C}$ . Above  $180^\circ\text{C}$ , the third reaction pathway sets in, and a small fraction of  $\text{NH}_3$  ( $< 2\%$ ) is observed.

### 9.3.3 Evolution of the structure and chemical composition of Pd NP catalysts under *operando* condition (XANES, EXAFS)

Pd K-edge XANES spectra of ZrO<sub>2</sub>-supported Pd NPs, acquired *in situ* under different reaction conditions together with reference spectra for bulk metallic Pd and PdO are shown in Fig. 74. The K-edge XANES probes the electronic transition from 1s to 5p orbitals and is sensitive to the chemical state of the Pd atoms. After the removal of the encapsulating polymeric ligands in oxygen at high temperature, the XANES spectrum of the NPs (labeled as-prepared) shows a strong resemblance with the reference spectrum for bulk PdO, indicating the oxidation of the NPs.

After the subsequent reduction treatment in H<sub>2</sub> at 240°C, the complete decomposition of the Pd oxides and the appearance of metallic Pd features are observed in the XANES spectrum measured at RT. The characteristic near-edge peaks, however, show a distinct shift to lower energy. Upon initial sample exposure to the reactants (NO and H<sub>2</sub>) at RT, the metallic features remain, but shift slightly back to higher energies. Additionally, the latter spectrum also exhibits a small feature at ~24.37 keV indicating the presence of cationic Pd species (Pd<sup>δ+</sup>). The latter contribution becomes more pronounced as the temperature is further increased to 90°C and 120°C. Simultaneously, the intensity of the metallic peak at ~24.39 keV decreases significantly.

These effects are more clearly shown in Fig. 75, where the ΔXANES spectra of our NPs measured at different temperatures under NO + H<sub>2</sub> flow are shown.

The ΔXANES values displayed in Fig. 75 correspond to the difference between the Pd-K edge XANES spectrum of our NPs measured at the temperatures indicated and that of bulk metallic Pd measured at RT.

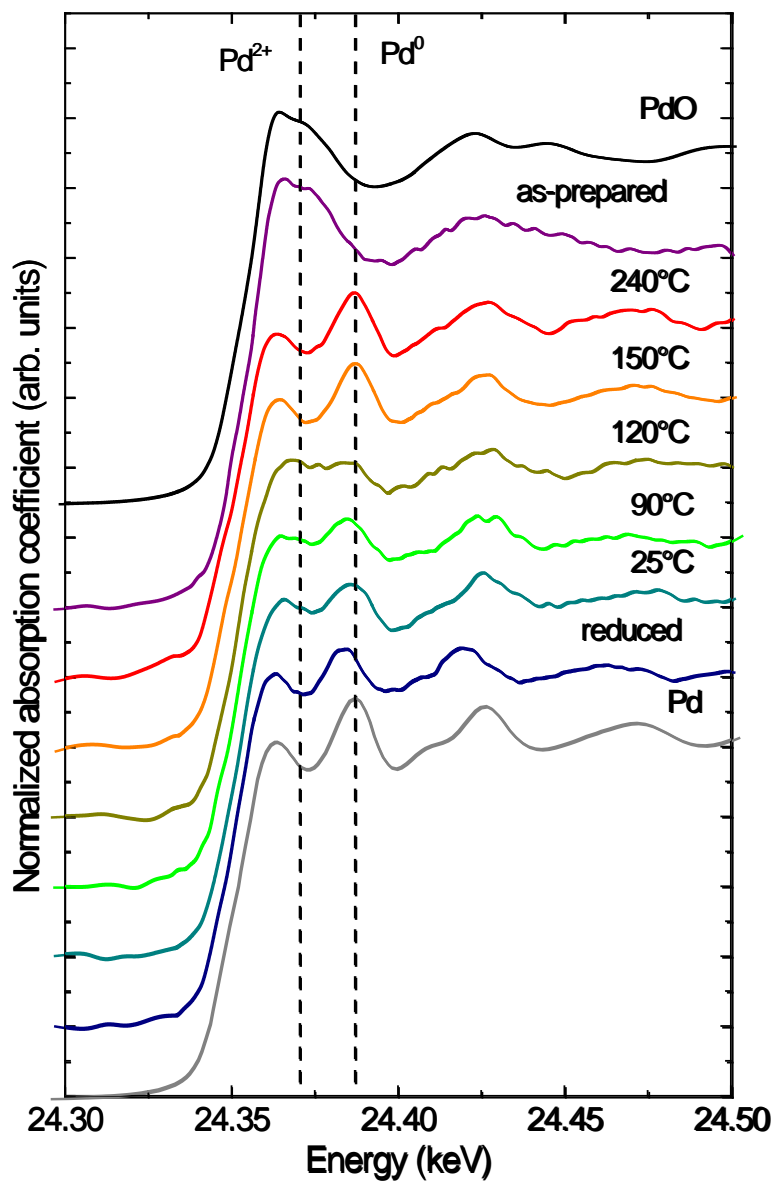


Fig. 74:: Pd-K edge XANES spectra recorded after polymer removal (in O<sub>2</sub> at 375°C, as-prepared), after reduction (in H<sub>2</sub> at 240°C), and at different temperatures during the H<sub>2</sub>-SCR NO reduction. Reference spectra for PdO and bulk Pd are shown as well.

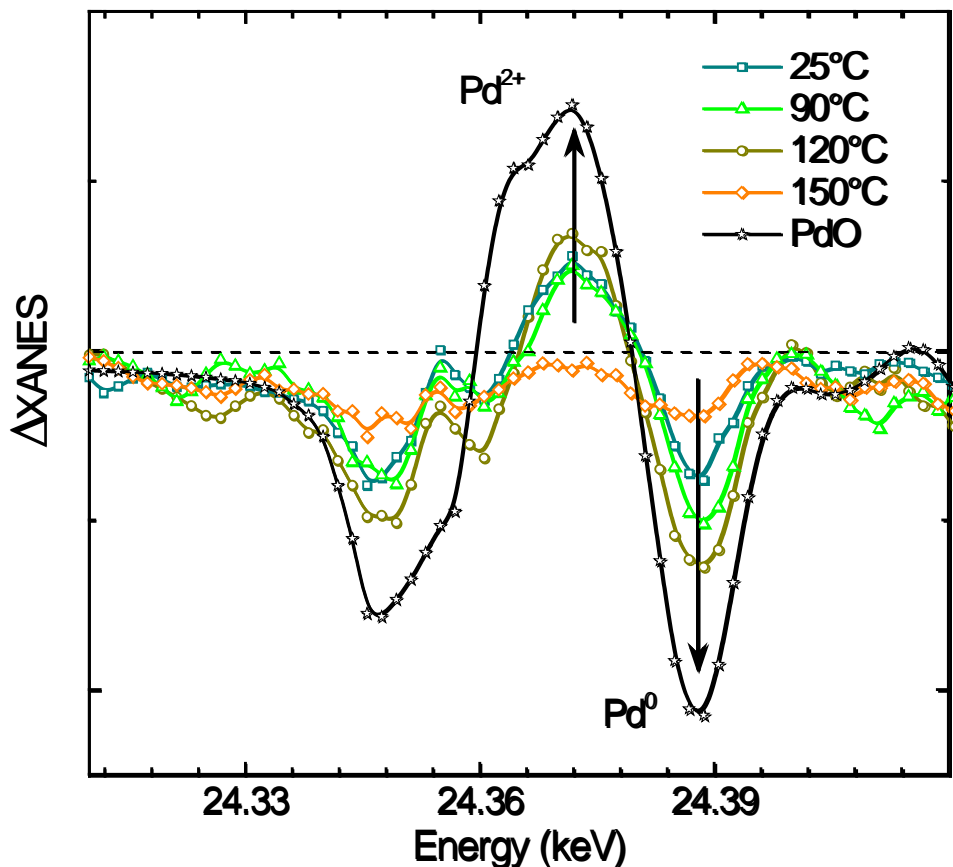


Fig. 75:  $\Delta$ XANES spectra obtained at various stages of the  $\text{H}_2$ -SCR NO reduction. The data correspond to XANES spectra acquired at different temperatures from which the spectrum of the bulk-like Pd foil measured at RT has been subtracted.

Our data reveal that a  $\text{Pd}^{\delta+}$  state, similar to the  $\text{Pd}^{2+}$  state in bulk PdO, appears upon introducing the reactant mixture at  $25^\circ\text{C}$ , showing its maximum contribution at  $120^\circ\text{C}$ . This change correlates with the gradual decrease of the metallic state with increasing temperature up to  $120^\circ\text{C}$ . However, the metallic features remain present even at  $120^\circ\text{C}$ , as can be seen in Fig. 74 and in the EXAFS spectra shown in Fig. 76.

At  $150^\circ\text{C}$ , the XANES spectrum in Fig. 74 changes drastically, becoming nearly identical to that of pure metallic Pd. However, no shift of the metallic  $\text{Pd}^0$  feature to lower

energy is observed with respect to the bulk Pd spectrum. The return to the metallic state is also evidenced by the nearly featureless  $\Delta$ XANES spectrum observed in Fig. 75 at 150°C. As the reaction temperature is further increased up to 240°C, no additional changes are observed, and the XANES spectra of the NPs remain very similar to those of bulk metallic Pd.

The Fourier transformed  $k^2$ -weighted Pd K-edge EXAFS data of the Pd NPs acquired *in situ* under different reaction conditions are displayed in Fig. 76 along with reference data for bulk metallic Pd and bulk PdO. Comparing the as-prepared spectrum with the PdO reference reveals that the Pd NPs are almost completely oxidized after the polymer removal treatment, in good agreement with our XANES results. Upon reduction in H<sub>2</sub>, the radial distribution exhibits a large resemblance with the metallic Pd state, but with a clear shift of the main features to higher distances. Upon the introduction of the reactants (NO + H<sub>2</sub>) and the subsequent increase in temperature, the EXAFS spectra continue to exhibit characteristic metallic features, although the expansion of the Pd-Pd lattice has disappeared.

Furthermore, the intensity of the main metallic Pd peak in the radial distribution at 2.5 Å (phase uncorrected) is considerably reduced at 120°C, while the characteristic metallic Pd feature at 2 Å (phase uncorrected) did not decrease, hinting at the presence of an overlapping additional scatter pair at a shorter distance than the Pd-Pd.

Further, after the initial reduction pre-treatment in H<sub>2</sub>, none of the characteristic features of Pd-oxide at 1.6, 2.7 and 3.1 Å (phase uncorrected) are observed throughout the entire reaction cycle.<sup>326</sup> Guided by the analysis of the XANES data we attribute the second component to a Pd-X signal, where X stands for a low Z scatterer, i.e. N or O.

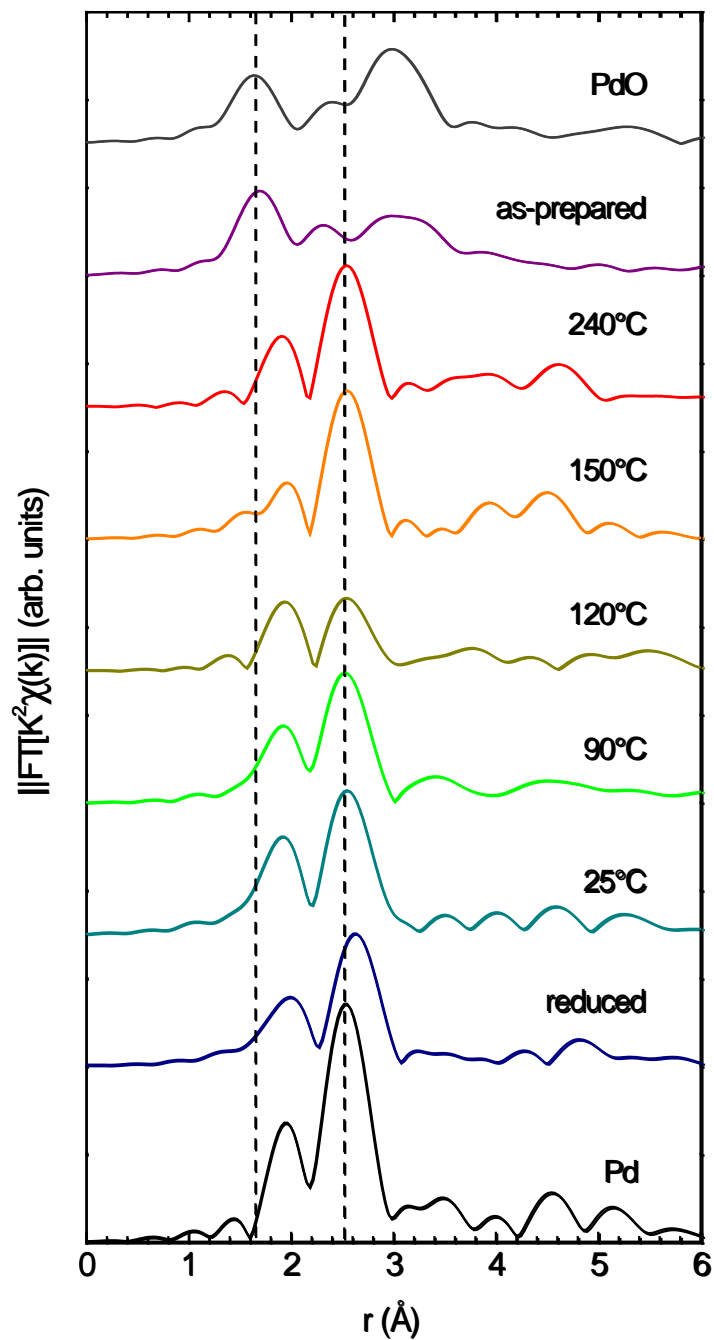


Fig. 76:  $k^2$ -weighted Fourier transform Pd K-edge EXAFS spectra (r-space) taken after reduction and during various stages of the  $H_2$ -SCR NO reduction. Bulk Pd and PdO spectra are shown as reference. The k-range for the Fourier transform was  $2.5 \text{ \AA}^{-1} < k < 10 \text{ \AA}^{-1}$ .



The EXAFS data were fitted with two theoretical contributions: one originating from Pd in a metallic environment (Pd-Pd), and a second component corresponding to cationic Pd atoms (Pd-X) with a large starting value of the Pd-X distance of 2.5 Å, which was subsequently varied in the fit. A representative fit is shown in Fig. 77(a) for EXAFS data acquired at 120°C under reaction conditions. The fits yield information on the 1<sup>st</sup> nearest neighbor (NN1) coordination numbers [ $N_{\text{Pd-Pd}}$ ,  $N_{\text{Pd-X}}$ , Fig. 77(b)] and the corresponding distances [ $d_{\text{Pd-Pd}}$ ,  $d_{\text{Pd-X}}$ , Fig. 77(c)] for each spectrum. The details on the fit results and related fit quality parameters are presented in Table 17.

The respective values for the H<sub>2</sub>-reduced NPs (*i.e.* the starting configuration) and a bulk Pd reference are shown by the dashed lines. After NP reduction in H<sub>2</sub>, a Pd-Pd coordination of  $10.8 \pm 0.9$  and a distance of  $2.82 \pm 0.01$  Å were obtained. When the reactants are first injected into the gaseous stream, the Pd-Pd 1<sup>st</sup> NN coordination slightly decreases, while the average Pd-Pd distance returns to its bulk-like value of 2.74 Å.

With increasing reaction temperature, the coordination number further decreases to  $5.6 \pm 2.0$  at 120°C. Despite the presence of a reducing reaction environment, a small cationic Pd-X contribution appears after the introduction of the reactants at RT ( $2.55 \pm 0.08$  Å), concomitant with the decrease of the initial H<sub>2</sub> flow from 50% H<sub>2</sub> in He to 1% H<sub>2</sub> + 1% NO in He.

According to the changes observed in the EXAFS spectra, the relative content of the latter component was found to increase with increasing temperature up to 120°C. We will elaborate on the origin of this component in the discussion below.

Table 17: Summary of the EXAFS results acquired on micellar Pd NPs supported on ZrO<sub>2</sub>: 1<sup>st</sup> NN coordination numbers [ $N_{\text{Pd-Pd}}$ ,  $N_{\text{Pd-O}}$ ], the corresponding distances [ $d_{\text{Pd-Pd}}$ ,  $d_{\text{Pd-O}}$ ], and Debye Waller factors [ $\sigma^2_{\text{Pd-Pd}}$ ,  $\sigma^2_{\text{Pd-O}}$ ]. In addition, fit quality parameters such as the R-factor and reduced  $\chi^2$  are also given, together with the  $k$ - and  $r$ -ranges. Fit uncertainties are presented in parentheses.

	<b>N Pd-Pd</b>	<b>N Pd-O</b>	<b>d Pd-Pd (Å)</b>	<b>d Pd-O (Å)</b>	<b><math>\sigma^2</math> Pd-Pd (Å<sup>2</sup>)</b>	<b><math>\sigma^2</math> Pd-O (Å<sup>2</sup>)</b>	<b><math>r</math>-range (Å)</b>	<b><math>k</math>-range (Å<sup>-1</sup>)</b>	<b>R factor</b>	<b>Red. <math>\chi^2</math></b>
Reduced 25°C	10.7 (0.9)	-	2.823 (0.005)	-	0.0085 (0.0007)	-	1.85-3	1.5-12	0.008	7.6
25°C (NO+H <sub>2</sub> )	8.0 (2.4)	3.1 (3.9)	2.738 (0.015)	2.555 (0.061)	0.0061 (0.0032)	0.0043 (0.0217)	1.5-3.1	1.5-10	0.020	30
90°C (NO+H <sub>2</sub> )	7.5 (2.9)	1.5 (2.9)	2.734 (0.022)	2.478 (0.089)	0.0060 (0.0036)	0.0000 (0.0271)	1.5-3.0	2.0-10	0.010	65
120°C (NO+H <sub>2</sub> )	4.6 (1.4)	2.6 (2.0)	2.731 (0.026)	2.607 (0.047)	0.0060 (0.0029)	0.0000 (0.0115)	1.5-3.0	1.5-11	0.020	29
150°C (NO+H <sub>2</sub> )	12.0 (1.9)	-	2.739 (0.012)	-	0.0108 (0.0018)	-	1.7-3.0	2.0-10	0.022	72
210°C (NO+H <sub>2</sub> )	10.0 (1.7)	-	2.748 (0.011)	-	0.0082 (0.0017)	-	1.7-3.0	2.0-10	0.017	51
240°C (NO+H <sub>2</sub> )	11.8 (1.4)	-	2.736 (0.008)	-	0.0099 (0.0013)	-	1.7-3.0	2.0-10	0.010	19
25°C (H <sub>2</sub> )	12.7 (1.7)	-	2.815 (0.008)	-	0.0084 (0.0013)	-	1.5-3.0	1.5-10	0.018	7.4

At 150°C, the Pd-X contribution disappears and the Pd-Pd coordination number shows a sudden increase to  $12.0 \pm 1.9$ , consistent with the return to the pure metallic state as indicated by XANES. Above 150°C, the coordination number remains constant within the uncertainty. After the introduction of the reactants, the average Pd-Pd distance was found to be rather stable throughout the entire reaction cycle as shown in Fig. 77(c).

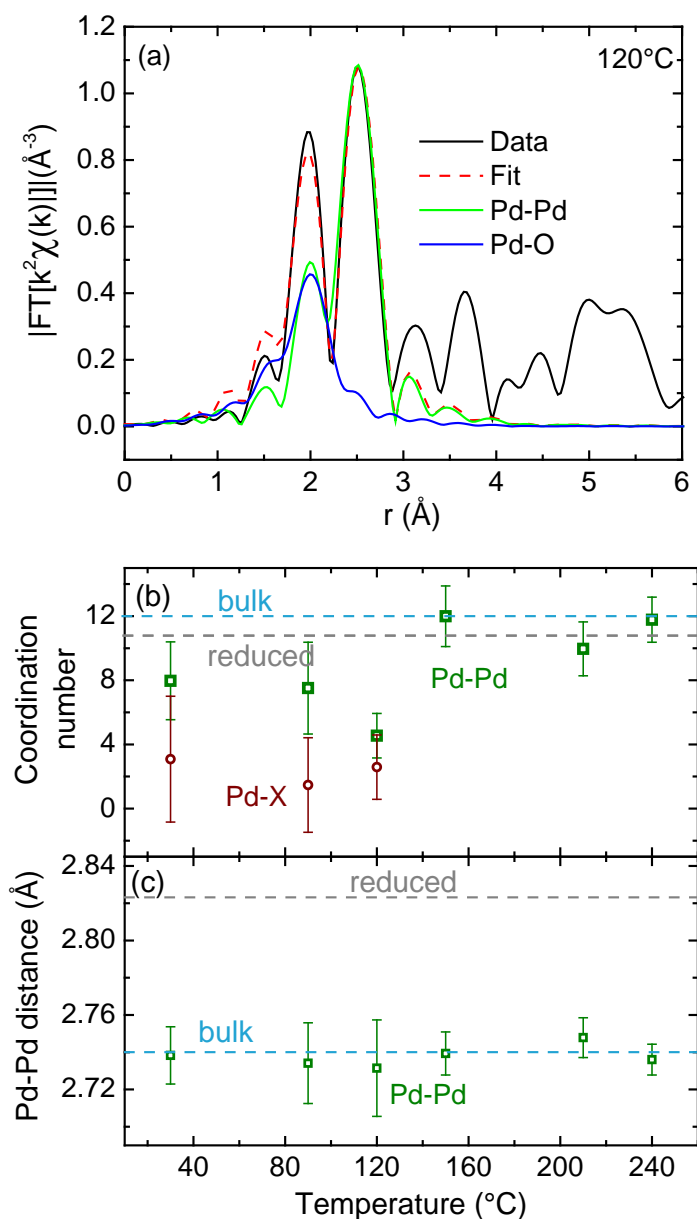


Fig. 77: (a) Fourier transform Pd K-edge EXAFS spectrum ( $r$ -space) recorded at 120°C, along with the total fit and the Pd-Pd and Pd-X contribution. (b) Dependence of the 1<sup>st</sup> NN coordination number on the reaction temperature during the H<sub>2</sub>-SCR NO reduction over Pd NPs supported on ZrO<sub>2</sub>: the Pd-Pd and the Pd-X contribution obtained from the fitting of *in situ* EXAFS spectra are shown. The dashed gray line indicates the Pd-Pd coordination number after NP reduction in H<sub>2</sub> and before reactant exposure. (c) Pd-Pd bond distance as a function of temperature. The dashed gray line indicates the Pd-Pd distance after NP reduction in H<sub>2</sub>, while the dashed blue line corresponds to the bulk value.

## 9.4 Discussion

The onset temperature  $T_{50}$  for the reduction of NO with H<sub>2</sub> over micellar Pd NPs supported on ZrO<sub>2</sub> was found to be 140°C. Once the conversion reaches 100 %, the activity remains stable with increasing temperature up to 240°C. At the onset of the reaction, the catalyst shows low selectivity toward N<sub>2</sub>, with N<sub>2</sub>O being the main reaction product. The N<sub>2</sub> selectivity was found to increase with increasing reaction temperature reaching ~80% at 150°C when 100% NO conversion is achieved. No changes were observed in the selectivity of our catalysts above 150°C. Our Pd NPs have a considerably lower onset reaction temperature as compared to Pd(111), where NO conversion was only observed above 200°C.<sup>344</sup> Interestingly, Pd/Al<sub>2</sub>O<sub>3</sub> catalysts from Yang *et al.*<sup>318</sup> showed already 100% NO conversion (with pure H<sub>2</sub>) at 70°C, but the N<sub>2</sub> selectivity remained below 50%. Barrera *et al.*<sup>345</sup> reported onset temperatures of 80-175°C for Pd/Al<sub>2</sub>O<sub>3</sub>-La<sub>2</sub>O<sub>3</sub> catalysts, although their N<sub>2</sub> selectivity did not exceed 60%. Granger *et al.*<sup>302</sup> described onset reaction temperatures of ~100°C for Pd/Al<sub>2</sub>O<sub>3</sub> catalysts, with 50% N<sub>2</sub> selectivity only above 300°C, with the parallel production of NH<sub>3</sub> resulting in a decrease in activity.<sup>302</sup> Similar Pd catalysts supported on LaCoO<sub>3</sub> exhibited a higher onset temperature (160°C), but showed a stable activity at high temperature, with a N<sub>2</sub> selectivity above 50% at 200°C.<sup>320</sup> Overall, our catalysts show a stable selectivity and activity pattern. Interestingly, a relatively low amount of NH<sub>3</sub> is produced throughout our entire reaction cycle (<2%), even at high temperatures. Significant NH<sub>3</sub> formation is often associated with H<sub>2</sub>-rich reaction conditions and as such, our low NH<sub>3</sub> production might be at least partially due to our relatively low H<sub>2</sub> concentration (i.e. NO:H<sub>2</sub> of 1:1). However, even in experiments with stoichiometric

concentrations, considerable  $\text{NH}_3$  formation is reported in the literature for similar catalysts<sup>302, 320</sup>, indicating that the specific nature of our micelle-based catalysts (size, shape, substrate dispersion and support) also plays a major role in the observed selectivity.<sup>320</sup> According to previous studies, the conversion and selectivity of  $\text{H}_2$ -SCR catalysts might be further improved by fine-tuning the inlet concentrations. For instance, reaction conditions involving excess  $\text{H}_2$  are known to result in an increase of the NO conversion, but they also facilitate the production of undesired  $\text{NH}_3$ .<sup>344</sup> In order to suppress the formation of ammonia, additional oxygen is often fed to the reactant stream, or a second metal added to the catalyst formulation. However, such modifications might also heavily compromise the overall activity, selectivity and temperature window of operation.<sup>302, 318, 319, 321, 322</sup> The optimization of the inlet reactant concentrations and catalyst composition will be the subject of future research for our micelle-based materials.

Contrary to the majority of the previous works, where the structural and chemical composition of the catalysts was only available in the as-prepared and reacted states, our *in situ* XAFS investigation allows to follow its evolution in the course of the NO reduction. This enables to establish structure, chemical state, and reactivity correlations. Prior to the reactant exposure, our Pd NPs were reduced in  $\text{H}_2$  (240°C), which leads to a clear lattice expansion due to the formation of Pd hydride species.<sup>220</sup> The observed expansion in the Pd-Pd distances of ~3.1 % is in agreement with previous studies.<sup>346-348</sup> The large (~11) 1st NN coordination number obtained by EXAFS for the reduced NPs evidences the presence of large metallic Pd NPs, in agreement with our TEM data (~5.3 nm average NP size).<sup>200, 220</sup> Upon the introduction of the reactants ( $\text{NO} + \text{H}_2$ ) at RT, the

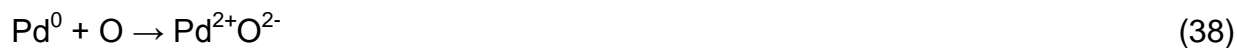
average Pd-Pd distance was found to decrease significantly, returning to the bulk Pd value, and suggesting the complete decomposition of the hydride. Furthermore, our XANES data clearly reveal the appearance of a large fraction of a Pd<sup>δ+</sup> component (Fig. 75 and Pd-X component in Fig. 77), along with a concomitant strong suppression of the Pd<sup>0</sup> contribution. With increasing temperature, the relative content of the Pd<sup>δ+</sup> component increases significantly at the expense of the Pd<sup>0</sup> contribution, as can be deduced from the ΔXANES spectra in Fig. 75. The Pd<sup>δ+</sup> or Pd-X contribution observed cannot be simply attributed to the formation of Pd-O bonds in a palladium oxide phase. In fact, the EXAFS spectra measured at the corresponding temperatures do not exhibit the features characteristic of PdO (i.e. the peaks at 1.65, 2.70 and 3.15 Å in the phase-shift uncorrected radial distribution of Fig. 76).<sup>326,334, 349</sup>

The fits of our EXAFS data acquired below 150°C reveal the existence of a Pd-X component with an average bond length of  $\sim 2.55 \pm 0.08$  Å. Based on available literature, this bond can be assigned to a long Pd-O bond, for example, due to the adsorption of H<sub>2</sub>O. In fact, distances between 2.37 and 2.59 Å have been reported for Pd(OH)<sub>2</sub>.<sup>350, 351</sup> A related possibility for a long Pd-O bond was proposed by Koningsberger and Gates<sup>267</sup>, who reported large metal-O distances (2.5-2.7 Å) for atoms within NPs in contact with O from the underlying oxide support when the samples were treated in H<sub>2</sub> below 350°C or when the supports were hydroxylated. Hydrogen is suggested to reduce the charge on the metal, which leads to a longer metal-support O distance. Our experimental findings can be explained following the former idea, since our samples were measured at low temperature (<240°C) in a reactant stream containing H<sub>2</sub> and under water-rich experimental conditions which are expected to lead

to the hydroxylation of the oxide support. Following Koningsberger and Gates<sup>267</sup>, we tentatively identify the location of hydrogen atoms at the NP/support interface, likely in the form of OH<sup>-</sup> species. Such model explains the observation of cationic Pd in the XANES data and the long Pd-X pair in EXAFS.

Our XAFS data reveal that a large fraction of the Pd atoms in our NPs reside in a non-metallic environment (Pd<sup>δ+</sup>) under reactant exposure in the temperature range from 25°C to 120°C. This is evidenced by the increase in the intensity of the XANES absorption peak (Pd<sup>δ+</sup>) and the decrease in the metallic Pd-Pd scattering which is accompanied by an increase of the additional Pd-X component, [Fig. 77(b)]. In addition, a strong decrease in the Pd-Pd coordination number is observed in parallel with the appearance of the Pd-X bonding. These effects suggest that our NPs undergo significant chemical and morphological changes at these temperatures. It should also be considered that due to the initial large size of our Pd NPs (~5 nm according to TEM), the volume-averaged EXAFS technique is not very sensitive to changes in the NP surface, and therefore, the strong modifications in the EXAFS spectra reported here must reflect drastic changes in the morphology and/or chemical composition of the NPs affecting a large number of atoms. The reactant-mediated structural changes extracted from the analysis of our EXAFS spectra might be attributed to the encapsulation of the Pd NPs by the ZrO<sub>2</sub> support. However, this effect is not consistent with our data, i.e. there is no concomitant deactivation, and Pd-Zr bonds are not observed. Furthermore, ZrO<sub>2</sub> decomposition has only been reported above 500°C.<sup>352,29</sup> A second possibility is the NO-induced disruption and redispersion of the Pd particles over the support, leading to individual ions or small clusters on the ZrO<sub>2</sub> surface. The low Pd-Pd CN obtained at

120°C and the detection of an additional interface/surface component [Pd-X] can be easily explained if Pd redispersion is considered. The phenomenon of NP redispersion on oxide supports has been previously reported by a number of groups, including NO-induced redispersion of Pd NPs.<sup>326, 327, 332-334, 353, 354</sup> For example, Okumura *et al.*<sup>326</sup> demonstrated that the oxidation of Pd NPs at high temperature leads to NP disintegration and the formation of dispersed PdO. The acidic nature of the support, giving rise to a strong interaction with the more basic PdO was found to underlie this effect. The oxidative redispersion of Pd NPs by NO adsorption at RT on Pd<sup>0</sup> was proven by Che *et al.*<sup>78</sup> and Aylor *et al.*<sup>333, 354</sup> They showed the decomposition of NO upon adsorption on the Pd crystallites and their subsequent oxidation:



The resulting Pd ions are known to be highly mobile due to the strong interaction with the acidic support, which facilitates their redispersion over the support surface as single ions or small clusters<sup>333, 334, 354</sup> The O<sup>2-</sup> ions produced in process (38) might not remain bonded to the Pd<sup>2+</sup> cations, but may react with H<sub>2</sub>, leading to Pd-OH complexes (e.g. Pd-OH<sub>2</sub>, with a Pd-O distance in agreement with our EXAFS observation).<sup>333, 354</sup> In fact, it was shown that protons are required to stabilize the Pd<sup>2+</sup> ions on zeolite surfaces.<sup>328, 355</sup> These can be provided by an acidic support or by H<sub>2</sub>, in the form of OH groups.<sup>355</sup> The ZrO<sub>2</sub> used in the present study is only weakly acidic and therefore, the H<sub>2</sub> available within the reactant stream or that initially absorbed in the Pd NPs (spilling over to the support), might play an important role in the stabilization of the Pd<sup>2+</sup> ions.<sup>356</sup>



<sup>357</sup> We note that the time scale (48 h) for the complete dispersion of 2 nm Pd crystallites under NO exposure reported by Che *et al.*<sup>354</sup>, is consistent with the progressive redispersion observed for our NPs with increasing annealing temperature (RT to 120°C).

As the NO conversion reaches 100% at 150°C, both XANES and EXAFS data show a pure metallic Pd spectrum. Consequently, the Pd-X contribution has completely vanished at this temperature (see Fig. 76). Moreover, the Pd-Pd coordination number of  $\sim 12 \pm 2$  at 150°C demonstrates the formation of large Pd<sup>0</sup> clusters. The reduction and aggregation of the Pd<sup>2+</sup> ions into stable metallic particles during NO conversion is likely to be a consequence of the desorption of the oxidative species (N<sub>2</sub>O and H<sub>2</sub>O) and was previously shown to occur in a H<sub>2</sub> atmosphere during the NO reduction with CH<sub>4</sub> above 330°C.<sup>327, 334</sup> Furthermore, if our Pd<sup>δ+</sup> species were stabilized at OH defects on the ZrO<sub>2</sub> surface, their stability will depend on the relative coverage of such species on the ZrO<sub>2</sub> surface under the different reaction conditions, which is expected to decrease with increasing annealing temperature.<sup>358</sup> The favorable role of OH species on the stabilization of small PVD-grown metal NPs supported on oxides against coarsening has been previously reported.<sup>113, 359, 360</sup>

The reduction and agglomeration of the Pd NPs in the present study above 120°C correlates with the shift of the reaction selectivity from N<sub>2</sub>O toward N<sub>2</sub>. This is in accordance with previous results indicating that the formation of N<sub>2</sub> is mainly governed by metallic Pd sites.<sup>302, 327, 330, 345, 361, 362</sup> Accordingly, our *in situ* XAFS data indicate that the active catalyst for the selective reduction of NO using H<sub>2</sub> are large (~5 nm) metallic NPs.

Further increasing the reaction temperature up to 240°C has no significant impact on the reactivity and selectivity of our Pd NPs, aside from the minor additional generation of NH<sub>3</sub>. Above 150°C, the XANES and EXAFS spectra remain nearly identical, indicating the lack of significant structural changes in our samples at these temperatures (see Fig. 76). This is reflected in the Pd-Pd coordination numbers and the Pd-Pd distances, which are constant within the uncertainty. Furthermore, based on a comparison of the initial (after reduction in H<sub>2</sub> but before the reaction) and final (after the reaction, i.e. after the NP disruption and subsequent re-agglomeration) Pd-Pd 1<sup>st</sup> NN CN numbers, the average particle size was found to remain nearly constant, although a slight increase might have occurred. Nevertheless, the increase in the CNs observed after the reaction is within the error bars. The analysis of the TEM data also revealed similar NP size distributions before and after the reaction, with a possible increase in the NP diameter after the reaction, which is also within the error margin of the corresponding NP size distribution,

After exposing our Pd NPs to the reactants for an extended period of time (18h) at 240°C, no decrease in catalytic activity was observed. This evidences that our catalysts did not suffer from poisoning by oxides or N-containing intermediates.

The evolution of the structure, morphology, and chemical state of our Pd nanocatalysts at different stages of the H<sub>2</sub>-SCR NO reduction is summarized in Fig. 78: (i) the initial oxidized state, (ii) the reduced particles with absorbed H, (iii) the exposure to the reactants at 90°C with the subsequent redispersion and stabilization of cationic Pd species, which are likely to be formed upon interaction of Pd with OH<sup>-</sup> groups on the ZrO<sub>2</sub> support, (iv) the maximum redispersion at 120°C, (v) the change in the chemical

state of the NPs back to metallic coinciding with their agglomeration and the conversion of NO to N<sub>2</sub>O and N<sub>2</sub> at 150°C and (vi) at 240°C.

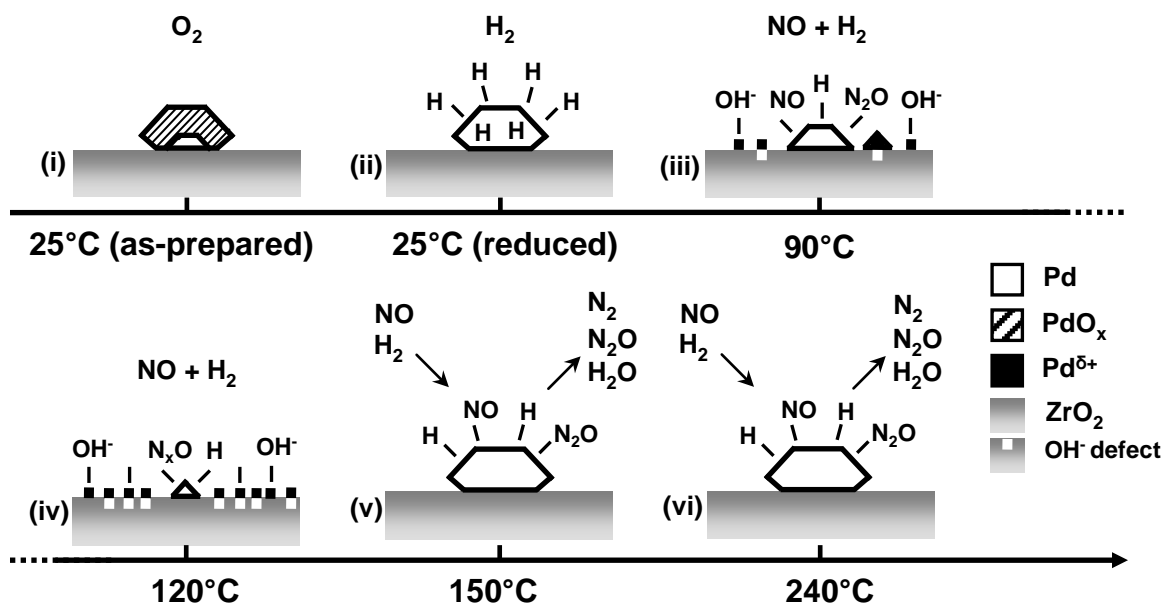


Fig. 78: Schematic representation of the structure and chemical state of our Pd nanocatalysts at various stages of the H<sub>2</sub>-SCR NO reduction.

## 9.5 Conclusions

The evolution of the structure and oxidation state of ZrO<sub>2</sub>-supported Pd nanocatalysts during the *in situ* reduction of NO with H<sub>2</sub> has been monitored using XAS spectroscopy. Our results show that our catalysts undergo significant structural and chemical changes. In particular, cationic Pd species are detected upon the introduction of the reactants. Furthermore, the redispersion of the Pd NPs on the ZrO<sub>2</sub> surface and the formation of small Pd clusters or ions was observed upon the introduction of the reactants (NO + H<sub>2</sub>) at RT until the onset temperature for NO reduction was reached (120°C). This phenomenon is the result of the interaction of NO with surface atoms in

the initially metallic Pd clusters supported on ZrO<sub>2</sub>. EXAFS data indicates the formation of Pd<sup>δ+</sup> species at the expense of Pd<sup>0</sup> from RT to 120°C. Nevertheless, our EXAFS data indicate that PdO<sub>x</sub> species are not formed, but that the cationic Pd species are likely stabilized at OH defects on the ZrO<sub>2</sub> surface. Possibly due to the redispersion phenomenon, a high selectivity for N<sub>2</sub>O was detected at the onset of the NO reduction reaction (≥120°C). As the reaction temperature increases (>150°C), the selectivity shifts mainly toward N<sub>2</sub> (~80%). Concomitant with the onset of the NO reduction reaction, the disappearance of the Pd<sup>δ+</sup> species and formation of larger metallic Pd aggregates are observed, evidencing that metallic Pd constitutes the active phase for the H<sub>2</sub>-reduction of NO over Pd NPs on ZrO<sub>2</sub>.

In conclusion, our results emphasize the importance of *in situ* structural and chemical information under *operando* conditions for the understanding of the mechanisms governing catalytic reactivity. The significant morphological changes observed in the current study can be exploited to tailor the next generation of selective catalysts.

## REFERENCES

1. C. R. Henry "*Surface studies of supported model catalysts.*" Surf. Sci. Rep. 31 **1998**, 231-325.
2. B. Roldan Cuenya "Synthesis and catalytic properties of metal nanoparticles: Size, shape, support, composition, and oxidation state effects." Thin Solid Films 518 **2010**, 3127-3150.
3. C. T. Campbell "Ultrathin metal films and particles on oxide surfaces: structural, electronic and chemisorptive properties." Surf. Sci. Rep. 27 **1997**, 1-111.
4. A. K. Santra and D. W. Goodman "*Oxide-supported metal clusters: models for heterogeneous catalysts.*" J. Phys.: Condens. Matter 14, **2002**, R31-R62.
5. S. Mostafa, F. Behafarid, J. R. Croy, L. K. Ono, L. Li, J. C. Yang, A. I. Frenkel and B. Roldan Cuenya "*Shape-Dependent Catalytic Properties of Pt Nanoparticles.*" J. Am. Chem. Soc. 132, **2010**, 15714-15719.
6. R. M. Rioux, H. Song, M. Grass, S. Habas, K. Niesz, J. D. Hoefelmeyer, P. Yang and G. A. Somorjai "Monodisperse platinum nanoparticles of well-defined shape: synthesis characterization, catalytic properties and future prospects." Top. Catal. 39, **2006**, 167-174.
7. V. Komanicky, H. Iddir, K. C. Chang, A. Menzel, G. Karapetrov, D. Hennessy, P. Zapol and H. You "*Shape-Dependent Activity of Platinum Array Catalyst.*" J. Am. Chem. Soc. 131, **2009**, 5732-5733.
8. P. Christopher and S. Linic "Engineering selectivity in heterogeneous catalysis: Ag nanowires as selective ethylene epoxidation catalysts." J. Am. Chem. Soc. 130, **2008**, 11264-11265.
9. A. Naitabdi, L. K. Ono and B. Roldan Cuenya "Local investigation of the electronic properties of size-selected Au nanoparticles by scanning tunneling spectroscopy." Appl. Phys. Lett. 89, **2006**, 043101.
10. J. J. Zou, C. Chen, C. J. Liu, Y. P. Zhang, Y. Han and L. Cui "Pt nanoparticles on TiO<sub>2</sub> with novel metal-semiconductor interface as highly efficient photocatalyst." Mater. Lett. 59, **2005**, 3437-3440.

11. P. Strasser, S. Koh, T. Anniyev, J. Greeley, K. More, C. F. Yu, Z. C. Liu, S. Kaya, D. Nordlund, H. Ogasawara, M. F. Toney and A. Nilsson "*Lattice-strain control of the activity in dealloyed core-shell fuel cell catalysts.*" Nat. Chem. 2, **2010**, 454-460.
12. A. T. Bell "The impact of nanoscience on heterogeneous catalysis." Science 299, **2003**, 1688-1691.
13. P. K. Jain, X. Huang, I. H. El-Sayed and M. A. El-Sayed "Review of Some Interesting Surface Plasmon Resonance-enhanced Properties of Noble Metal Nanoparticles and Their Applications to Biosystems." Plasmonics 2, **2007**, 107-118.
14. G. A. Somorjai, H. Frei and J. Y. Park "Advancing the Frontiers in Nanocatalysis, Biointerfaces, and Renewable Energy Conversion by Innovations of Surface Techniques." J. Am. Chem. Soc. 131, **2009**, 16589-16605.
15. N. R. Shiju and V. V. Gulians "Recent developments in catalysis using nanostructured materials." Appl. Catal. A-Gen 356, **2009**, 1-17.
16. V. Raffa, O. Vittorio, C. Riggio and A. Cuschieri "*Progress in nanotechnology for healthcare.*" Minim. Invasiv. Ther. 19, **2010**, 127-135.
17. P. Christopher, H. Xin and S. Linic "Visible-light-enhanced catalytic oxidation reactions on plasmonic silver nanostructures." Nat. Chem. 3, **2011**, 467-472.
18. X. Lai, T. P. St Clair, M. Valden and D. W. Goodman "Scanning tunneling microscopy studies of metal clusters supported on TiO<sub>2</sub>(110): Morphology and electronic structure." Prog. Surf. Sci. 59, **1998**, 25-52.
19. Q. S. Mei and K. Lu "Melting and superheating of crystalline solids: From bulk to nanocrystals." Prog. Mater. Sci. 52, **2007**, 1175-1262.
20. G. D. Barrera, J. A. O. Bruno, T. H. K. Barron and N. L. Allen "*Negative Thermal Expansion.*" J. Phys: Condens. Matter 17, **2005**, R217.
21. J. H. Kang, L. D. Menard, R. G. Nuzzo and A. I. Frenkel "Unusual non-bulk properties in nanoscale materials: Thermal metal-metal bond contraction of gamma-alumina-supported Pt catalysts." J. Am. Chem. Soc. 128, **2006**, 12068.

22. S. I. Sanchez, L. D. Menard, A. Bram, J. H. Kang, M. W. Small, R. G. Nuzzo and A. I. Frenkel "The emergence of non-bulk properties in supported metal clusters: negative thermal expansion and atomic disorder in Pt nanoclusters supported on  $\gamma$ -Al<sub>2</sub>O<sub>3</sub>." *Phys. Rev. B* 78, **2008**, 121404.
23. F. D. Vila, J. J. Rehr, J. Kas, R. G. Nuzzo and A. I. Frenkel "Dynamic structure in supported Pt nanoclusters: Real-time density functional theory and x-ray spectroscopy simulations." *Phys. Rev. B* 78, **2008**, 121404.
24. H. Yildirim, A. Kara and T. S. Rahman "*Structural, vibrational and thermodynamic properties of Ag<sub>n</sub>Cu<sub>34-n</sub> nanoparticles.*" *J. Phys.: Condens. Matter.* 21, **2009**, 084220.
25. A. Kara and T. S. Rahman "*Vibrational Properties of Metallic Nanocrystals.*" *Phys. Rev. Lett.* 81, **1998**, 1453-1456.
26. B. Roldan Cuenya, A. Naitabdi, J. Croy, W. Sturhahn, J. Y. Zhao, E. E. Alp, R. Meyer, D. Sudfeld, E. Schuster and W. Keune "*Atomic Vibrations in Iron Nanoclusters: nuclear resonant inelastic X-ray scattering and molecular dynamics simulations.*" *Phys. Rev. B* 76, **2007**, 195422.
27. B. Roldan Cuenya, W. Keune, R. Peters, E. Schuster, B. Sahoo, U. von Hörsten, W. Sturhahn, J. Zhao, T. S. Toellner, E. E. Alp and S. D. Bader "*High-Energy Phonon Confinement in Nanoscale Metallic Multilayers.*" *Phys. Rev. B* 77, **2008**, 165410.
28. A. Naitabdi, F. Behafarid and B. Roldan Cuenya "Enhanced thermal stability and nanoparticle-mediated surface patterning: Pt/TiO<sub>2</sub>(110)." *Appl. Phys. Lett.* 94, **2009**, 083102.
29. B. Fultz "*Vibrational Thermodynamics of Materials.*" *Prog. Mater. Sci.* 55, **2010**, 247-352.
30. S. I. Sanchez, L. D. Menard, A. Bram, J. H. Kang, M. W. Small, R. G. Nuzzo and A. I. Frenkel "The emergence of nonbulk properties in supported metal clusters: negative thermal expansion and atomic disorder in Pt nanoclusters supported on  $\gamma$ -Al<sub>2</sub>O<sub>3</sub>." *J. Am. Chem. Soc.* 131, **2009**, 7040-7054.

31. T. Comaschi, A. Balerna and S. Mobilio "Temperature dependence of the structural parameters of gold nanoparticles investigated with EXAFS." *Phys. Rev. B* 77, **2008**, 075432.
32. T. L. Hill "*Thermodynamics of Small Systems.*" *J. Chem. Phys.* 36, **1962**, 3182.
33. M. Schmidt, R. Kusche, B. von Issendorff and H. Haberland "*Irregular variations in the melting point of size-selected atomic clusters.*" *Nature* 393, **1998**, 238-240.
34. Z. Y. Lu, C. Z. Wang and K. M. Ho "Structures and dynamical properties of C, Si, Ge, and Sn clusters with n up to 13." *Phys. Rev. B* 61, **2000**, 2329-2334.
35. N. Fairley and A. Carrick, *The Casa cookbook* **2005**, Knutsford: Acolyte Science.
36. B. Roldan Cuenya, J. R. Croy, S. Mostafa, F. Behafarid, L. Li, Z. Zhang, J. C. Yang, Q. Wang and A. I. Frenkel "*Solving the structure of size-selected Pt nanocatalysts synthesized by inverse micelle encapsulation.*" *J. Am. Chem. Soc.* 132, **2010**, 8747.
37. B. Roldan Cuenya, A. I. Frenkel, S. Mostafa, F. Behafarid, J. R. Croy, L. K. Ono and Q. Wang "*Anomalous lattice dynamics and thermal properties of supported, size-and shape selected Pt nanoparticles.*" *Phys. Rev. B* 82, **2010**, 155450.
38. B. Roldan Cuenya, M. Alcántara Ortigoza, L. Ono, F. Behafarid, S. Mostafa, J. Croy, K. Paredis, G. Shafai, T. Rahman, L. Li, Z. Zhang and J. Yang "*Thermodynamic properties of Pt nanoparticles: Size, shape, support, and adsorbate effects.*" *Phys. Rev. B* 84, **2011**, 245438.
39. F. Behafarid and B. R. Cuenya "*Nanoepitaxy Using Micellar Nanoparticles.*" *Nano Lett* 11, **2011**, 5290-5296.
40. J. P. Spatz, S. Mössmer, C. Hartmann, M. Möller, T. Herzog, M. Krieger, H. G. Boyen, P. Ziemann and B. Kabius "*Ordered deposition of inorganic clusters from micellar block copolymer films.*" *16*, **2000**, 407-415.
41. F. Behafarid and B. Roldan Cuenya "Coarsening Phenomena of Metal Nanoparticles and the Influence of the Support Pre-treatment: Pt/TiO<sub>2</sub>(110 )." *Surf. Sci.* 606, **2011**, 908-918.
42. J. M. Thomas and W. J. Thomas, *Principles and practice of heterogeneous catalysis* **1997**, Weinheim: VCH.



43. M. Haruta "Size- and support-dependency in the catalysis of gold " *Catal. Today* 36, **1997**, 153-166.
44. L. M. Petkovic, D. M. Ginosara, H. W. Rollinsa, K. C. Burcha, C. Deianab, H. S. Silvab, M. F. Sardellab and D. Granadosb "*Activated carbon catalysts for the production of hydrogen via the sulfur–iodine thermochemical water splitting cycle.*" *Int. J. Hydrogen Energ.* 34, **2009**, 4057-4064.
45. V. R. Choudhary, K. C. Mondal and A. S. Mamman "High-temperature stable and highly active/selective supported NiCoMgCeOx catalyst suitable for autothermal reforming of methane to syngas." *J. Catal.* 233, **2005**, 36-40.
46. D. M. Ginosar, H. W. Rollins, L. M. Petkovic, K. C. Burch and M. J. Rush1 "*High-temperature sulfuric acid decomposition over complex metal oxide catalysts.*" *Int. J. Hydrogen Energ.* 34, **2009** 4065-4073.
47. S. N. Rashkeev, D. M. Ginosar, L. M. Petkovic and H. H. Farrell "*Catalytic activity of supported metal particles for sulfuric acid decomposition reaction.*" *Catal. Today* 139 **2009**, 291-298.
48. L. M. Petkovic, D. M. Ginosar, H. W. Rollins, K. C. Burch, P. J. Pinhero and H. H. Farrell "*Pt/TiO<sub>2</sub> (rutile) catalysts for sulfuric acid decomposition in sulfur-based thermochemical water-splitting cycles.*" *Appl. Catal. A-Gen.* 338, **2008**, 27-36.
49. M. Ni, M. K. H. Leung, D. Y. C. Leung and K. Sumathy "A review and recent developments in photocatalytic water-splitting using TiO<sub>2</sub> for hydrogen production." *Renew. Sust. Energ. Rev.* 11, **2007**, 401-425.
50. A. L. Linsebigler, G. Lu and J. T. Yates "Photocatalysis on TiO<sub>2</sub> Surfaces: Principles, Mechanisms and Selected Results." *Chem. Rev.* 95 **1995**, 735-758.
51. S. C. Parker and C. T. Campbell "Reactivity and sintering kinetics of Au/TiO<sub>2</sub>(110) model catalysts: particle size effects." *Top. Catal.* 44, **2007**, 3-13.
52. C. T. Campbell, S. C. Parker and D. E. Starr "The effect of size-dependent nanoparticle energetics on catalyst sintering." *Science* 317, **2002**, 44.
53. S. C. Parker and C. T. Campbell "Kinetic model for sintering of supported metal particles with improved size-dependent energetics and applications to Au on TiO<sub>2</sub>(110)." *Phys. Rev. B* 75, **2007**, 035430.

54. P. A. Thiel, M. Shen, D. J. Liu and J. W. Evans "Coarsening of Two-Dimensional Nanoclusters on Metal Surfaces." *J. Phys. Chem. C* 113, **2009**, 5047-5067.
55. M. J. J. Jak, PhD thesis, *An Atomic Scale View on a Model Catalyst: Pd Nanoparticles on TiO<sub>2</sub>*, 2000, Leiden University: Leiden. p. 143.
56. M. J. J. Jak, C. Konstapel, A. van Kreuningen, J. Chrost, J. Verhoeven and J. W. M. Frenken "The influence of substrate defects on the growth rate of palladium nanoparticles on a TiO<sub>2</sub>(110) surface." *Surf. Sci.* 474, **2001**, 28-36.
57. M. J. J. Jak, C. Konstapel, A. van Kreuningen, J. Verhoeven and J. W. M. Frenken "Scanning tunnelling microscopy study of the growth of small palladium particles on TiO<sub>2</sub>(110)." *Surf. Sci.* 457, **2000**, 295-310.
58. A. El-Azab, S. Gan and Y. Liang "Binding and diffusion of Pt nanoclusters on anatase TiO<sub>2</sub>(001)-(1x4) surface." *Surf. Sci.* 506, **2002**, 93-104.
59. A. K. Datye, X. Qing, K. C. Kharas and J. M. McCarty "Particle size distributions in heterogeneous catalysts: What do they tell us about the sintering mechanism?" *Catal. Today* 111, **2006**, 59.
60. C. E. J. Mitchell, A. Howard, M. Carney and R. G. Egdell "Direct observation of behaviour of Au nanoclusters on TiO<sub>2</sub>(110) at elevated temperatures." *Surf. Sci.* 490, **2001**, 196-210.
61. P. Stone, S. Poulston, R. A. Bennett and M. Bowker "Scanning tunnelling microscopy investigation of sintering in a model supported catalyst: nanoscale Pd on TiO<sub>2</sub>(110)." *Chem. Commun.*, **1998**, 1369-1370.
62. M. v. Smoluchowski *Phys. Z.* 17, **1916**, 585.
63. M. v. Smoluchowski *Z. Phys. Chem.* 92, **1917**, 129.
64. P. Wynblatt and N. A. Gjostein "Supported metal crystallites " *Prog. Solid State Ch.* 9, **1975**, 21-58.
65. P. Wynblatt and N. A. Gjostein "Particle growth in model supported metal catalysts—I. Theory." *Acta Metall. Mater.* 24, **1976**, 1165-1174.
66. D. Kandel "Selection of the scaling solution in a cluster coalescence model." *Phys. Rev. Lett.* 79, **1997**, 4238-4241.

67. C. G. Granqvist and R. A. Buhrman "Size distributions for supported metal catalysts: Coalescence growth versus ostwald ripening." *J. Catal.* 42, **1976**, 477-479.
68. J. G. McCarty, G. Malukhin, D. M. Poojary, A. K. Datye and Q. Xu "*Thermal Coarsening of Supported Palladium Combustion Catalysts.*" *J. Phys. Chem. B* 109, **2005**, 2387-2391.
69. R. S. Goeke and A. Datye "Model oxide supports for studies of catalyst sintering at elevated temperatures." *Top. Catal.* 46, **2007**, 3.
70. B. Roldan Cuenya, S. H. Baeck, T. F. Jaramillo and E. W. McFarland "Size- and support-dependent electronic and catalytic properties of Au<sup>0</sup>/Au<sup>3+</sup> nanoparticles synthesized from block copolymer micelles." *J. Am. Chem. Soc.* 125, **2003**, 12928-12934.
71. G. M. Veith, A. R. Lupini, S. Rashkeev, S. J. Pennycook, D. R. Mullins, V. Schwartz, C. A. Bridges and N. J. Dudney "*Thermal stability and catalytic activity of gold nanoparticles supported in silica.*" *J. Catal.* 262, **2009**, 92-101.
72. U. Diebold "*The surface science of titanium dioxide.*" *Surf. Sci. Rep.* 48, **2003**, 53.
73. A. Naitabdi, L. K. Ono, F. Behafarid and B. Roldan Cuenya "Thermal Stability and Segregation Processes in Self-Assembled Size-Selected Au<sub>x</sub>Fe<sub>1-x</sub> Nanoparticles Deposited on TiO<sub>2</sub>(110): Composition Effects." *J. Phys. Chem. C* 113, **2009**, 1433-1446.
74. L. K. Ono and B. Roldan Cuenya "Formation and Thermal Stability of Au<sub>2</sub>O<sub>3</sub> on Gold Nanoparticles: Size and Support Effects." *J. Phys. Chem. C* 112, **2008**, 4676-4686.
75. A. Naitabdi and B. Roldan Cuenya "Formation, thermal stability, and surface composition of size-selected AuFe nanoparticles." *Appl. Phys. Lett.* 91, **2007**, 113110
76. L. K. Ono, B. Yuan, H. Heinrich and B. Roldan Cuenya "Formation and Thermal Stability of Platinum Oxides on Size-Selected Platinum Nanoparticles: Support Effects." *J. Phys. Chem. C* 114, **2010**, 22119
77. C. Xu, X. F. Lai and D. W. Goodman "Local electronic structure of metal particles on metal oxide surfaces: Ni on alumina." *Faraday Discuss.* 105, **1996**, 247-261.

78. J. B. Park, S. F. Conner and D. A. Chen "Bimetallic Pt-Au Clusters on TiO<sub>2</sub>(110): Growth, Surface Composition, and Metal-Support Interactions." J. Phys. Chem. C 112, **2008**, 5490-5500.
79. K. Paredis, L. K. Ono, S. Mostafa, L. Li, Z. F. Zhang, J. C. Yang, L. Barrio, A. I. Frenkel and B. Roldan Cuenya "*Structure, Chemical Composition, And Reactivity Correlations during the In Situ Oxidation of 2-Propanol.*" J. Am. Chem. Soc. 133, **2011**, 6728-6735.
80. L. K. Ono, J. R. Croy, H. Heinrich and B. Roldan Cuenya "Oxygen Chemisorption, Formation, and Thermal Stability of Pt Oxides on Pt Nanoparticles Supported on SiO<sub>2</sub>/Si(001): Size Effects." J. Phys. Chem. C 115, **2011**, 16856-16866.
81. J. R. Croy, S. Mostafa, H. Heinrich and B. Roldan Cuenya "Size-selected Pt Nanoparticles Synthesized via Micelle Encapsulation: Effect of Pretreatment and Oxidation State on the Activity for Methanol Decomposition and Oxidation." Catal. Lett. 131, **2009**, 21-32.
82. J. Matos, L. K. Ono, F. Behafarid, J. R. Croy, S. Mostafa, A. T. DeLaRiva, A. K. Datye, A. I. Frenkel and B. Roldan Cuenya "*In situ coarsening study of inverse micelle-prepared Pt nanoparticles supported on  $\gamma$ -Al<sub>2</sub>O<sub>3</sub>: pretreatment and environmental effects.*" Phys. Chem. Chem. Phys. 14, **2012**, 11457-11467.
83. B. Ravel and M. Newville "ATHENA, ARTEMIS, HEPHAESTUS: data analysis for X-ray absorption spectroscopy using IFEFFIT." J. Synchrotron Rad. 12, **2005**, 537-541.
84. M. Newville "*IFEFFIT: interactive XAFS analysis and FEFF fitting.*" J. Synchrotron Rad. 8, **2001**, 322-324.
85. B. Ravel and M. Newville "ATHENA and ARTEMIS: Interactive graphical data analysis using IFEFFIT." Phys. Scr. T115, **2005**, 1007-1010.
86. S. Zabinsky, J. Rehr, A. Ankudinov, R. Albers and M. Eller "*Multiple-scattering calculations of x-ray-absorption spectra.*" Phys. Rev. B 52, **1995**, 2995-3009.
87. J. Y. Yang, W. Y. Hu, S. G. Chen and J. F. Tang "*Surface Self-Diffusion Behavior of a Pt Adatom on Wulff Polyhedral Clusters.*" J. Phys. Chem. C 113, **2009**, 21501-21505.

88. O. Dulub, W. Hebenstreit and U. Diebold "Imaging Cluster Surfaces with Atomic Resolution: The Strong Metal-Support Interaction State of Pt Supported on  $\text{TiO}_2(110)$ ." *Phys. Rev. Lett.* 84, **2000**, 3646-3649.
89. J. Szoko and A. Berko "Tunnelling spectroscopy of Pt nanoparticles supported on  $\text{TiO}_2(110)$  surface." *Vacuum* 71, **2003**, 193-199.
90. L. R. Houk, S. R. Challa, B. Grayson, P. Fanson and A. K. Datye "*The Definition of "Critical Radius" for a Collection of Nanoparticles Undergoing Ostwald Ripening.*" *Langmuir* 25, **2009**, 11225-11227.
91. F. Yang, M. S. Chen and D. W. Goodman "*Sintering of Au Particles Supported on  $\text{TiO}_2(110)$  during CO Oxidation.*" *J. Phys. Chem. C* 113, **2009**, 254-260.
92. D. N. Belton, Y.-M. Sun and J. M. White "Thin-Film Models of Strong Metal-Support Interaction Catalysts. Platinum on Oxidized Titanium." *J. Phys. Chem.* 88, **1984**, 1690-1695.
93. S. J. Tauster "*Strong Metal-Support Interactions.*" *Acc. Chem. Res.* 20, **1987**, 389-394.
94. E. Wahlström, N. Lopez, R. Schaub, P. Thostrup, A. Rønnau, C. Africh, E. Lægsgaard, J. Nørskov and F. Besenbacher "*Bonding of Gold Nanoclusters to Oxygen Vacancies on Rutile  $\text{TiO}_2(110)$ .*" *Phys. Rev. Lett.* 90, **2003**, 026101.
95. D. C. Schlober, K. Morgenstern, L. K. Verheij, G. Rosenfeld, F. Besenbacher and G. Comsa "*Kinetics of island diffusion on  $\text{Cu}(111)$  and  $\text{Ag}(111)$  studied with variable-temperature STM.*" *Surf. Sci.* 465 **2000**, 19-39.
96. J. Zhou, Y. C. Kang and D. A. Chen "Controlling island size distributions: a comparison of nickel and copper growth on  $\text{TiO}_2(110)$ ." *Surf. Sci.* 537 **2003**, 429-434.
97. C. Xu, X. Lai, G. W. Zajac and D. W. Goodman "Scanning tunneling microscopy studies of the  $\text{TiO}_2(110)$  surface: Structure and the nucleation growth of Pd." *Phys. Rev. B* 56, **1997**, 13464-13482.
98. A. Howard, C. E. J. Mitchell and R. G. Egdell "Real time STM observation of Ostwald ripening of Pd nanoparticles on  $\text{TiO}_2(110)$  at elevated temperature." *Surf. Sci.* 515, **2002**, 504-508.

99. N. Panagiotides and N. I. Papanicolaou "Diffusion of platinum adatoms and dimers on Pt(111) surface by molecular-dynamics simulation." *Int. J. Quantum Chem.* 110, **2009**, 202-209.
100. H. Iddir, S. Ögüt, N. D. Browning and M. M. Disko "Adsorption and diffusion of Pt and Au on the stoichiometric and reduced TiO<sub>2</sub> rutile (110) surfaces." *Phys. Rev. B* 72, **2005**, 081407.
101. H. Iddir, V. Skavysh, S. Ögüt, N. D. Browning and M. M. Disko "*Preferential growth of Pt on rutile TiO<sub>2</sub>*." *Phys. Rev. B* 73, **2006**, 041403.
102. M. Bott, M. Hohage, M. Morgenstern, T. Michely and G. Comsa "*New Approach for Determination of Diffusion Parameters of Adatoms*." *Phys. Rev. Lett.* 76, **1996**, 1304-1307.
103. J. W. Hardin, J. M. Hilbe and J. Hilbe, *Generalized Linear Models and Extensions, 2nd Edition* **2007**: Stata press. 387.
104. J. Carrey, J. L. Maurice, F. Petroff and A. Vaurès "Growth of Au Clusters on Amorphous Al<sub>2</sub>O<sub>3</sub>: Evidence of Cluster Mobility above a Critical Size." *Phys. Rev. Lett.* 86, **2001**, 4600-4603.
105. A. I. Frenkel "Solving the structure of nanoparticles by multiple-scattering EXAFS analysis." *J. Synchrotron Rad.* 6, **1999**, 293-5.
106. J. H. Kang, L. D. Menard, R. G. Nuzzo and A. I. Frenkel "Unusual Non-Bulk Properties in Nanoscale Materials: Thermal Metal–Metal Bond Contraction of  $\gamma$ -Alumina-Supported Pt Catalysts." *J. Am. Chem. Soc.* 128, **2006**, 12068-12069.
107. W. Setthapun, W. D. Williams, S. M. Kim, H. Feng, J. W. Elam, F. A. Rabuffetti, K. R. Poeppelmeier, P. C. Stair, E. A. Stach, F. H. Ribeiro, J. T. Miller and C. L. Marshall "*Genesis and Evolution of Surface Species during Pt Atomic Layer Deposition on Oxide Supports Characterized by in Situ XAFS Analysis and Water-Gas Shift Reaction*." *J. Phys. Chem. C* 114, **2010**, 9758-9771.
108. K. Paredis, L. K. Ono, F. Behafarid, Z. F. Zhang, J. C. Yang, A. I. Frenkel and B. Roldan Cuenya "*Evolution of the Structure and Chemical State of Pd Nanoparticles during the in Situ Catalytic Reduction of NO with H<sub>2</sub>*." *J. Am. Chem. Soc.* 133, **2011**, 13455-13464.

109. S. I. Sanchez, L. D. Menard, A. Bram, J. H. Kang, M. W. Small, R. G. Nuzzo and A. I. Frenkel "The emergence of non-bulk properties in supported metal clusters: negative thermal expansion and atomic disorder in Pt nanoclusters supported on Y-Al<sub>2</sub>O<sub>3</sub>." J. Am. Chem. Soc. 131, **2009**, 7040-7054.
110. L. K. Ono and B. Roldan Cuenya "Effect of interparticle interactions on the low temperature oxidation of CO over size-selected Au nanocatalysts supported on ultrathin TiC films." Catal. Lett. 113, **2007**, 86-94.
111. H. Feng, J. A. Libera, P. C. Stair, J. T. Miller and J. W. Elam "*Subnanometer Palladium Particles Synthesized by Atomic Layer Deposition.*" ACS Catal. 1, **2011**, 665-673.
112. O. Alexeev, d.-w. Kim, G. W. Graham, M. Shelef and B. C. Gates "Temperature-Programmed Desorption of Hydrogen from Platinum Particles on g-Al<sub>2</sub>O<sub>3</sub>: Evidence of Platinum-Catalyzed Dehydroxylation of g-Al<sub>2</sub>O<sub>3</sub>." J. Catal. 185, **1999**, 170.
113. M. A. Brown, E. Carrasco, M. Sterrer and H.-J. Freund "*Enhanced Stability of Gold Clusters Supported on Hydroxylated MgO(001) Surfaces.*" J. Am. Chem. Soc. 132, **2010**, 4064-4065.
114. M. C. R. Jensen, K. Venkataramani, S. Helveg, B. S. Clausen, M. Reichling, F. Besenbacher and J. V. Lauritsen "*Morphology, Dispersion, and Stability of Cu Nanoclusters on Clean and Hydroxylated (alpha-Al<sub>2</sub>O<sub>3</sub>(0001) Substrates.*" J. Phys. Chem. C 112, **2008**, 16953-16960.
115. G. I. Straguzzi, H. R. Aduriz and C. E. Gigola "*Redispersion of Platinum on Alumina Support.*" J. Catal. 66, **1980**, 171-183.
116. T. J. Lee and Y. G. Kim "*Dispersion of supported platinum catalysts in Oxygen.*" Korean J. Chem. Eng. 2, **1985**, 119-124.
117. S. W. Weller and A. A. Montagna "O<sub>2</sub> Chemisorption at High Temperatures on Platinum-Alumina and Platinum-Zeolite." J. Catal. 20, **1971**, 394-407.
118. P. Loof, B. Stenbom, H. Norden and B. Kasemo "Rapid Sintering in No of Nanometer-Sized Pt Particles on Gamma-Al<sub>2</sub>O<sub>3</sub> Observed by Co Temperature-Programmed Desorption and Transmission Electron-Microscopy." J. Catal. 144, **1993**, 60-76.

119. S. B. Simonsen, I. Chorkendorff, S. Dahl, M. Skoglundh, J. Sehested and S. Helveg "Direct Observations of Oxygen-induced Platinum Nanoparticle Ripening Studied by In Situ TEM." J. Am. Chem. Soc. 132, **2010**, 7968-7975.
120. J. E. Stulga, P. Wynblatt and J. K. Tien "Particle splitting and redispersion phenomena in model alumina-supported platinum catalysts." J. Catal. 62, **1980**, 59-69.
121. E. Ruckenstein and Y. F. Chu "Redispersion of Platinum Crystallites Supported on Alumina - Role of Wetting." J. Catal. 59, **1979**, 109-122.
122. M. Valden, X. Lai and D. W. Goodman "Onset of Catalytic Activity of Gold Clusters on Titania with the Appearance of Nonmetallic Properties." Science 281, **1998**, 1647.
123. F. Pesty, H. P. Steinruck and T. E. Madey "Thermal-Stability of Pt Films on TiO<sub>2</sub>(110) - Evidence for Encapsulation." Surf. Sci. 339, **1995**, 83-95.
124. F. Cosandey, L. Zhang and T. E. Madey "Effect of substrate temperature on the epitaxial growth of Au on TiO<sub>2</sub>(110)." Surf. Sci. 474, **2001**, 1-13.
125. A. Linsebigler, C. Rusu and J. T. Yates "Absence of platinum enhancement of a photoreaction on TiO<sub>2</sub>-CO photooxidation on Pt/TiO<sub>2</sub>(110)." J. Am. Chem. Soc. 118, **1996**, 5284-5289.
126. K. Tamura, M. Owari and Y. Nihei "Structure of Platinum Particles Deposited on Titanium-Dioxide (110) Surface Studied by X-Ray Photoelectron Diffraction." Bull. Chem. Soc. Jpn. 61, **1988**, 1539-1544.
127. F. Besenbacher "Scanning tunnelling microscopy studies of metal surfaces." Rep. Prog. Phys. 59, **1996**, 1737-1802.
128. A. Berko, J. Szoko and F. Solymosi "High temperature postgrowing of Pt-nanocrystallites supported and encapsulated on TiO<sub>2</sub>(110) surface." Surf. Sci. 532, **2003**, 390-395.
129. S. G. Azatyan, M. Iwami and V. G. Lifshits "Mn clusters on Si(111) surface: STM investigation." Surf. Sci. 589, **2005**, 106-113.



130. M. Haupt, S. Miller, A. Ladenburger, R. Sauer, K. Thonke, J. P. Spatz, S. Riethmuller, M. Moller and F. Banhart "Semiconductor nanostructures defined with self-organizing polymers." J. Appl. Phys. 91, **2002**, 6057-6059.
131. B. Roldan Cuenya, L. K. Ono, J. R. Croy, A. Naitabdi, H. Heinrich, J. Zhao, E. E. Alp, W. Sturhahn and W. Keune "Structure and phonon density of states of supported size-selected (57)FeAu nanoclusters: A nuclear resonant inelastic x-ray scattering study." Appl. Phys. Lett. 95, **2009**, 143103
132. F. Besenbacher, J. V. Lauritsen and S. Wendt "STM studies of model catalysts." Nano Today 2, **2007**, 30-39.
133. S. J. Tauster, S. C. Fung and R. L. Garten "Strong Metal-Support Interactions - Group-8 Noble-Metals Supported on TiO<sub>2</sub>." J. Am. Chem. Soc. 100, **1978**, 170-175.
134. G. Z. Wulff "Zur Frage der Geschwindigkeit des Wachstums und der Auflösung der Kristallflächen." Kristallogr 34, **1901**, 449.
135. J. A. Enterkin, K. R. Poeppelmeier and L. D. Marks "Oriented Catalytic Platinum Nanoparticles on High Surface Area Strontium Titanate Nanocuboids." Nano Lett. 11, **2011**, 993-997.
136. H. Iddir, V. Komanicky, S. Ogut, H. You and P. Zapol "Shape of platinum nanoparticles supported on SrTiO<sub>3</sub>: Experiment and theory." J. Phys. Chem. C 111, **2007**, 14782-14789.
137. J. Y. Yang, W. Y. Hu and S. G. Chen "Surface self-diffusion of adatom on Pt cluster with truncated octahedron structure." Thin Solid Films 518, **2010**, 4041-4045.
138. C. R. Henry "Morphology of supported nanoparticles." Prog. Surf. Sci. 80, **2005**, 92-116.
139. P. L. Hansen, J. B. Wagner, S. Helveg, J. R. Rostrup-Nielsen, B. S. Clausen and H. Topsoe "Atom-resolved imaging of dynamic shape changes in supported copper nanocrystals." Science 295, **2002**, 2053-2055.
140. J. Goniakowski, A. Jelea, C. Mottet, G. Barcaro, A. Fortunelli, Z. Kuntova, F. Nita, A. C. Levi, G. Rossi and R. Ferrando "Structures of metal nanoparticles adsorbed on MgO(001). II. Pt and Pd." J. Chem. Phys. 130, **2009**.

141. J. A. Rodriguez, G. Liu, T. Jirsak, J. Hrbek, Z. P. Chang, J. Dvorak and A. Maiti "Activation of gold on titania: Adsorption and reaction of SO<sub>2</sub> on Au/TiO<sub>2</sub>(110)." J. Am. Chem. Soc. 124, **2002**, 5242-5250.
142. V. L. Nguyen, D. C. Nguyen, T. Hayakawa, H. Hirata, G. Lakshminarayana and M. Nogami "The synthesis and characterization of platinum nanoparticles: a method of controlling the size and morphology." Nanotechnology 21, **2010**, 035605.
143. Y. D. Li, R. Xu, D. S. Wang and J. T. Zhang "Shape-dependent catalytic activity of silver nanoparticles for the oxidation of styrene." Chem-Asian J. 1, **2006**, 888-893.
144. I. V. Yudanov, A. Genest and N. Rösch "DFT Studies of Palladium Model Catalysts: Structure and Size Effects." J. Cluster Sci., **2011**.
145. Y. Ikuhara and P. Pirouz "Orientation relationship in large mismatched bicrystals and coincidence of reciprocal lattice points (CRLP)." Mater. Sci. Forum. 207-209, **1996**, 121-124.
146. M. Klimenkov, S. Nepijko, H. Kühlenbeck, M. Baumer, R. Schlogl and H. J. Freund "The structure of Pt-aggregates on a supported thin aluminum oxide film in comparison with unsupported alumina: a transmission electron microscopy study." Surf. Sci. 391, **1997**, 27-36.
147. P. Müller and R. Kern "Equilibrium nano-shape changes induced by epitaxial stress (generalised Wulff-Kaishew theorem)." Surf. Sci. 457, **2000**, 229-253.
148. J. Wan, Y. L. Fan, D. W. Gong, S. G. Shen and X. Q. Fan "Surface relaxation and stress of fcc metals: Cu, Ag, Au, Ni, Pd, Pt, Al and Pb." Model Simul. Mater. Sc. 7, **1999**, 189-206.
149. A. K. Datye, D. S. Kalakkad, M. H. Yao and D. J. Smith "Comparison of Metal-Support Interactions in Pt/TiO<sub>2</sub> and Pt/CeO<sub>2</sub>." J. Catal. 155, **1995**, 148-153.
150. S. B. Bonanni, S., K. Ait-Mansour, H. Brune and W. Harbich "Overcoming the Strong Metal-Support Interaction State: CO Oxidation on TiO<sub>2</sub>(110)-Supported Pt Nanoclusters." ACS Catal. 1, **2011**, 385-389.
151. L. D. Marks "Experimental Studies of Small-Particle Structures." Rep. Prog. Phys. 57, **1994**, 603-649.

152. Q. L. Guo, K. Luo, K. A. Davis and D. W. Goodman "*Initial growth of Au on oxides.*" Surf. Interface Anal. 32, **2001**, 161-165.
153. H. Takahashi, R. Watanabe, Y. Miyauchi and G. Mizutani "Discovery of deep and shallow trap states from step structures of rutile TiO<sub>2</sub> vicinal surfaces by second harmonic and sum frequency generation spectroscopy." J. Chem. Phys. 134, **2011**, 154704.
154. A. Berko, O. Hakkel, J. Szoko and F. Solymosi "Thermally induced formation of vacancy-islands on the atomic terraces of TiO<sub>2</sub>(110) surface covered by Pt." Surf. Sci. 507, **2002**, 643-648.
155. M. Bowker and R. A. Bennett "*The flexible surface or the rigid surface?*" Top. Catal. 14, **2001**, 85-94.
156. P. Stone, R. D. Smith and M. Bowker "The structure and reactivity of anchored nanoparticles on a reducible support." Faraday Discuss. 125, **2004**, 379-390.
157. R. A. Bennett, P. Stone and M. Bowker "Scanning tunnelling microscopy studies of the reactivity of the TiO<sub>2</sub>(110) surface: Re-oxidation and the thermal treatment of metal nanoparticles." Faraday Discuss. 114, **1999**, 267-277.
158. M. H. Kim, J. M. Baik, J. P. Zhang, C. Larson, Y. L. Li, G. D. Stucky, M. Moskovits and A. M. Wodtke "*TiO<sub>2</sub> Nanowire Growth Driven by Phosphorus-Doped Nanocatalysis.*" J. Phys. Chem. C 114, **2010**, 10697-10702.
159. J. C. Lee, K. S. Park, T. G. Kim, H. J. Choi and Y. M. Sung "*Controlled growth of high-quality TiO<sub>2</sub> nanowires on sapphire and silica.*" Nanotechnology 17, **2006**, 4317-4321.
160. A. Berko, A. M. Kiss and I. Szoko "Formation of vacancy islands tailored by Pt nanocrystallites and Ar<sup>+</sup> sputtering on TiO<sub>2</sub>(110) surface." Appl. Surf. Sci. 246, **2005**, 174-182.
161. M. Bowker and R. A. Bennett "The role of Ti<sup>3+</sup> interstitials in TiO<sub>2</sub>(110) reduction and oxidation." J. Phys-Condens Mat. 21, **2009**.
162. M. A. Henderson "A surface perspective on self-diffusion in rutile TiO<sub>2</sub>." Surf. Sci. 419, **1999**, 174-187.

163. M. Bowker and E. Fourre "Direct interactions between metal nanoparticles and support: STM studies of Pd on TiO<sub>2</sub>(110)." Appl. Surf. Sci. 254, **2008**, 4225-4229.
164. H. Iddir, S. Ogut, P. Zapol and N. D. Browning "Diffusion mechanisms of native point defects in rutile TiO<sub>2</sub>: Ab initio total-energy calculations." Phys. Rev. B 75, **2007**.
165. K. Hoshino, N. L. Peterson and C. L. Wiley "*Diffusion and Point-Defects in TiO<sub>2-x</sub>*." J. Phys. Chem. Solids 46, **1985**, 1397-1411.
166. P. A. Mulheran, M. Nolan, C. S. Browne, M. Basham, E. Sanvillee and R. A. Bennett "*Surface and interstitial Ti diffusion at the rutile TiO<sub>2</sub>(110) surface.*" Phys. Chem. Chem. Phys. 12, **2010**, 9763-9771.
167. J. Jacobsen "Island shapes in homoepitaxial growth of Pt(111)." Surf. Sci. 359, **1996**, 37-44.
168. D. C. Cronemeyer "Electrical and Optical Properties of Rutile Single Crystals." Phys. Rev. 87, **1952**, 876-886.
169. V. Juve, A. Crut, P. Maioli, M. Pellarin, M. Broyer, N. del Fatti and F. Vallee "*Probing elasticity at the nanoscale: Terahertz acoustic vibration of small metal nanoparticles.*" Nano Lett. 10, **2010**, 1853.
170. P. Buffat and J.-P. Borel "*Size effect on the melting temperature of gold particles.*" Phys. Rev. A 13, **1976**, 2287-2298.
171. B. Gilbert, F. Huang, H. Zhang, G. A. Waychunas and J. F. Banfield "*Nanoparticles: Strained and Stiff.*" Science 305, **2004**, 651.
172. J. Rockenberger, L. Troger, A. Kornowski, T. Vossmeier, A. Eychmuller, J. Feldhaus and H. Weller "*EXAFS studies of size dependence of structural and dynamic properties of CdS nanoparticles.*" J. Phys. Chem. B 101, **1997**, 2691-2701.
173. J. Rockenberger, L. Troger, A. L. Rogach, M. Tischer, M. Grundmann, A. Eychmuller and H. Weller "*The contribution of particle core and surface strain, disorder and vibrations in thiolcapped CdTe nanocrystals.*" J. Chem. Phys. 108, **1998**, 7807-7815.

174. L. J. Giovanetti, J. M. Ramallo-Lopez, F. G. Requejo, D. I. Garcia-Gutierrez, M. J. Yakaman and A. F. Craievich "Anomalous Vibrational Properties Induced by Surface Effects in Capped Pt Nanoparticles." *J. Phys. Chem. C* 111, **2007**, 7599-7604.
175. L. L. Araujo, P. Kluth, G. M. Azevedo and M. C. Ridway "Vibrational properties of Ge nanocrystals determined by EXAFS." *Phys. Rev. B* 74, **2006**, 184102.
176. M. Dubiel, J. Haug, H. Kruth, H. Hofmeister and W. Seifert "Temperature dependence of EXAFS cumulants of Ag nanoparticles in glass." *J. Phys.: Conf. Series* 190, **2009**, 012123.
177. J. H. Kang, L. D. Menard, R. G. Nuzzo and A. I. Frenkel "Unusual non-bulk properties in nanoscale materials: Thermal metal-metal bond contraction of  $\gamma$ -alumina-supported Pt catalysts." *J. Am. Chem. Soc.* 128, **2006**, 12068.
178. S. I. Sanchez, L. D. Menard, A. Bram, J. H. Kang, M. W. Small, R. G. Nuzzo and A. I. Frenkel "The emergence of non-bulk properties in supported metal clusters: negative thermal expansion and atomic disorder in Pt nanoclusters supported on  $\gamma$ -Al<sub>2</sub>O<sub>3</sub>." *J. Am. Chem. Soc.* 131, **2009**, 7040-7054.
179. W.-H. Li, S. Y. Wu, C. C. Yang, S. K. Lai, K. C. Lee, H. L. Huang and H. D. Yang "Thermal Contraction of Au Nanoparticles." *Phys. Rev. Lett.* 89, **2002**, 135504.
180. A. L. Ankudinov, J. J. Rehr, J. J. Low and S. R. Bare "Effect of Hydrogen Adsorption on the X-Ray Absorption Spectra of Small Pt Clusters." *Phys. Rev. Lett.* 86, **2001**, 1642-1645.
181. M. K. Oudenhuijzen, J. H. Bitter and K. D. C. "The nature of the Pt-H bonding for strongly and weakly bonded hydrogen on platinum. A XAFS spectroscopy study of the Pt-H antibonding shaperesonance and Pt-H EXAFS." *J. Phys. Chem. B* 105, **2001**, 4616.
182. S. N. Reifsnyder, M. M. Otten, D. E. Sayers and H. H. Lamb "Hydrogen chemisorption on silica-supported Pt clusters: In situ X-ray absorption spectroscopy." *J. Phys. Chem. B* 101, **1997**, 4972-4977.
183. S. C. Badescu, K. Jacobi, Y. Wang, K. Bedurftig, G. Ertl, P. Salo, T. Ala-Nissila and S. C. Ying "Vibrational states of a H monolayer on the Pt(111) surface." *Phys. Rev. B* 68, **2003**, 205401.

184. P. Z. Pawlow Phys. Chem. 65, **1909**, 545.
185. G. L. Allen, R. A. Bayles, W. W. Giles and W. A. Jesser "*Small particle melting of pure metals.*" Thin Solid Films 144, **1986**, 297-308.
186. T. Yokoyama, S. Kimoto and T. Ohta "Temperature-dependent EXAFS study of supported silver and palladium clusters." Jpn. J. Appl. Phys. 28, **1989**, 851.
187. M. Dippel, A. Maier, V. Gimple, H. Wider, W. E. Evenson, R. L. Rasera and G. Schatz "*Size-dependent melting of self-assembled indium nanostructures.*" Phys. Rev. Lett. 87, **2001**, 095505.
188. S. L. Lai, J. Y. Guo, V. Petrova, G. Ramanath and L. H. Allen "*Size-dependent melting properties of small tin particles: Nanocalorimetric measurements.*" Phys. Rev. Lett. 77, **1996**, 99-102.
189. B. H. Morrow and A. Striolo "Platinum nanoparticles on carbonaceous materials: the effect of support geometry on nanoparticle mobility, morphology, and melting." Nanotechnology 19, **2008**, 195711.
190. Y. H. Wen, H. Fang, Z. Z. Zhu and S. G. Sun "Molecular dynamics investigation of shape effects on thermal characteristics of platinum nanoparticles." Phys. Lett. A 373, **2009**, 272.
191. R. Giulian, L. L. Araujo, P. Kluth, D. J. Sprouster, C. S. Schnohr, G. J. Foran and M. C. Ridway "*Temperature-dependent EXAFS analysis of embedded Pt nanocrystals.*" J. Phys. Condens. Matter 21, **2009**, 155302.
192. Q. F. Gu, G. Krauss, W. Steurer, F. Gramm and A. Cervellino "*Unexpected high stiffness of Ag and Au Nanoparticles.*" Phys. Rev. Lett. 100, **2008**, 045502.
193. F. A. Lindemann Physik Z. 11, **1910**, 609.
194. H.-J. Hoffmann "*On Lindemann's Melting Criterion.*" Material. Wiss. Werkst. 35, **2004**, 79-81.
195. Q. Xu, I. D. Sharp, C. W. Yuan, D. O. Yi, C. Y. Liao, A. M. Glaeser, A. M. Minor, J. W. Beeman, M. C. Ridgway, P. Kluth, J. W. Ager, D. C. Chrzan and E. E. Haller "*Large Melting-Point Hysteresis of Ge Nanocrystals Embedded in SiO<sub>2</sub>.*" Phys. Rev. Lett. 97, **2006**, 155701.

196. S. W. Marshall and R. M. Wilenzick "Effect of Crystal Size on Mössbauer Recoil-Free Fraction in Au<sup>197</sup>." Phys. Rev. Lett. 16, **1966**, 219-221.
197. K. Lu and Z. H. Jin "Melting and superheating of low-dimensional materials." Curr. Opin. Solid St. M. 5, **2001**, 39-44.
198. R. W. Cahn "Melting and the Surface." Nature 323, **1986**, 668.
199. M. Newville "IFEFFIT : interactive XAFS analysis andFEFFfitting." J. Synchrotron Rad. 8, **2001**, 322-324.
200. A. I. Frenkel, C. W. Hills and R. G. Nuzzo "A View from the Inside: Complexity in the Atomic Scale Ordering of Supported Metal Nanoparticles." J. Phys. Chem. B. 105, **2001**, 12689.
201. E. Sevillano, H. Meuth and J. J. Rehr "Extended x-ray absorption fine structure Debye-Waller factors. I. Monatomic crystals." Phys. Rev. B 20, **1979**, 4908-4911.
202. P. P. Lottici "Extended x-ray-absorption fine-structure Debye-Waller factors and vibrational density of states in amorphous arsenic." Phys. Rev. B 35, **1987**, 1236-1241.
203. A. I. Frenkel and J. J. Rehr "Thermal expansion and x-ray-absorption fine-structure cumulants." Phys. Rev. B 48, **1993**, 585-588.
204. A. L. Ankudinov, J. J. Rehr, J. J. Low and S. R. Bare "Sensitivity of Pt x-ray absorption near edge structure to the morphology of small Pt clusters." J. Chem. Phys. 116, **2002**, 1911-1919.
205. H. Kuroda, T. Yokoyama, K. Asakura and Y. Iwasawa "Temperature dependence of EXAFS spectra of supported small metal particles." Farady Discuss. 92, **1991**, 189.
206. A. Jentys "Estimation of mean size and shape of small metal particles by EXAFS." Phys. Chem. Chem. Phys. 1, **1999**, 4059.
207. Z. H. Jin and K. Lu, *Encyclopedia of Materials: Science and Technology* **2002**, Amsterdam: Elsevier.
208. Y. S. Touloukian, *Thermophysical Properties of Matter*. Vol. 12. **1975**, New York: Plenum Press.

209. W. Y. Ching, L. Ouyang, P. Rulis and H. Yao "Ab initio study of the physical properties of  $\gamma$ - $\text{Al}_2\text{O}_3$ : Lattice dynamics, bulk properties, electronic structure, bonding, optical properties, and ELNES/XANES spectra." *Phys. Rev. B* 78, **2008**, 014106.
210. Q. S. Mei, S. C. Wang, H. T. Cong, Z. H. Jin and K. Lu "Determination of pressure effect on the melting point elevation of Al nanoparticles encapsulated in  $\text{Al}_2\text{O}_3$  without epitaxial interface." *Phys. Rev. B* 70, **2004**, 125421.
211. S. I. Ahmed, G. Dalba, P. Fornasini, M. Vaccari, F. Rocca, A. Sanson, J. Li and A. W. Sleight "Negative thermal expansion in crystals with the delafossite structure: An extended x-ray absorption fine structure study of  $\text{CuScO}_2$  and  $\text{CuLaO}_2$ ." *Phys. Rev. B* 79, **2009**, 104302.
212. G. Beni and P. M. Platzman "Temperature and polarization dependence of extended x-ray absorption fine-structure spectra." *Phys. Rev. B* 14, **1976**, 1514-1518.
213. R. Heid and K. P. Bohnen "*Ab initio* lattice dynamics of metal surfaces." *Phys. Rep.* 387, **2003**, 151-213.
214. M. Alcántara Ortigoza, G. Shafai and T. S. Rahman, **2011**.
215. G. Shafai, S. Hong, M. Bertino and T. S. Rahman "*Effect of Ligands on the Geometric and Electronic Structure of  $\text{Au}_{13}$  Clusters.*" *J. Phys. Chem. C* 113, **2009**, 12072-12078.
216. G. A. Narvaez, J. Kim and J. W. Wilkins "*Effects of morphology on phonons in nanoscopic silver grains.*" *Phys. Rev. B* 72, **2005**, 155411.
217. H. Rosner and G. Wilde "The impact of altered interface structures on the melting behaviour of embedded nanoparticles." *Scripta Mater.* 55, **2006**, 119-122.
218. D. Bazin, D. Sayers, J. J. Rehr and C. Mottet "Numerical Simulation of the Platinum LIII Edge White Line Relative to Nanometer Scale Clusters." *J. Phys. Chem. B* 101, **1997**, 5332-5336.
219. J. Zhou, X. Zhou, X. Sun, R. Li, M. Murphy, Z. Ding, X. Sun and T.-K. Sham "*Interaction between Pt nanoparticles and carbon nanotubes – An X-ray absorption near edge structures (XANES) study.*" *Chem. Phys. Lett.* 437, **2007**, 229-232.



220. M. W. Tew, J. T. Miller and J. A. van Bokhoven "Particle Size Effect of Hydride Formation and Surface Hydrogen Adsorption of Nanosized Palladium Catalysts: L3Edge vs K Edge X-ray Absorption Spectroscopy." *J. Phys. Chem. C* 113, **2009**, 15140-15147.
221. D. E. Ramaker, B. L. Mojet, M. T. Garriga Oostenbrink, J. T. Miller and D. C. Koningsberger "Contribution of shape resonance and Pt-H EXAFS in the Pt L2,3 X-ray absorption edges of supported Pt particles: Application and consequences for catalyst characterization." *Phys. Chem. Chem. Phys.* 1, **1999**, 2293-2302.
222. K. Asakura, T. Kubota, W. J. Chun, Y. Iwasawa, K. Ohtani and T. Fujikawa "*Pt L3-edge XANES studies about the hydrogen adsorption on small Pt particles.*" *J. Synchrotron Rad.* 6, **1999**, 439-441.
223. Y. Lei, J. Jelic, L. C. Nitsche, R. Meyer and J. Miller "Effect of Particle Size and Adsorbates on the L3, L2 and L1 X-ray Absorption Near Edge Structure of Supported Pt Nanoparticles." *Top. Catal.* 54, **2011**, 334-348.
224. C. G. Zhou, J. P. Wu, A. H. Nie, R. C. Forrey, A. Tachibana and H. S. Cheng "*On the sequential hydrogen dissociative chemisorption on small platinum clusters: A density functional theory study.*" *J. Phys. Chem. C* 111, **2007**, 12773-12778.
225. A. L. Ankudinov, J. J. Rehr, J. J. Low and S. R. Bare "*Pt L-edge XANES as a probe of Pt clusters.*" *J. Synchrotron Rad.* 8, **2001**, 578-580.
226. N. Guo, B. R. Fingland, W. D. Williams, V. F. Kispersky, J. Jelic, W. N. Delgass, F. H. Ribeiro, R. J. Meyer and J. T. Miller "*Determination of CO, H<sub>2</sub>O and H<sub>2</sub> coverage by XANES and EXAFS on Pt and Au during water gas shift reaction.*" *Phys. Chem. Chem. Phys.* 12, **2010**, 5678-5693.
227. D. E. Ramaker and D. C. Koningsberger "The atomic AXAFS and Delta mu XANES techniques as applied to heterogeneous catalysis and electrocatalysis." *Phys. Chem. Chem. Phys.* 12, **2010**, 5514-5534.
228. E. Bus and J. A. van Bokhoven "Hydrogen chemisorption on supported platinum, gold, and platinum-gold-alloy catalysts." *Phys. Chem. Chem. Phys.* 9, **2007**, 2894.

229. T. Kubota, K. Asakura, N. Ichikuni and Y. Iwasawa "A new method for quantitative characterization of adsorbed hydrogen on Pt particles by means of Pt L-edge XANES." *Chem. Phys. Lett.* 256, **1996**, 445-448.
230. J. A. van Bokhoven and J. T. Miller "d Electron Density and Reactivity of the d Band as a Function of Particle Size in Supported Gold Catalysts." *J. Phys. Chem. C* 111, **2007**, 9245-9249.
231. N. Ichikuni and Y. Iwasawa "In situ d electron density of Pt particles on supports by XANES." *Catal. Lett.* 20, **1993**, 87-95.
232. A. L. Ankudinov, J. J. Rehr, J. J. Low and S. R. Bare "*Theoretical interpretation of XAFS and XANES in Pt clusters.*" *Top. Catal.* 18, **2002**, 3-7.
233. M. K. Oudenhuijzen, J. A. van Bokhoven, J. T. Miller, D. E. Ramaker and D. C. Koningsberger "Three-Site Model for Hydrogen Adsorption on Supported Platinum Particles: Influence of Support Ionicity and Particle Size on the Hydrogen Coverage." *J. Am. Chem. Soc.* 127, **2005**, 1530-1540.
234. T. Kubota, K. Asakura and Y. Iwasawa "Quantitative analysis of hydrogen adsorbed on Pt particles on SiO<sub>2</sub> in the presence of coadsorbed CO by means of L<sub>3</sub>-edge X-ray absorption near-edge structure spectroscopy." *Catal. Lett.* 46, **1997**, 141-144.
235. N. Schweitzer, H. Xin, E. Nikolla, J. T. Miller and S. Linic "Establishing Relationships Between the Geometric Structure and Chemical Reactivity of Alloy Catalysts Based on Their Measured Electronic Structure." *Top. Catal.* 53, **2010**, 348-356.
236. M. S. Nashner, A. I. Frenkel, D. L. Adler, J. R. Shapley and R. G. Nuzzo "Structural Characterization of Carbon-Supported Platinum–Ruthenium Nanoparticles from the Molecular Cluster Precursor PtRu<sub>5</sub>C(CO)<sub>16</sub>." *J. Am. Chem. Soc.* 119, **1997**, 7760-7771.
237. M. S. Nashner, D. M. Somerville, P. D. Lane, D. L. Adler, J. R. Shapley and R. G. Nuzzo "*Bimetallic Catalyst Particle Nanostructure. Evolution from Molecular Cluster Precursors.*" *J. Am. Chem. Soc.* 118, **1996**, 12964-12974.

238. R. Prins and D. C. Koningsberger, X-ray absorption. Principles, applications, techniques of EXAFS, SEXAFS, and XANES, in X-ray absorption. Principles, applications, techniques of EXAFS, SEXAFS, and XANES, D.C. Koningsberger and R. Prins, Editors. 1988, Wiley: New York.
239. J. T. Miller, B. L. Mojet, D. E. Ramaker and D. C. Koningsberger "A new model for the metal-support interaction - Evidence for a shift in the energy of the valence orbitals." *Catal. Today* 62, **2000**, 101-114.
240. B. L. Mojet, J. T. Miller, D. E. Ramaker and D. C. Koningsberger "A *new model describing the metal-support interaction in noble metal catalysts.*" *J. Catal.* 186, **1999**, 373-386.
241. M. Vaarkamp, B. L. Mojet, M. J. Kappers, J. T. Miller and D. C. Koningsberger "Hydrogen as a Modifier of the Structure and Electronic Properties of Platinum in Acidic Zeolite LTL: A Combined Infrared and X-ray Absorption Spectroscopy Study." *J. Phys. Chem.* 99, **1995**, 16067-16075.
242. A. N. Mansour, J. W. Cook and D. E. Sayers "Quantitative Technique for the Determination of the Number of Unoccupied D-Electron States in a Platinum Catalyst Using the L<sub>2,3</sub> X-Ray Absorption-Edge Spectra." *J. Phys. Chem.* 88, **1984**, 2330-2334.
243. L. Chen, A. C. Cooper, G. P. Pez and H. Cheng "*Density Functional Study of Sequential H<sub>2</sub> Dissociative Chemisorption on a Pt<sub>6</sub> Cluster.*" *J. Phys. Chem. C* 111, **2007**, 5514-5519.
244. A. Vargas, G. Santarossa and A. Baiker "Ab Initio Molecular Dynamics investigation of the Coadsorption of Acetaldehyde and Hydrogen on a Platinum Nanocluster." *J. Phys. Chem. C* 115, **2011**, 10661-10667.
245. C. Mager-Maury, C. Chizallet, P. Sautet and P. Raybaud "Platinum Nanoclusters Stabilized on  $\gamma$ -Alumina by Chlorine Used As a Capping Surface Ligand: A Density Functional Theory Study." *ACS. Catal.* 2, **2012**, 1346-1357.
246. M. Vaarkamp, J. T. Miller, F. S. Modica, G. S. Lane and D. C. Koningsberger "*The Influence of Metal-Support Interactions on the Whiteline Intensity.*" *Jpn. J. Appl. Phys.* 32, Suppl. 32-2, **1993**, 454-456.

247. M. M. Otten, M. J. Clayton and H. H. Lamb "Platinum-Mordenite Catalysts for n-Hexane Isomerization: Characterization by X-Ray Absorption Spectroscopy and Chemical Probes." *J. Catal.* 149, **1994**, 211-222.
248. M. G. Samant and M. Boudart "Support effects on electronic structure of platinum clusters in Y zeolite." *J. Phys. Chem.* 95, **1991**, 4070-4074.
249. A. V. Soldatov, S. Della Longa and A. Bianconi "Relevant Role of Hydrogen-Atoms in the Xanes of Pd Hydride - Evidence of Hydrogen Induced Unoccupied States." *Solid State Commun.* 85, **1993**, 863-868.
250. T. Matsuura, T. Fujikawa and H. Kuroda "Theoretical Studies of the X-Ray Absorption Near-Edge Structures (XANES) of Hydrogen Adsorbed Metals." *J. Phys. Soc. Jpn.* 52, **1983**, 3275-3282.
251. S. R. Bare, S. D. Kelly, F. D. Vila, E. Boldingh, E. Karapetrova, J. Kas, G. E. Mickelson, F. S. Modica, N. Yang and J. J. Rehr "*Experimental (XAS, STEM, TPR, and XPS) and Theoretical (DFT) Characterization of Supported Rhenium Catalysts.*" *J. Phys. Chem. C* 115, **2011**, 5740-5755.
252. F. Behafarid, L. K. Ono, S. Mostafa, J. R. Croy, G. Shafai, S. Hong, T. S. Rahman, S. R. Bare and B. Roldan Cuenya "Electronic properties and charge transfer phenomena in Pt nanoparticles on  $\gamma$ -Al<sub>2</sub>O<sub>3</sub>: size, shape, support, and adsorbate effects." *Phys. Chem. Chem. Phys.* 14, **2012**, 11766.
253. V. R. Cooper, A. M. Kolpak, Y. Yourdshahyan and A. M. Rappe "*Supported metal electronic structure: Implications for molecular adsorption.*" *Phys. Rev. B* 72, **2005**, 081409(R).
254. M. Sugimoto, H. Katsuno, T. Hayasaka, N. Ishikawa and K. Hirasawa "*Electronic-State of Platinum Supported on the Monochlorotrifluoromethane-Treated Alkaline L-Zeolite.*" *Appl. Catal. A-Gen.* 102, **1993**, 167-180.
255. D. C. Koningsberger, J. de Graaf, B. L. Mojet, D. E. Ramaker and J. T. Miller "The metal-support interaction in Pt/Y zeolite: evidence for a shift in energy of metal d-valence orbitals by Pt-H shape resonance and atomic XAFS spectroscopy." *Appl. Catal. A-Gen.* 191, **2000**, 205-220.
256. L. Spenadel and M. Boudart "*Dispersion of Platinum on Supported Catalysts.*" *J. Phys. Chem.* 64, **1960**, 204-207.

257. B. J. Kip, F. B. M. Duivenvoorden, D. C. Koningsberger and R. Prins "Determination of Metal-Particle Size of Highly Dispersed Rh, Ir, and Pt Catalysts by Hydrogen Chemisorption and Exafs." *J. Catal.* 105, **1987**, 26-38.
258. X. Liu, H. Dilger, R. A. Eichel, J. Kunstmann and E. Roduner "A small paramagnetic platinum cluster in an NaY zeolite: characterization and hydrogen adsorption and desorption." *J. Phys. Chem. B* 110, **2006**, 2013-2023.
259. J. H. Kwak, J. Hu, D. Mei, C.-W. Yi, D. H. Kim, C. H. F. Peden, L. F. Allard and J. Szanyi "*Coordinatively Unsaturated Al<sup>3+</sup> Centers as Binding Sites for Active Catalyst Phases of Platinum on  $\gamma$ -Al<sub>2</sub>O<sub>3</sub>.*" *Science* 325, **2009**, 1670-3.
260. H.-J. Freund "*Adsorption of Gases on Complex Solid Surfaces.*" *Angew. Chem. Int. Edit. Engl.* 36, **1997**, 452-475.
261. V. I. Parvulescu, P. Grange and B. Delmon "*Catalytic removal of NO.*" *Catal. Today* 46, **1998**, 233-316.
262. G. A. Somorjai and J. Y. Park "*Molecular Factors of Catalytic Selectivity.*" *Angew. Chem. Int. Ed. Engl.* 47, **2008**, 9212-9228.
263. F. Zaera "The New Materials Science of Catalysis: Toward Controlling Selectivity by Designing the Structure of the Active Site." *J. Phys. Chem. Lett.* 1, **2010**, 621-627.
264. A. K. Santra and D. W. Goodman "*Oxide-supported metal clusters: models for heterogeneous catalysts.*" *J. Phys: Condens. Mat.* 15, **2003**, R31-R62.
265. H.-J. Freund "Metal-supported ultrathin oxide film systems as designable catalysts and catalyst supports." *Surf. Sci.* 601, **2007**, 1438-1442.
266. J. K. Norskov, T. Bligaard, J. Rossmeisl and C. H. Christensen "*Towards the computational design of solid catalysts.*" *Nat. Chem.* 1, **2009**, 37-46.
267. D. C. Koningsberger and B. C. Gates "Nature of the metal-support interface in supported metal catalysts: Results from X-ray absorption spectroscopy." *Catal. Lett.* 14, **1992**, 271-277.
268. K. P. McKenna and A. L. Shluger "*Shaping the morphology of gold nanoparticles by CO adsorption.*" *J. Phys. Chem. C* 111, **2007**, 18848-18852.

269. M. A. Newton, C. Belver-Coldeira, A. Martinez-Arias and M. Fernandez-Garcia "Dynamic in situ observation of rapid size and shape change of supported Pd nanoparticles during CO/NO cycling." *Nat. Mater.* 6, **2007**, 528-532.
270. M. A. Newton, M. D. Michiel, A. Kubacka and M. Fernandez-Garcia "Combining Time-Resolved Hard X-ray Diffraction and Diffuse Reflectance Infrared Spectroscopy To Illuminate CO Dissociation and Transient Carbon Storage by Supported Pd Nanoparticles during CO/NO Cycling." *J. Am. Chem. Soc.* 132, **2010**, 4540-4541.
271. P. Nolte, A. Stierle, N. Y. Jin-Phillip, N. Kasper, T. U. Schulli and H. Dosch "Shape Changes of Supported Rh Nanoparticles During Oxidation and Reduction Cycles." *Science* 321, **2008**, 1654-1658.
272. F. Mittendorfer, N. Seriani, O. Dubay and G. Kresse "Morphology of mesoscopic Rh and Pd nanoparticles under oxidizing conditions." *Phys. Rev. B* 76, **2007**, 233413.
273. S. Giorgio, M. Cabie and C. R. Henry "Dynamic observations of Au catalysts by environmental electron microscopy." *Gold Bull.* 41, **2008**, 167-173.
274. S. Giorgio, S. Sao Joao, S. Nitsche, D. Chaudanson, G. Sitja and C. R. Henry "Environmental electron microscopy (ETEM) for catalysts with a closed E-cell with carbon windows." *Ultramicroscopy* 106, **2006**, 503-507.
275. P. J. Crutzen and C. Brohl "Catalysis by NO<sub>x</sub> the Main Cause of the Spring to Fall Stratospheric Ozone Decline in the Northern Hemisphere." *J. Phys. Chem. A* 105, **2001**, 1579-1582.
276. A. R. Ravishankara "Introduction: Atmospheric Chemistry Long-Term Issues." *Chem. Rev.* 103, **2003**, 4505-4508.
277. M. Chiron "Effects of Motor Vehicle Pollutants on Health." *Stud. Surf. Sci. Catal.* 30, **1987**, 1-10.
278. D. L. Mauzerall, B. Sultan, N. Kim and D. F. Bradford "NO<sub>x</sub> emissions from large point sources: variability in ozone production, resulting health damages and economic costs." *Atmos. Environ.* 39, **2005**, 2851-2866.
279. A. Fritz and V. Pitchon "The current state of research on automotive lean NO<sub>x</sub> catalysis." *Appl. Catal. B* 13, **1997**, 1-25.

280. J. Fenger "Air pollution in the last 50 years - from local to global." *Atmos. Environ.* 43, **2009**, 13-22.
281. J. A. Geddes, J. G. Murphy and D. K. Wang "Long term changes in nitrogen oxides and volatile organic compounds in Toronto and the challenges facing local ozone control." *Atmos. Environ.* 43, **2009**, 3407-3415.
282. Y. Hu, K. Griffiths and P. R. Norton "Surface science studies of selective catalytic reduction of NO: Progress in the last ten years." *Surf. Sci.* 603, **2009**, 1740-1750.
283. S. Roy, M. S. Hegde and G. Madras "*Catalysis for NO<sub>x</sub> abatement.*" *Appl. Energ.* 86, **2009**, 2283-2297.
284. M. Shelef "Nitric Oxide: Surface Reactions and Removal from Auto Exhaust." *Catal. Rev. Sci. Eng.* 11, **1975**, 1 - 40.
285. M. D. Amiridis, T. J. Zhang and R. J. Farrauto "*Selective catalytic reduction of nitric oxide by hydrocarbons.*" *AApl. Catal. B* 10, **1996**, 203-227.
286. G. Busca, L. Lietti, G. Ramis and F. Berti "Chemical and mechanistic aspects of the selective catalytic reduction of NO<sub>x</sub> by ammonia over oxide catalysts: A review." *Appl. Catal. B* 18, **1998**, 1-36.
287. J. N. Armor "Catalytic Reduction of Nitrogen-Oxides with Methane in the Presence of Excess Oxygen - a Review." *Catal. Today* 26, **1995**, 147-158.
288. R. Burch, J. P. Breen and F. C. Meunier "A review of the selective reduction of NO<sub>x</sub> with hydrocarbons under lean-burn conditions with non-zeolitic oxide and platinum group metal catalysts." *Appl. Catal. B* 39, **2002**, 283-303.
289. R. Burch "Knowledge and know-how in emission control for mobile applications." *Catal. Rev. Sc. Eng.* 46, **2004**, 271-333.
290. J. P. Breen and R. Burch "A review of the effect of the addition of hydrogen in the selective catalytic reduction of NO<sub>x</sub> with hydrocarbons on silver catalysts." *Top. Catal.* 39, **2006**, 53-58.
291. G. Centi and S. Perathoner "Opportunities and prospects in the chemical recycling of carbon dioxide to fuels." *Catal. Today* 148, **2009**, 191-205.

292. H. S. Gandhi, G. W. Graham and R. W. McCabe "Automotive exhaust catalysis." J. Catal. 216, **2003**, 433-442.
293. F. Garin "Environmental catalysis." Catal. Today 89, **2004**, 255-268.
294. F. Garin "Mechanism of NO<sub>x</sub> decomposition." Appl. Catal. A-Gen. 222, **2001**, 183-219.
295. R. M. Heck "Catalytic abatement of nitrogen oxides-stationary applications." Catal. Today 53, **1999**, 519-523.
296. Y. Traa, B. Burger and J. Weitkamp "Zeolite-based materials for the selective catalytic reduction of NO<sub>x</sub> with hydrocarbons." Micropor. Mesopor. Mat. 30, **1999**, 3-41.
297. R. W. McCabe and J. M. Kisenyi "Advances in Automotive Catalyst Technology." **1995**, 605-608.
298. Z.-P. Liu, S. J. Jenkins and D. A. King "Why Is Silver Catalytically Active for NO Reduction? A Unique Pathway via an Inverted (NO)<sub>2</sub> Dimer." J. Am. Chem. Soc. 126, **2004**, 7336-7340.
299. D. Sengupta, J. B. Adams, W. F. Schneider and K. C. Hass "Theoretical Analysis of N<sub>2</sub>O to N<sub>2</sub> Conversion During the Catalytic Decomposition of NO by Cu-Zeolites." Catal. Lett. 74, **2001**, 193-199.
300. H. Bosch and F. Janssen "Formation and control of nitrogen oxides." Catal. Today 2, **1988**, 369-379.
301. F. Janssen and R. Meijer "Quality control of DeNO<sub>x</sub> catalysts: Performance testing, surface analysis and characterization of DeNO<sub>x</sub> catalysts." Catal. Today 16, **1993**, 157-185.
302. P. Granger, F. Dhainaut, S. Pietrzik, P. Malfoy, A. Mamede, L. Leclercq and G. Leclercq "An overview: Comparative kinetic behaviour of Pt, Rh and Pd in the NO+CO and NO+H<sub>2</sub> reactions." Top. Catal. 39, **2006**, 65-76.
303. B. K. Cho "Mechanistic Importance of Intermediate N<sub>2</sub>O + CO Reaction in Overall NO + CO Reaction System .: II. Further Analysis and Experimental Observations." J. Catal. 148, **1994**, 697-708.



304. A. Ali, W. Alvarez, C. J. Loughran and D. E. Resasco "State of Pd on H-ZSM-5 and other acidic supports during the selective reduction of NO by CH<sub>4</sub> studied by EXAFS/XANES." Appl. Catal. B 14, **1997**, 13-22.
305. E. A. Lombardo, G. A. Sill, J. L. d'Itri and W. K. Hall "The Possible Role of Nitromethane in the SCR of NO<sub>x</sub> with CH<sub>4</sub> over M-ZSM5 (M=Co, H, Fe, Cu)." J. Catal. 173, **1998**, 440-449.
306. T. Miyadera "Alumina-supported silver catalysts for the selective reduction of nitric oxide with propene and oxygen-containing organic compounds." Appl. Catal. B 2, **1993**, 199-205.
307. F. Klingstedt, K. Eränen, L. E. Lindfors, S. Andersson, L. Cider, C. Landberg, E. Jobson, L. Eriksson, T. Ilkenhans and D. Webster "A highly active Ag/alumina catalytic converter for continuous HC-SCR during lean-burn conditions: from laboratory to full-scale vehicle tests." Top. Catal. 30-31, **2004**, 27-30.
308. W. C. Hecker and A. T. Bell "Reduction of NO by H<sub>2</sub> over silica-supported rhodium: Infrared and kinetic studies." J. Catal. 92, **1985**, 247-259.
309. C. A. de Wolf and B. E. Nieuwenhuys "Oscillatory behaviour in the NO-hydrogen reactions over Pt-group metal surfaces." Catal. Today 70, **2001**, 287-300.
310. B. Frank, G. Emig and A. Renken "Kinetics and mechanism of the reduction of nitric oxides by H<sub>2</sub> under lean-burn conditions on a Pt–Mo–Co/α-Al<sub>2</sub>O<sub>3</sub> catalyst." Appl. Catal. B 19, **1998**, 45-57.
311. R. B. Getman and W. F. Schneider "DFT-Based Characterization of the Multiple Adsorption Modes of Nitrogen Oxides on Pt(111)." J. Phys. Chem. C 111, **2007**, 389-397.
312. M. Shelef and H. S. Gandhi "Ammonia Formation in Catalytic Reduction of Nitric Oxide by Molecular Hydrogen. II. Noble Metal Catalysts." Ind. Eng. Chem. Prod. Res. Dev. 11, **1972**, 393-396.
313. K. C. Taylor and R. L. Klimisch "The catalytic reduction of nitric oxide over supported ruthenium catalysts." J. Catal. 30, **1973**, 478-484.
314. G. Pirug and H. P. Bonzel "A low-pressure study of the reduction of NO by H<sub>2</sub> on polycrystalline platinum." J. Catal. 50, **1977**, 64-76.

315. J. Rempel, J. Greeley, L. B. Hansen, O. H. Nielsen, J. K. Norskov and M. Mavrikakis "Step Effects on the Dissociation of NO on Close-Packed Rhodium Surfaces." J. Phys. Chem. C 113, **2009**, 20623-20631.
316. T. P. Kobylinski and B. W. Taylor "The catalytic chemistry of nitric oxide : II. Reduction of nitric oxide over noble metal catalysts." J. Catal. 33, **1974**, 376-384.
317. S. Roy, M. S. Hegde, S. Sharma, N. P. Lalla, A. Marimuthu and G. Madras "Low temperature NO<sub>x</sub> and N<sub>2</sub>O reduction by H<sub>2</sub>: Mechanism and development of new nano-catalysts." Appl. Catal. B 84, **2008**, 341-350.
318. J.-B. Yang, O.-Z. Fu, D.-Y. Wu and S.-D. Wang "DRIFTS study of NO-H<sub>2</sub> reaction over Pd/Al<sub>2</sub>O<sub>3</sub> with excess oxygen." Appl. Catal. B 49, **2004**, 61-65.
319. D. D. Miller and S. S. C. Chuang "Pulse Transient Responses of NO Decomposition and Reduction with H<sub>2</sub> on Ag-Pd/Al<sub>2</sub>O<sub>3</sub>." J. Phys. Chem. C 113, **2009**, 14963-14971.
320. F. Dhainaut, S. Pietrzyk and P. Granger "Kinetics of the NO+H<sub>2</sub> reaction over supported noble metal based catalysts: Support effect on their adsorption properties." Appl. Catal. B 70, **2007**, 100-110.
321. A. Ueda, T. Nakao, M. Azuma and T. Kobayashi "Two conversion maxima at 373 and 573 K in the reduction of nitrogen monoxide with hydrogen over Pd/TiO<sub>2</sub> catalyst." Catal. Today 45, **1998**, 135-138.
322. N. Macleod, R. Cropley, J. M. Keel and R. M. Lambert "Exploiting the synergy of titania and alumina in lean NO<sub>x</sub> reduction: in situ ammonia generation during the Pd/TiO<sub>2</sub>/Al<sub>2</sub>O<sub>3</sub>-catalysed H<sub>2</sub>/CO/NO/O<sub>2</sub> reaction." J. Catal. 221, **2004**, 20-31.
323. M. Meng, P. Lin and Y. Fu "The catalytic removal of CO and NO over Co-Pt(Pd, Rh)/γ-Al<sub>2</sub>O<sub>3</sub> catalysts and their structural characterizations." Catal. Lett. 48, **1997**, 213-222.
324. K. Okumura, R. Yoshimoto, K. Suzuki and M. Niwa "Selective Catalytic Reduction of NO by Methane over Pd Loaded on Heteropolyacids/SiO<sub>2</sub> at Low Temperature." Bull. Chem. Soc. Jpn. 78, **2005**, 361-366.

325. B. J. Savatsky and A. T. Bell, *Nitric-Oxide Reduction by Hydrogen over Rhodium Using Transient-Response Techniques*, in *Catalysis Under Transient Conditions*, Catalysis Under Transient Conditions, ACS Symposium Series, Vol. 178, 1982. p. 105-141.
326. K. Okumura, J. Amano, N. Yasunobu and M. Niwa "X-ray Absorption Fine Structure Study of the Formation of the Highly Dispersed PdO over ZSM-5 and the Structural Change of Pd Induced by Adsorption of NO." *J. Phys. Chem. B* 104, **2000**, 1050-1057.
327. L. J. Lobree, A. W. Aylor, J. A. Reimer and A. T. Bell "*NO Reduction by CH<sub>4</sub> in the Presence of O<sub>2</sub> over Pd-H-ZSM-5.*" *J. Catal.* 181, **1999**, 189-204.
328. B. J. Adelman and W. M. H. Sachtler "The effect of zeolitic protons on NO<sub>x</sub> reduction over Pd/ZSM-5 catalysts." *Appl. Catal. B* 14, **1997**, 1-11.
329. M. Ogura, M. Hayashi and E. Kikuchi "Role of zeolite structure on reduction of NO<sub>x</sub> with methane over In- and Pd-based catalysts." *Catal. Today* 45, **1998**, 139-145.
330. N. Macleod, R. Cropley and R. M. Lambert "Efficient Reduction of NO<sub>x</sub> by H<sub>2</sub> Under Oxygen-Rich Conditions over Pd/TiO<sub>2</sub> Catalysts: An in situ DRIFTS Study." *Catal. Lett.* 86, **2003**, 69-75.
331. Y. H. Chin, A. Pisanu, L. Serventi, W. E. Alvarez and D. E. Resasco "*NO reduction by CH<sub>4</sub> in the presence of excess O<sub>2</sub> over Pd/sulfated zirconia catalysts.*" *Catal. Today* 54, **1999**, 419-429.
332. Y. Nishihata, J. Mizuki, T. Akao, H. Tanaka, M. Uenishi, M. Kimura, T. Okamoto and N. Hamada "*Self-regeneration of a Pd-perovskite catalyst for automotive emissions control.*" *Nature* 418, **2002**, 164-167.
333. A. W. Aylor, L. J. Lobree, J. A. Reimer and A. T. Bell "*Investigations of the Dispersion of Pd in H-ZSM-5.*" *J. Catal.* 172, **1997**, 453-462.
334. K. Okumura, R. Yoshimoto, T. Uruga, H. Tanida, K. Kato, S. Yokota and M. Niwa "*Energy-Dispersive XAFS Studies on the Spontaneous Dispersion of PdO and the Formation of Stable Pd Clusters in Zeolites.*" *J. Phys. Chem. B* 108, **2004**, 6250-6255.

335. F. Boccuzzi, E. Guglielminotti, G. Martra and G. Cerrato "*Nitric-Oxide Reduction by CO on Cu TiO<sub>2</sub> Catalysts.*" J. Catal. 146, **1994**, 449-459.
336. R. Hierl, H. P. Urbach and H. Knozinger "*Chemisorption of Nitric-Oxide on Copper Alumina Catalysts.*" J. Chem. Soc., Faraday Trans. 88, **1992**, 355-360.
337. P. Fornasiero, R. Dimonte, G. R. Rao, J. Kaspar, S. Meriani, A. Trovarelli and M. Graziani "*Rh-Loaded CeO<sub>2</sub>-ZrO<sub>2</sub> Solid-Solutions as Highly Efficient Oxygen Exchangers - Dependence of the Reduction Behavior and the Oxygen Storage Capacity on the Structural-Properties.*" J. Catal. 151, **1995**, 168-177.
338. T. Murota, T. Hasegawa, S. Aozasa, H. Matsui and M. Motoyama "*Production Method of Cerium Oxide with High Storage Capacity of Oxygen and Its Mechanism.*" J. Alloy. Compd. 193, **1993**, 298-299.
339. S. H. Oh and C. C. Eickel "Influence of Metal-Particle Size and Support on the Catalytic Properties of Supported Rhodium - CO-O<sub>2</sub> and CO-NO Reactions." J. Catal. 128, **1991**, 526-536.
340. X. P. Xu and D. W. Goodman "The Effect of Particle-Size on Nitric-Oxide Decomposition and Reaction with Carbon-Monoxide on Palladium Catalysts." Catal. Lett. 24, **1994**, 31-35.
341. S.-H. Chien, M.-C. Kuo, C.-H. Lu and K.-N. Lu "*Spectroscopic studies of NO reduction on Pt/TiO<sub>2</sub> catalysts.*" Catal. Today 97, **2004**, 121-127.
342. M. Newville, P. Livins, Y. Yacoby, J. J. Rehr and E. A. Stern "*Near-edge x-ray-absorption fine structure of Pb: A comparison of theory and experiment.*" Phys. Rev. B 47, **1993**, 14126-14131.
343. W. Setthapun, W. D. Williams, S. M. Kim, H. Feng, J. W. Elam, F. A. Rabuffetti, K. R. Poeppelmeier, P. C. Stair, E. A. Stach, F. H. Ribeiro, J. T. Miller and C. L. Marshall "*Genesis and Evolution of Surface Species during Pt Atomic Layer Deposition on Oxide Supports Characterized by in Situ XAFS Analysis and Waterâˆ“Gas Shift Reaction.*" J. Phys. Chem. C 114, **2010**, 9758-9771.
344. C. A. de Wolf and B. E. Nieuwenhuys "*The NO-H<sub>2</sub> reaction over Pd(111).*" Surf. Sci. 469, **2000**, 196-203.

345. A. Barrera, M. Viniegra, P. Bosch, V. H. Lara and S. Fuentes "Pd/Al<sub>2</sub>O<sub>3</sub>-La<sub>2</sub>O<sub>3</sub> catalysts prepared by sol-gel: characterization and catalytic activity in the NO reduction by H<sub>2</sub>." *Appl. Catal. B* 34, **2001**, 97-111.
346. A. Rose, S. Maniguet, R. J. Mathew, C. Slater, J. Yao and A. E. Russell "*Hydride phase formation in carbon supported palladium nanoparticle electrodes investigated using in situ EXAFS and XRD.*" *Phys. Chem. Chem. Phys.* 5, **2003**, 3220-3225.
347. R. J. Davis, S. M. Landry, J. A. Horsley and M. Boudart "*X-ray-absorption study of the interaction of hydrogen with clusters of supported palladium.*" *Phys. Rev. B* 39, **1989**, 10580-10583.
348. E. Wicke, H. Brodowsky and H. Zuchner, *Hydrogen in Metals II, Vol 29 of Topics in Applied Physics*. Hydrogen in Metals II, Vol 29 of Topics in Applied Physics **1978**, Berlin: Springer.
349. J.-D. Grunwaldt, M. Maciejewski and A. Baiker "*In situ X-ray absorption study during methane combustion over Pd/ZrO<sub>2</sub> catalysts.*" *Phys. Chem. Chem. Phys.* 5, **2003**, 1481-1488.
350. Y. Cao and Z.-X. Chen "Theoretical studies on the adsorption and decomposition of H<sub>2</sub>O on Pd(1 1 1) surface." *Surf. Sci.* 600, **2006**, 4572-4583.
351. J. Kua and W. A. Goddard "Oxidation of Methanol on 2nd and 3rd Row Group VIII Transition Metals (Pt, Ir, Os, Pd, Rh, and Ru): Application to Direct Methanol Fuel Cells." *J. Am. Chem. Soc.* 121, **1999**, 10928-10941.
352. K. Asakura, Y. Iwasawa, S. K. Purnell, B. A. Watson, M. A. Barteau and B. C. Gates "*Zirconium oxide supported on Pd(100): Characterization by scanning tunneling microscopy and tunneling spectroscopy.*" *Catal. Lett.* 15, **1992**, 317-327.
353. S. T. Homeyer and W. M. H. Sachtler "Elementary steps in the formation of highly dispersed palladium in NaY : I. Pd ion coordination and migration." *J. Catal.* 117, **1989**, 91-101.
354. M. Che, J. F. Dutel, P. Gallezot and M. Primet "A study of the chemisorption of nitric oxide on PdY zeolite. Evidence for a room temperature oxidative dissolution of palladium crystallites." *J. Phys. Chem.* 80, **1976**, 2371-2381.

355. M. J. Rice, A. K. Chakraborty and A. T. Bell "Site Availability and Competitive Siting of Divalent Metal Cations in ZSM-5." *J. Catal.* 194, **2000**, 278-285.
356. L. Xiao and W. F. Schneider "Influence of [alpha]-alumina supports on oxygen binding to Pd, Ag, Pt, and Au." *Chem. Phys. Lett.* 484, **2010**, 231-236.
357. A. V. Ivanov and L. M. Kustov "Influence of support acidity on electronic state of platinum in oxide systems promoted by  $\text{SO}_4^{2-}$  anions." *Russ. Chem. Bull.* 47, **1998**, 1061-1066.
358. E. Carrasco, M. A. Brown, M. Sterrer, H.-J. Freund, K. Kwapien, M. Sierka and J. Sauer "Thickness-Dependent Hydroxylation of  $\text{MgO}(001)$  Thin Films." *J. Phys. Chem. C* 114, **2010**, 18207-18214.
359. M. C. R. Jensen, K. Venkataramani, S. Helveg, B. S. Clausen, M. Reichling, F. Besenbacher and J. V. Lauritsen "Morphology, Dispersion, and Stability of Cu Nanoclusters on Clean and Hydroxylated  $\alpha\text{-Al}_2\text{O}_3(0001)$  Substrates." *J. Phys. Chem. C* 112, **2008**, 16953-16960.
360. M. Heemeier, S. Stempel, S. K. Shaikhutdinov, J. Libuda, M. Bäumer, R. J. Oldman, S. D. Jackson and H. J. Freund "On the thermal stability of metal particles supported on a thin alumina film." *Surf. Sci.* 523, **2003**, 103-110.
361. J. W. Niemantsverdriet, *Spectroscopy in Catalysis* Spectroscopy in Catalysis **1993**: VCH Verlagsgesellschaft mbH, D-69451 Weinheim, Federal Republic of Germany. 265.
362. C. Dujardin, A. S. Mamede, E. Payen, B. Sombret, J. P. Huvenne and P. Granger "Influence of the Oxidation State of Rhodium in Three-Way Catalysts on Their Catalytic Performances: An in situ FTIR and Catalytic Study." *Top. Catal.* 30-31, **2004**, 347-352.

## LIST OF PUBLICATIONS

1. S. Porsgaard, L. R. Merte, Luis K. Ono, F. Behafarid, J. Matos, S. Helveg, M. Salmeron, B. Roldan Cuenya, and F. Besenbacher, "Stability of Pt Nanoparticles Supported on SiO<sub>2</sub>/Si(111): A high pressure x-ray photoelectron spectroscopy study" ACS nano 2012 accepted.
2. L.R. Merte, F. Behafarid, D.J. Miller, D. Friebel, S. Cho, F. Mbuga, D. Sokaras, R. Alonso-Mori, T.-C. Weng, D. Nordlund, Anders Nilsson, B. Roldan Cuenya "Electrochemical oxidation of size-selected Pt nanoparticles studied using in situ high-energy-resolution x-ray absorption spectroscopy." ACS Catal. 2, 2012, 2371–2376.
3. F. Behafarid, B. Roldan Cuenya "Nano Pinstripes: TiO<sub>2</sub> Nanostripe Formation by Nanoparticle-Mediated Pinning of Step Edges.", J. Phys. Chem. Lett. 3, **2012**, 608-612.
4. J. Matos, L. K. Ono, F. Behafarid, J. R. Croy, S. Mostafa, A. T. DeLaRiva, A. K. Datye, A. I. Frenkel and B. Roldan Cuenya "In situ coarsening study of inverse micelle-prepared Pt nanoparticles supported on  $\gamma$ -Al<sub>2</sub>O<sub>3</sub>: pretreatment and environmental effects." Phys. Chem. Chem. Phys. 14, **2012**, 11457-11467.
5. F. Behafarid, L. K. Ono, S. Mostafa, J. R. Croy, G. Shafai, S. Hong, T. S. Rahman, S. R. Bare and B. Roldan Cuenya "Electronic properties and charge transfer phenomena in Pt nanoparticles on  $\gamma$ -Al<sub>2</sub>O<sub>3</sub>: size, shape, support, and adsorbate effects." Phys. Chem. Chem. Phys. 14, **2012**, 11766.
6. B. Roldan Cuenya, M. Alcántara Ortigoza, L. Ono, F. Behafarid, S. Mostafa, J. Croy, K. Paredis, G. Shafai, T. Rahman, L. Li, Z. Zhang and J. Yang "Thermodynamic properties of Pt nanoparticles: Size, shape, support, and adsorbate effects." Phys. Rev. B 84, **2011**, 245438.
7. K. Paredis, L. K. Ono, F. Behafarid, Z. F. Zhang, J. C. Yang, A. I. Frenkel and B. Roldan Cuenya "Evolution of the Structure and Chemical State of Pd Nanoparticles during the in Situ Catalytic Reduction of NO with H<sub>2</sub>." J. Am. Chem. Soc. 133, **2011**, 13455-13464.

8. F. Behafarid and B. Roldan Cuenya "Coarsening Phenomena of Metal Nanoparticles and the Influence of the Support Pre-treatment: Pt/TiO<sub>2</sub>(110 )." Surf. Sci. 606, **2011**, 908-918.
9. F. Behafarid and B. Roldan Cuenya "Nanoepitaxy Using Micellar Nanoparticles." Nano Lett 11, **2011**, 5290-5296.
10. B. Roldan Cuenya, A. I. Frenkel, S. Mostafa, F. Behafarid, J. R. Croy, L. K. Ono and Q. Wang "Anomalous lattice dynamics and thermal properties of supported, size-and shape selected Pt nanoparticles." Phys. Rev. B 82, **2010**, 155450.
11. B. Roldan Cuenya, J. R. Croy, S. Mostafa, F. Behafarid, L. Li, Z. Zhang, J. C. Yang, Q. Wang and A. I. Frenkel "Solving the structure of size-selected Pt nanocatalysts synthesized by inverse micelle encapsulation." J. Am. Chem. Soc. 132, **2010**, 8747.
12. S. Mostafa, F. Behafarid, J. R. Croy, L. K. Ono, L. Li, J. C. Yang, A. I. Frenkel and B. Roldan Cuenya "Shape-Dependent Catalytic Properties of Pt Nanoparticles." J. Am. Chem. Soc. 132, **2010**, 15714-15719.
13. A. Naitabdi, L. K. Ono, F. Behafarid and B. Roldan Cuenya "Thermal Stability and Segregation Processes in Self-Assembled Size-Selected AuxFe<sub>1-x</sub> Nanoparticles Deposited on TiO<sub>2</sub>(110): Composition Effects." J. Phys. Chem. C 113, **2009**, 1433-1446.
14. A. Naitabdi, F. Behafarid and B. Roldan Cuenya "Enhanced thermal stability and nanoparticle-mediated surface patterning: Pt/TiO<sub>2</sub>(110)." Appl. Phys. Lett. 94, **2009**, 083102.